

Mizellen als Nanoreaktoren für Fluoreszenzlöschungen und Photoionisierungen

Dissertation

zur Erlangung des Doktorgrades der Naturwissenschaften
(Dr. rer. nat.)

der

Naturwissenschaftlichen Fakultät II
Chemie, Physik und Mathematik

der Martin-Luther-Universität
Halle-Wittenberg

vorgelegt von

Herrn Tim Kohlmann
geb. am 28.01.1994 in Dessau

1. Gutachter: Prof. Dr. Martin Goez
2. Gutachter: Prof. Dr. Heiko Ihmels

Halle (Saale), den 28.10.2021

Datum der Verteidigung: 09.03.2022

Vorwort

Die vorliegende Arbeit ist in der Zeit zwischen Februar 2018 und September 2021 in der Arbeitsgruppe von Prof. Dr. Martin Goetz entstanden. Es handelt sich hierbei um eine kumulative Dissertationsschrift, deren Inhalte und Forschungsergebnisse bereits in international anerkannten Zeitschriften publiziert wurden. Die folgende Arbeit soll einen Überblick über die wichtigsten Ergebnisse und deren Einordnung in den gegenwärtigen Forschungsstand geben, sowie eine übergreifende Diskussion und Zusammenfassung darstellen. Details zur experimentellen Arbeit und eine ausführliche Darstellung aller Ergebnisse können den jeweiligen angehängten Publikationen entnommen werden.

Inhaltsverzeichnis

1	Einleitung	1
2	Grundlagen	4
2.1	Mizellen – Eigenschaften, Charakterisierung, Verwendung	4
2.2	Fluoreszenz und Fluoreszenzlöschung	6
2.3	Photoionisierungen und hydratisierte Elektronen	9
3	Ergebnisse und Diskussion	13
3.1	Fluoreszenzlöschung in Mizellen	13
3.1.1	Fluoreszenzlöschung von Pyren mit Viologen in SDS (Publ. A) . .	14
3.1.2	Fluoreszenzlöschung von Pyren mit Viologen in SDS (Publ. B) . .	18
3.1.3	Fluoreszenzlöschung von Pyren mit Methylviologen in <i>n</i> -Alkylsulfaten (Publ. C)	21
3.2	Photoionisierungen in Mizellen	25
3.2.1	Photoionisierung von 2-Aminoanthracen in SDS (Publ. D)	26
3.2.2	Photoionisierung von Quercetin in homogener Lösung und Triton X- 100 Mizellen (Publ. E, F)	30
4	Zusammenfassung	38
5	Literaturverzeichnis	42
6	Abkürzungsverzeichnis	52
7	Anhang	54
7.1	Publikation A	55
7.2	Publikation B	66
7.3	Publikation C	75
7.4	Publikation D	81
7.5	Publikation E	87
7.6	Manuskript F	96

1 Einleitung

Amphiphile Moleküle können spontan zu Mizellen aggregieren, diese weisen dann ein hydrophobes Inneres und eine hydrophile Hülle auf. Mizellen und ihre Lösungen zeigen dadurch ganz andere Eigenschaften als einfache homogene Lösungsmittel und bieten damit eine Vielzahl weiterer Möglichkeiten. Obwohl Mizellen schon lange bekannt^[1,2] und auch viele Grundlagen schon ausgiebig untersucht sind, so bleiben sie immer noch Gegenstand aktueller Forschung. In den letzten 10 Jahren sind laut SciFinder über 3000 Publikationen erschienen, die direkt Mizellen zum Gegenstand haben. Besonders das Bestreben, sie für konkrete Anwendungen zu nutzen, gewinnt an Bedeutung. So können Mizellen als Mikroreaktoren dienen^[3] und zur Katalyse^[4] genutzt oder in der Medizin als Biosensoren zur Diagnostik^[5] und zum Transport von Arzneimitteln im Körper^[6-8] verwendet werden.

Um sie gezielt anzuwenden oder gar maßgeschneidert herstellen zu können, ist ein genaues Verständnis über die physikalischen Eigenschaften der Mizelle von Nöten. Mizellen lassen sich durch mehrere Parameter charakterisieren. Die wichtigsten sind sicherlich die kritische Mizellkonzentration und die Aggregationszahl. Letztere ist besonders von Bedeutung, denn sie ist unmittelbar für die Größe der Mizelle verantwortlich. Typischerweise werden zur Bestimmung der Mizellgröße bzw. der Aggregationszahl Streumethoden verwendet^[9-15]. Aber auch Fluoreszenzmethoden haben sich etabliert^[16-18]. Bei letzteren wird sich häufig zunutze gemacht, dass die dynamische Fluoreszenzlöschung von Mizell-gebundenen Fluorophoren von der Aggregationszahl abhängt. Allerdings sind statische oder kombinierte Löschprozesse oftmals interessanter als rein dynamische^[19-23], welche häufig diffusionskontrolliert und damit unabhängig vom Fluorophor-Löscher-Paar sind. Denn aus der für das statische Löschen nötigen Komplexbildung lassen sich nicht nur Eigenschaften der Mizelle ableiten sondern auch von Fluorophor und Löscher. Für die Beschreibung des dynamischen Löschens in den Mizellen gibt es die akzeptierte Infelta-Tachiya-Theorie, die von einer Poisson-Verteilung von Fluorophor und Löscher über die Mizellen ausgeht^[24-26]. Für statische oder kombinierte Prozesse finden sich in der Literatur hingegen nur wenige konsistente Beschreibungen^[17,27-29].

Das große Potential von Mizellen zeigt sich auch, wenn Moleküle in ihnen nicht nur zur Fluoreszenz angeregt werden, sondern auch bei der Photoionisierung und der damit einhergehenden Erzeugung hydratisierter Elektronen. Das hydratisierte Elektron ist ein Universalreduktionsmittel, welches mit einer Vielzahl von Verbindungen reagieren kann^[30]. Es sind bereits einige wenige Systeme bekannt, die hydratisierte Elektronen katalytisch erzeugen können^[31-36]. So lässt sich durch die Verwendung von SDS beispielsweise ein Photokatalyse-Zyklus basierend auf Tris(bipyridin)ruthenium konstruieren, der mittels einer grünen LED hydratisierte Elektronen erzeugt^[35]. Dieser wurde auch schon für synthetische Anwendungen genutzt^[37,38]. Ein intrinsischer Nachteil ist hier jedoch die sehr geringe vorliegende Konzentration an hydratisierten Elektronen. Verwendet man hingegen Laserlicht zur

Photoionisierung, sind deutlich höhere Konzentrationen und damit auch andere Reaktionen möglich. So zum Beispiel Wurtz-Kupplungen, die eine hohe Konzentration der zu kombinierenden Radikale voraussetzen. Bei der Konstruktion eines katalytischen Systems für solch eine Aufgabe ist aber nicht nur die hohe Elektronenkonzentration von Bedeutung, sondern auch eine möglichst lange Lebenszeit der entstehenden Radikale, um untereinander reagieren zu können. Außerdem sollten sie nicht mit anderen eventuell in der Lösung vorhandenen Spezies abreagieren. Gleichzeitig darf der Katalysator nicht leicht zerstört werden.

Die Photoionisierung bietet allerdings auch einen geschickten Zugang zur Untersuchung von Antioxidantien. Mit Hilfe von Mizellen können hier Spektren von beteiligten Radikalen und Reparaturkinetiken so untersucht werden, als befänden sie sich in biologischen Systemen. Beispielsweise eignen sich Antioxidantien mit phenolischer Struktur gut für solche Untersuchungen. Sie absorbieren in der Regel im UV-A-Bereich (315 – 380 nm) und dort steht mit 355 nm aus einem frequenzverdreifachten Nd:YAG-Laser eine attraktive Ionisierungswellenlänge zur Verfügung. Daher ist hier auch häufig nur eine vergleichsweise geringe Laserintensität nötig, um eine geeignete Konzentration an Radikalen zu erhalten und Nebenreaktionen zu vermeiden. Diese direkte Erzeugung der zu untersuchenden Radikale bietet deutliche Vorteile gegenüber herkömmlichen Inkubationsexperimenten oder einer elektrochemischen oder pulsradiolytischen Erzeugung. Denn mittels Laserblitzlicht-Photolyse können die Radikale innerhalb weniger Nanosekunden sehr homogen erzeugt werden und dann die initialen Prozesse auf einer sehr kurzen Zeitskala verfolgt werden, ohne dass Folgeprodukte stören. Außerdem können leicht Parameter wie Temperatur, pH-Wert oder Lösungszusätze variiert werden. Diese Methode der Erzeugung wurde beispielsweise schon für das Resveratrol^[39] oder das α -Tocopherol^[40], aber auch für nicht-phenolische Antioxidantien wie das Vitamin C genutzt^[41]. Noch nicht verwendet wurde es für die Untersuchung des Super-Antioxidans Quercetin^[42]. Quercetin ist eines der am häufigsten vorkommenden Antioxidantien überhaupt^[43]. Es wird mit einer Reihe von positiven Effekten auf die Gesundheit in Verbindung gebracht^[44]. So soll es antibakterielle^[45], entzündungshemmende^[46], antivirale^[47,48] sowie antitumorale^[49] und Anti-aging^[50] Eigenschaften aufweisen. Allerdings gibt es nur zwei experimentelle kinetische Studien, die sich mit den anfänglichen Prozessen auf sehr kurzer Zeitskala auseinandersetzen^[51,52]. Von Interesse sind aber nicht nur die Antioxidans-Radikale selbst, sondern vor allem auch ihre Wechselwirkung mit anderen Co-Antioxidantien. Hier bietet sich zur Untersuchung Vitamin C an, da es ebenfalls ein sehr verbreitetes Antioxidans ist. Außerdem lassen sich Reaktionen damit sehr gut untersuchen, da das Ascorbat-Monoanion bei der Ionisierungswellenlänge 355 nm nicht absorbiert. Jedoch ist Quercetin schwer wasserlöslich (0,4 mg/l^[53]) und damit auch die Bioverfügbarkeit gering. Diese kann erhöht werden, indem es in einem Carrier eingeschlossen ist oder eine Glykosylierung erfolgt. Solch ein Carrier kann beispielsweise ein Liposom^[54] oder eine Nanoemulsion^[55] oder eben auch eine Mizelle^[56] sein. Im Körper wird die Bioverfügbarkeit beispielsweise durch Mizellen von Bile-Salzen im Dünndarm erhöht^[57]. Aber auch die Gly-

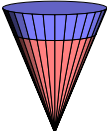
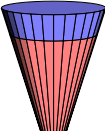
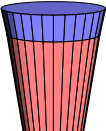
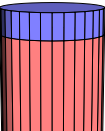
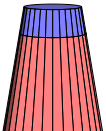
kosylierung macht sich die Natur zu Nutze. Durch sie entsteht beispielsweise das deutlich besser wasserlösliche Rutin (Quercetin-3-O-rutinosid). Neben den glykosylierten Verbindungen sind aber in der Natur auch eine Reihe von methylierten Derivaten anzutreffen. In der Literatur existiert, abgesehen vom Rutin, nur wenig darüber. Insbesondere über ihre Radikale und das Verhalten auf kurzen Zeitskalen sind nur vereinzelt Beiträge zu finden. Die vorliegende Arbeit mit dem zentralen Element der Mizellen behandelt zwei Hauptaspekte: zum einen die Untersuchung und theoretische Beschreibung der kombinierten Fluoreszenzlöschung in Mizellen und zum anderen die Anwendung von Mizellen bei Photoionisierungen. Zur Untersuchung dienen vor allem spektroskopische Methoden wie statische Absorptions- und Fluoreszenzspektroskopie, sowie zeitkorrelierte Einzelphotonenzählung und Nanosekunden-Laserblitzlicht-Photolyse mit optischer Detektion.

2 Grundlagen

2.1 Mizellen – Eigenschaften, Charakterisierung, Verwendung

Amphiphilie beschreibt die Eigenschaft, dass innerhalb eines Moleküls sowohl hydrophile als auch hydrophobe Bereiche auftreten. Amphiphile Substanzen bestehen meist aus einer hydrophilen Kopfgruppe und einem hydrophoben (Alkyl-) Rest. Die Hydrophilie kann entweder durch eine Ladung oder durch stark hydrophile ungeladene Gruppen, vornehmlich Hydroxylgruppen, erreicht werden. Es existieren demzufolge anionische, kationische, zwitterionische und neutrale Amphiphile. Löst man solche Substanzen in ausreichend hoher Konzentration in Wasser, so aggregieren diese Monomere aufgrund des hydrophoben Effektes^[58], so dass der Kontakt der hydrophilen Reste so weit wie möglich reduziert wird und andersherum die hydrophilen Kopfgruppen möglichst maximalen Kontakt zum Wasser haben. Je nach Aufbau des Amphiphils selbst sind so verschiedene Formen von Aggregaten möglich. Einen Einfluss auf die grundsätzliche Form hat vor allem das Verhältnis des Volumens des hydrophoben Restes zur eingenommenen Fläche der Kopfgruppe an der Grenzfläche und diese multipliziert mit der Länge des Restes. Diese Größe wird auch Packungsparameter P genannt^[59]. Tabelle 2.1 zeigt eine Übersicht über die möglichen Verhältnisse und daraus resultierenden Formen. Ist der Packungsparameter $\leq 1/2$, also die Kopfgruppe im Vergleich relativ groß, so bilden sich Mizellen aus.

Tabelle 2.1: Packungsparameter P für exemplarische Amphiphile und daraus resultierende Aggregate.^[59]

P	$\leq 1/3$	$1/3 - 1/2$	$1/2 - 1$	≈ 1	> 1
Monomer					
Aggregat	spherische Mizelle	zylindrische Mizelle	Vesikel, flexible Doppelschichten	planare Doppelschichten	inverse Mizelle
Beispiel	SDS, DTAB	SDS bei hoher Salzkonzentration	α -Lecithin	Phospholipide mit 2 sperrigen Resten, kleinen Kopfgruppen	

Voraussetzung hierfür ist jedoch auch eine ausreichend hohe Konzentration des Amphiphils. Ist sie sehr klein, so kann eine Adsorption an der Wasser-Luft-Grenzfläche, eine Lösung der Einzelmoleküle oder die Bildung premizellarer Cluster^[60,61] beobachtet werden. Erst oberhalb einer bestimmten Konzentration aggregieren die Amphiphile zu Mizellen. Diese wird als kritische Mizellkonzentration (engl. critical micell concentration, cmc) bezeichnet. Um den engen Bereich der cmc verändern sich damit auch zahlreiche physikalische Eigenschaften,

wie Oberflächenspannung, osmotischer Druck, Leitfähigkeit oder Streueigenschaften von Strahlung. Bei ionischen Mizellen liegt die cmc in der Regel im Bereich von $10^{-3} - 10^{-2}$ M und bei nicht-ionischen niedriger bei $10^{-4} - 10^{-3}$ M^[62]. Sie verringert sich mit steigendem hydrophoben Charakter des Monomers und damit auch mit steigender Kettenlänge des Restes. Ein weiterer wichtiger Parameter bei der Bildung von Mizellen ist die Krafft-Temperatur (T_K). Ein einfaches Konzentrations-Temperatur-Phasendiagramm zeigt, dass die Löslichkeit eines Amphiphils mit steigender Temperatur stark zunimmt und ab einer gewissen Konzentration die weniger stark temperaturabhängige cmc-Kurve hinzu kommt. Der Tripelpunkt, an dem sich Löslichkeitskurve und cmc-Kurve treffen, nennt sich Krafft-Punkt und definiert die dazugehörige Temperatur. Unterhalb dieser ist keine Mizellbildung möglich, es liegen Monomere beziehungsweise der Feststoff vor.

Die gebildeten Mizellen besitzen alle ein hydrophobes Inneres, den sogenannten Kern, und eine hydrophile Grenzschicht. Bei geladenen Mizellen kann letztere analog zu Betrachtungen der Vorgänge an Elektroden auch als Stern-Schicht bezeichnet werden. Mitunter wird als hydrophober Kern nur das Innerste aufgefasst und darauf folgt eine Übergangsschicht, die Palisadenschicht. Durch diesen Aufbau herrschen in der Mizelle je nach Lokalisierung ganz unterschiedliche Viskositäten und Polaritäten (effektive Dielektrizitätskonstanten)^[63–65]. Damit beeinflussen Mizellen beispielsweise auch Säure-Base-Gleichgewichte. Der pK_a -Wert wird durch die effektive Dielektrizitätskonstante, je nach Lokalisierung der Substanz in der Mizelle, und bei geladenen Mizellen durch die Ladungsverteilung um diese herum, maßgeblich beeinflusst. Der hydrophobe Kern bevorzugt generell ungeladene Spezies, dazu kommt allerdings, dass positiv geladene Mizellen in ihrer Stern-Schicht wiederum negative und negativ geladene Mizellen positive Spezies stabilisieren. Zweitens verändert die Ladungsverteilung an der Oberfläche die Protonenverteilung um die Mizelle. Es gibt dadurch einen Unterschied zwischen dem lokalen pH verglichen zum pH der wässrigen Phase^[66]. Die Protonendichte ist an anionischen Mizellen erhöht und dadurch die protonierte Form bevorzugt, andersherum verhält es sich bei kationischen Mizellen. Durch diese Effekte, wobei der Ladungseffekt der bedeutsamere ist, verringert sich der pK_a -Wert in der Regel in kationischen Mizellen merklich und erhöht sich in anionischen. In neutralen Mizellen ist er meist ähnlich zu dem in Wasser. Es sind teils drastische Abweichungen von den pK_a -Werten in homogener Lösung möglich (z.B. Methylrot in Wasser / DTAB (kationisch) / SDS (anionisch) / TX-100 (neutral): 4,95 / 3,68 / 5,18 / 6,63^[67]).

Die Mizellen werden aber nicht nur durch die cmc und die Krafft-Temperatur charakterisiert, sondern auch durch die Aggregationszahl (N_{agg}). Diese beschreibt die Anzahl der Monomere in einer Mizelle. Die Aggregationszahl ist deutlich von der Temperatur^[12,68,69] und von Zusätzen in der Lösung^[70–73] abhängig, aber auch vom Druck^[74–76] oder dem pH-Wert^[77–79]. Insbesondere bei ionischen Mizellen zeigt die Aggregationszahl eine starke Abhängigkeit

von der Ionenstärke^[80,81]. Der Wert der Aggregationszahl ist gleichzeitig ein Maß für die Größe der Mizelle, aus ihr kann auch das Mizellvolumen berechnet werden. Sie kann außerdem einen Hinweis auf Stabilität oder Form der Mizellen^[82–84] liefern und für praktische Anwendungen wichtig sein. Zur Untersuchung des Aggregationsverhaltens und der Aggregationszahl werden überwiegend Streutechniken wie Röntgen- und Neutronenstreuung (SAXS^[9,10], SANS^[11,12]), sowie dynamische oder statische Lichtstreuung (DLS,SLS)^[13–15] verwendet. Aber auch andere Untersuchungsmethoden wie beispielsweise Scanning- oder Isotherme-Titrations-Kalorimetrie^[85,86], cryo-TEM^[87] oder Fluoreszenzmethoden^[16–18].

Die Struktur der Mizelle mit ihren hydrophoben und hydrophilen Domänen vereint damit auch hydrophobe und hydrophile Eigenschaften. Mizellen können so als Container für hydrophobe Substanzen dienen, die normalerweise sehr schlecht oder unlöslich in Wasser sind. Dabei wird die Substanz in das hydrophobe Innere der Mizellen aufgenommen. Diese Eigenschaft wird sich bei der Verwendung als Emulgatoren und Waschmittel zu Nutze gemacht. Aber sie können auch als Nanoreaktoren für zahlreiche Reaktionen eingesetzt werden^[88]. Sie besitzen auch direkt eine biologische Bedeutung. Die Bildung von Mizellen aus Gallensalzen ist essentiell, um die Bioverfügbarkeit von fettlöslichen Vitaminen (A, D, E, K) und speziellen Lipiden zu erhöhen und die Aufnahme im Darm zu erleichtern^[89–91]. Außerdem können Mizellen als einfaches Modell für andere Bioaggregate wie Liposome, Vesikel oder ausge dehnte Membranen^[92,93] dienen. Die Ähnlichkeit zu biologischen Systemen wird sich auch bei der zielgerichteten Applikation von Arzneistoffen zu Nutze gemacht^[94]. Dabei sollen die häufig schlecht wasserlöslichen Pharmaka in die Mizelle aufgenommen, durch den Körper transportiert und dann möglichst an der gewünschten Stelle wieder freigesetzt werden.

2.2 Fluoreszenz und Fluoreszenzlöschung

Der bei der Absorption von Licht gebildete elektronisch angeregte Zustand eines Moleküls besitzt zahlreiche Möglichkeiten zu relaxieren. Typischerweise geht ein höher angeregter Zustand durch interne Umwandlung (engl. internal conversion, IC) zunächst in unter einer Picosekunde in den ersten elektronisch angeregten S_1 -Zustand. Von dort stehen dann zahlreiche weitere Deaktivierungspfade zur Verfügung. So ist hier eine direkte strahlungslose Rückkehr in den S_0 -Grundzustand möglich oder aber auch unter spontaner Emission von Licht als erlaubter Fluoreszenzübergang. Auf der anderen Seite ist aber unter bestimmten Umständen auch ein strahlungsloser Übergang in den Triplett-Zustand T_1 möglich (engl. intersystem crossing, ISC) und von dort ist dann wiederum eine strahlungslose oder, als Phosphoreszenz, Licht-emittierende Rückkehr zum S_0 -Grundzustand möglich. Im Bereich der Photophysik wird versucht, diese ganzen Prozesse zu charakterisieren. Besonders gut geeignet für Untersuchungen ist hierbei die Fluoreszenz. Die Fluoreszenzspektroskopie besitzt eine extrem hohe Empfindlichkeit, da sie als Nullmethode nur emittierte Photonen

misst und mit Lebenszeiten im Bereich von einigen Nanosekunden ist die Fluoreszenz auch zeitaufgelöst gut zu untersuchen.

Ein mizellares Medium kann nun direkt die Photophysik beeinflussen^[95,96]. Insbesondere Moleküle, die eine ausgeprägte Fluorophor-Lösungsmittel-Interaktion zeigen, können stark beeinflusst werden. Denn durch Interaktion des Fluorophors mit der Mizelle können analog die Form und Lage der Potentialkurven sowie Besetzung der Energieniveaus verändert werden. Das führt daraufhin dann zu einem veränderten Absorptions- und Fluoreszenzverhalten. Die Polarität und Viskosität in Mizellen verändert wiederum die Mobilität und Orientierung von Fluorophoren im Vergleich zu einem homogenen Lösungsmittel^[97–100].

Befinden sich neben dem angeregten Molekül noch andere Substanzen in der Lösung, so eröffnet sich ein weiterer Deaktivierungsweg, bei dem diese als sogenannte Löscher (engl. quencher, Q) agieren und den S_1 so deaktivieren. Dieser Prozess kann sehr gut über die Fluoreszenz verfolgt werden. In homogener Lösung wird die Abhängigkeit der, an einem statischen Fluoreszenzspektrometer ermittelten, Gesamtfluoreszenzintensität I von der Konzentration der Löscher durch die allseits-bekanntes Stern-Volmer-Gleichungen beschrieben^[101]. Dabei muss jedoch berücksichtigt werden, dass bei der Fluoreszenzlöschung außerdem zwischen dynamischer und statischer Löschung unterschieden werden kann. Bei der dynamischen Fluoreszenzlöschung nimmt die Lebenszeit τ des angeregten Zustandes mit steigender Quencherkonzentration ab, denn die Wahrscheinlichkeit einer zur Deaktivierung führenden Kollision zwischen dem Quencher und dem angeregten Fluorophor steigt. Diese Abnahme kann durch zeitaufgelöste Fluoreszenzspektroskopie auch direkt beobachtet werden. Aus einfachen kinetischen Überlegungen für Parallelreaktionen ergibt sich $\tau = \tau_0 / (1 + \tau_0 k[Q])$. Damit nimmt auch die gemessene Gesamt-Fluoreszenzintensität ab und die Stern-Volmer-Gleichung lautet: $I_0/I = (k\tau_0[Q] + 1)$. Bei der statischen Löschung hingegen bildet sich aus dem Fluorophor und dem Quencher ein nicht-fluoreszierender Komplex. Aus dem Massenwirkungsgesetz kann einfach abgeleitet werden, dass dadurch automatisch die Fluoreszenzintensität sinkt. Bei zeitaufgelösten Messungen ist ein Absinken der initialen Intensität (entspricht der Höhe der Fluoreszenzkurven), aber eine Konstanz in der Lebenszeit zu sehen. Die zugehörige Stern-Volmer-Gleichung lautet: $I_0/I = (K[Q] + 1)$. Trägt man jeweils I_0/I gegen die Quencher-Konzentration auf, so ergibt sich offensichtlich für beide Löschemechanismen eine Gerade. Treten hingegen beide Szenarien gleichzeitig auf, so ist der Stern-Volmer-Plot gekrümmt (Abb. 2.1).

Die vorangegangenen Gleichungen gelten jedoch nur für homogene Lösungen. Wie bereits eingangs erwähnt, können Mizellen praktisch als kleine Container innerhalb der wässrigen Lösung angesehen werden, die wiederum in Gleichgewichten Fluorophor und/oder Quencher an sich binden können. Dadurch gibt es keine homogene Gleichverteilung von Fluorophor und Quencher. Lässt man den Quencher zunächst außen vor und nimmt an, dass der

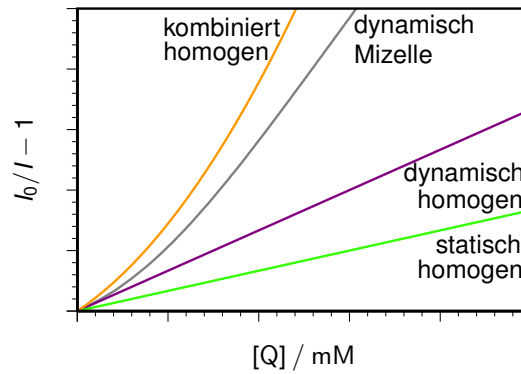


Abbildung 2.1: Exemplarische Stern-Volmer-Plots für die Szenarien: dynamische, statische und kombinierte Löschung in homogener Lösung und zusätzlich dynamische Löschung in Mizellen (Gl. 2.2); während in homogener Lösung nur die kombinierte Löschung eine Krümmung erzeugt, ist dies in Mizellen auch schon bei rein dynamischer Löschung der Fall, dies kann leicht zu falschen Schlussfolgerungen führen.

Fluorophor vollständig an die Mizellen gebunden ist (immobile probe), so zeigt sich, dass dieser über alle Mizellen Poisson-verteilt ist^[26]. Nun ist es in den meisten Fällen so, dass die Fluorophor-Konzentration klein ist im Vergleich zur Konzentration an Mizellen. Dadurch ergibt sich praktisch, dass jede Mizelle maximal einen Fluorophor gebunden hat. Ist auch der Quencher vollständig an die Mizelle gebunden, resultiert das immobile-probe/immobile-quencher-Szenario. Unter der Voraussetzung, dass es keine Wechselwirkung zwischen Fluorophor und Löscher gibt, also nur dynamische und keine statische Fluoreszenzlöschung auftritt, ist auch der Quencher unabhängig vom Fluorophor über alle Mizellen Poisson-verteilt. In diesem Fall ist die Konzentration des Quenchers jedoch häufig im Bereich der Mizell-Konzentration oder größer und damit auch eine Mehrfachbesetzung möglich. Dies geht in der bekannten Infelta-Tachyia-Theorie^[24–26] auf. Diese beschreibt den Fall des dynamischen Löschens mit den Gleichungen für die zeitabhängige Fluoreszenz und die Gesamtfluoreszenzintensität, analog zum Stern-Volmer-Verhalten:

$$I(t) = I(0) \sum_{n=0}^{\infty} \left(\frac{\langle q \rangle^n \exp[-\langle q \rangle]}{n!} \exp[-t(1/\tau + nk)] \right) \quad (2.1)$$

$$\frac{I_0}{I} = \left(\sum_{n=0}^{\infty} \frac{\langle q \rangle^n \exp[-\langle q \rangle]}{n!(1 + nk\tau)} \right)^{-1} \quad (2.2)$$

Wobei $\langle q \rangle$ die mittlere Besetzung der Mizellen mit Quencher darstellt, also gegeben ist durch:

$$\langle q \rangle = \frac{[Q]}{[M]_{\text{tot}}} = \frac{N_{\text{agg}}[Q]}{[\text{Surf}]_{\text{tot}} - \text{cmc}} \quad (2.3)$$

$[M]_{\text{tot}}$ ist die Gesamtmizell-Konzentration und kann aus der Einwaage des Amphiphils Surf bei Kenntnis der cmc und der Aggregationszahl bestimmt werden.

Die Gültigkeit dieser Gleichungen wurde schon in einer Vielzahl von Experimenten bestätigt^[18,28,102–105]. Wie man erkennen kann, ist die Aggregationszahl der Mizelle von entscheidender Bedeutung, denn sie bestimmt, wie viele Mizellen aus einer bestimmten Amphiphil-

Konzentration gebildet werden können, und hat damit auch direkten Einfluss auf die Verteilung. Außerdem wird die intramizellare Löschengeschwindigkeit k natürlich durch die Struktur und die Eigenschaften der Mizelle beeinflusst. Die Untersuchung der Fluoreszenz kann also nicht nur genutzt werden um den Fluorophor in einer mizellaren Umgebung zu untersuchen, sondern auch um die Mizelle zu charakterisieren. Später wurde der Ansatz von Infelta und Tachiya auch für komplexere Szenarien, z.B. den Austausch des Quenchers zwischen den Mizellen (mobile quencher) erweitert^[17,106]. Eine Auftragung von I_0/I gegen die Löscherkonzentration zeigt, dass auch bei Vorliegen ausschließlich dynamischer Löschung ein gekrümmter Stern-Volmer-Plot erhalten wird (Abb. 2.1). Es kann also nicht einfach aus einer Krümmung auf eine kombinierte Löschung geschlossen werden. Für den Fall der kombinierten dynamischen und statischen Fluoreszenzlöschung in Mizellen gibt es einen Mangel in der Literatur, stattdessen wird in dieser häufig fälschlicherweise einfach die Gleichung für das Löschen in homogener Lösung angenommen^[107–110].

2.3 Photoionisierungen und hydratisierte Elektronen

Unter Photoionisierungen versteht man im Allgemeinen die Bildung von Ionen aus Atomen oder Molekülen unter Bestrahlung mit Licht im UV- oder sichtbaren Bereich. Das überschüssige Elektron kann dann bei Vorhandensein eines geeigneten Lösungsmittels in der Lösung stabilisiert werden, diese werden dann solvatisierte Elektronen genannt. Führt man die Photoionisierung in wässriger Lösung durch, so entstehen hydratisierte Elektronen^[111,112] als ein Spezialfall der solvatisierten Elektronen. Allen solvatisierten Elektronen ist gemein, dass sie durch Wechselwirkungen mit der Solvathülle stabilisiert werden^[113,114]. Als erstes wurden sie phänomenologisch als tief blaue Farbe beim Lösen von Alkalimetallen in flüssigem Ammoniak beschrieben. Anfang des 20. Jahrhunderts wurden dann solvatisierte Elektronen als Ursache bekannt^[115]. Der erste spektroskopische Nachweis von hydratisierten Elektronen erfolgte 1962^[116]. Das Spektrum (Abb. 2.2 (a)) besitzt eine breite Absorptionsbande im Blauen mit einem Maximum bei 720 nm und einem Extinktionskoeffizienten von 22700 M^{-1} ^[117]. In reinem Wasser ist es bis zu einigen hundert Mikrosekunden stabil^[118], die Lebenszeit wird aber durch vorhandene reduzierbare Substanzen schnell in den Bereich von wenigen Mikrosekunden oder darunter gedrückt. Durch das hohe Reduktionspotential $-2,9 \text{ V}$ ^[30] und die Eigenschaft, dass es bei einer Reaktion praktisch verschwindet, stellt es ein universelles Reduktionsmittel dar, welches für Reaktionen gezielt genutzt werden kann (Abb. 2.2 (b))^[119–123]. Ein sehr gute Übersicht über die zahlreichen möglichen Reaktionen bietet die Literatur^[30]. Dabei geht es jedoch häufig um die prinzipielle Machbarkeit, wie bei der Reduktion von Kohlenstoffdioxid^[121] oder molekularem Stickstoff^[122], oder beispielsweise um die konkrete Anwendung zur Detoxifizierung von Abwässern durch reduktive Dehalogenierung oder andere Reduktionsreaktionen. Hierbei steht der Abbau persistenter Umweltgifte wie z.B. Chloressigsäure^[124], Vinylchlorid^[125] oder Chlorphenolen^[126] oder Pharmaka wie

Diclofenac^[127], Atenolol^[123] oder Triclosan^[128] im Vordergrund. Recht selten werden die hydratisierten Elektronen tatsächlich für synthetische Anwendungen genutzt. Erst in den letzten Jahren hat sich dort mehr etabliert^[36,38,129–131].

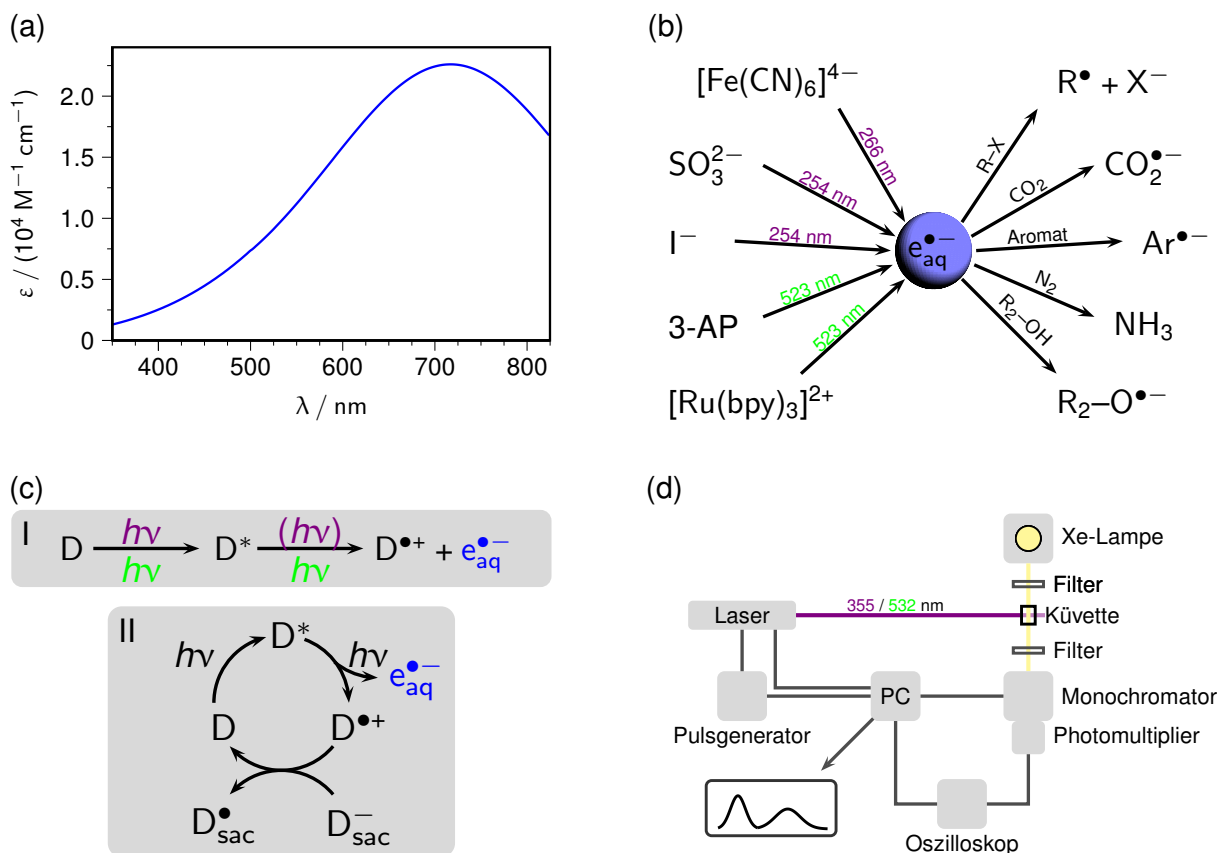


Abbildung 2.2: Photoionisierungen zur Erzeugung hydratisierter Elektronen und ihre Untersuchung; (a) Absorptionsspektrum des hydratisierten Elektrons $e_{aq}^{\bullet-}$; (b) mögliche Darstellungsmethoden hydratisierter Elektronen und Reaktionen anhand ausgewählter repräsentativer Beispiele (3-AP = 3-Aminoperylen); (c) I: Linearer Photoionisierungsmechanismus eines Elektronendonors D, es sind monophotonische Ionisierungen mit einem UV-Photon und biphotonische Ionisierungen mit zwei Photonen im UV- aber auch im sichtbaren Wellenlängenbereich bekannt; II: Cyclische Photoionisierung bei dem der Donor D durch einen Opferdonor D_{sac} regeneriert wird, hier ist eine photokatalytische Erzeugung der $e_{aq}^{\bullet-}$ möglich; (d) schematische Darstellung der Laserblitzlicht-Photolyse-Apparatur zur Untersuchung der Photoionisierungs- und Reparaturreaktionen, für den detaillierten Aufbau in der AG Goetz siehe^[31].

Neben der Möglichkeit hydratisierte Elektronen durch Photoionisierung freizusetzen sei auch noch die pulsradiolytische Methode erwähnt. Hier werden diese durch ionisierende Strahlung (z.B. Gamma-Strahlung) aus Wasser freigesetzt^[132–135]. Der Grund dafür, dass die Pulsradiolyse trotz seiner immanenten Nachteile (inhomogene Elektronenerzeugung in „Spurs“ und unerwünschte Nebenreaktionen^[136], hohe Sicherheitsanforderungen^[137],...) auch heute noch Anwendung findet, liegt ein Stück weit auch in der Thermodynamik der Photoionisierungen begründet, da für die Freisetzung des hydratisierten Elektrons ($E = -2,9 \text{ V}$) eine erhebliche Menge an Energie aufgebracht werden muss. Im UV-Bereich sind Beispiele bekannt, bei denen diese Energie durch ein einzelnes Photon ($E_{355\text{nm}} = 3,5 \text{ eV}$)

aufgebracht werden kann (monophotonische Ionisierung)^[138–141]. Mit Licht im sichtbaren Bereich ($E_{532\text{nm}} = 2,3\text{ eV}$) ist eine Ionisierung praktisch nur durch Absorption von zwei Photonen (biphotonische Ionisierung) möglich^[142]. Ein Spezialfall der letzteren stellt die konsekutive Absorption von zwei Photonen dar, bei der die Energie in einem stabilen Intermediat gespeichert wurde. Ausführliche Arbeiten dazu erfolgten am Tris(bipyridin)ruthenium ($\text{Ru}(\text{bpy})_3$)^[31,35,130]. Klassische Substanzen zur Erzeugung von hydratisierten Elektronen sind Metall-Komplexe wie Hexacyanoferrat^[143], das bereits erwähnte $\text{Ru}(\text{bpy})_3$, aber auch Sulfit-Ionen^[144] und elektronenreiche Aromaten^[112] (Abb. 2.2 (b)). Diese können in einem linearen Ionisierungsmechanismus eine Elektronenmenge erzeugen, die der eingesetzten Substanzmenge entspricht (Abb. 2.2 (c)). Eine Möglichkeit den Elektronenvorläufer, besonders wenn dieser teuer oder aufwendig zu synthetisieren ist, katalytisch einzusetzen und mehr als ein Elektron pro Molekül zu bekommen, besteht in der Verwendung eines Opferdonors, welcher in der Lage ist den Elektronenvorläufer reduktiv zu regenerieren^[145,146]. Solch ein Katalysezyklus wurde auch schon mit sichtbarem Licht^[31,36,142] und sogar mit einer LED-Bestrahlung^[35] realisiert. Es wurde gezeigt, dass die Photoionisierung zur Freisetzung von hydratisierten Elektronen in vielerlei Hinsicht der Pulsradiolyse überlegen ist. Kombiniert man die Photoionisierung mit der Verwendung von Mizellen, so ist die Erzeugung von hydratisierten Elektronen aus Vorläufern möglich, die sonst nicht oder nur sehr schlecht wasserlöslich sind. Beispielhaft sei hier die Ionisierung von wasserunlöslichen Aromaten wie Pyren, Perylen und 3-Aminoperylen^[142,147–149] oder schlecht wasserlöslichen aromatischen Ketonen^[150] aufgeführt. Außerdem können die Mizellen auch genutzt werden, um die zu ionisierenden Substanzen innerhalb der Mizelle gegen Reaktanden außerhalb der Mizelle abzuschirmen, sei es das ausgeworfene hydratisierte Elektron oder in Folgereaktionen entstehende Radikale. Die schnelle Rekombinationsreaktion als Umkehr der Photoionisierung kann so z.B. effektiv unterbunden werden^[151–153].

Mizellen beeinflussen auch direkt das photophysikalische Verhalten der Elektronenvorläufer. Durch den Aufbau der Mizelle und den damit unterschiedlichen Umgebungen innerhalb der Mizelle und ihren Eigenschaften kann, wie bereits beschrieben, die Photophysik verändert werden. So wurden z.B. für anionische, neutrale und kationische Mizellen mit der gleichen Substanz ganz unterschiedliche Ionisierungseffizienzen und damit Elektronenausbeuten gefunden^[153].

Neben der Erzeugung von hydratisierten Elektronen, können Photoionisierungen allerdings auch für die Untersuchung der erzeugten Radikalspezies genutzt werden. Nach der Photoionisierung verbleibende Radikalkationen oder Radikale können mittels Laserblitzlicht-Photolyse (engl. laser flash photolysis, LFP) innerhalb weniger Nanosekunden homogen verteilt erzeugt und dann spektroskopisch untersucht werden (Abb. 2.2 (d)). Gewöhnlich wird die LFP mit Absorptions- und Fluoreszenzspektroskopie gekoppelt^[154–156], sie kann aber auch mit EPR-^[157,158] und NMR-Techniken (z.B. CIDNP)^[159,160] kombiniert werden.

So können angeregte Singlet- und Triplett-Zustände, kurzlebige Radikale und chemische Reaktionen auf einer sub- μs -Zeitskala beobachtet werden. Ein besonderes Interesse hat sich für die Untersuchung von Antioxidantien mit ihren verschiedenen Radikalspezies und ihrem Wirkungs- und Regenerationsmechanismus entwickelt^[40,161–171]. Besonders hier können Mizellen mit ihrer strukturellen und funktionellen Ähnlichkeit zu biologischen Systemen wie Liposomen oder Biomembranen punkten. Eine Untersuchung zur Reparatur des α -Tocopheroxyl-Radikals durch das Ascorbat-Monoanion zeigt, dass diese in den negativen Mizellen um drei Größenordnungen kleiner ist als in den positiv geladenen Mizellen^[40]. Ein ähnliches Verhalten wurde auch bei der Reparatur des Resveratrol durch Ascorbat beobachtet^[171]. Die Reaktivität einer ganzen Reihe von Antioxidantien gegenüber photolytisch erzeugten Pyranine-Radikalen wurde erst kürzlich in homogener Lösung und in Triton TX-100-Mizellen untersucht und dabei herausgefunden, dass die Verteilung zwischen den Mizellen und der wässrigen Phase und die Austrittsgeschwindigkeiten aus den Mizellen stark die Reparatur beeinflussen^[170].

3 Ergebnisse und Diskussion

3.1 Fluoreszenzlöschung in Mizellen

Wie bereits dargelegt, kann die Verwendung von Mizellen allerlei photophysikalische Prozesse beeinflussen. Damit kann durch die Aufnahme eines Fluorophors in eine Mizelle auch die Mizelle selbst untersucht werden. Die Löschung der Fluoreszenz eines mizellgebundenen Fluorophors mit einem mizellgebundenen Löscher (immobile-probe/immobile-quencher) bietet relativ einfach eine solche Möglichkeit. Während es für die rein dynamische Fluoreszenzlöschung eine vielfach validierte Beschreibung durch die Infelta-Tachiya-Theorie existiert, ist die kombinierte statische/dynamische Löschung in Mizellen viel weniger gut untersucht.

Als Weiterführung der in der Literatur bekannten kombinierten Fluoreszenzlöschung von Pyren mit Methylviologen in SDS wird eine Ausdehnung auf eine Reihe von verschiedenen substituierten Viologen gezeigt. Dazu wurde ein Modell basierend auf einfachen statistischen Überlegungen entwickelt, dem eine Poisson-Statistik zu Grunde liegt und welches dann zur Beschreibung der zeitaufgelösten und Stern-Volmer-Fluoreszenzmessungen dient. Dabei sind drei Parameter von Bedeutung: die Aggregationszahl der Mizelle und zum anderen sowohl die dynamische und als auch die statische Quenchkonstante. Aus den Experimenten ergibt sich eine scheinbare Abhängigkeit der erhaltenen Aggregationszahl von der Komplexbildungskonstante.

Nachfolgend ist eine Weiterführung der Quenchemperimente von Pyren in SDS mit einer homologen Reihe von Viologen dargelegt. Eine formal-kinetische Betrachtung der Verteilung von Fluorophor, Quencher und Fluorophor-Quencher-Komplex liefert die richtigen Gleichungen zur Beschreibung der zeitaufgelösten und der Stern-Volmer-Daten für kombiniertes Quenchen. Ein entwickeltes Protokoll ermöglicht die kombinierte Auswertung beider Datensätze. Die erhaltenen Aggregationszahlen sind unabhängig vom Viologen und stimmen mit denen aus der Literatur für SDS überein. Die dynamische und statische Quenchkonstante zeigen, dass es sich bei allen Viologen um eine diffusionskontrollierte Löschung handelt, die Stärke der Komplexbildung allerdings von der Länge der Reste am Viologen abhängt. Abschließend wird gezeigt, dass sich das einfache System des Quenchens von Pyren durch Methylviologen ausgezeichnet auf andere n -Alkylsulfate ($9 \leq n \leq 14$) erweitern lässt. Aus den Gleichungen für kombiniertes Quenchen lassen sich die Aggregationszahlen der Mizellbildner einfach ermitteln. Das resultierende Mizellvolumen variiert bei den Experimenten um einen Faktor von mehr als 4. Beachtet man dies, dann zeigen die weiterhin erhaltenen intramizellaren dynamischen und statischen Quenchkonstanten, dass sie nicht abhängig von der Mizellgröße sind. Zusätzlich wurde die Temperaturabhängigkeit der Parameter untersucht.

3.1.1 Fluoreszenzlöschung von Pyren mit Viologenen in SDS (Publ. A)

Obwohl bereits seit langer Zeit bekannt ist, dass in mizellarer Lösung die Fluorophor- und Löschermoleküle nicht über alle Mizellen gleichverteilt sind, finden sich in der Literatur immer wieder Beispiele, bei denen die Stern-Volmer-Gleichung für die homogene Lösung angewendet wird und aus einer Krümmung des Plots auf die gleichzeitige Anwesenheit von statischer und dynamischer Löschung geschlossen wird^[107–110]. Dies muss aber nicht der Fall sein, denn in mizellaren Lösungen ergibt auch eine rein dynamische Löschung eine Krümmung. In der Literatur ist ein Beispiel bekannt, bei dem auf jeden Fall eine statische Komponente zu finden ist: die Löschung von Pyren mit Methylviologen in SDS^[29]. Im folgenden wurde diese Löschung aufgegriffen und auf weitere substituierte Viologene ausgedehnt (Abb. 3.1). Um den Löschvorgang und die Komplexbildung möglichst vollständig untersuchen zu können, wurden nicht-zeitaufgelöste und zeitaufgelöste Fluoreszenzmessungen sowie Absorptionmessungen durchgeführt.

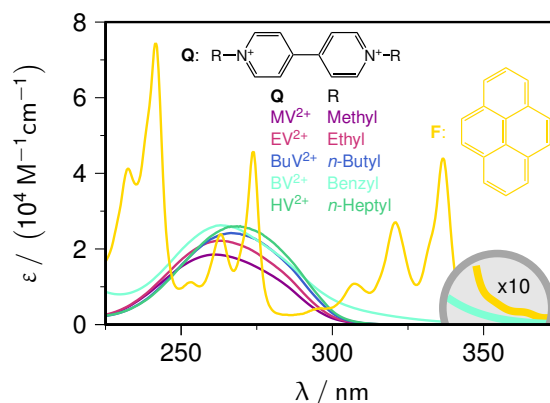


Abbildung 3.1: Absorptionsspektren des Fluorophors (F) Pyren und der als Löscher (Q) verwendeten substituierten Viologene in 50 mM SDS-Lösung.

Das System Pyren in Kombination mit Viologenen bietet sehr gute Voraussetzungen für die Untersuchung des immobile-probe/ immobile-quencher-Szenarios, denn es erfüllt alle folgenden Voraussetzungen: (i) ausschließlich intramizellares Quenching, (ii) kein Austausch von Fluorophor^[172] oder Löscher^[29] während der beobachteten Lumineszenz und (iii) keine Selbstlöschung des Fluorophors. Außerdem besitzt Pyren mit fast 350 ns in SDS-Lösung eine sehr lange Fluoreszenzlebenszeit.

Der Ansatz von Infelta und Tachiya, dass Fluorophor und Löscher über die Mizellen Poissonverteilt sind, ist allgemein akzeptiert und stellt den Ausgangspunkt für die Herleitung für kombiniertes Löschen in Mizellen dar. Die Wahrscheinlichkeit, n Moleküle in einer Mizelle zu finden, ist gegeben durch:

$$P(n) = \frac{\langle q \rangle^n \exp[-\langle q \rangle]}{n!} \quad (3.4)$$

wobei $\langle q \rangle$ die mittlere Besetzung der Mizellen darstellt und aus der Einwaagekonzentration

des Löschers [Q] und des Amphiphils [Surf] bei Kenntnis der cmc und N_{agg} berechnet werden kann:

$$\langle q \rangle = \frac{N_{\text{agg}}[\text{Q}]}{[\text{Surf}]_{\text{tot}} - \text{cmc}} \quad (3.5)$$

Da die Fluorophor- im Vergleich zur Mizellkonzentration sehr klein ist, gibt es keine Doppelbesetzung mit Fluorophor. Unter diesen Umständen befinden sich in jeder Mizelle mit einem angeregte Pyren $n = 0, 1, \dots$ Quenchemoleküle und diese können das Pyren löschen. Die Fluoreszenzquantenausbeute relativ zu der in Quencher-freien Mizellen hängt nur von n und dem jeweiligen Löschemechanismus (statisch, dynamisch, kombiniert) ab. Mit der Wahrscheinlichkeit $P(n)$ die Anzahl n an Löschern in einer jeweiligen Mizelle zu finden, ergibt sich für die Stern-Volmer-Gleichung allgemein:

$$\frac{I_0}{I} = \left(\sum_{n=0}^{\infty} P(n) \phi_{\text{mech}}(n) \right)^{-1} \quad (3.6)$$

und für die einzelnen Quenchemechanismen:

$$\phi_{\text{dyn}}(n) = \frac{1}{1 + k_m \tau_0 n} \quad (3.7)$$

$$\phi_{\text{stat}}(n) = \frac{1}{1 + K_m n} \quad (3.8)$$

$$\phi_{\text{komb}}(n) = \phi_{\text{dyn}}(n) \phi_{\text{stat}}(n) \quad (3.9)$$

Unter Verwendung der Gleichungen Gl. 3.6 und 3.7 erhält man die Infelta-Tachiya-Gleichung für dynamisches Quenchen in Mizellen. Für das kombinierte Löschen erhält man aus Gleichung 3.6 und 3.9, und Umwandlung der Summe in eine Gamma-Funktion:

$$\left(\frac{I_0}{I} \right)_{\text{komb}} = \frac{(k_m \tau_0 - K_m) \exp(\langle q \rangle)}{(-\langle q \rangle)^{-1/(k_m \tau_0)} \gamma(1/(k_m \tau_0), -\langle q \rangle) - (-\langle q \rangle)^{-1/K_m} \gamma(1/K_m, -\langle q \rangle)} \quad (3.10)$$

Der Formalismus kann auch auf die Änderung der Absorption durch die Bildung eines Grundzustand-Komplexes angewendet werden. Sei ε_F der Extinktionskoeffizient des Fluorophors und ε_{FQ} der des Komplexes FQ, dann lässt sich der beobachtete Extinktionskoeffizient beschreiben durch:

$$\varepsilon = (\varepsilon_F - \varepsilon_{\text{FQ}}) \frac{\exp(-\langle q \rangle)}{K_m} (-\langle q \rangle)^{-1/K_m} \gamma(1/K_m, -\langle q \rangle) + \varepsilon_{\text{FQ}} \quad (3.11)$$

Durch globale Anpassung der Stern-Volmer-Daten mit Gl. 3.10 und der aufgenommenen Absorptionsdaten mit Gl. 3.11 können damit die gewünschten Löschemechanismen k_m und K_m

und die Aggregationszahl N_{agg} bestimmt werden (Abb. 3.2).

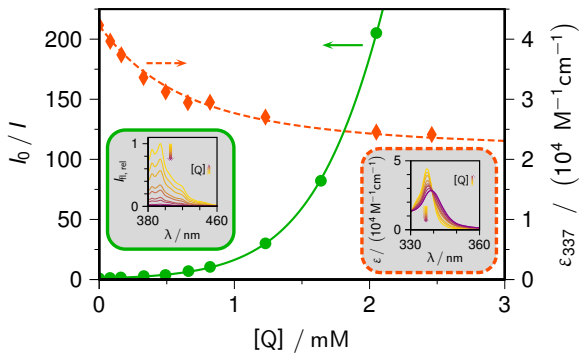


Abbildung 3.2: Kombinierte Anpassung der Stern-Volmer-Daten (grün, Anregung bei 355 nm, Emission bei 394 nm) mit Gl. 3.10 und der Absorptionsdaten (orange, Extinktion bei 337 nm) mit Gl. 3.11 von MV^{2+} und Pyren ($10 \mu\text{M}$) in SDS-Lösung (50 mM), beste globale Fitparameter $N_{\text{agg}} = 122$, $K_m = 0,95$, $k_m = 18$, Parameter, $\varepsilon_{\text{FQ},337} = 21500 \text{ M}^{-1} \text{ cm}^{-1}$; die Insets zeigen die tatsächlich gemessenen Spektren.

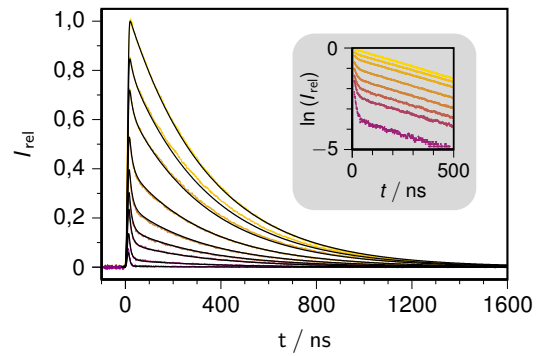


Abbildung 3.3: Zeitaufgelöste Fluoreszenzmessung der Löschung von Pyren ($10 \mu\text{M}$) mit MV^{2+} in SDS (50 mM) (Anregung mit 5 ns 355 nm -Laserspuls, Emission bei 394 nm) mit den Fits basierend auf Gl. 3.12; Inset: logarithmierte Abklingkurven. Erhaltene globale Fitparameter $N_{\text{agg}} = 122$, $K_m = 0,95$, $\tau_0 = 338 \text{ ns}$, $k_m = 6,6 \cdot 10^7 \text{ s}^{-1}$.

Alternativ können durch zeitaufgelöste Fluoreszenzmessung alle drei Parameter auf einmal gewonnen werden. Bei einer typischen Abklingkurve (vgl. Abb. 3.3) können bei Anwesenheit eines Löschers drei Prozesse auf ganz unterschiedlichen Zeitskalen ausgemacht werden. Statisches Quenchen ist instantan und verringert damit die initiale Höhe bei $t = 0$ der Abklingkurve. Das dynamische Löschen findet auf einer Skala unter 100 ns statt. Nach dieser Zeit sind nur angeregte Fluorophore zu beobachten, die sich in einer Quencher-freien Mizelle befinden und damit auch nicht gelöscht werden können. Daher ist in letzterem Bereich die Abklinggeschwindigkeit immer konstant τ_0 . Die Fit-Funktion für den gesamten Zeitbereich ist gegeben durch:

$$I(t) = I_0 \exp(-t/\tau_0) \frac{\exp(-\langle q \rangle)}{K_m} [-\langle q \rangle \exp(-k_m t)]^{-1/K_m} \gamma [1/K_m, -\langle q \rangle \exp(-k_m t)] \quad (3.12)$$

Tabelle 3.1 zeigt eine Übersicht über alle erhaltenen Parameter der zeitaufgelösten Messungen mit den verschiedenen Viologenen.

Da die verwendeten alkylsubstituierten Viologene alle das gleiche Redoxpotential aufweisen^[173], muss der Unterschied in der Komplexbildung entropische Gründe haben. Es ist bekannt, dass sterische Wechselwirkungen einen starken Einfluss auf die Assoziation bei Komplexen mit π - π -Wechselwirkung ausüben^[174]. In der Mizelle befindet sich das Pyren bekanntlich etwas unterhalb der Stern-Schicht im Inneren der Mizelle^[175] und das Viologen haftet von außen an dieser. In der komplexierten Anordnung, bei der Viologen und Pyren gestapelt in der Mizelle vorliegen, können die Seitenketten nicht mehr alle möglichen Konformere einnehmen (Abb. 3.4). Das planare Pyren und das steife Viologen-Grundgerüst (bis zu

Tabelle 3.1: Aus den zeitaufgelösten Fluoreszenzmessungen (Quenchexperimente und Auswertung analog zu Abb. 3.3) erhaltene Parameter k_m , K_m und N_{agg} für die verschiedenen untersuchten Viologene.

Viologen	$k_m / (10^7 \text{ s}^{-1})$	K_m	N_{agg}
MV ²⁺	6,6	0,95	122
EV ²⁺	6,2	0,74	112
BV ²⁺	6,3	0,45	104
BuV ²⁺	5,9	0,43	100
HV ²⁺	6,7	0,15	88

den jeweils ersten C-Atomen der Seitenkette) liegen in Deckung übereinander, so dass sich die Van-der-Waals-Oberflächen berühren. Je länger die Seitenkette nun ist, bzw. je mehr Rotoren sie besitzt, desto stärker werden diese in ihren Freiheitsgraden eingeschränkt, denn ein erheblicher Teil des Volumens unterhalb des Viologens ist durch das Pyren versperrt.

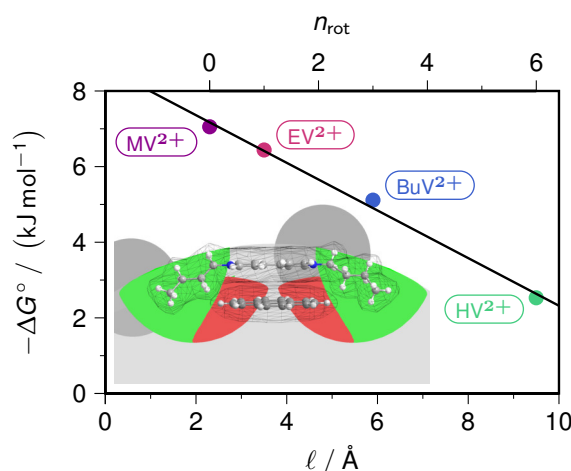


Abbildung 3.4: Entropiekontrollierte Komplexbildung der verschiedenen substituierten Viologene mit Pyren, Abhängigkeit der freien Enthalpie ΔG° der Komplexbildung von der Länge ℓ bzw. der Anzahl an Rotoren n_{rot} der Viologen-Seitenkette; Inset: Darstellung eines Komplexes von Pyren mit BuV²⁺ in einer SDS-Mizelle, Stacking-Distanz 3,7 Å, die grünen Volumenbereiche sind für die Seitenketten zugänglich und die roten nicht.

Die Aggregationszahl zeigt eine unerwartete Abhängigkeit, denn sie sollte theoretisch ≈ 80 für eine 50 mM SDS-Lösung sein^[12] und nicht wesentlich von dem eingesetzten Viologen abhängen. Als Erklärung dient, dass die Komplexbildung zwischen Viologen und Pyren die Besetzung der Mizellen verzerrt. Denn je größer das ermittelte K_m , desto größer war auch N_{agg} . Für die beobachtete Aggregationszahl ließ sich folgende Abhängigkeit von der tatsächlichen N'_{agg} finden:

$$N_{agg} = N'_{agg}(1 + \alpha K_m) \quad (3.13)$$

Solch ein Verhalten wurde in der Literatur bisher noch nicht beschrieben.

3.1.2 Fluoreszenzlöschung von Pyren mit Viologenen in SDS (Publ. B)

Ausgehend von dem beobachteten Verhalten, dass unterschiedliche Pyren-Viologen-Paare unter ansonsten gleichen Bedingungen unterschiedliche Aggregationszahlen liefern, wurden weitere Experimente durchgeführt. Die Reihe der Viologene wurde um das Dipropyl-Derivat erweitert und temperaturabhängige Messungen durchgeführt.

Zur Beschreibung der erhaltenen Stern-Volmer-Daten und der zeitabhängigen Fluoreszenzmessungen wurde diesmal ein rigoroser formalkinetischer Ansatz gewählt, der voraussetzungsfrei im Bezug auf die Verteilung ist, d.h. nicht initial eine Poisson-Verteilung der Löscher-moleküle annimmt. Hierzu wurde der Ansatz von Moroi^[176] adaptiert.

Die Mizellen können entsprechend ihrer Anzahl an Gastmolekülen F (i) und Q (j) sowie dem Komplex FQ (n) eingeteilt werden und sollen durch einen Tripleindex spezifiziert und als $\mathcal{M}_{i,j,n}$ bezeichnet werden.

Es existieren fünf entscheidende Gleichgewichte: drei für die Aufnahme in die Mizelle (für F, Q und FQ), also zwischen Mizelle und wässriger Phase, und zwei für die Komplexbildung von FQ (einmal in der wässrigen Phase und einmal in der Mizelle). Diese lassen sich alle durch entsprechende Gleichgewichtskonstanten charakterisieren. Aus all diesen Gleichgewichten erhält man eine gekoppelte Poisson-Verteilung:

$$[\mathcal{M}_{i,j,n}] = [\mathcal{M}_{0,0,0}] \frac{(K_F[F])^i}{i!} \frac{(K_Q[Q])^j}{j!} \frac{(K_F[F]K_Q[Q]K_m)^n}{n!} \quad (3.14)$$

Es kann eine Reduktion auf eine Zwei-Variablen-Darstellung durchgeführt werden, die auf der Gesamtanzahl an F und Q in der Mizelle beruht, unabhängig davon, ob es frei oder komplexiert als FQ vorliegt. Dann beschreibt $M_{r,s}$ die Mizellen mit einer Gesamtanzahl r an F und s an Q, wobei offensichtlich $r = i + n$ und $s = j + n$ gilt. Unter der Annahme, dass sich F ausschließlich in der Mizelle befindet und seine Konzentration $[F]_{\text{tot}}$ sehr klein und damit eine Mehrfachbesetzung der Mizellen mit F ausgeschlossen ist, erhält man als abschließendes Ergebnis für den Anteil an Mizellen mit genau s Löscher-molekülen an allen Fluorophor-besetzten Mizellen (nur diese sind interessant, denn nur sie können in den Fluoreszenzexperimenten überhaupt beobachtet werden und ihre Konzentration entspricht $[F]_{\text{tot}}$):

$$\frac{[M_{1,s}]}{[F]_{\text{tot}}} = \frac{\exp(-\langle q \rangle) (\langle q \rangle)^s}{1 + \langle q \rangle K_m} \frac{1}{s!} (1 + sK_m) \quad (3.15)$$

Zu einem tatsächlichen Fluoreszenzsignal beitragen können davon nur die Mizellen, die unkomplexiertes F enthalten. Dieser Anteil wird erhalten durch Division von Gl. 3.15 durch $(1 + sK_m)$. Die Fluoreszenz von diesen Mizellen mit s Löscher-molekülen klingt mit $\exp[-(1/\tau_0 + k_m s)t]$ ab. Damit ergibt sich für die zeitabhängige Fluoreszenz:

$$I(t) = I_0 \exp(-t/\tau_0) \frac{\exp(-\langle q \rangle)}{1 + \langle q \rangle K_m} \exp[\langle q \rangle \exp(-k_m t)] \quad (3.16)$$

und für die Stern-Volmer-Gleichung:

$$\frac{I_0}{I} = \frac{1 + \langle q \rangle K_m}{\exp(-\langle q \rangle)} \frac{k_m \tau_0}{(-\langle q \rangle)^{-1/(k_m \tau_0)} \gamma [1/(k_m \tau_0), -\langle q \rangle]} \quad (3.17)$$

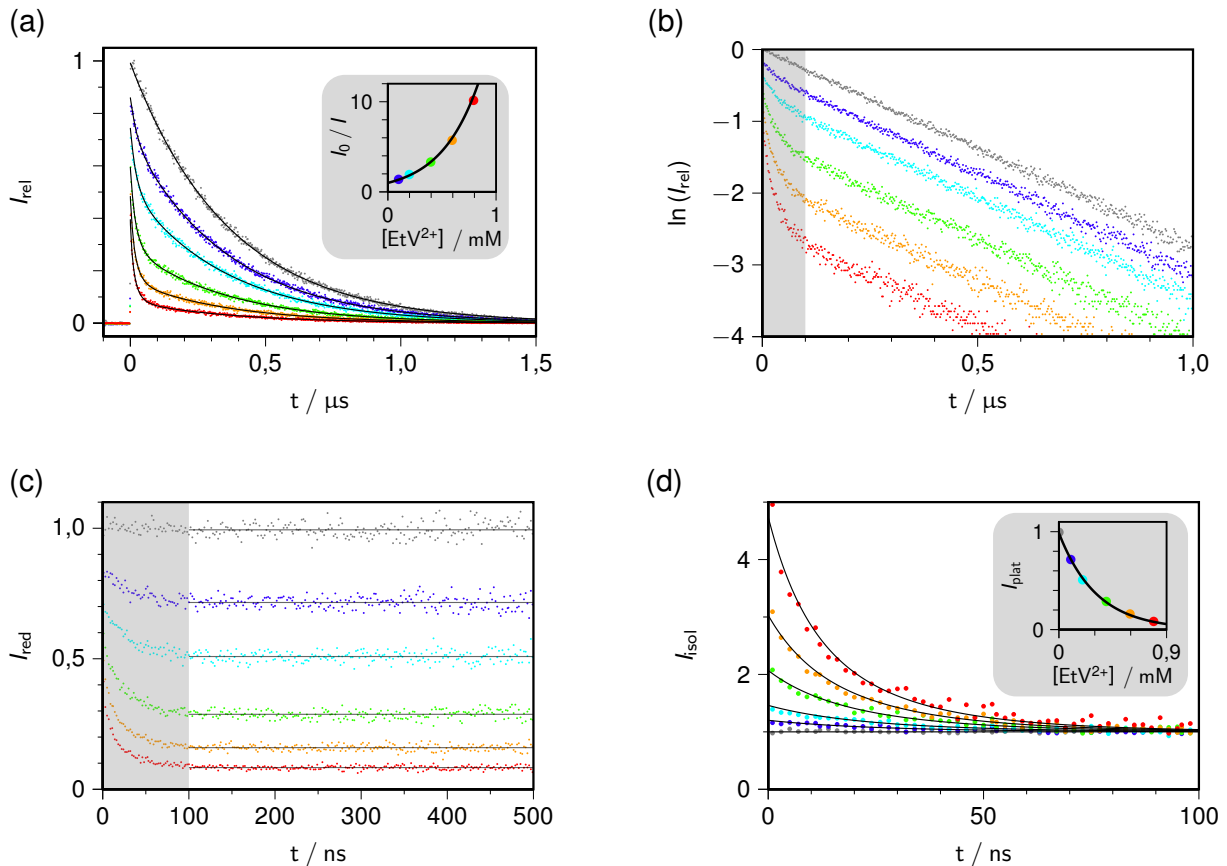


Abbildung 3.5: Methode zur Bestimmung aller relevanten Parameter aus den Fluoreszenzmessungen, exemplarisch an der Löschung von Pyren (10 μM) mit Ethylviologen EtV^{2+} in 50 mM SDS bei 283 K, Anregung, 341 nm; Emission, 395 nm; (a) zeitaufgelöste Fluoreszenzkurven mit den Fits basierend auf Gl. 3.16 und den isolierten Parametern aus (b) - (d); (b) logarithmierte Daten, erhaltener Parameter τ_0 ; (c) Kurven nach der Multiplikation $\exp(+t/\tau_0)$; die konstanten Endwerte hängen von $\langle q \rangle$ und K_m ab, (d); Separation des dritten und zweiten (Inset) Faktors der Gl. 3.16; ein globaler Fit in Abhängigkeit von $[EtV^{2+}]$ ergibt N_{agg} , und k_m sowie K_m (Inset). Erhaltene Parameter: $\tau_0 = 360$ ns, $N_{agg} = 77$, $K_m = 0,92$, $k_m = 3,7 \cdot 10^7$ s $^{-1}$.

Abbildung 3.5 zeigt beispielhaft die Fluoreszenzdaten für das Paar Pyren-Ethylviologen. Anstatt alle Kurven global über den gesamten Zeitbereich zu fiten, was eine schlechte Konvergenz und manchmal eine Unzuverlässigkeit im Bezug auf die Eindeutigkeit der Parameter mit sich bringt, wurde eine Methode entwickelt, welche die zeitaufgelösten Daten in die bereits beschriebenen drei Zeitdomänen unterteilt und dort fitet. Dadurch werden die Parameter effektiv voneinander isoliert. Das ist besonders eindrucksvoll zu sehen, wenn die

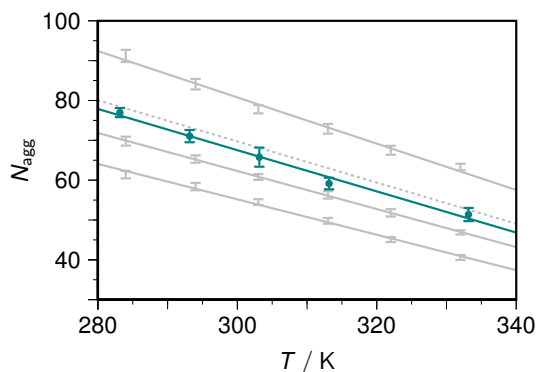


Abbildung 3.6: Einfluss der Temperatur auf die Aggregationszahl des SDS; die grünen Punkte und Fehlerbalken repräsentieren die ermittelten N_{agg} von allen fünf Viologenen in 50 mM SDS; die grauen Geraden, Datenpunkte und Fehlerbalken stammen aus der Literatur^[12] für die SDS-Konzentrationen 17,4 mM, 34,7 mM und 69,4 mM SDS, die grau gestrichelte Gerade zeigt die Interpolation für 50 mM.

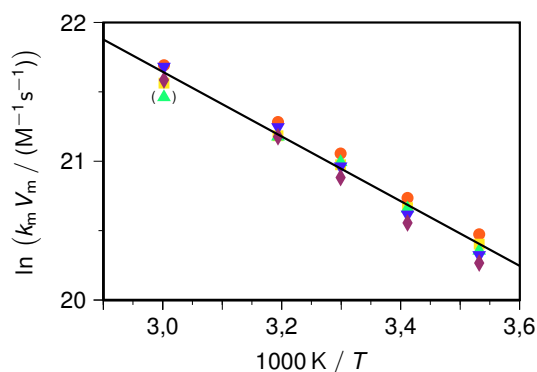


Abbildung 3.7: Arrhenius-Plot für die dynamische intramizellare Löschung des Pyrens durch Viologene; der Anstieg der Geraden liefert $E_A = 19,4 \text{ kJ mol}^{-1}$.

Abklingkurven logarithmiert werden (Abb. 3.5 (b)). Auf den langen Zeitskalen von $> 100 \text{ ns}$ sind dort parallele Kurven zu sehen, welche von Mizellen ohne Quencher-molekül herrühren und dort der Fluorophor demnach immer entsprechend des Terms $\exp(-t/\tau_0)$ in der Gl. 3.16 abklingt. Aber es kann aus diesem Bereich nicht nur τ_0 extrahiert werden, sondern eine Multiplikation mit $\exp(+t/\tau_0)$ entfernt diesen Beitrag vollständig. Dadurch entstehen im Plot Kurven, die nach 100 ns einen konstanten Beitrag erreichen (Abb. 3.5 (c)). Abbildung 3.5 (d) zeigt die Ergebnisse der vollständigen Separation. Das Abklingen des dynamischen Quenchprozesses und die Konzentrationsabhängigkeit des Anteils an Quencher-freien Mizellen entsprechen dem zweiten und dritten Term der Gl. 3.16. Ein simultaner Fit dieser Daten mit den verbleibenden Termen aus Gl. 3.16 konvergiert sehr schnell und liefert eindeutige Parameter. Fits mit den durch diese Auswerteprozedur erhaltenen k_m , K_m , N_{agg} und τ_0 geben die Kurven extrem gut wieder (Abb.3.5 (a)).

Durch Auswertung aller temperaturabhängigen Fluoreszenzmessungen kann nun ein großes Datenset untersucht werden. Zunächst soll die Aggregationszahl genauer betrachtet werden. Eine Analyse zeigt, dass sie nicht von dem verwendeten Viologen-Derivat, wohl aber von der Temperatur abhängt. Das Verhalten stimmt sehr gut mit dem aus einer aktuellen Neutronenstreuungsstudie (SANS) zum Aggregationsverhalten von SDS^[12] überein (Abb. 3.6). Es ist also keine hochspezielle SANS- oder SAXS-Apparatur nötig, sondern es genügt ein einfaches zeitaufgelöstes Fluoreszenzspektrometer, das die meisten photochemisch orientierten Gruppen besitzen werden. Diese gute Übereinstimmung steht im Gegensatz zu der einfachen Bestimmung von N_{agg} aus $\exp(-\langle q \rangle)$, bei der unter vergleichbaren Bedingungen ganz verschiedene N_{agg} erhalten werden.

Um k_m und K_m in die geläufigen volumenbezogenen Größen zu transformieren, ist eine Multiplikation mit dem Mizellvolumen V_m (in l mol^{-1} , berechnet aus der Literatur^[12]) nötig.

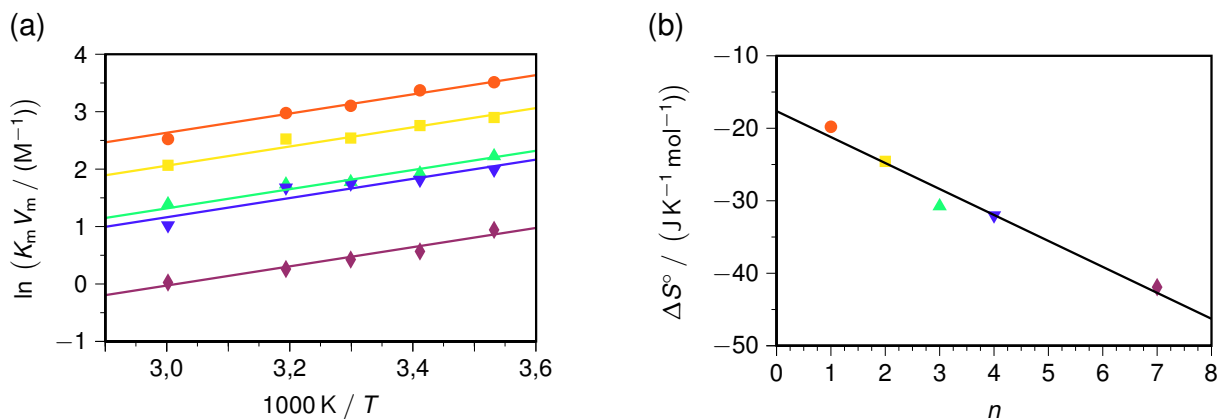


Abbildung 3.8: Statisches intramizellares Löschen des Pyrens durch Viologene; (a) van-'t-Hoff-Plot; Anpassung über alle Kurven liefert eine Standardenthalpie von $\Delta H^\circ = -13,9 \text{ kJ mol}^{-1}$ und eine löscherspezifische Entropie ΔS° ; (b) ΔS° in Abhängigkeit der Anzahl der Kohlenstoffatome in der Seitenkette n (lineare Regression liefert $-(17,7 + 3,58n) \text{ J K}^{-1} \text{ mol}^{-1}$).

Abbildung 3.7 zeigt die Temperaturabhängigkeit von $k_m V_m$ für alle fünf Löscher als Arrhenius-Plot. Alle Viologene zeigen praktisch identische Geschwindigkeitskonstanten, welche für eine Diffusionskontrolle sprechen. Im Gegensatz dazu zeigt K_m eine deutliche Abhängigkeit von der Substitution des Viologens. Abbildung 3.8 zeigt den zugehörigen van-'t-Hoff-Plot. Der Löschprozess kann für alle Viologene mit der gleichen Standardenthalpie ΔH° ($-13,9 \text{ kJ mol}^{-1}$) aber unterschiedlichen Standardentropien ΔS° beschrieben werden. Letzteres kann durch einen Verlust von Rotationsfreiheitsgraden der Seitenketten bei dem π - π -Stacking im Grundzustandskomplex erklärt werden (siehe Abschnitt 3.1.1).

3.1.3 Fluoreszenzlöschung von Pyren mit Methylviologen in n -Alkylsulfaten (Publ. C)

Im nächsten Schritt wurden das statische und dynamische Löschen von Pyren mit Methylviologen in verschiedenen Natrium- n -Alkylsulfat-Mizellen (S_nS mit der Kettenlänge n) untersucht. Das experimentelle Vorgehen und die Auswertung der Fluoreszenzabklingkurven erfolgte analog zu dem vorangegangenen Abschnitt. Es hat sich gezeigt, dass die Methode wunderbar geeignet ist, um die Mizelle hinsichtlich ihrer Aggregationszahl zu charakterisieren. Diese ist aber nicht nur von der Temperatur abhängig, sondern auch von der Ionenstärke^[81]. Dieser Einfluss wurde durch Zugabe von verschiedenen Mengen NaCl zur Pyren-MV²⁺-Lösung untersucht. Dazu soll zunächst das SDS (S12S) noch einmal genauer betrachtet werden, denn hierfür existiert die größte Datenbasis im Bezug auf den Einfluss der Ionenstärke auf die mizellaren Eigenschaften.

Bisher waren die Fluoreszenzabklingkurven nach dem Logarithmieren nach 100 ns, innerhalb derer das intramizellare dynamische Löschen vollständig stattfindet, immer streng parallel zueinander, was auf die angeregten Fluorophore in Löscher-freien Mizellen zurückzuführen ist (Abb. 3.9). Die Unabhängigkeit von τ von der Löscherkonzentration bestätigt die immobile-

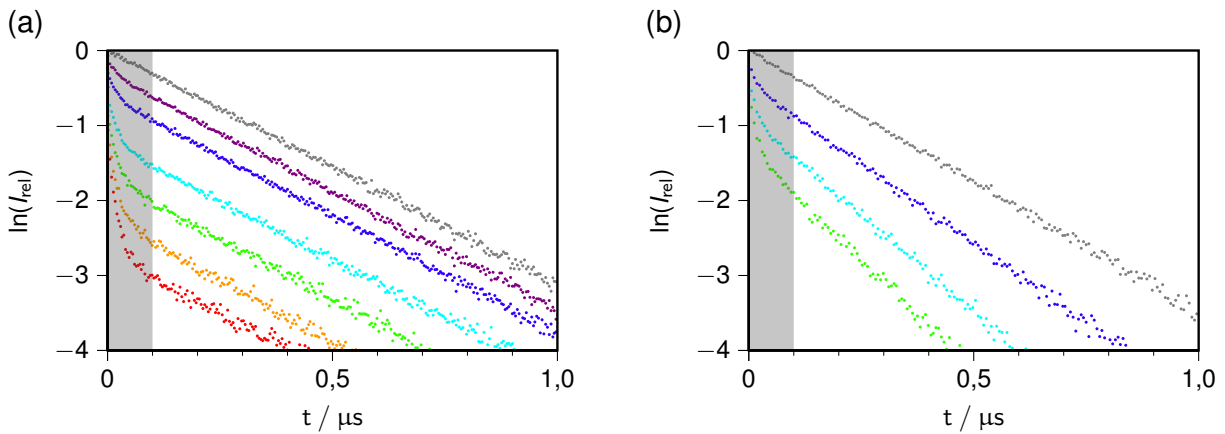


Abbildung 3.9: Logarithmierte Fluoreszenzabklingkurven der Löschung von Pyren (10 μM) durch Methylviologen (Anregung 341 nm, Emission 395 nm, Einwaagekonzentrationen in mM: grau, 0; violett, 0,085; dunkelblau, 0,17; cyan, 0,34; grün, 0,51; orange, 0,68; rot, 0,85); (a) in 50 mM S13S bei 30 °C, die ersten 100 ns, in denen das intramizellare Löschen stattfindet, sind grau hinterlegt; (b) in 50 mM S12S bei 40 °C und mit 250 mM NaCl, die nicht parallelen Kurven werden durch ein Löschen durch die Mizelle-Wasser-Grenzfläche hervorgerufen.

quencher-Annahme. Bei Zugabe größerer Mengen NaCl und Temperaturerhöhung zeigt sich jedoch, dass die geraden Linien mit zunehmender MV^{2+} -Konzentration steiler werden (Abb. 3.9). Dies spricht für ein dynamisches Quenchen durch die Mizelle-Wasser-Grenzfläche. Dieses Löschen folgt einem Geschwindigkeitsgesetz pseudo-erster Ordnung. Ein Teil des MV^{2+} befindet sich also offensichtlich in der wässrigen Phase. Es ist bekannt, dass Na^+ -Ionen es teilweise von der Mizelloberfläche verdrängen können^[177]. Durch Messung der Änderung des Absorptionsspektrums von gebundenem und freiem MV^{2+} konnte der Anteil in wässriger Lösung bestimmt werden [Q_{aq}], der bei der höchsten NaCl-Konzentration und Temperatur fast 40 % beträgt. Durch Auswertung der Fluoreszenzabklingkurven nach 100 ns ergab sich für alle NaCl-Konzentration die gleiche Geschwindigkeitskonstante von $2,2 \cdot 10^{10} \text{ M}^{-1} \text{ s}^{-1}$ für die Löschung durch [Q_{aq}] über die Phasengrenze hinweg (bei Hinzunahme der anderen Temperaturen ergibt sich $E_A = 15 \text{ kJ mol}^{-1}$). Die Kenntnis von [Q_{aq}] ist entscheidend für die richtige Berechnung der mizellgebundenen Löscherkonzentration [Q_{m}], die ihrerseits ausschlaggebend für die korrekte Auswertung der intramizellaren kombinierten Löschung und damit verlässliche Parameter k_{m} , K_{m} und N_{agg} ist. Globale Fits lieferten so die Aggregationszahl $N_{\text{agg}}(n, T, c_{\text{ad}})$ als Funktion der Kettenlänge n , der Temperatur T und – nur für S12S – der NaCl-Konzentration c_{ad} .

In der Literatur gut beschrieben (allerdings nur für bestimmte Temperaturen^[81,178]) ist die Abhängigkeit von N_{agg} von [Na_{aq}^+] in der Lösung. Die Gleichung enthält die Mizellbildnerspezifischen Parameter cmc ohne Salzzugabe cmc_0 , die Aggregationszahl $N_{\text{agg},0}$ und den Exponenten γ . In der variablen Größe [Na_{aq}^+] ist noch der Dissoziationsgrad α inbegriffen, der die Menge an Na^+ berücksichtigt, welche direkt von der Mizelle stammt.

$$N_{\text{agg}}(T) = N_{\text{agg},0}(T) \left(\frac{[\text{Na}_{\text{aq}}^+]}{\text{cmc}_0(T)} \right)^\gamma \quad (3.18)$$

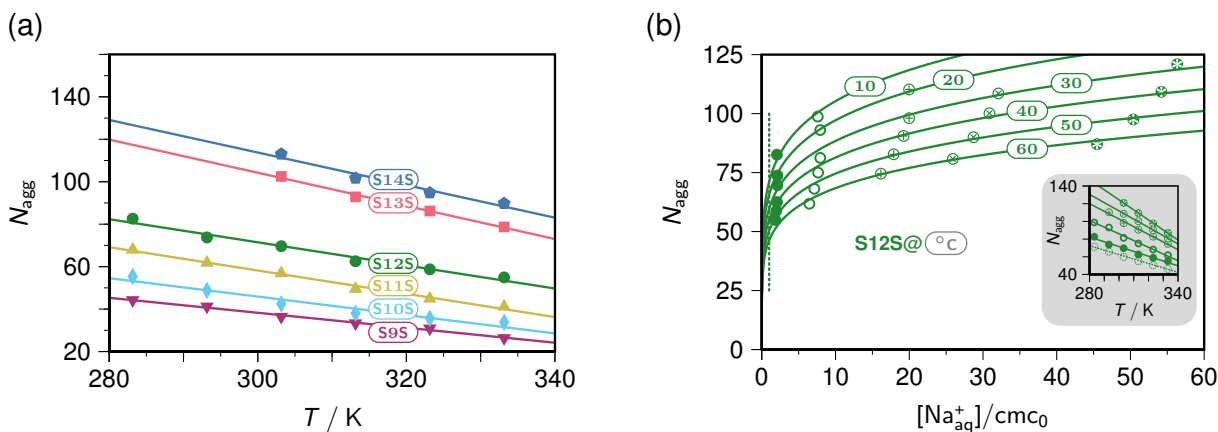


Abbildung 3.10: Aggregationszahl N_{agg} bestimmt durch Fluoreszenzlöschexperimente; (a) für verschiedene Natriumalkylsulfate S_nS als Funktion von T mit entsprechenden linearen Fits; (b) für S12S bei verschiedenen Temperaturen als Funktion der Gesamtnatriumkonzentration $[Na_{aq}^+]$ (Variation realisiert durch Zugabe von NaCl) angepasst mit Gl. 3.18 ($N_{agg,0}$ an der gestrichelten Linie), Inset: N_{agg} und $N_{agg,0}$ (gestrichelt) als Funktion von T mit linearen Fits.

Die Anpassung für alle $[Na_{aq}^+]$ und T ergab ein globales γ (mit 0,17 liegt der Wert etwas tiefer als der in der Literatur angegebene^[81,179]) und lokale $N_{agg,0}$, die linear von der Temperatur abhängen. Zur Temperaturabhängigkeit von N_{agg} von verschiedenen S_nS gibt es in der Literatur nur vereinzelt etwas^[12,180], insbesondere ungeradzahlige n sind schlecht untersucht. Abbildung 3.10 zeigt, dass N_{agg} immer eine lineare Funktion von T ist.

Die Wichtigkeit der Aggregationszahl für die Beschreibung der intramizellaren Löschvorgänge liegt in der direkten Verknüpfung zum Mizellvolumen $V_m = \Phi_m N_{agg}$. Durch Interpolation von partiellen molaren Volumina Φ_m aus der Literatur^[181,182] wurden die Mizellvolumina berechnet. Sie ergeben eine Varianz über alle S_nS und Temperaturen mit einem Faktor von mehr als 4. Die Abhängigkeit der erhaltenen Parameter k_m und K_m von der Kettenlänge ist wiederum invers zu der von V_m .

Nach einer Multiplikation von V_m und k_m und K_m (welche auf der Löscheranzahl beruhen) zur Umwandlung in die typischen konzentrationsbasierten Konstanten k und K zeigt sich, dass der Unterschied zwischen den verschiedenen S_nS praktisch verschwindet (Abb. 3.11). In einem Arrhenius-Plot lassen sich alle k mit einer Geraden anpassen, E_A beträgt 24 kJ mol^{-1} , und in einem van-'t-Hoff-Plot ist ebenfalls eine gemeinsame Anpassung aller Daten möglich, so dass man eine Enthalpie $\Delta H^\circ = -16 \text{ kJ mol}^{-1}$ und eine Entropie $\Delta S^\circ = -27 \text{ J K}^{-1} \text{ mol}^{-1}$ erhält. Es scheint also so zu sein, dass die Geschwindigkeits- und Komplexbildungskonstanten nicht von der Mizellgröße abhängen und es sich nur um einen Volumeneffekt handelt, insbesondere auch, weil die Werte erstaunlich gut mit denen in Methanol (welches die gleiche Mikropolarität wie die S_nS Mizellen aufweist^[104], $\Delta H^\circ = -14 \text{ kJ mol}^{-1}$, $\Delta S^\circ = -21 \text{ J K}^{-1} \text{ mol}^{-1}$) übereinstimmen. Auch bei den S12S-Daten, bei welchen die Volumenvariation durch Zusatz von NaCl realisiert wird, fallen für die jeweiligen Temperaturen die Datenpunkte nach der Multiplikation mit V_m zusammen.

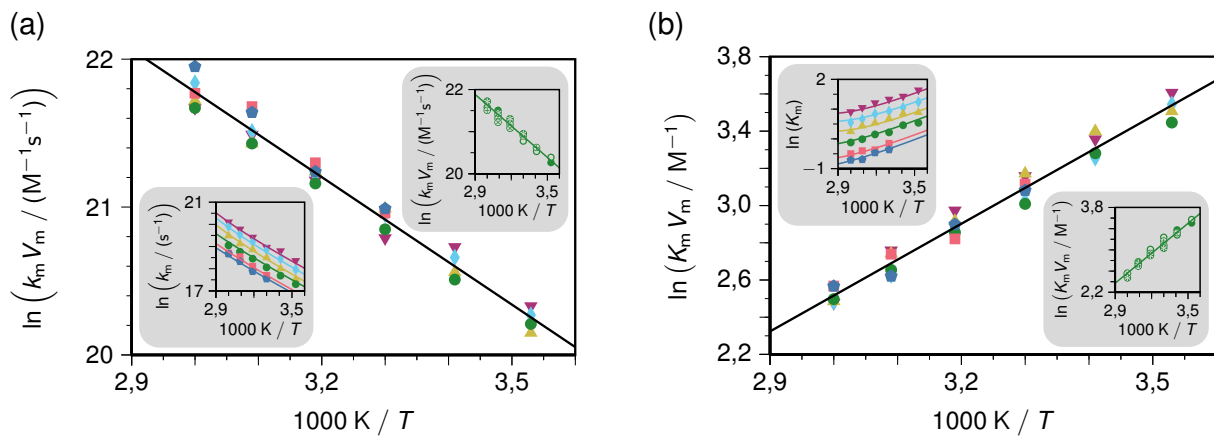


Abbildung 3.11: Dynamische (a) und statische (b) intramizellare Löschung von Pyren mit MV^{2+} in S7S Mizellen (Symbole und Farbgestaltung analog zu Abb. 3.10); (a) Arrhenius-Plot für $k = k_m V_m$ ($E_A = 24 \text{ kJ mol}^{-1}$), Inset (links): Arrhenius-Plot für k_m ; (b) van-'t-Hoff-Plot für $K = K_m V_m$ ($\Delta H^\circ = -16 \text{ kJ mol}^{-1}$, $\Delta S^\circ = -27 \text{ J K}^{-1} \text{ mol}^{-1}$), Inset (links): van-'t-Hoff-Plot für K_m ; die beiden jeweils rechten Insets zeigen die entsprechenden Plots für S12S mit Zusatz von NaCl (vgl. Abb. 3.10 (b)) mit $k_m V_m$ bzw. $K_m V_m$.

3.2 Photoionisierungen in Mizellen

Wie bereits in Kapitel 2 dargelegt, bieten Mizellen auch für Photoionisierungen ein geeignetes Medium. Im Gegensatz zur Fluoreszenz, bei der es sich um einen rein photophysikalischen Prozess handelt, der auf einer Zeitskala von ns bis zu wenigen μ s vollständig abgeklungen ist, sind Photoionisierungen häufig mit anschließenden chemischen Prozessen verknüpft, deren Produkte mit der Laserblitzlicht-Photolyse-Apparatur in einem Bereich von ein paar Zehntel μ s bis zu einigen ms untersucht werden können. Durch die Verwendung von mizellaren Lösungen können einige Vorzüge entstehen. Zum einen verbessern sie erheblich die Löslichkeit von hydrophoben Substanzen in Wasser durch Aufnahme in die Mizelle, zum anderen kann die Mizelle auch gegen äußere Einflüsse aus der Lösung abschirmen oder sie dient als Modell für natürliche in biologischen Systemen vorkommende Mizellen, oder es können gar stark vereinfachte Liposome oder Biomembranen nachempfunden werden.

Im Folgenden soll anhand von zwei Systemen die Nützlichkeit von Photoionisierung mittels Laserblitzlicht-Photolyse in mizellarer Umgebung demonstriert werden.

Die Photoionisierung von 2-Aminoanthracen in SDS-Mizellen mittels 355 nm-Laserlicht dient zur Erzeugung hoher Konzentrationen hydratisierter Elektronen. Letztere werden für zahlreiche Reaktionen insbesondere reduktive Dehalogenierungen, aber auch die Reduktion von Carbonylverbindungen verwendet. Bei den entstehenden Radikalen ist dann eine Wurtz-artige Kupplung möglich. Durch Rückgewinnung des 2-Aminoanthracens aus seinem entstandenen Radikalkation durch das preiswerte hydrophobe und damit mizellgebundene Reduktionsmittel Palmitoylascorbat kann ein Katalysezyklus entworfen werden, der zur Produktion von hydratisierten Elektronen dient. Dadurch ist eine Synthese der Kupplungsprodukte im Labormaßstab möglich.

Im Fall der Photoionisierung des Quercetins geht es hingegen nicht um das hydratisierte Elektron. Hier ist das verbleibende Radikal von Interesse. Es wird gezeigt, dass die Photoionisierung mittels Laserblitzlicht-Photolyse ein hervorragendes Werkzeug ist, um den Mechanismus und die beteiligten Radikalspezies bei der Wirkung von Antioxidantien aufzuklären. Zum einen wurden grundlegende Experimente in homogener Lösung durchgeführt, um zu demonstrieren, dass eine Erzeugung und Untersuchung der Quercetin-Radikale mittels Photoionisierung überhaupt möglich ist. Zum anderen wurde die Methode dann für eine Reihe von Quercetin-Derivaten in Mizellen, in diesem Fall das neutrale Triton X-100, angewendet. Auch hierbei dient die Mizelle praktisch als Container für die zu untersuchenden Substanzen und ihre entstehenden Radikalspezies. Die Mizelle dient aber nicht nur zur Verbesserung der schlechten Wasserlöslichkeit des Quercetins und seiner Derivate, was bei der Untersuchung bessere Messbedingungen ermöglicht und z.B. im menschlichen Körper eine höhere Bioverfügbarkeit bedeuten würde, sondern sie weist auch eine Ähnlichkeit zu biologischen Systemen auf, was für Target-Applikationen interessant sein kann.

3.2.1 Photoionisierung von 2-Aminoanthracen in SDS (Publ. D)

Nur durch die Verwendung von Mizellen ist es überhaupt möglich, hydrophobe Moleküle wie das 2-Aminoanthracen (AntNH_2) in ausreichender Menge in wässrige Lösung zu bringen, um es zu untersuchen. In SDS-mizellarer Lösung ist es ausreichend gut löslich. Das AntNH_2 befindet sich mit dem aromatischen System innerhalb der Mizelle und die Aminogruppe ragt zwischen die Kopfgruppen. Die Aminogruppe kann im Sauren protoniert werden ($\text{p}K_a = 6,1$) und das entstehenden AntNH_3^+ ist wiederum eine Photosäure ($\text{p}K_a = 0,2$). Eine genaue Untersuchung der Photoionisierung mittels Laserblitzlichtphotolyse (355 nm, 5 ns Pulsdauer) zeigt, dass es sich um einen biphotonischen Mechanismus handelt. Dazu wurde sowohl die Abhängigkeit der Ausbeute an hydratisiertem Elektron $e_{\text{aq}}^{\bullet-}$ von der Laserintensität I_{355} als auch gleichzeitig die Abhängigkeit der Fluoreszenz davon verfolgt. Bei einer monophotonischen Ionisierung sind Elektronenauswurf und Fluoreszenz Parallelreaktionen und müssten daher den gleichen Kurvenverlauf zeigen. Dies ist aber nicht der Fall, stattdessen durchläuft die Fluoreszenz ein Maximum, was charakteristisch für konsekutive biphotonische Ionisierungen ist (Abb. 3.12). Es ist auch zu sehen, dass ein einzelner Laserpuls mit 100 mJ cm^{-2} bereits mehr als 50 % des AntNH_2 ionisieren kann. Außerdem kann AntNH_2 praktisch über den gesamten untersuchten pH-Bereich nahezu die gleiche Elektronenmenge liefern, auch wenn die elektronenschiebende Eigenschaft der Aminogruppe durch Protonierung entfällt. Allerdings ist die Verwendbarkeit des $e_{\text{aq}}^{\bullet-}$ bei pH-Werten unter 4,5 zusehends stark eingeschränkt, denn hier reagiert es schnell mit H^+ -Ionen ab (Abb. 3.12).

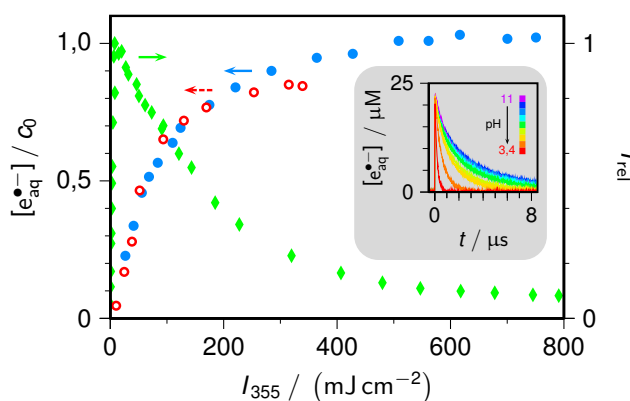


Abbildung 3.12: Intensitätsabhängigkeiten bei der Photoionisierung von AntNH_2 (35 μM) in SDS (50 mM), blau: Ausbeute an $e_{\text{aq}}^{\bullet-}$ bei pH 8,5, rot: Ausbeute an $e_{\text{aq}}^{\bullet-}$ bei pH 4,0, grün: Fluoreszenzintensität; Inset: Abklingkurven des $e_{\text{aq}}^{\bullet-}$ bei verschiedenen pH-Werten (3,4, 4,0, 4,5, 5,0, 5,5, 6,0, 6,4, 8,5, 11,0).

Das bei der Photoionisierung ebenfalls entstehende Radikalkation $\text{AntNH}_2^{\bullet+}$ besitzt eine sehr lange Lebenszeit von 450 μs . Hier zeigen sich klar die Vorzüge bei der Verwendung von SDS-Mizellen. Das hydratisierte Elektron wird in die wässrige Phase ausgestoßen und das $\text{AntNH}_2^{\bullet+}$ verbleibt in der Mizelle. Dabei schützt diese es vor Rekombination mit $e_{\text{aq}}^{\bullet-}$ oder der Reaktion mit anderen Spezies aus der wässrigen Phase. Die Abschirmung in der Mizelle hat allerdings auch zur Folge, dass die gewünschte Reparatur des $\text{AntNH}_2^{\bullet+}$

zur Regeneration von AntNH_2 durch das sich komplett in der wässrigen Phase befindliche Ascorbat-Monoanion AscH^- vergleichsweise langsam abläuft (Abb. 3.13 (a)). Einige zehn mM werden benötigt, um die Regeneration in ca. 100 μs abzuschließen ($k = 7 \cdot 10^6 \text{ M}^{-1} \text{ s}^{-1}$).

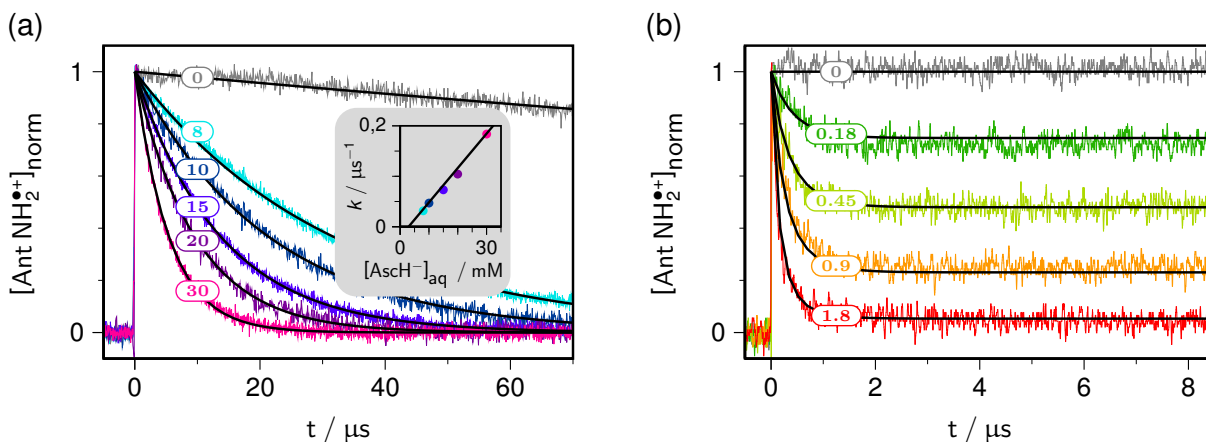


Abbildung 3.13: Regeneration des AntNH_2 (35 μM) in SDS (50 mM) durch verschiedene Konzentrationen (Beschriftung an den Kurven, in mM) an Opferdonor AscH^- (a) oder PAscH^- (b), ($I_{355} = 100 \text{ mJ cm}^{-2}$); (a) transiente Absorption mit den besten monoexponentiellen Fits, daraus ergibt sich eine Geschwindigkeitskonstante von $k = 7 \cdot 10^6 \text{ M}^{-1} \text{ s}^{-1}$.

Auf der anderen Seite zeigt Abb. 3.13 (b) die Regeneration mit dem hydrophoben Palmitoyl-Derivat PAscH^- . Dieses befindet sich quantitativ in der Mizelle und tritt auch nur auf einer ms-Zeitskala aus. Dadurch ist eine komplette intramizellare Löschung möglich. Diese läuft, obwohl natürlich die gleiche thermodynamische Treibkraft wie beim AscH^- zugrunde liegt, einige Größenordnungen schneller ab. Bei kleinen PAscH^- -Konzentrationen läuft sie allerdings nicht vollständig ab, da es nach der Poisson-Statistik auch Mizellen ohne PAscH^- -Molekül gibt. Der Anteil des nicht regenerierten AntNH_2 wird allerdings bereits bei 10 mM vernachlässigbar klein ($< 1 \text{ ppm}$). Während die Ascorbat-Monoanionen in der Lage sind das AntNH_2 zu regenerieren, ist es mit den vollständig protonierten Formen ($\text{p}K_a(\text{PAscH}_2) = 6,5$) nicht möglich. Außerdem hydrolysiert die Esterbindung des PAscH^- bei pH-Werten über 10. Zusammen mit der ohnehin bestehenden Einschränkung durch die Reaktion von $\text{e}_{\text{aq}}^{\bullet-}$ mit H^+ im Säuren, ergibt sich für praktische Anwendungen ein pH-Bereich zwischen 5 und 10.

Diese ganzen Ergebnisse aus den Experimenten zur linearen Photoionisierung wurden dann zu einem Katalysezyklus kombiniert (Abb. 3.14). Der Katalysator AntNH_2 gibt in einer biphotonischen Photoionisierung über den angeregten Zustand AntNH_2^* ein $\text{e}_{\text{aq}}^{\bullet-}$ in die wässrige Phase ab, während $\text{AntNH}_2^{\bullet+}$ in der Mizelle verbleibt und dort durch einen Opferdonor AscH^- oder PAscH^- zum Ausgangsmolekül AntNH_2 regeneriert wird. Um die katalytische Produktion von $\text{e}_{\text{aq}}^{\bullet-}$ zu demonstrieren, wurde die Laserblitzlicht-Photolyse-Apparatur so modifiziert, dass die Lösung in der Küvette nicht wie gewöhnlich nach jedem Laserpuls ausgetauscht wird, sondern dass mehrere Pulse auf dieselbe Lösung treffen. Bei der genutzten Intensität wurden mehr als 50 % des AntNH_2 pro Puls ionisiert und damit konnte über alle 21 Pulse auf dieselbe Lösung eine Elektronenmenge erhalten werden, die mehr als das

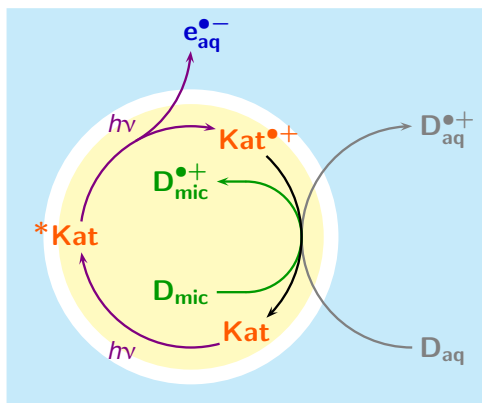


Abbildung 3.14: Katalysezyklus zur Erzeugung hydratisierter Elektronen in SDS-Mizellen; der Katalysator Kat ist AntNH₂, die Opferdonatoren D_{aq} und D_{mic} stehen für AscH⁻ und PAscH⁻.

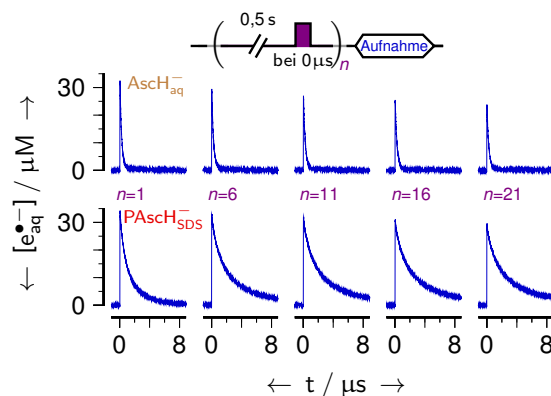


Abbildung 3.15: Demonstrationsexperiment zur Regenerierung des AntNH₂ (70 µM) durch PAscH⁻ und AscH⁻ (10 mM) in SDS-Lösung (50 mM, pH 8); dargestellt ist die Elektronenabsorption nach dem *n*-ten Puls umgerechnet in Konzentrationen, die Abfolge der Pulse ist schematisch dargestellt, zwischen den Pulsen wurde die Lösung nicht ausgetauscht.

10-fache der AntNH₂-Katalysatorkonzentration ist (Abb. 3.15). Der Katalysatorverlust beträgt pro Puls 1,5 % mit AscH⁻ und 0,6 % mit PAscH⁻.

Als Modellreaktion für die praktische Anwendbarkeit wurde die reduktive Dehalogenierung von Chloracetat durch e_{aq}^{•-} gewählt. Das entstehende Carboxymethyl-Radikal kann nun durch Dimerisierung zum Succinat reagieren oder ein Wasserstoff abstrahieren und so zum Acetat werden. Es zeigt sich, dass die Verwendung von PAscH⁻, also der Einschluss des Katalysators AntNH₂ und des Opferdonors einige Vorteile mit sich bringt. Da sich kein Donor bzw. mögliche Donor-Folgeprodukte oder -Radikale in der wässrigen Phase befinden, dort wo sich das Carboxymethyl aufhält, wird zum Einen die Anzahl möglicher Nebenreaktionen drastisch reduziert und zum Anderen steigt signifikant der Anteil des Dimerisierungsprodukts. Fast 90 % Succinat werden gebildet, wenn der Zugang zum Wasserstoff-Donor Ascorbat durch Einschluss in die Mizelle als PAscH⁻ eingeschränkt wird. Das System wurde auf eine Standard-Küvette (1 cm x 1 cm) hochskaliert und für eine Reihe anderer Substrate angewendet (Tab. 3.2).

Nach der initialen Reaktion der Substrate mit e_{aq}^{•-} können die gebildeten Radikale entweder dimerisieren oder ein Wasserstoffatom abstrahieren. PAscH⁻ favorisiert die Dimerisierung oder macht dieses sogar überhaupt erst möglich. Mit AscH⁻ können nur Radikale mit guten Ausbeuten dimerisiert werden, die nur eine geringe Tendenz zur H-Abstraktion aufweisen, so z.B. die stark stabilisierten aromatischen Ketylradikale des Benzaldehyds und Acetophenons, sowie das Benzylradikal ausgehend vom Benzylchlorid und das Fluor-substituierte Radikal vom Chlorodifluoroacetat. Wenn das Substrat selbst oder sein Reaktionsprodukt ein guter Wasserstoff-Donor ist, kann auch mit PAscH⁻ keine effektive Dimerisierung stattfinden, wie im Fall des Cysteins oder der aliphatischen Ketone. Phenylradikale geben generell kein Dimerisierungsprodukt^[183], was auch durch das verwendete Chlorobenzoat bestätigt wird.

Tabelle 3.2: Ergebnisse der Umsetzungen mit AntNH_2 als katalytische $e_{\text{aq}}^{\bullet-}$ -Quelle, das Verhältnis Substrat:Opferdonor:Katalysator betrug immer 100:100:1.

Substrat	Umsetzung / %		Dimerisierungs- produkt	Ausbeute / %		H-Abstraktions- produkt	Ausbeute / %	
	AsCH ⁻	PAsCH ⁻		AsCH ⁻	PAsCH ⁻		AsCH ⁻	PAsCH ⁻
Chloracetat	87	100	Succinat	25	89	Acetat	11	9
Chlordifluoracetat	65	96	Tetrafluorsuccinat	80	91	Difluoracetat	8	1
2-Chlorpropionat	68	100	2,3-Dimethylsuccinat	7	46	Propionat	29	42
2-Chlorbutyrat	71	100	-	-	-	Butyrat	23	47
3-Chlorpropionat	28	85	Adipat	-	58	Propionat	9	-
3-Chlorpivalat	24	86	2,2,5,5-Tetramethyladipat	-	73	Pivalat	38	16
2-Chlorethanol	25	100	1,4-Butandiol	-	39	Ethanol	57	20
Benzylchlorid	16	61	1,2-Diphenylethan	50	90	Toluol	12	5
4-Chlorbenzoat	100	100	-	-	-	Benzoat	94	95
Aceton	72	100	Pinacol	5	2	2-Propanol	93	92
Pinacolon	40	100	-	-	-	Pinakolyalkohol	95	90
Acetophenon	64	66	2,3-Diphenyl-2,3-butandiol	76	97	-	-	-
Benzaldehyd	84	81	1,2-Diphenyl-1,2-ethandiol	67	98	Benzylalkohol	-	1
Cystein	67	83	-	-	-	Alanin	66	61

Zusammenfassend wurde gezeigt, dass das System AntNH_2 als Katalysator und PAsCH^- als Opferdonor in SDS-mizellarer Lösung ein geeignetes System zur Erzeugung hydratisierter Elektronen und damit für laserinduzierte Dimerisierungen darstellt.

3.2.2 Photoionisierung von Quercetin in homogener Lösung und Triton X-100 Mizellen (Publ. E, F)

Zunächst wurde untersucht, ob sich das Antioxidans Quercetin photoionisieren lässt und ob sich damit mittels Laserblitzlicht-Photolyse die entstehenden Radikale untersuchen lassen. Um keine weiteren Einflüsse zu haben, geschah dies zunächst in homogener wässriger Lösung. Als wichtige Grundlage für weitere Untersuchungen konnte durch Absorptions- und Fluoreszenzmessungen bei verschiedenen pH-Werten zunächst der pK_a -Wert des Quercetins in Wasser bestimmt werden. Grund hierfür ist, dass in der Literatur Werte zwischen 5,50^[184] und 7,65^[185] für den ersten pK_a zu finden sind. In dem untersuchten pH-Bereich von pH 2 - 9 spielt demnach nur die neutrale vollständig protonierte Form H_2Q und die einfach deprotonierte Form HQ^- eine Rolle. Das Absorptionsspektrum zeigt für H_2Q ein Maximum bei 368 nm ($\epsilon = 16200 \text{ M}^{-1} \text{ cm}^{-1}$) und für HQ^- ein Maximum bei ca. 395 nm ($\epsilon \approx 17500 \text{ M}^{-1} \text{ cm}^{-1}$). Allerdings ist nur bis pH 8,5 ein gut definierter isosbestischer Punkt zu finden. Grund dafür ist, dass ab dort weitere Deprotonierungsstufen eine Rolle spielen. Die Absorptionsmessungen liefern einen $pK_a \approx 7,5$. Bei der Auswertung der Fluoreszenzkurven besteht dieses Problem nicht. Während das neutrale HQ nur sehr schwach fluoresziert ($\lambda_{\text{max}} = 521 \text{ nm}$), fluoresziert HQ^- deutlich stärker ($\lambda_{\text{max}} = 554 \text{ nm}$). Die Titrationskurve ergibt einen klaren $pK_a = 7,3$. Bei der Bestrahlung mit Laserlicht der Wellenlänge 355 nm wurde in Argon-gesättigter Lösung von H_2Q und HQ^- die charakteristische breite Absorptionsbande des $e_{\text{aq}}^{\bullet-}$ gefunden, welche bei Sättigung der Lösung mit N_2O verschwindet. Dies ist ein klarer Beleg für die Photoionisierbarkeit des Quercetins. Unter N_2O verbleibt die Absorption der entstehenden Quercetin-Radikale. Die kalibrierten Spektren sind in Abbildung 3.16 dargestellt. Das nach der Photoionisierung entstehende Radikalkation deprotoniert quasi instantan. Bei niedrigen pH-Werten liegt dann das neutrale Radikal HQ^{\bullet} ($pK_a = 4,5$) vor und am oberen Ende des untersuchten pH-Bereiches das Radikalanion $Q^{\bullet-}$. Beide Radikale reagieren auf einer Zeitskala von einigen hundert μs zu anderen Spezies.

Bei Anwesenheit des Co-Antioxidans Ascorbat verkürzt sich die Lebenszeit der Radikale. Das Ascorbat kann das Quercetin komplett regenerieren und nach einigen μs dominiert die Absorptionsbande des $Asc^{\bullet-}$. Bei konstantem pH-Wert folgt die Reparatur einer Kinetik pseudo-erster Ordnung, d.h. die beobachtete Geschwindigkeitskonstante k_{obs} ist linear von der Gesamtascorbat-Konzentration c_{Asc} abhängig (Abb. 3.17 (a)). Allerdings ist k_{obs} auch vom pH-Wert der Lösung abhängig (Abb. 3.17 (b)). Es zeigt sich, dass der Zusammenhang durch eine glockenförmige Kurve beschrieben wird. Im Bereich von pH 2 bis 9 existieren die Radikale HQ^{\bullet} und $Q^{\bullet-}$ und das Vitamin C als Ascorbinsäure $AscH_2$ und Monoanion $AscH^-$. Damit sind vier Möglichkeiten zur Reaktion von Radikal und Co-Antioxidans denkbar. Da bei niedrigen pH-Werten aber keinerlei Regeneration beobachtet werden kann, scheidet das Paar $HQ^{\bullet}/AscH_2$ sofort aus. Im leicht basischen ist hingegen eine sehr langsame Reaktion

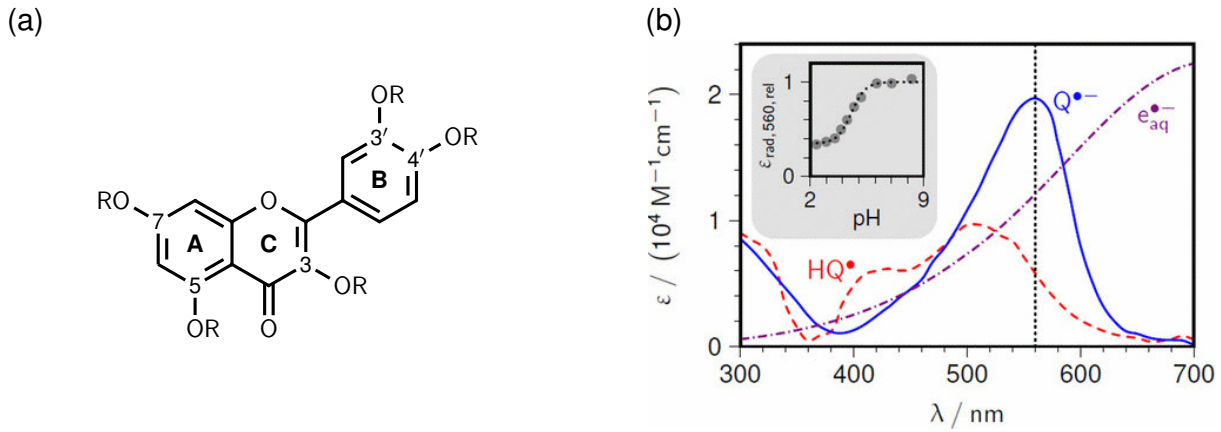


Abbildung 3.16: (a) Strukturformel des Quercetins (alle R = H) mitsamt der systematischen Nummerierung der Kohlenstoffatome und der Bezeichnung der Ringe; (b) kalibrierte Absorptionsspektren des $e_{aq}^{\bullet-}$ und der Quercetin-Radikale HQ^{\bullet} und $Q^{\bullet-}$; Inset: pH-Abhängigkeit des Extinktionskoeffizienten bei 560 nm liefert einen $pK_a(HQ^{\bullet}) = 4,5$.

zu beobachten. Es wurde für die Reaktion von $Q^{\bullet-}$ mit $AscH^-$ eine Geschwindigkeitskonstante von $3,0 \cdot 10^6 \text{ M}^{-1} \text{ s}^{-1}$ gefunden.

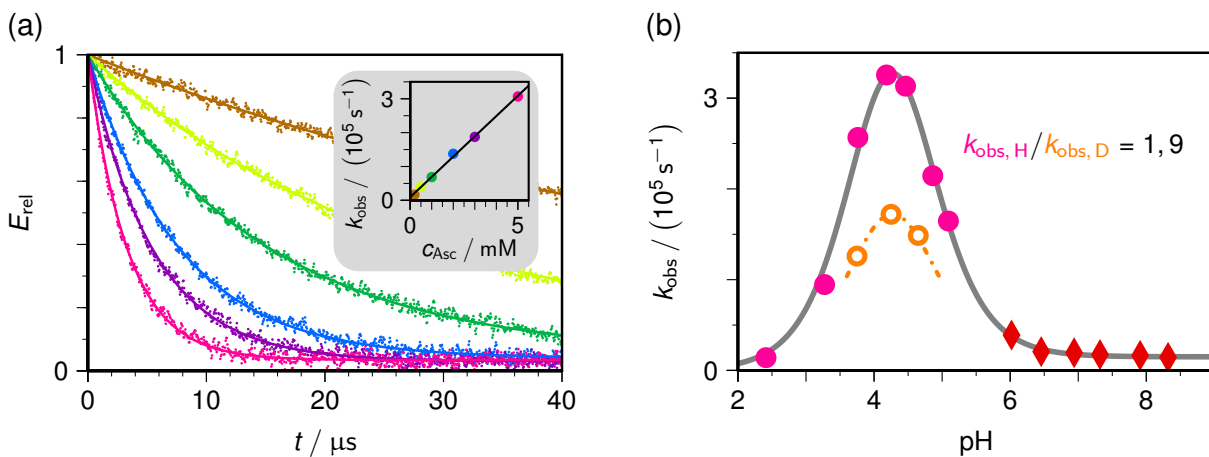
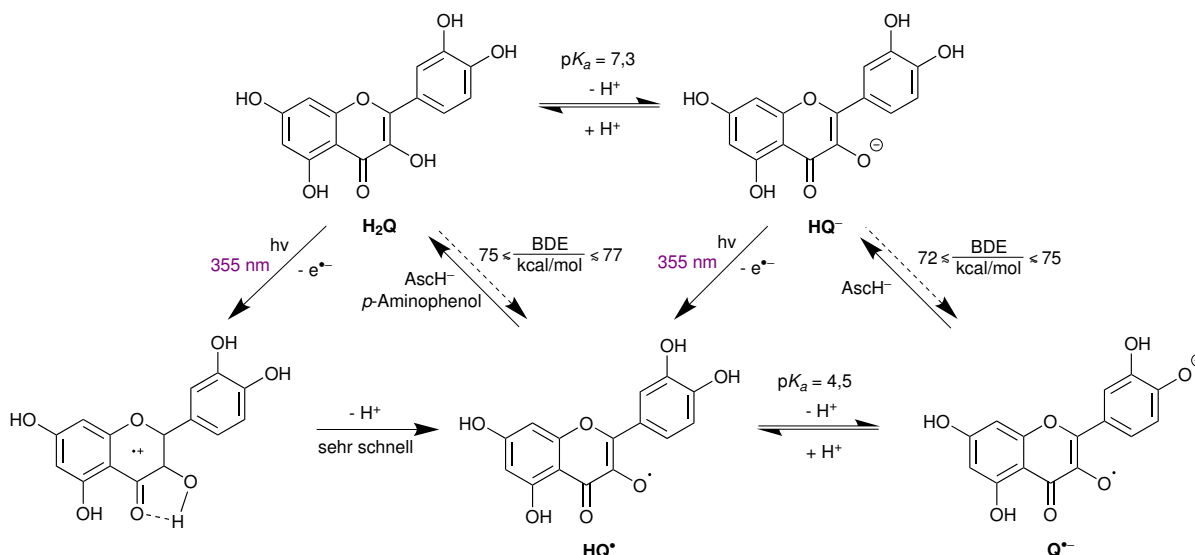


Abbildung 3.17: Regeneration der Quercetin-Radikale mit Ascorbat; (a) Abklingkurven der Quercetin-Radikale bei 515 nm mit entsprechenden monoexponentiellen Fit-Kurven bei verschiedenen Gesamtascorbat-Konzentrationen c_{Asc} ; Inset: Abhängigkeit der beobachteten Geschwindigkeitskonstante k_{obs} von c_{Asc} bei pH 4,25; (b) Einfluss des pH-Wertes in H_2O (magenta und rot) und D_2O (orange) auf die beobachtete Reparaturgeschwindigkeit k_{obs} der Quercetin-Radikale durch das Co-Antioxidans Ascorbat bei konstanter c_{Asc} , 5 mM (magenta und orange) und für eine höhere Genauigkeit im Neutralen 100 mM (rot), aber k_{obs} zurückgerechnet auf 5 mM.

In dem pH-Bereich zwischen 3 und 6 liegen sowohl die Quercetin-Radikale in beiden Protonierungsstufen HQ^{\bullet} und $Q^{\bullet-}$ vor, als auch das Co-Antioxidans als $AscH_2$ und $AscH^-$. Da $AscH_2$ ein deutlich schlechteres Antioxidans als $AscH^-$ und die Reaktion von letzterem mit $Q^{\bullet-}$ sehr langsam ist, ist eine Regeneration durch $AscH_2$ praktisch ausgeschlossen. Demnach ist alleinig das Paar $HQ^{\bullet}/AscH^-$ für die Regeneration in diesem pH-Bereich ursächlich. Da mit steigendem pH-Wert die Konzentration an HQ^{\bullet} durch Deprotonierung abnimmt und gegenläufig die Konzentration an $AscH^-$ zunimmt, ist eine solche Glockenform



Schema 3.1: Quercetin-Spezies und Reaktionswege sowie pK_a-Werte und BDE in wässriger Lösung, untersucht durch Photoionisierung mit 355 nm Laserlicht, in Abwesenheit und Gegenwart von Co-Antioxidantien.

zu beobachten. Eine kinetische Analyse unter Berücksichtigung aller Protonierungsgleichgewichte liefert für das Paar HQ^{•+}/AscH⁻ $k = 1,6 \cdot 10^8 \text{ M}^{-1} \text{ s}^{-1}$. Durch Wiederholung der Messungen in D₂O konnte für die Reaktion HQ^{•+} mit AscH⁻ ein kinetischer Isotopeneffekt (KIE) von 1,9 ermittelt und damit auf einen Proton-gekoppelten Elektronen-Transfer (PCET) als Reaktionsmechanismus geschlossen werden.

Für die Bindungsdissoziationsenergie (BDE) der Quercetin-Spezies liefern theoretische Rechnungen zwischen 71,3 kcal mol⁻¹ und 83,1 kcal mol⁻¹ für H₂Q^[186,187] und zwischen 70,9 kcal mol⁻¹ und 75,0 kcal mol⁻¹ für HQ⁻^[186,187]. Genaue experimentelle Werte sind in der Literatur nicht verfügbar, aber die Ergebnisse aus der Reaktion oder Nicht-Reaktion der Radikale mit Ascorbat lassen eine recht präzise Abschätzung zu. Denn ein PCET ist thermodynamisch nur dann möglich, wenn die BDE des Co-Antioxidans kleiner ist als die BDE des regenerierten Quercetins (H₂Q bzw. HQ⁻). Durch die beobachtete Regeneration mit AscH⁻ (BDE, 71,8 kcal mol⁻¹^[188]) und die ausbleibende Reaktion mit AscH₂ (BDE, 78,0 kcal mol⁻¹^[188]) kann ein oberes und unteres Limit für die BDE gesetzt werden. Auch sind Reaktionen mit Glutathione (BDE, 87,2 kcal mol⁻¹^[188]), Hydroquinone (BDE, 79,7 kcal mol⁻¹^[188]) und Trolox (BDE, 76,7 kcal mol⁻¹^[188]) nicht zu beobachten. *p*-Aminophenol (BDE, 75,0 kcal mol⁻¹^[188]) wiederum kann HQ^{•+} reparieren aber nicht Q^{•-}.

In homogener wässriger Lösung im pH-Bereich von 2 bis 9 konnten damit die beiden beteiligten Spezies des Quercetins H₂Q und HQ⁻ und die abgeleiteten Radikale HQ^{•+} und Q^{•-} ausgemacht und die BDE von H₂Q und HQ⁻ recht genau eingegrenzt werden (Schema 3.1).

In der Literatur herrscht allerdings trotz zahlreicher Beiträge Uneinigkeit darüber, welches Radikal tatsächlich das stabilste ist^[187,189-193]. Grundlage dafür sind quantenchemische Berechnungen, aber die Radikale liegen energetisch zu dicht beieinander, um eine verlässli-

che Aussage treffen zu können. Allerdings ist die Kenntnis der Radikalposition wichtig für Erklärungen zur antioxidativen Funktion des Quercetins und seiner Derivate. Durch die fünf Hydroxylgruppen sind theoretisch fünf Sauerstoff-zentrierte Radikale und zehn Radikalanionen denkbar. Statt nur den Berechnungen zu vertrauen, wurden systematisch Experimente mit Quercetin-Derivaten durchgeführt, bei denen die Sauerstoffatome durch Alkylierung für eine Radikalbildung blockiert sind. Durch die sehr begrenzte Wasserlöslichkeit der untersuchten Substanzen wurde in mizellarer Lösung gearbeitet. Hierfür bietet sich Triton X-100 an. Die niedrige cmc des Triton X-100^[194] hält die Konzentration an unnützen freien Molekülen in der Lösung klein. Für eine Übertragung auf biologische Systeme sind seine gute Membrangängigkeit, die Target-Applikationen ermöglicht^[195], und die Tatsache, dass nicht-ionische Amphiphile physiologisch besser verträglich sind als ionische^[196], erwähnenswert. Die Konzentration an Triton wurde immer so gewählt, dass die zugrundeliegende Poisson-Statistik sicherstellt, dass sich nur ein Molekül pro Mizelle aufhält. Eine Photoionisierung mit 355 nm ist für alle Derivate analog zum Quercetin möglich.

Im Folgenden sollen zur besseren Übersichtlichkeit alle Quercetin-Derivate als Q in Kombination mit einer Kennzeichnung des alkylierten Sauerstoffatoms bezeichnet werden. Die blockierte Position wird durch einen Strich über der entsprechenden Position gekennzeichnet, z.B. Rhamnetin = 7-Methoxyquercetin, Q $\bar{7}$. Handelt es sich nicht um ein methyliertes Derivat, sondern um ein glykosyliertes so ist ein kleines „g“ angefügt, z.B. Rutin = Quercetin-3-O-rutinosid, Q $\bar{3}_g$.

Abbildung 3.18 zeigt die transienten Absorptionsspektren nach der Laserblitzlichtphotolyse von Quercetin (nach $\approx 20 \mu\text{s}$), fünf seiner Monoether und drei seiner Diether im Sauren (pH 3) und im fast Neutralen (pH 6,5).

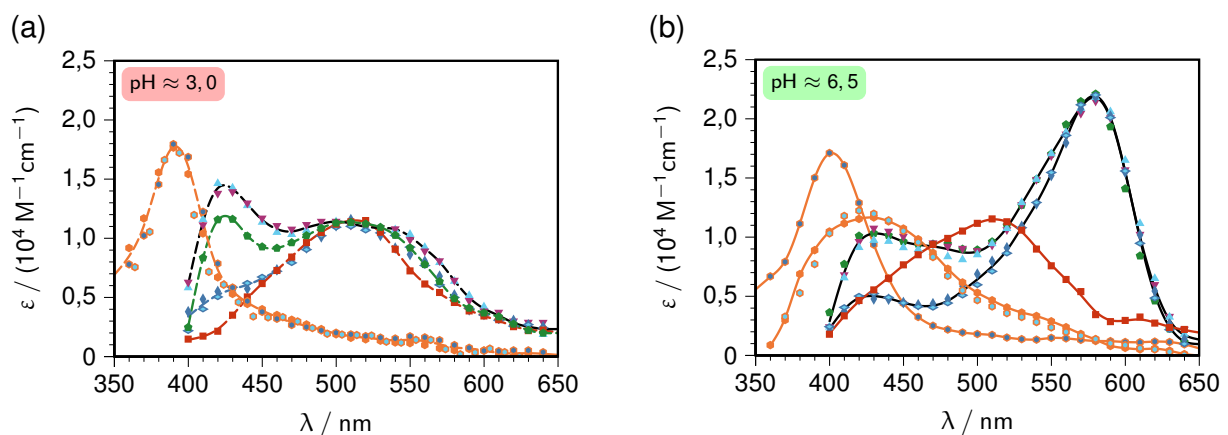


Abbildung 3.18: Kalibrierte Absorptionsspektren der Radikale des Quercetins und seiner Derivate: Quercetin Q, grün; 3-Methylquercetin Q $\bar{3}$, orange; Azaleatin Q $\bar{5}$, violett; Rhamnetin Q $\bar{7}$, hellblau; Isorhamnetin Q $\bar{3}$, dunkelblau; Tamarixetin Q $\bar{4}$, rot; Rhamnazin Q $\bar{3}\bar{7}$, hellblau-dunkelblau; Narcissin, Q $\bar{3}_g\bar{3}$, orange-dunkelblau; Rhamnetin-3-galactoside, Q $\bar{3}_g\bar{7}$, orange-hellblau (10 μM Substanz ionisiert mit 355 nm in 50 mM Triton X-100); (a) Neutralradikale im sauren Medium (pH 3); (b) Radikalanionen im fast Neutralen (pH 6,5).

Im Sauren (pH 3) entstehen die entsprechenden Neutralradikale (NR_x). Da diese nur an den Positionen *x* lokalisiert sein können, an denen keine Alkylierung vorliegt, können die Radikale durch systematische Auswertung der aufgenommenen Spektren der Quercetin-Derivate mit den verschiedenen Substitutionsmustern zugeordnet werden. Beim Blick auf die Spektren sind klar Sätze von sehr ähnlichen Spektren je nach Substitutionsmuster des Derivates zu erkennen. Aus der Lage der Banden könnte zunächst die Beteiligung von drei Radikalspezies vermutet werden, allerdings reduziert sich diese auf zwei, wenn beachtet wird, dass bei einer Substitution an der 3-Position bereits im Grundzustand eine deutliche Blauverschiebung zu erkennen ist, während eine Substitution an den anderen Positionen die Absorptionseigenschaften nicht ändert. Das heißt auch, dass die verschiedenen Spektren ganz klar aus den verschiedenen gebildeten NR_x resultieren müssen.

Die identischen Spektren des Rhamnetin $\overline{Q7}$ und des Azaleatin $\overline{Q5}$ schließen also eine Beteiligung eines NR₅ und eines NR₇ zweifelsfrei aus. Die ebenfalls identischen Spektren des Isorhamnetin $\overline{Q3'}$ und des Rhamnazin $\overline{Q3'7}$ schließen das NR_{3'} aus und bestätigen auch noch einmal die Abwesenheit von NR₇. Ein Vergleich der Spektren des 3-*O*-Methylquercetin $\overline{Q3}$ (und die davon nicht unterscheidbaren Spektren seines glycosylierten Analogons Rutin $\overline{Q3_g}$ und der beiden disubstituierten Derivate Narcissin $\overline{Q3_g3'}$ und Rhamnetin-3-galactosid $\overline{Q3_g7}$) mit dem des Tamarixetin $\overline{Q4'}$ lässt damit nur einen Schluss zu: die scharfe Bande gehört zum NR₄ und die breite langwelligere zum NR₃.

Ebenso können die gebildeten Radikalanionen (RAN_{xy}) bei pH 6,5 zugeordnet werden. Azaleatin $\overline{Q5}$ und Rhamnetin $\overline{Q7}$ zeigen ein identisches Spektrum wie das Quercetin *Q* selbst, daher können weder Spin noch Ladung am Sauerstoffatom 5 oder 7 lokalisiert sein. Außerdem zeigen *Q*, $\overline{Q5}$ und $\overline{Q7}$ die gleiche dominante Bande um 580 nm, wie auch Isorhamnetin $\overline{Q3'}$ und Rhamnazin $\overline{Q3'7}$, demnach kann diese nichts mit der 3'-Position zu tun haben, sondern muss auf das Radikalanion RAN_{34'} zurückzuführen sein. Dies wird durch ein Fehlen dieser Bande bei Derivaten, wo eine dieser Positionen blockiert ist (3-*O*-Methylquercetin $\overline{Q3}$, Narcissin $\overline{Q3_g3'}$, Rhamnetin-3-galactosid $\overline{Q3_g7}$ und Tamarixetin $\overline{Q4'}$), untermauert.

Bei der Schulter bei 430 nm sind zwei Gruppen unterscheidbar. Die mit einer freien 3'-Position *Q*, $\overline{Q5}$ und $\overline{Q7}$ zeigen eine kleine zusätzliche Absorption im Gegensatz zu denen mit einer blockierten 3'-Position $\overline{Q3'}$ und $\overline{Q3'7}$. Diese stammt von dem in kleinem Maße gebildeten RAN_{3'4'}. Die Derivate, welche entweder die 3- oder die 4'-Position blockiert haben, zeigen ein gänzlich anderes Verhalten, denn hier sind RAN_{34'} und RAN_{3'4'} nicht möglich. Eine Beteiligung der 5-Position ist sehr unwahrscheinlich, da hier die starke Wasserstoffbrückenbindung zwischen OH und dem Carbonyl-Sauerstoff zerstört würde^[197], und kann auch experimentell nicht belegt werden. Beim Tamarixetin $\overline{Q4'}$ kann das RAN₃₇ und beim Narcissin $\overline{Q3_g3'}$ das RAN_{4'7} zugeordnet werden. Abschließend lässt die Auswertung der Spektren von $\overline{Q3}$ und $\overline{Q3_g7}$ nur den Schluss zu, dass hier RAN_{3'4'} für die Absorption verantwortlich ist.

Durch DFT-Rechnungen mit Gaussian 16^[198] (B3LYP, 6-311++g(2d,2p), PCM mit Methanol als Lösungsmittel) wurden die Geometrien für alle denkbaren NR_x für die verschiedenen Derivate optimiert und die Energien, sowie die Absorptionsspektren mit TDDFT berechnet (Abb. 3.19).

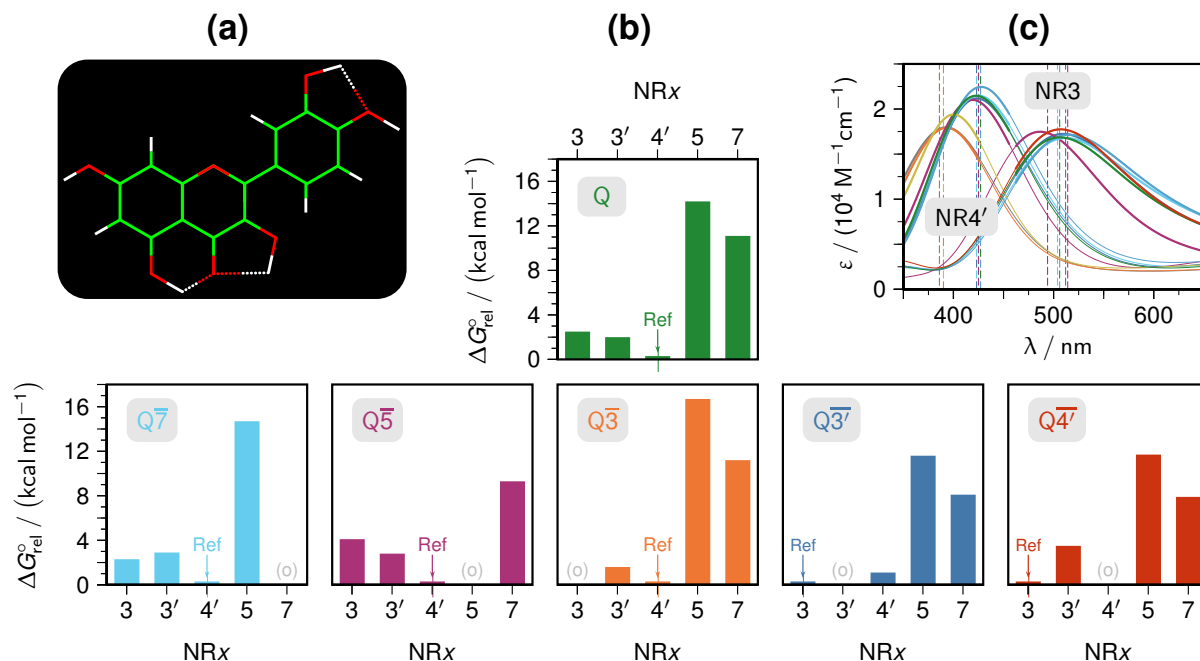


Abbildung 3.19: Ergebnisse der DFT-Rechnungen für die Neutralradikale; (a) optimierte Struktur des Quercetins mit eingezeichneten Wasserstoffbrückenbindungen; (b) berechnete freie Enthalpien ΔG° der NR_x des Quercetins und der monosubstituierten Derivate relativ zur niedrigsten erhaltenen Enthalpie, die als Referenz auf Null gesetzt ist; Radikale, die durch die Alkylierung nicht möglich sind, sind mit „(o)“ gekennzeichnet; (c) Vergleich der experimentellen Bandenmaxima (gestrichelte vertikale Linien, siehe Abb. 3.18 (a)) mit den mittels TDDFT berechneten Spektren (durchgezogene Kurven) für NR3 und NR4'.

Die Berechnungen sind in weiten Teilen konsistent mit den experimentellen Ergebnissen, aber nicht gänzlich. Die berechneten Energien schließen ganz klar eine Beteiligung der NR5 und NR7 aus. Allerdings liegen NR3, NR3' und NR4' dicht beisammen und das NR3 wird mehrmals als instabiler im Vergleich zu den anderen angegeben, obwohl NR3 experimentell klar zu beobachten ist. Dieses berechnete Verhalten ist besonders überraschend, da in der Literatur^[187] eine Berechnung des Quercetins mit einer älteren Gaussian Version (Gaussian 03) und einem kleineren Basissatz (6-311+g(d,p)) mit NR3 < NR4' < NR3' eine realistischere Energieabfolge liefert. Dieses Ergebnis ist näherungsweise im Kompatibilitätsmodus reproduzierbar. Der Grund für das beobachtete Verhalten liegt darin, dass das Lösungsmittel-Modell ab der Version 09 deutlich verbessert wurde. Die berechneten Absorptionsspektren für NR3 und NR4 stimmen gut mit den beobachteten überein.

Abbildung 3.20 zeigt die Ergebnisse der DFT-Rechnungen für die RAN_xy. Hier sind allerdings drei Aspekte zu berücksichtigen, die die Zuverlässigkeit der Berechnungen einschränken: 1) da die Spezies geladen sind, spielen Lösungsmittelleffekte eine viel größere Rolle als bei Neutralradikalen; 2) die größere Anzahl an möglichen Radikalanionen führt zu mehr

Absorptionsbanden in dem gemessenen Bereich und 3) mehr Übergänge beinhalten nicht das SOMO und zeigen daher in größerem Maße Spinkontamination^[199]. Die berechneten Energien schließen jedoch offenkundig in Übereinstimmung mit den Experimenten eine Beteiligung der Position 5 aus. Außerdem wird deutlich, dass RAN34' das günstigste Radikalanion ist, wenn es strukturell möglich ist (Q, Q $\bar{5}$, Q $\bar{7}$ und Q $\bar{3'7}$). Des Weiteren werden die Radikalanionen RAN37 für Q $\bar{4'}$ und RAN3'4' für Q $\bar{3}/\bar{Q3g}$ in Übereinstimmung mit den Experimenten als stabilste berechnet. Beim Isorhamnetin Q $\bar{3'}$ wird allerdings das RAN37 marginal günstiger bewertet als das experimentell beobachtete RAN34'.

Die Aussagekraft der berechneten RAN-Spektren ist deutlich geringer als der Neutralradikale. Beim Quercetin zeigt sich, dass die Bandenmaxima aller sechs berechneten RANxy nur jeweils um ca. 20 nm voneinander verschieden sind. Dazu kommt, dass das Spektrum von RAN34' bereits um das Doppelte dieser Differenz verschoben werden muss, um zu den experimentellen Daten zu passen und weitere Verschiebungen ± 15 nm sind nötig, um berechnete aber nicht beobachtete Unterschiede der Spektren von Q, Q $\bar{5}$, Q $\bar{7}$, Q $\bar{3'7}$ und Q $\bar{3'}$ auszugleichen. Auch bei den RAN47 für Q $\bar{3'3'}$ und RAN37 für das Tamarixetin Q $\bar{4'}$ sind die berechneten Spektren mehr qualitativer Natur. Durch die besonders starke Spinkontamination beim Radikal RAN3'4' und die damit verbundene offensichtliche Unzuverlässigkeit der Berechnung wurde das Spektrum nicht mit in die Abbildung 3.20 (b) aufgenommen.

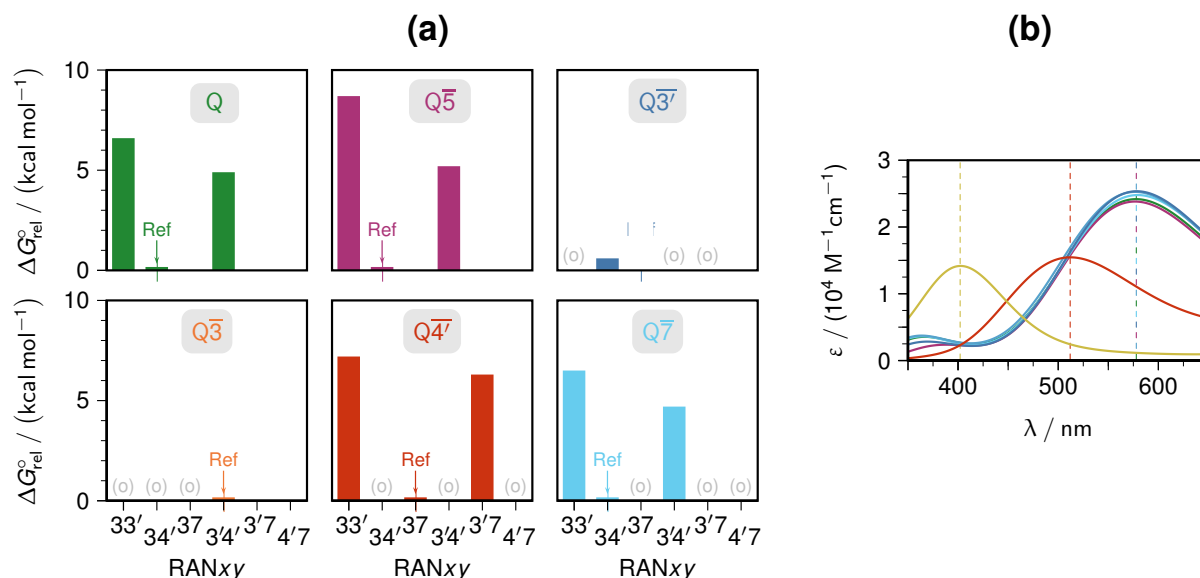


Abbildung 3.20: Ergebnisse der DFT-Rechnungen für die Radikalanionen; (a) berechnete freie Enthalpien der RANxy des Quercetins und der monosubstituierten Derivate relativ zur niedrigsten erhaltenen Enthalpie, die als Referenz auf Null gesetzt ist; Radikalanionen, die durch die Alkylierung nicht möglich sind, sind mit „(o)“ gekennzeichnet; Radikalanionen, die durch die Experimente ausgeschlossen werden können, sind verblasst dargestellt; (b) Vergleich der experimentellen Bandenmaxima (gestrichelte vertikale Linien, siehe Abb. 3.18 (b)) mit den mittels TDDFT berechneten Spektren (durchgezogene Kurven) für RAN4'7, RAN3'7 und RAN34', mittlere Verschiebung des Peak Maximums zur besseren Vergleichbarkeit 0,17 eV.

Zusätzlich zur Analyse der Spektren der Neutralradikale und Radikalanionen wurde auch deren Umwandlung ineinander genauer untersucht. Exemplarisch für die Umwandlung

von NR3 nach RAN34' ist in Abbildung 3.21 die Deprotonierung des NR3 des Quercetins gezeigt (ein ganz ähnliches Verhalten kann für Azaleatin Q5, Rhamnetin Q7, Isorhamnetin Q3' und Rhamnazin 3'7' beobachtet werden). Eine Auswertung der Endabsorptionswerte ergibt in Triton X-100 Mizellen einen pK_a von 4,95. Unter Einbeziehung der oben erwähnten Derivate ergibt sich für das NR3 ein einheitlicher pK_a von $4,78 \pm 0,15$. Eine Auswertung der Kinetik liefert für die Deprotonierung von NR3 $k_{\text{dep}} 3,3 \cdot 10^5 \text{ s}^{-1}$ und andersherum für die diffusionskontrollierte Protonierung von RAN34' $k_p = 2,9 \cdot 10^{10} \text{ M}^{-1} \text{ s}^{-1}$. Unter Einbeziehung der anderen Derivate erhält man $k_p = (3,0 \pm 0,6) \cdot 10^{10} \text{ M}^{-1} \text{ s}^{-1}$.

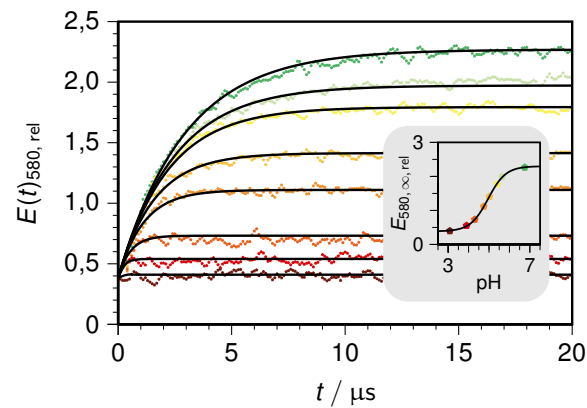


Abbildung 3.21: Deprotonierung des NR3 des Quercetins ($10 \mu\text{M}$) in Triton X-100 mizellarer Lösung (50 mM), Absorption bei 580 nm , der beste Fit liefert $k_{\text{dep}} 3,3 \cdot 10^5 \text{ s}^{-1}$; Inset: Endabsorptionswerte in Abhängigkeit des pH-Wertes liefern $pK_a = 4,95$.

4 Zusammenfassung

Mizellaren Systemen kommt in der Photophysik und der Photochemie eine besondere Bedeutung zu. Zum einen lassen sie sich insbesondere durch fluoreszenzspektroskopische Methoden gut untersuchen, denn sie beeinflussen eine Reihe von photophysikalischen Eigenschaften. Zum anderen verschaffen sie auch einen Zugang zur Untersuchung und Nutzung von Spezies, die in die Mizelle aufgenommen sind. Mizellen bieten ein breites Anwendungsspektrum, welches in den letzten Jahren offenkundig immer mehr erweitert wird. Sie eignen sich z.B. um in ihnen Reaktionen durchzuführen, die sonst nicht möglich sind, oder zur Untersuchung von Antioxidantien in einfachen Modellen für biologische Membranen.

Auch wenn die Löschung der Fluoreszenz in Mizellen schon vielfach untersucht wurde, so fehlte es bisher an konsistenten und ausführlich überprüften Theorien zur Beschreibung der kombinierten statischen und dynamischen Löschung in Mizellen. Die Untersuchung dieses Aspektes bildet den ersten Schwerpunkt (I.) der vorliegenden Arbeit.

Der II. Schwerpunkt befasst sich mit der Anwendung von Mizellen für photochemische Fragestellungen. Der Mizellbildner SDS eignet sich sehr gut als Kapsel für ein photokatalytisches System zur Erzeugung hydratisierter Elektronen. Dieses wurde genutzt, um damit gezielt Wurtz-Kupplungen durchzuführen. Die Photoionisierung ist zudem außerordentlich nützlich, um das Super-Antioxidans Quercetin und seine Radikalspezies genauer zu untersuchen.

I. Kombinierte Fluoreszenzlöschung in Mizellen

Es wurde sehr stringent eine Theorie zur kombinierten intramizellaren Löschung aus formal-kinetischen Überlegungen zur Komplexierung von Fluorophor und Löscher und deren Ein- und Austritt in die Mizellen abgeleitet. Die Entwicklung einer Auswerterroutine zur Separation der wichtigen Parameter ermöglicht eine eindeutige und schnelle Bestimmung dieser. Auf Grundlage dessen lieferten temperaturabhängige Messungen zur Löschung von Pyren mit verschiedenen Viologen in SDS-Mizellen die thermodynamischen Parameter der Grundzustandskomplexe aus dem statischen Anteil der Löschung sowie die Aktivierungsenergie der Mikroviskosität von SDS aus dem dynamischen Anteil und die Temperaturabhängigkeit der Aggregationszahl der Mizellen. Die erhaltenen Aggregationszahlen und ihre Unsicherheiten stimmen mit den akzeptierten Werten aus Kleinwinkelstreuungs-Experimenten überein. Die zunächst gewonnene Komplexbildungskonstante und die Geschwindigkeitskonstante für die dynamische Löschung sind zunächst nicht mit den typischen Größen in homogener Lösung vergleichbar, denn sie beziehen sich auf die Anzahl der Löscher in der Mizelle und nicht auf

ein Volumen und damit eine Konzentration. Um sie in den typischen Einheiten zu erhalten, ist eine Multiplikation der Parameter mit dem Mizellvolumen V_m nötig. Abgeleitete Größen wie die Standard-Entropie und Enthalpie der Komplexbildung und die Aktivierungsenergie der dynamischen Löschung, hängen von der Umwandlung ab. Bei Kenntnis des Mizellvolumens sind jedoch die korrekten Werte zugänglich. Aus den erhaltenen Komplexbildungskonstanten konnte klar abgeleitet werden, dass die Assoziation entropiekontrolliert ist. Es gibt einen Zusammenhang zwischen der Länge der Viologen-Seitenkette bzw. der Anzahl der Rotoren in ihr und der Komplexbildungskonstante. Zurückzuführen ist diese auf eine Einschränkung der möglichen Konformere der Seitenkette durch die π - π -Stacking-Anordnung des Komplexes. Die vorgestellte Methode zur Untersuchung von Mizellen eignet sich für jedes standardmäßig ausgestattete photochemische Labor. Insbesondere die Bestimmung der Aggregationszahl ist hier ohne die Anwendung von Streumethoden wie SAXS oder SANS einfach möglich. Eine Erweiterung auf verschiedene n -Alkylsulfate (S_nS) bei verschiedenen Temperaturen ermöglichte die genaue Untersuchung des Einflusses des Mizellvolumens. Es stellte sich heraus, dass bereits das einfachste Modell, bei dem die Konzentration der intramizellaren Reaktionspartner mit dem Mizellvolumen errechnet wird, sehr gut ist. Bei den konzentrationsbasierten Größen der dynamischen Löschkonstante und der Komplexbildungskonstante hat das Mizellvolumen nämlich keinerlei Einfluss und damit auch nicht auf die abgeleiteten thermodynamischen Größen wie Aktivierungsenergie oder Enthalpie und Entropie der Komplexbildung. Vielmehr ist es sogar so, dass die Größen mit denen in homogener Methanol-Lösung vergleichbar sind. Durch die Verwendung von Mizellen kann aber die effektive Konzentration der Reaktionspartner im Vergleich zu homogener Lösung stark gesteigert werden: eine mittlere Belegung der Mizellen von Eins, in den durchgeführten Experimenten mit ca. 1 mM Löscherkonzentration bezogen auf die gesamte Lösung erreicht, entspricht einer lokalen Konzentration in der Mizelle von V_m^{-1} , was einen Konzentrationschub um einen Faktor zwischen 30 (S14S) und 130 (S9S) bedeutet. Diese Erkenntnis ist ausgesprochen interessant für die Planung und Verbesserung von Synthesen. Durch die intramizellare Reaktionsführung könnten sie beispielsweise beschleunigt werden.

II. Photoionisierungen in Mizellen

(a) Bei der Photoionisierung von 2-Aminoanthracen konnte gezeigt werden, dass eine Aufnahme in eine Mizelle viele Vorteile mit sich bringt. Das gesamte photokatalytische System ist in der Mizelle lokalisiert. Das 2-Aminoanthracen liefert in der SDS-Mizelle eine hohe Elektronenausbeute und kann damit Elektronenkonzentrationen pro Laserpuls liefern, die etwa der Hälfte der eingesetzten Menge an 2-Aminoanthracen entsprechen. Durch die Verwendung des komplett mizellgebundenen Palmitoylascorbat zur Regeneration des 2-Aminoanthracens ist intramizellar eine sehr schnelle und vor allem vollständige Regeneration auch bei kleinen Konzentrationen des Opferdonors möglich. Dies spiegelt sich ebenfalls in der hohen

möglichen Produktivität des Katalysators wieder. Alle diese Aspekte führen dazu, dass eine große lokale Radikalkonzentration auftritt, wenn das hydratisierte Elektron mit dem Substrat reagiert. Da das System aber gleichzeitig auch eine geringe Tendenz zur Funktion als Wasserstoff-Donor aufweist, weil das Palmitolyascorbat in der Mizelle verankert ist, sind Radikaldimerisierungen bevorzugt. Häufig ist sogar eine nahezu quantitative Umsetzung möglich. Es wurde ein praktikables System für laserinduzierte Dimerisierungen mit hydratisierten Elektronen entworfen, welches anhand einer Reihe von Verbindungen getestet wurde.

(b) Die Photoionisierung mit einem 355 nm-Laser bietet einen eleganten Zugang zu den Radikalen des Quercetins. Innerhalb weniger Nanosekunden konnte mit der Laserblitzlicht-Photolyse-Apparatur eine gut zu untersuchende Konzentration an Quercetin-Radikalen erzeugt werden. Auch wenn das Quercetin in reinem Wasser schwer löslich ist, konnten grundlegende Erkenntnisse zunächst in homogener Lösung gewonnen werden. Dies geschah über einen breiten pH-Bereich (2 – 9), der auch mit dem Bereich von pH-Werten, die im menschlichen Körper vorkommen, deckungsgleich und damit für eine Verknüpfung zur Biologie oder Medizin besonders interessant ist. Hier liegt das Quercetin im Grundzustand entweder neutral oder als Anion vor ($pK_a = 7,3$). Das nach der Photoionisierung entstehende Radikalkation deprotoniert praktisch sofort zum Quercetin-Radikal. Dieses wiederum kann je nach pH-Wert der Lösung auch weiter zum Radikalanion deprotoniert werden ($pK_a = 4,5$). Es gelang von beiden Spezies ein kalibriertes Spektrum aufzunehmen. Diese Grundlagen ermöglichten die Untersuchung der Reparatur mit dem typischen Co-Antioxidans Ascorbat und anderen Substanzen wie 4-Aminophenol. Durch Auswertung der kinetischen Messung und Vergleich der Reparatur mit den verschiedenen Substanzen war es möglich, die Bindungsdissoziationsenergie des Quercetins, welche für die antioxidative Wirkung maßgeblich ist, genauer einzugrenzen, als es bisher durch quantenchemische Rechnungen realisierbar war. Die Regeneration des Quercetins ist mit Ascorbat vollständig möglich und läuft über einen Protonen-gekoppelten Elektronentransfer ab. Allerdings ist sie bei typischen physiologischen pH-Werten (≈ 7) und typischen Ascorbat-Konzentrationen nicht vollständig möglich, da das Quercetin-Radikalanion im Vergleich zum neutralen Quercetin eine mehr als 50-fach niedrigere Reaktivität gegenüber dem Ascorbat-Monoanion besitzt.

Da es in der Literatur immer wieder Unklarheiten darüber gibt, an welcher Position das Radikal beim Quercetin tatsächlich lokalisiert ist, wurde eine systematische Untersuchung von an verschiedenen Positionen *O*-alkylierten Quercetin-Derivaten durchgeführt. Dadurch sind bestimmte Radikale, nämlich jene an denen der Sauerstoff verethert ist, nicht möglich. Dieses Vorgehen stellte sich als sehr wertvoll bei der spektralen Zuordnung der Neutralradikale und Radikalanionen heraus. Durch die Verwendung von Triton X-100-Mizellen konnte auch mit den noch schlechter löslichen Methylethern des Quercetins eine praktikable Konzentration erzielt und die Kinetiken gut untersucht werden. Es stellte sich heraus, dass das neutrale O3-Radikal im Chromanring das bevorzugte Quercetin-Radikal ist. Die pK_a -Werte aller

Derivate mit O3-zentriertem Radikal liegen um 4,8. Die Deprotonierung erfolgt dabei am O4'. Die zusätzlich durchgeführten DFT-Rechnungen sind nicht vollständig konsistent mit den experimentellen Ergebnissen. Sie geben das O4'-Radikal als etwas energetisch günstiger im Vergleich zum O3-Radikal an. Vermutlich ist dies auf eine ungenaue Berechnung des Beitrags der intramolekularen Wasserstoffbrückenbindungen zurückzuführen, die eine ausgesprochen wichtige Rolle im Quercetin spielen. Dies zeigt, dass trotz des Fortschritts bei den Berechnungsmethoden und der Rechenleistung experimentelle Untersuchungen noch lange nicht überflüssig sind. Die vorgestellten Methoden zur Untersuchung des Quercetins sollten auch auf andere polyphenolische Antioxidantien übertragbar sein.

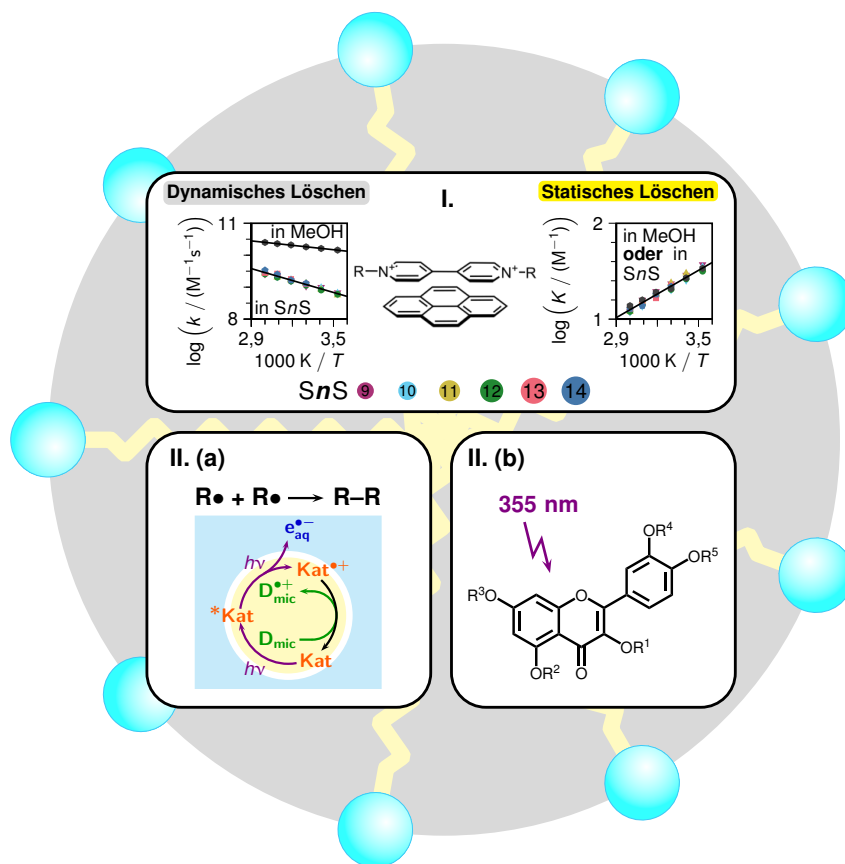


Abbildung 4.1: Übersicht der Hauptaspekte der vorliegenden Dissertation: I. durch Entwicklung einer Theorie zur Beschreibung von kombinierten Fluoreszenzlöschprozessen in Mizellen konnte der Löschprozess von Pyren mit Viologen in *n*-Alkylsulfat-Mizellen genau untersucht werden, wird das tatsächliche Volumen der Mizellen berücksichtigt, sind die typischen Löschparameter k und K unabhängig vom Mizellbildner und sogar mit denen in homogener Lösung vergleichbar; II. (a) Verwendung von SDS-Mizellen als Container für ein photokatalytisches System zur Produktion von hydratisierten Elektronen, welche zur Erzeugung von Radikalen für Wurtz-Kupplungen genutzt werden, basierend auf 2-Aminoanthracen als Katalysator und dem lipophilen Palmitoylascorbat als Regenerationsmittel; (b) Untersuchung des Antioxidans Quercetin und seinen Derivaten in Triton X-100-Mizellen und homogener Lösung durch Erzeugung der dazugehörigen Radikale mittels Laserblitzlichtphotolyse bei 355 nm zeigt unter anderem, dass das Quercetin-Neutralradikal an der 3-Position das stabilste ist, bei höheren pH-Werten wird es zum 34'-Radikalanion deprotoniert.

5 Literaturverzeichnis

- [1] J. W. McBain, *Trans. Faraday Soc.* **1913**, *9*, 99–101.
- [2] G. S. Hartley, *Aqueous Solutions of Paraffin-chain Salts - A Study in Micelle Formation*, Hermann cie, Paris, **1962**.
- [3] T. Dwars, E. Paetzold, G. Oehme, *Angew. Chem. Int. Ed.* **2005**, *44*, 7174–7199.
- [4] G. La Sorella, G. Strukul, A. Scarso, *Green Chem.* **2015**, *17*, 644–683.
- [5] S. Shukla, P. Govender, A. Tiwari in *Advances in Biomembranes and Lipid Self-Assembly, Vol. 24*, Elsevier, **2016**, pp. 143–161.
- [6] S. Kim, Y. Shi, J. Y. Kim, K. Park, J.-X. Cheng, *Expert Opin. Drug Deliv.* **2010**, *7*, 49–62.
- [7] Y. Lu, E. Zhang, J. Yang, Z. Cao, *Nano Res.* **2018**, *11*, 4985–4998.
- [8] S. M. Tawfik, S. Azizov, M. R. Elmasry, M. Sharipov, Y.-I. Lee, *Nanomaterials* **2021**, *11*, 70.
- [9] J. Lipfert, L. Columbus, V. B. Chu, S. A. Lesley, S. Doniach, *J. Phys. Chem. B* **2007**, *111*, 12427–12438.
- [10] R. C. Oliver, J. Lipfert, D. A. Fox, R. H. Lo, S. Doniach, L. Columbus, *PloS one* **2013**, *8*, e62488.
- [11] S.-H. Chen, *Annu. Rev. Phys. Chem.* **1986**, *37*, 351–399.
- [12] B. Hammouda, *J. Res. Natl. Inst. Stand. Technol.* **2013**, *118*, 151–167.
- [13] E. Anacker, H. Ghose, *J. Phys. Chem.* **1963**, *67*, 1713–1716.
- [14] J. Mishic, M. Fisch, *J. Chem. Phys.* **1990**, *92*, 3222–3229.
- [15] G. Guerin, F. Qi, G. Cambridge, I. Manners, M. A. Winnik, *J. Phys. Chem. B* **2012**, *116*, 4328–4337.
- [16] A. Malliaris, *Int. Rev. Phys. Chem.* **1988**, *7*, 95–121.
- [17] M. H. Gehlen, F. C. De Schryver, *Chem. Rev.* **1993**, *93*, 199–221.
- [18] L. Piñeiro, M. Novo, W. Al-Soufi, *Adv. Colloid Interface Sci.* **2015**, *215*, 1–12.
- [19] D. Wang, J. Wang, D. Moses, G. C. Bazan, A. J. Heeger, *Langmuir* **2001**, *17*, 1262–1266.

- [20] C.-Q. Jiang, M.-X. Gao, J.-X. He, *Anal. Chim. Acta* **2002**, *452*, 185–189.
- [21] Y.-J. Hu, Y. Liu, L.-X. Zhang, R.-M. Zhao, S.-S. Qu, *J. Mol. Struct.* **2005**, *750*, 174–178.
- [22] S. Doose, H. Neuweiler, M. Sauer, *Chem. Phys. Chem.* **2009**, *10*, 1389–1398.
- [23] K. Campbell, A. Zappas, U. Bunz, Y. S. Thio, D. G. Bucknall, *J. Photochem. Photobiol. A* **2012**, *249*, 41–46.
- [24] P.-P. Infelta, M. Gratzel, J. Thomas, *J. Phys. Chem.* **1974**, *78*, 190–195.
- [25] M. Tachiya, *Chem. Phys. Lett.* **1975**, *33*, 289–292.
- [26] P. P. Infelta, M. Grätzel, *J. Chem. Phys.* **1979**, *70*, 179–186.
- [27] M. Eftink, C. Ghiron, *J. Phys. Chem.* **1976**, *80*, 486–493.
- [28] M. Van der Auweraer, J. Dederen, E. Gelade, F. De Schryver, *J. Chem. Phys.* **1981**, *74*, 1140–1147.
- [29] M. H. Gehlen, F. C. De Schryver, *J. Phys. Chem.* **1993**, *97*, 11242–11248.
- [30] G. V. Buxton, C. L. Greenstock, W. P. Helman, A. B. Ross, *J. Phys. Chem. Ref. Data* **1988**, *17*, 513–886.
- [31] M. Goez, C. Kerzig, R. Naumann, *Angew. Chem.* **2014**, *126*, 10072–10074.
- [32] C. Kerzig, M. Goez, *Phys. Chem. Chem. Phys.* **2015**, *17*, 13829–13836.
- [33] C. Kerzig, M. Goez, *Chem. Sci.* **2016**, *7*, 3862–3868.
- [34] T. Kohlmann, R. Naumann, C. Kerzig, M. Goez, *Photochem. Photobiol. Sci.* **2017**, *16*, 1613–1622.
- [35] R. Naumann, F. Lehmann, M. Goez, *Angew. Chem., Int. Ed.* **2018**, *57*, 1078–1081.
- [36] C. Kerzig, X. Guo, O. S. Wenger, *J. Am. Chem. Soc.* **2019**, *141*, 2122–2127.
- [37] R. Naumann, M. Goez, *Chem. Eur. J.* **2018**, *24*, 9833–9840.
- [38] R. Naumann, M. Goez, *Green Chem.* **2019**, *21*, 4470–4474.
- [39] C. Kerzig, S. Henkel, M. Goez, *Phys. Chem. Chem. Phys.* **2015**, *17*, 13915–13920.
- [40] R. H. Bisby, A. W. Parker, *FEBS Letters* **1991**, *290*, 205–208.
- [41] M. Brautzsch, C. Kerzig, M. Goez, *Green Chem.* **2016**, *18*, 4761–4771.

- [42] C. A. Rice-evans, N. J. Miller, P. G. Bolwell, P. M. Bramley, J. B. Pridham, *Free Radic. Res.* **1995**, *22*, 375–383.
- [43] B. Sultana, F. Anwar, *Food Chem.* **2008**, *108*, 879–884.
- [44] A. T. Jan, M. R. Kamli, I. Murtaza, J. B. Singh, A. Ali, Q. Haq, *Food Rev. Int.* **2010**, *26*, 302–317.
- [45] T. T. Cushnie, A. J. Lamb, *Int. J. Antimicrob. Agents* **2005**, *26*, 343–356.
- [46] S. C. Bischoff, *Curr. Opin. Clin. Nutr. Metab. Care* **2008**, *11*, 733–740.
- [47] W. Wu, R. Li, X. Li, J. He, S. Jiang, S. Liu, J. Yang, *Viruses* **2016**, *8*, 6.
- [48] P. K. Agrawal, C. Agrawal, G. Blunden, *Nat. Prod. Commun.* **2020**, *15*, 1–10.
- [49] Y. J. Moon, X. Wang, M. E. Morris, *Toxicol. in Vitro* **2006**, *20*, 187–210.
- [50] N. Chondrogianni, S. Kapeta, I. Chinou, K. Vassilatou, I. Papassideri, E. S. Gonos, *Exp. Gerontol.* **2010**, *45*, 763–771.
- [51] W. Bors, C. Michel, S. Schikora, *Free Radic. Biol. Med.* **1995**, *19*, 45–52.
- [52] S. V. Jovanovic, S. Steenken, Y. Hara, M. G. Simic, *J. Chem. Soc., Perkin Trans. 2* **1996**, 2497–2504.
- [53] Y. Zheng, I. S. Haworth, Z. Zuo, M. S. Chow, A. H. Chow, *J. Pharm. Sci.* **2005**, *94*, 1079–1089.
- [54] P. G. Cadena, M. A. Pereira, R. B. Cordeiro, I. M. Cavalcanti, B. B. Neto, C. Maria do Carmo, J. L. Lima Filho, V. L. Silva, N. S. Santos-Magalhães, *Biochim. Biophys. Acta Biomembr.* **2013**, *1828*, 309–316.
- [55] H. Pool, S. Mendoza, H. Xiao, D. J. McClements, *Food Funct.* **2013**, *4*, 162–174.
- [56] L. Dian, E. Yu, X. Chen, X. Wen, Z. Zhang, L. Qin, Q. Wang, G. Li, C. Wu, *Nanoscale Res. Lett.* **2014**, *9*, 1–11.
- [57] G. T. Rich, M. Buchweitz, M. S. Winterbone, P. A. Kroon, P. J. Wilde, *Nutrients* **2017**, *9*, 111.
- [58] N. T. Southall, K. A. Dill, A. Haymet, *J. Phys. Chem. B* **2002**, *106*, 521–533.
- [59] J. N. Israelachvili, D. J. Mitchell, B. W. Ninham, *J. Chem. Soc., Faraday Trans. 2* **1976**, *72*, 1525–1568.
- [60] C.-H. Chang, E. I. Franses, *Colloids Surf. A: Physicochem. Eng. Asp.* **1995**, *100*, 1–45.

- [61] R. Hadgiivanova, H. Diamant, *J Phys. Chem. B* **2007**, *111*, 8854–8859.
- [62] P. Mukerjee, K. J. Mysels, *Critical micelle concentrations of aqueous surfactant systems, Vol. 36*, Stand. Ref. Data Ser., Nat. Bur. Stand.(US), **1971**.
- [63] H. Tavernier, A. Barzykin, M. Tachiya, M. Fayer, *J. Phys. Chem. B* **1998**, *102*, 6078–6088.
- [64] S. Vass, *J. Phys. Chem. B* **2001**, *105*, 455–461.
- [65] K. Hayashi, H. Sugimura, T. Kamei, T. Shimanouchi, H. Nakamura, H. Umakoshi, *J. Phys. Chem. B* **2021**, *125*, 6192–6200.
- [66] M. S. Fernandez, P. Fromherz, *J. Phys. Chem.* **1977**, *81*, 1755–1761.
- [67] M. Montal, C. Gitler, *J. Bioenerg.* **1973**, *4*, 363–382.
- [68] A. Malliaris, J. Le Moigne, J. Sturm, R. Zana, *J. Phys. Chem.* **1985**, *89*, 2709–2713.
- [69] R. Zana, C. Weill, *J. Physique Lett.* **1985**, *46*, 953–960.
- [70] M. Almgren, S. Swarup, *J. Phys. Chem.* **1982**, *86*, 4212–4216.
- [71] M. Almgren, S. Swarup, *J. Colloid Interface Sci.* **1983**, *91*, 256–266.
- [72] M. Almgren, S. Swarup, *J. Phys. Chem.* **1983**, *87*, 876–881.
- [73] E. Caponetti, D. C. Martino, M. Floriano, R. Triolo, *J. Mol. Struct.* **1996**, *383*, 133–143.
- [74] S. Kaneshina, M. Tanaka, T. Tomida, R. Matuura, *J. Colloid Interface Sci.* **1974**, *48*, 450–460.
- [75] H. W. Offen, *Rev. Phys. Chem. Jpn.* **1980**, *50*, 97–118.
- [76] N. Baden, O. Kajimoto, K. Hara, *J. Phys. Chem. B* **2002**, *106*, 8621–8624.
- [77] J. Bloor, J. Morrison, C. Rhodes, *J. Pharm. Sci.* **1970**, *59*, 387–391.
- [78] D. Attwood, R. Natarajan, *J. Pharm. Pharmacol.* **1981**, *33*, 136–140.
- [79] V. Patel, N. Dharaiya, D. Ray, V. K. Aswal, P. Bahadur, *Colloids Surf. A: Physicochem. Eng. Asp.* **2014**, *455*, 67–75.
- [80] M. Emèrson, A. Holtzer, *J. Phys. Chem.* **1965**, *69*, 3718–3721.
- [81] R. Ranganathan, L. Tran, B. L. Bales, *J. Phys. Chem. B* **2000**, *104*, 2260–2264.
- [82] A. I. Rusanov, *Langmuir* **2014**, *30*, 14443–14451.

- [83] G. Porte, J. Appell, *J. Phys. Chem.* **1981**, *85*, 2511–2519.
- [84] S. Lebecque, J.-M. Crowet, M. N. Nasir, M. Deleu, L. Lins, *J. Mol. Graph. Model.* **2017**, *72*, 6–15.
- [85] P. R. Majhi, A. Blume, *Langmuir* **2001**, *17*, 3844–3851.
- [86] G. Olofsson, W. Loh, *J. Braz. Chem. Soc.* **2009**, *20*, 577–593.
- [87] D. Danino, *Curr. Opin. Colloid Interface Sci.* **2012**, *17*, 316–329.
- [88] D. M. Vriezema, M. Comellas Aragonès, J. A. Elemans, J. J. Cornelissen, A. E. Rowan, R. J. Nolte, *Chem. Rev.* **2005**, *105*, 1445–1490.
- [89] A. Hofmann, *Biochem. J.* **1963**, *89*, 57–68.
- [90] M. C. Carey, D. M. Small, *Arch. Intern. Med.* **1972**, *130*, 506–527.
- [91] P. Borel, B. Pasquier, M. Armand, V. Tyssandier, P. Grolier, M.-C. Alexandre-Gouabau, M. Andre, M. Senft, J. Peyrot, V. Jaussan, et al., *Am. J. Physiol. - Gastrointest. Liver Physiol.* **2001**, *280*, 95–103.
- [92] P. Scrimin, P. Tecilla, *Curr. Opin. Chem. Biol.* **1999**, *3*, 730–735.
- [93] D. V. Tulumello, C. M. Deber, *Biochemistry* **2009**, *48*, 12096–12103.
- [94] V. P. Torchilin, *Pharm. Res.* **2007**, *24*, 1–16.
- [95] L. A. Singer, *Solution Behavior of surfactants* **1982**, 73–112.
- [96] R. v. Wandruszka, *Crit. Rev. Anal. Chem.* **1992**, *23*, 187–215.
- [97] N. C. Maiti, M. Krishna, P. Britto, N. Periasamy, *J. Phys. Chem. B* **1997**, *101*, 11051–11060.
- [98] E. L. Quitevis, A. H. Marcus, M. D. Fayer, *J. Phys. Chem.* **1993**, *97*, 5762–5769.
- [99] M. Krishna, R. Das, N. Periasamy, R. Nityananda, *J. Chem. Phys.* **2000**, *112*, 8502–8514.
- [100] H. Shirota, Y. Tamoto, H. Segawa, *J. Phys. Chem. A* **2004**, *108*, 3244–3252.
- [101] O. Stern, M. Volmer, *Physik. Z.* **1919**, *20*, 183–188.
- [102] A. Yekta, M. Aikawa, N. J. Turro, *Chem. Phys. Lett.* **1979**, *63*, 543–548.
- [103] J. Dederen, M. Van der Auweraer, F. De Schryver, *J. Phys. Chem.* **1981**, *85*, 1198–1202.

- [104] R. Ranganathan, C. Vautier-Giongo, B. L. Bales, *J. Phys. Chem. B* **2003**, *107*, 10312–10318.
- [105] F. H. Quina, *Curr. Opin. Colloid Interface Sci.* **2013**, *18*, 35–39.
- [106] N. Boens, M. Van der Auweraer, *Chem. Phys. Chem.* **2005**, *6*, 2352–2358.
- [107] H.-J. Timpe, G. Israel, H. Becker, I. R. Gould, N. J. Turro, *Chem. Phys. Lett.* **1983**, *99*, 275–280.
- [108] C. Lunardi, J. Bonilha, A. Tedesco, *J. Lumin.* **2002**, *99*, 61–71.
- [109] C. Tablet, I. Matei, M. Hillebrand, *J. Mol. Liq.* **2011**, *160*, 57–62.
- [110] A. R. Soemo, J. E. Pemberton, *J. Fluoresc.* **2014**, *24*, 295–299.
- [111] M. S. Matheson, W. Mulac, J. Rabani, *J. Phys. Chem.* **1963**, *67*, 2613–2617.
- [112] L. Grossweiner, H. Joschek, *Advan. Chem. Series* **1965**, *50*, 279–288.
- [113] B. Abel, U. Buck, A. Sobolewski, W. Domcke, *Phys. Chem. Chem. Phys.* **2012**, *14*, 22–34.
- [114] J. M. Herbert, M. P. Coons, *Annu. Rev. Phys. Chem.* **2017**, *68*, 447–472.
- [115] C. A. Kraus, *J. Am. Chem. Soc.* **1908**, *30*, 1323–1344.
- [116] E. J. Hart, J. W. Boag, *J. Am. Chem. Soc.* **1962**, *84*, 4090–4095.
- [117] P. M. Hare, E. A. Price, D. M. Bartels, *J. Phys. Chem. A* **2008**, *112*, 6800–6802.
- [118] U. Schindewolf, *Angew. Chem. Int. Ed.* **1968**, *7*, 190–203.
- [119] E. J. Hart, S. Gordon, J. Thomas, *J. Phys. Chem.* **1964**, *68*, 1271–1274.
- [120] D. Marketos, A. Marketou-Mantaka, G. Stein, *J. Phys. Chem.* **1974**, *78*, 1987–1992.
- [121] L. Zhang, D. Zhu, G. M. Nathanson, R. J. Hamers, *Angew. Chem.* **2014**, *126*, 9904–9908.
- [122] D. Zhu, L. Zhang, R. E. Ruther, R. J. Hamers, *Nat. Mater.* **2013**, *12*, 836–841.
- [123] X. Liu, T. Zhang, L. Wang, Y. Shao, L. Fang, *Chem. Eng. J.* **2015**, *260*, 740–748.
- [124] X. Li, J. Ma, G. Liu, J. Fang, S. Yue, Y. Guan, L. Chen, X. Liu, *Environ. Sci. Technol.* **2012**, *46*, 7342–7349.
- [125] X. Liu, S. Yoon, B. Batchelor, A. Abdel-Wahab, *Sci. Total Environ.* **2013**, *454*, 578–583.

- [126] Y. Peng, S. He, J. Wang, W. Gong, *Radiat. Phys. Chem.* **2012**, *81*, 1629–1633.
- [127] H. Yu, E. Nie, J. Xu, S. Yan, W. J. Cooper, W. Song, *Water Res.* **2013**, *47*, 1909–1918.
- [128] Z. Zhang, X. Wang, Y. Xue, H. Li, W. Dong, *Chem. Eng. J.* **2015**, *263*, 186–193.
- [129] J. Ferris, F. Antonucci, *J. Am. Chem. Soc.* **1972**, *94*, 8091–8095.
- [130] R. Naumann, C. Kerzig, M. Goez, *Chem. Sci.* **2017**, *8*, 7510–7520.
- [131] R. Naumann, F. Lehmann, M. Goez, *Chem. Eur. J.* **2018**, *24*, 13259–13269.
- [132] J. Baxendale, E. Fielden, C. Capellos, *Nature* **1964**, *201*, 468–470.
- [133] C. von Sonntag, H.-P. Schuchmann, *Meth. Enzymol.* **1994**, *233*, 3–20.
- [134] G. Baldacchino, *Radiat. Phys. Chem.* **2008**, *77*, 1218–1223.
- [135] E. Alizadeh, L. Sanche, *Chem. Rev.* **2012**, *112*, 5578–5602.
- [136] G. V. Buxton in *Radiation chemistry. Principles and applications*, VCH Publishers, Inc, New York, **1987**, pp. 321–350.
- [137] W. P. Swanson, *Radiological safety aspects of the operation of electron linear accelerators*, Stanford Linear Accelerator Center, CA (USA), **1979**.
- [138] U. Lachish, A. Shafferman, G. Stein, *J. Chem. Phys.* **1976**, *64*, 4205–4211.
- [139] M. Bazin, L. Patterson, R. Santus, *J. Phys. Chem.* **1983**, *87*, 189–190.
- [140] P. D. Wood, L. J. Johnston, *J. Phys. Chem. A* **1998**, *102*, 5585–5591.
- [141] S. Navaratnam, J. Claridge, *Photochem. Photobiol.* **2000**, *72*, 283–290.
- [142] T. Kohlmann, R. Naumann, C. Kerzig, M. Goez, *Photochem. Photobiol. Sci.* **2017**, *16*, 185–192.
- [143] S.-i. Ohno, *Bull. Chem. Soc. Jpn.* **1967**, *40*, 1779–1783.
- [144] E. Hayon, A. Treinin, J. Wilf, *J. Am. Chem. Soc.* **1972**, *94*, 47–57.
- [145] M. Goez, V. Zubarev, *Chem. Phys.* **2000**, *256*, 107–116.
- [146] M. Goez, B. H. M. Hussein, *Angew. Chem. Int. Ed.* **2003**, *42*, 1659–1661.
- [147] S. C. Wallace, M. Grätzel, J. Thomas, *Chem. Phys. Lett.* **1973**, *23*, 359–362.
- [148] M. Grätzel, J. Thomas, *J. Phys. Chem.s* **1974**, *78*, 2248–2254.

- [149] S. Hauteclouque, D. Grand, A. Bernas, *J. Phys. Chem.* **1985**, *89*, 2705–2708.
- [150] R. Boch, M. Whittlesey, J. Scaiano, *J. Phys. Chem.* **1994**, *98*, 7854–7857.
- [151] A. Bernas, D. Grand, S. Hauteclouque, *Int. J. Radiat. Appl. Instrum. C Radiat. Phys. Chem.* **1988**, *32*, 309–314.
- [152] S. El-Gogary, G. Grabner, *Photochem. Photobiol. Sci.* **2006**, *5*, 311–316.
- [153] N. Dhenadhayalan, C. Selvaraju, P. Ramamurthy, *J. Phys. Chem. B* **2011**, *115*, 10892–10902.
- [154] G. Porter, M. R. Topp, *Proc. R. Soc. A* **1970**, *315*, 163–184.
- [155] J. Scaiano, *Acc. Chem. Res.* **1982**, *15*, 252–258.
- [156] U. Schmidhammer, S. Roth, E. Riedle, A. A. Tishkov, H. Mayr, *Rev. Sci. Instrum.* **2005**, *76*, 093111.
- [157] J. A. Baban, J. P. Goddard, B. P. Roberts, *J. Chem. Soc., Perkin Trans. 2* **1986**, 1269–1274.
- [158] S. Jockusch, N. J. Turro, *J. Am. Chem. Soc.* **1998**, *120*, 11773–11777.
- [159] R. Miller, G. Closs, *Rev. Sci. Instrum.* **1981**, *52*, 1876–1885.
- [160] M. Goez, *Annu. Rep. NMR Spectrosc.* **2009**, *66*, 77–147.
- [161] R. H. Bisby, A. W. Parker, *J. Am. Chem. Soc.* **1995**, *117*, 5664–5670.
- [162] R. H. Bisby, A. W. Parker, *Arch. Biochem. Biophys.* **1995**, *317*, 170–178.
- [163] S. V. Jovanovic, Y. Hara, S. Steenken, M. G. Simic, *J. Am. Chem. Soc.* **1995**, *117*, 9881–9888.
- [164] A. Mortensen, L. H. Skibsted, *FEBS Letters* **1997**, *417*, 261–266.
- [165] F. Böhm, R. Edge, E. J. Land, D. J. McGarvey, T. G. Truscott, *J. Am. Chem. Soc.* **1997**, *119*, 621–622.
- [166] H. Zhu, H. Zhao, Z. Zhang, W. Wang, S. Yao, *Radiat. Environ. Biophys.* **2006**, *45*, 73–77.
- [167] K. Li, M. Wang, T. Wang, D. Sun, R. Zhu, X. Sun, X. Wu, S.-L. Wang, *Photochem. Photobiol.* **2013**, *89*, 1064–1070.
- [168] Y. Sueishi, M. Hori, M. Ishikawa, K. Matsu-Ura, E. Kamogawa, Y. Honda, M. Kita, K. Ohara, *J. Clin. Biochem. Nutr.* **2014**, *54*, 67–74.

- [169] A. El-Agamey, M. A. El-Hagrasy, T. Suenobu, S. Fukuzumi, *J. Photochem. Photobiol. B* **2015**, *146*, 68–73.
- [170] A. Aspée, C. Aliaga, L. Maretti, D. Zúñiga-Núñez, J. Godoy, E. Pino, G. Cárdenas-Jirón, C. Lopez-Alarcon, J. C. Scaiano, E. I. Alarcon, *J. Phys. Chem. B* **2017**, *121*, 6331–6340.
- [171] C. Kerzig, M. Hoffmann, M. Goetz, *Chem. Eur. J.* **2018**, *24*, 3038–3044.
- [172] M. Almgren, F. Grieser, J. K. Thomas, *J. Am. Chem. Soc.* **1979**, *101*, 279–291.
- [173] M. Montalti, A. Credi, L. Prodi, M. T. Gandolfi, *Handbook of photochemistry*, CRC press, **2006**.
- [174] R. Rathore, S. V. Lindeman, J. K. Kochi, *J. Am. Chem. Soc.* **1997**, *119*, 9393–9404.
- [175] N. J. Turro, P. L. Kuo, *Langmuir* **1985**, *1*, 170–172.
- [176] Y. Moroi, *J. Phys. Chem.* **1980**, *84*, 2186–2190.
- [177] T. Tominaga, H. Ohtaka-Saiki, Y. Nogami, H. Iwata, *J. Mol. Liq.* **2006**, *125*, 147–150.
- [178] H. F. Huisman, *Proc. Kon. Ned. Akad. Wetensch.* **1964**, *B67*, 407–424.
- [179] F. H. Quina, P. M. Nassar, J. B. Bonilha, B. L. Bales, *J. Phys. Chem.* **1995**, *99*, 17028–17031.
- [180] S. Vass, *Struct. Chem.*, **1991**, *2*, 375–397.
- [181] S. Vass, T. Torok, G. Jakli, E. Berecz, *J. Phys. Chem.* **1989**, *93*, 6553–6559.
- [182] A. Bhattarai, S. K. Chatterjee, T. K. Deo, T. P. Niraula, *J. Chem. Eng. Data* **2011**, *56*, 3400–3405.
- [183] R. G. Kryger, J. P. Lorand, N. R. Stevens, N. R. Herron, *J. Am. Chem. Soc.* **1977**, *99*, 7589–7600.
- [184] T. Momić, J. Savić, U. Černigoj, P. Trebše, V. Vasić, *Collect. Czech. Chem. Commun.* **2007**, *72*, 1447–1460.
- [185] K. Lemańska, H. van der Woude, H. Szymusiak, M. G. Boersma, A. Gliszczyńska-Świąto, I. M. Rietjens, B. Tyrakowska, *Free Radic. Res.* **2004**, *38*, 639–647.
- [186] D. Amić, V. Stepanić, B. Lučić, Z. Marković, J. M. D. Marković, *J. Mol. Model.* **2013**, *19*, 2593–2603.
- [187] R. Amorati, A. Baschieri, A. Cowden, L. Valgimigli, *Biomimetics* **2017**, *2*, 9.

- [188] J. J. Warren, T. A. Tronic, J. M. Mayer, *Chem. Rev.* **2010**, *110*, 6961–7001.
- [189] M. Leopoldini, T. Marino, N. Russo, M. Toscano, *Theor. Chem. Acc.* **2004**, *111*, 210–216.
- [190] S. Fiorucci, J. Golebiowski, D. Cabrol-Bass, S. Antonczak, *J. Agric. Food Chem.* **2007**, *55*, 903–911.
- [191] Y.-Z. Zheng, G. Deng, Q. Liang, D.-F. Chen, R. Guo, R.-C. Lai, *Sci. Rep.* **2017**, *7*, 7543.
- [192] Z. Li, M. Moalin, M. Zhang, L. Vervoort, E. Hursel, A. Mommers, G. R. Haenen, *Int. J. Mol. Sci.* **2020**, *21*, 6015.
- [193] M. Spiegel, T. Andruniów, Z. Sroka, *Antioxidants* **2020**, *9*, 461.
- [194] S. K. Hait, S. P. Moulik, *J. Surfactants Deterg.* **2001**, *4*, 303–309.
- [195] A. L. Van de Ven, K. Adler-Storthz, R. R. Richards-Kortum, *J. Biomed. Opt.* **2009**, *14*, 021012.
- [196] S. Schreier, S. V. Malheiros, E. de Paula, *Biochem. Biophys. Acta* **2000**, *1508*, 210–234.
- [197] R. Amorati, L. Valgimigli, *Org. Biomol. Chem.* **2012**, *10*, 4147–4158.
- [198] M. J. Frisch, G. W. Trucks, H. B. Schlegel, G. E. Scuseria, M. A. Robb, J. R. Cheeseman, G. Scalmani, V. Barone, G. A. Petersson, H. Nakatsuji, X. Li, M. Caricato, A. V. Marenich, J. Bloino, B. G. Janesko, R. Gomperts, B. Mennucci, H. P. Hratchian, J. V. Ortiz, A. F. Izmaylov, J. L. Sonnenberg, D. Williams-Young, F. Ding, F. Lipparini, F. Egidi, J. Goings, B. Peng, A. Petrone, T. Henderson, D. Ranasinghe, V. G. Zakrzewski, J. Gao, N. Rega, G. Zheng, W. Liang, M. Hada, M. Ehara, K. Toyota, R. Fukuda, J. Hasegawa, M. Ishida, T. Nakajima, Y. Honda, O. Kitao, H. Nakai, T. Vreven, K. Throssell, J. A. Montgomery, Jr., J. E. Peralta, F. Ogliaro, M. J. Bearpark, J. J. Heyd, E. N. Brothers, K. N. Kudin, V. N. Staroverov, T. A. Keith, R. Kobayashi, J. Normand, K. Raghavachari, A. P. Rendell, J. C. Burant, S. S. Iyengar, J. Tomasi, M. Cossi, J. M. Millam, M. Klene, C. Adamo, R. Cammi, J. W. Ochterski, R. L. Martin, K. Morokuma, O. Farkas, J. B. Foresman, D. J. Fox, *Gaussian16 Revision C.01*, **2016**, Gaussian Inc. Wallingford CT.
- [199] A. Ipatov, F. Cordova, L. J. Doriol, M. E. Casida, *J. Mol. Struct.-Theochem.* **2009**, *914*, 60–73.

6 Abkürzungsverzeichnis

AntNH ₂	2-Aminoanthracen
AntNH ₂ ^{•+}	2-Aminoanthracen-Radikalkation
Asc ^{•-}	Ascorbat-Radikalanion
AscH ₂	Ascorbinsäure
AscH ⁻	Ascorbat-Monoanion
BDE	Bindungsdissoziationsenergie
ClAc ⁻	Chloracetat
cmc	critical micelle concentration, kritische Mizellkonzentration
D _{sac}	Opferdonor
DFT	Dichtefunktionaltheorie
DTAB	Dodecyltrimethylammoniumbromid
e _{aq} ^{•-}	hydratisiertes Elektron
F	Fluorophor
FQ	Fluorophor-Quencher-Komplex
H ₂ Q	Quercetin
HQ ⁻	Quercetin-Monoanion
HQ [•]	Quercetin-Radikal
LFP	engl. Laser flash photolysis, Laserblitzlicht-Photolyse
Nd:YAG	Neodym-dotierter Yttrium-Aluminium-Granat
NR	Neutralradikal
PAscH ₂	6- <i>O</i> -Palmitoylascorbinsäure
PAscH ⁻	6- <i>O</i> -Palmitoylascorbat-Monoanion
PCET	engl. Proton-coupled electron transfer, Proton-gekoppelter Elektronentransfer
Q	Quencher, Löscher
Q ^{•-}	Quercetin-Radikalanion
RAN	Radikalanion
SANS	engl. Small-angle neutron scattering, Kleinwinkelneutronstreuung
SAXS	engl. Small-angle X-ray scattering, Kleinwinkelröntgenstreuung
SDS	Natriumdodecylsulfat
<i>SnS</i>	Natrium- <i>n</i> -alkylsulfat
TDDFT	engl. time-dependent DFT; zeitabhängige DFT

E	Extinktion
ε	molarer Extinktionskoeffizient
I	Intensität
k	Geschwindigkeitskonstante
K	Komplexbildungskonstante
λ	Wellenlänge
N_{agg}	Aggregationszahl
Φ	Fluoreszenzquantenausbeute
Φ_m	Partielles molares Mizellvolumen
$\langle q \rangle$	mittlere Besetzung mit Quencher
t	Zeit
τ	Lebenszeit
V_m	Mizellvolumen

7 Anhang

Die für die vorliegende Arbeit maßgeblichen Publikationen (Publ. A–E) sind nachfolgend aufgelistet und in ihrer Endfassung angefügt. Das Manuskript F wurde zur Begutachtung eingereicht und ist in der eingereichten Form mitsamt dem Teil „Electronic Supplementary Information“ angehängt.

7.1 **„Combined static and dynamic intramolecular fluorescence quenching: effects on stationary and time-resolved Stern–Volmer experiments“, A**

Reproduced from *Phys. Chem. Chem. Phys.* **2019**, *21*, 10075-10085 with permission from the Royal Society of Chemistry.

7.2 **„Pyrene–viologen complexes in SDS micelles: quenching parameters and use as probes of aggregation numbers“, B**

Reproduced from *Photochem. Photobiol. Sci.* **2020**, *19*, 71-79 with permission from the Royal Society of Chemistry.

7.3 **„Do equilibrium and rate constants of intramolecular reactions depend on micelle size?“, C**

Reproduced from *Phys. Chem. Chem. Phys.* **2021**, *23*, 9709-9714 with permission from the Royal Society of Chemistry.

7.4 **„Laser-Induced Wurtz-Type Syntheses with a Metal-Free Photoredox Catalytic Source of Hydrated Electrons“, D**

Reproduced from *Chem. Eur. J.* **2019**, *25*, 9991-9996 with permission from Wiley-VCH.

7.5 **„Laser Access to Quercetin Radicals and Their Repair by Co-antioxidants“, E**

Reproduced from *Chem. Eur. J.* **2020**, *26*, 17428-17436 with permission from Wiley-VCH.

7.6 **„The radicals of quercetin-derived antioxidants in Triton X-100 micelles“, F**

Eingereichtes Manuskript, *Phys. Chem. Chem. Phys.* **2021**.

7.1 Publikation A



PCCP

PAPER

[View Article Online](#)[View Journal](#) | [View Issue](#)

Cite this: *Phys. Chem. Chem. Phys.*,
2019, 21, 10075

Combined static and dynamic intramicellar fluorescence quenching: effects on stationary and time-resolved Stern–Volmer experiments

Tim Kohlmann and Martin Goez *

We have conducted a theoretical and experimental study of Stern–Volmer experiments in micellar systems for the important case that fluorophore and quencher remain confined to their micelle during the luminescence decay (the “immobile probe/immobile quencher” scenario) and exhibit static quenching followed by dynamic quenching. By a comparative mathematical analysis, we have exposed inherent physical and mathematical contradictions of earlier theories. We present a general framework that allows a very simple derivation of consistent solutions. Even with the correct model, strong parameter correlations severely compromise fit uniqueness when the stationary luminescence is the only observable, but these correlations can be removed by parallel absorption measurements and do not occur in time-resolved luminescence experiments. The application of our protocol to pyrene quenching by substituted viologens in SDS micelles revealed a linear dependence of the apparent aggregation number of the surfactant on the equilibrium constant of formation of ground-state complexes, which can be quantitatively explained by a preference of the quencher for micelles containing the fluorophore. The complex formation is entropy controlled, as evidenced by a driving force that decreases linearly with the number of free rotors in the viologen sidechains.

Received 6th December 2018,
Accepted 29th April 2019

DOI: 10.1039/c8cp07486k

rsc.li/pccp

1 Introduction

Distribution, localization, and interactions of guest molecules in micellar systems are highly topical issues because micelles find more and more widespread usage as nanocarriers of medicines,¹ as membrane mimetics,² and as nanoreactors for chemical transformations.³ Fluorescence methods, in particular quenching studies, have proven invaluable tools for investigating all these aspects.^{4–8}

Exclusively dynamic intramicellar quenching is well understood, with the original Infelta–Tachiya model^{9,10} later extended to more complex scenarios including migration between micelles.^{4,11} However, for micellar systems there is a lack of theories that consistently describe combined quenching, that is, instantaneous static quenching in preexisting ground-state complexes between fluorophore and quencher followed by slower dynamic quenching of those fluorophore molecules that were uncomplexed at the moment of the photon absorption. Hence, the mathematical description faces two difficulties: first, the guest molecules are distributed non-

uniformly among the micelles; and second, the initial condition for the dynamic quenching deviates from that distribution owing to the removal of all statically quenched fluorophores.

The analysis of intramicellar quenching by using the classical Stern–Volmer relationship has a long tradition,^{12–15} but is completely wrong on both counts because it assumes a homogeneous distribution of fluorophore and quencher; in consequence, it not only yields kinetic parameters that are worthless but also suggests combined quenching when there is only dynamic one, as we will show. The only model of combined intramicellar quenching previously reported by others¹⁶ that respects the initial distribution of the guest molecules employs that distribution as the starting condition for the dynamic quenching as well; and we will prove that this violation of the second criterion entails internal inconsistencies and invalid fit results. We have recently presented a kinetic investigation of the intramolecular repair of an extremely long-lived radical cation by an antioxidant, and hypothesized that our treatment should also be applicable to combined intramicellar quenching, not only in time-resolved but also in stationary experiments.¹⁷ Herein, we derive that model by a simpler and much more general route and analyze it in depth, with particular emphasis on fit

Martin-Luther-Universität Halle-Wittenberg, Institut für Chemie, Kurt-Mothes-Str. 2,
D-06120 Halle (Saale), Germany. E-mail: martin.goez@chemie.uni-halle.de

uniqueness. As will emerge, time-resolved experiments on their own are sufficient for obtaining reliable parameters, whereas stationary luminescence measurements need to be complemented by absorption measurements.

Owing to the large exergonicity, dynamic quenching is often diffusion limited, hence merely probes the hydrodynamic properties of the medium. Much more diverse information can be obtained from static quenching, for example on the strength of complexes^{18–20} the nature of the interactions holding them together,^{21,22} mechanistic details of the quenching process itself,²³ and important structural factors.^{24,25} In the confined space of a micelle, static quenching plays a much more prominent role than in homogeneous solution, on account of the very high local concentrations.

In this work, we have applied our new theory to complexes of pyrene with a series of viologens in SDS micelles. As we will show, the complex formation is entropy controlled, with the loss of rotational degrees of freedom in the viologen sidechains being the governing factor. We further present the first experimental evidence that the complexation enriches the fluorophore and/or quencher in micelles containing the respective other component: this modification of the micellar occupations causes the apparent aggregation number N_{agg} of the surfactant to be a linear function of the equilibrium constant of formation of the ground-state complex. As N_{agg} is a key parameter for the fits, this observation provides an important caveat, which seems to have remained unrecognized in all previous studies of static intramicellar quenching.

2 Experimental

1,1'-Dibutyl-4,4'-bipyridinium dibromide was synthesized by alkylating 4,4'-bipyridine in acetonitrile with *n*-butyl bromide, washed twice with the solvent, and dried. All other chemicals were obtained commercially and used as received. The water content of the viologens was determined by thermogravimetry in order to prepare all solutions to the desired quencher concentrations. The solvent was ultrapure Millipore Milli-Q water (specific resistance, 18.2 MΩ cm⁻¹), and all solutions were deoxygenated by bubbling argon 5.0 through them for 30 min before the experiments. An argon atmosphere was also maintained above the solutions during the measurements.

Stationary absorption and fluorescence spectra were recorded with a Shimadzu UV-1800 and a PerkinElmer LS 50B spectrometer, both equipped with thermostatted cell holders. To avoid filter effects, all solutions were kept optically thin.

Time-resolved fluorescence experiments were carried out with a laser-flash photolysis setup described in more detail elsewhere.²⁶ Flash parameters are 355 nm, 6 ns full width at half maximum, 2 mm optical pathlength for the excitation. The instrument response function has a Gaussian profile, which we measured in independent experiments and used for iterative deconvolution of the fit functions in Fig. 5.

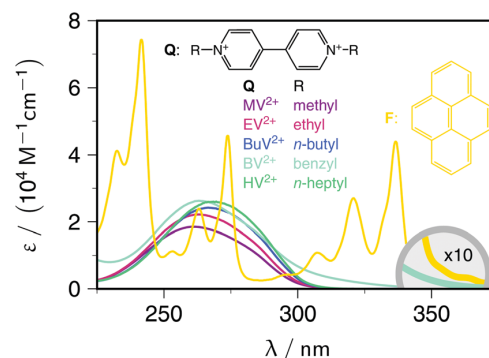


Fig. 1 Structural formulas and calibrated absorption spectra of the fluorophore (probe) pyrene F and the quenchers Q, substituted viologens RV^{2+} , used in this work. Medium, 50 mM aqueous SDS. The same colour code is used for the abbreviations and spectra of the substances. The excitation wavelength (355 nm) lies at the centre of the enlarged circle. For further explanation, see text.

3 Results and discussion

3.1 Choice and properties of the systems

This work treats the important “immobile probe/immobile quencher” case of intramicellar quenching.¹¹ The epithet “immobile” exclusively refers to intermicellar exchange during the luminescence decay: on that timescale, each micelle represents a closed system with regard to probe and quencher molecules; within each micelle, the access of the quencher to the probe is not barred; and on longer timescales, intermicellar exchange also takes place and establishes equilibrium, including with respect to ground-state complexes of probe and quencher.

Systems comprising pyrene as fluorophore (*i.e.*, probe) F, viologens (1,1'-disubstituted 4,4'-bipyridinium dication) RV^{2+} as quenchers Q, and sodium dodecylsulfate SDS as surfactant meet all these requirements. For the abbreviations, formulas, and absorption spectra of F and Q, see Fig. 1. The strong hydrophobicity of the probe (octanol-water partition coefficient $\log P_{\text{ow}}$, 4.88)²⁷ ensures that it resides practically exclusively inside the SDS micelles; and an unquenched radiative lifetime of F in this medium of about 350 ns^{16,28} renders noncompetitive an exit from the micelles (rate constant, $4 \times 10^3 \text{ s}^{-1}$).²⁹ Similarly, the strong Coulombic attraction causes the dicationic quenchers to be localized almost completely at the negatively charged micellar surface, with the molar fraction in the aqueous phase lower than 1.4% even for their most hydrophilic representative MV^{2+} ,³⁰ and there is also no intermicellar exchange of Q during the lifetime of excited F.¹⁶

The reaction medium is completely transparent above 250 nm. The fluorescence of F globally decreases when Q is added, but its spectral shape remains invariant (see below, left inset of Fig. 4 in Section 3.4); and at its 394 nm maximum, the emission can be recorded without interference by parasitic absorptions even in the most strongly quenched samples.

Exciting the samples at 355 nm brings three benefits. First, the stationary experiments can be complemented by time-resolved experiments with laser flash photolysis at exactly the same wavelength. Second, the low extinction coefficient of F at 355 nm allows keeping the solutions optically thin and thus avoiding inner filter effects.³¹ Third, all our quenchers with aliphatic substituents R are nonabsorbing at 355 nm; hence, even high concentrations of them do not reduce the intensity of the exciting light. As can be seen in the enlarged part of Fig. 1, the situation is different for BV²⁺. Therefore, we investigated BV²⁺ only by the time-resolved approach, which renders the quencher absorbance uncritical through a five times shorter excitation pathlength.

In contrast to the fluorescence spectrum, the absorption spectrum of F changes shape when Q is added.^{32,33} The interpretation by the formation of ground-state complexes F ··· Q is vindicated by clear isosbestic points (compare the example with MV²⁺ below, right inset of Fig. 4 in Section 3.4) in combination with the occurrence of static quenching.¹⁶ We stress that in such a case the composition-dependent absorption spectrum does not impose any constraints on the excitation wavelength and, in particular, does not require excitation at an isosbestic point: excited F ··· Q is nonluminescent because of the static quenching; hence, it plays no role if the extinction coefficient of the ground-state complex causes its excitation efficiency to deviate from that of F.

3.2 Derivation of the models

In a previous publication on the thermal reduction of the 3-aminoperylene radical cation by ascorbyl palmitate in SDS micelles,¹⁷ we derived a closed-form integrated rate law for the chemical decay, which should also be applicable to any luminescence decay $I(t)$ in combined static and dynamic intramolecular quenching,

$$\frac{I(t)}{I(0)} = \exp(-t/\tau_0) \frac{\exp(-\langle q \rangle)}{K} \left\{ [-\langle q \rangle \exp(-k_q t)]^{-1/K} \times \gamma[1/K, -\langle q \rangle \exp(-k_q t)] \right\} \quad (1)$$

We further integrated $I(t)$ over t to obtain an analytical expression for the Stern-Volmer observable I_0/I , but the nonemitting chemical system did not lend itself to a verification.

The lower incomplete Gamma function in eqn (1),

$$\gamma(a, z) = \int_0^z \zeta^{a-1} \exp(-\zeta) d\zeta \quad (2)$$

becomes complex for negative z and positive a , but its product with z^{-a} is then always real; and all the final expressions in this work will contain this combination, $(-x)^{-a} \cdot \gamma(a, -x)$ with $a, x > 0$.

Static and dynamic quenching are described by an equilibrium constant K and a rate constant k_q , respectively. Because the treatment of intramolecular quenching is based on the numbers, and not on the concentrations, of the quencher molecules in the micelles, K is dimensionless and k_q is an apparent first-order rate constant. In all expressions for I_0/I , k_q

will appear paired with the unquenched lifetime τ_0 of the excited fluorophore in the micellar surroundings. Henceforth, the dimensionless constant k ,

$$k = k_q \tau_0 \quad (3)$$

will denote this combination. In addition, we shall use k' and K' when we mean the constants of unit M⁻¹ instead of the dimensionless ones.

The average occupancy $\langle q \rangle$ of the micelles by the quencher not only is a key parameter of eqn (1), but also constitutes the independent variable in Stern-Volmer experiments through its proportionality to the quencher weight-in concentration $[Q]$,

$$\langle q \rangle = \frac{N_{\text{agg}}}{[\text{Surf}] - \text{cmc}} \cdot [Q] \quad (4)$$

The surfactant weight-in concentration $[\text{Surf}]$ can be reliably specified. However, the critical micelle concentration cmc and above all the aggregation number N_{agg} depend on the conditions; and an uncertainty of N_{agg} propagates to an equally large relative error of $\langle q \rangle$. Furthermore, as our analysis in Section 3.5 will reveal, N_{agg} is not more than an apparent quantity, which differs from the true aggregation number when F and Q form complexes.

For the normalized probability $P(n)$ that a micelle is occupied by n quencher molecules ($n = 0, 1, \dots$), the Poisson distribution is universally accepted,

$$P(n) = \frac{\langle q \rangle^n \cdot \exp(-\langle q \rangle)}{n!} \quad (5)$$

Our previous approach¹⁷ yielded a complete picture of time-resolved and stationary luminescence but is clearly wasteful when only the Stern-Volmer result I_0/I is desired. In the following, we show that our treatment for obtaining the time dependence can be adapted to find closed-form expressions for the stationary observables direct, that is, without the detour *via* the time-dependent result. As before, the requirements for its applicability are, (i) strictly intramolecular quenching, (ii) no exchange of the fluorophore or the quencher on the timescale of the observed luminescence; and (iii) no self quenching of the fluorophore, tantamount to not more than one molecule of F per micelle.

Under these circumstances, each excited fluorophore shares a compartment with n quencher molecules ($n = 0, 1, \dots$) and is quenched by them through a defined quenching mechanism (subscript “mech”; with the possibilities herein being “stat”, “dyn”, and “comb” for static, dynamic, and combined quenching). The luminescence quantum yield $\Phi_{\text{mech}}(n)$ taken relative to that in a quencher-free compartment depends on the number n in a way specific for the quenching mechanism. With the normalized probability $P(n)$ of finding n quenchers in a compartment, the Stern-Volmer observable I_0/I is thus given by the master equation

$$\frac{I_0}{I} = \left(\sum_{n=0}^{\infty} P(n) \cdot \Phi_{\text{mech}}(n) \right)^{-1} \quad (6)$$

The expressions for $\Phi_{\text{mech}}(n)$,

$$\Phi_{\text{stat}}(n) = \frac{1}{1 + K \cdot n} \quad (7a)$$

$$\Phi_{\text{dyn}}(n) = \frac{1}{1 + k \cdot n} \quad (7b)$$

$$\begin{aligned} \Phi_{\text{comb}}(n) &= \frac{1}{1 + K \cdot n} \cdot \frac{1}{1 + k \cdot n} \\ &= \frac{1}{k - K} \left(\frac{k}{1 + k \cdot n} - \frac{K}{1 + K \cdot n} \right) \end{aligned} \quad (7c)$$

are the same in homogenous and in micellar solution except for the above-mentioned change in the units of the equilibrium constant and the Stern-Volmer constant, which contain reciprocal concentrations in the homogeneous case and no concentrations in the micellar one.

Combined static and dynamic quenching in homogeneous solution can be treated with eqn (6) and (7c) by setting $P(n)$ to zero except for $n = N_A V [Q]$ where it is unity. The well-known result is reproduced here

$$\begin{aligned} \left(\frac{I_0}{I} \right)_{\text{comb,hom}} &= (1 + K' \cdot [Q]) \times (1 + k' \cdot [Q]) \\ &= 1 + (K' + k') \cdot [Q] + (K'k') \cdot [Q]^2 \end{aligned} \quad (8)$$

because it is frequently, and without any theoretical justification, used for interpreting Stern-Volmer experiments in micelles.^{12–15}

By inserting eqn (7b) and (5) into eqn (6) and transforming the result with the series expansion³⁴ of the lower incomplete Gamma function, one obtains the Stern-Volmer relationship for purely dynamic intramicellar quenching,

$$\begin{aligned} \left(\frac{I_0}{I} \right)_{\text{dyn,mic}} &= \left(\sum_{n=0}^{\infty} \frac{\langle q \rangle^n \cdot \exp(-\langle q \rangle)}{n!(1 + k \cdot n)} \right)^{-1} \\ &= \frac{k \cdot \exp(+\langle q \rangle)}{(-\langle q \rangle)^{-1/k} \cdot \gamma(1/k, -\langle q \rangle)} \end{aligned} \quad (9)$$

Pertinent properties of this function will be discussed in the next section.

Owing to the identical structure of eqn (7a) and (7b), the Stern-Volmer observable for exclusive static quenching is that of eqn (9) with k replaced by K throughout. Hence, the formula is not reproduced here, in particular because isolated static quenching would seem to be confined to fluorophores with τ_0 so short as to make dynamic quenching kinetically noncompetitive: thermodynamically, exergonic static quenching would also entail exergonic dynamic quenching.

However, the frequently occurring absorption changes caused by the formation of a ground-state complex provide a much more relevant case that can be treated by the same formalism. Let the extinction coefficients of the fluorophore F and of the complex $F \cdot \cdot Q$ be ε_F and ε_{FQ} . The r.h.s. of eqn (7a) specifies the probability of finding a free fluorophore in a micelle with n quencher molecules, and the observed extinction

coefficient $\varepsilon(\langle q \rangle)_{\text{mic}}$ is obtained by inserting the Poisson statistics of eqn (5) and summing up,

$$\begin{aligned} \varepsilon(\langle q \rangle)_{\text{mic}} &= \varepsilon_F \sum_{n=0}^{\infty} P(n) \cdot \frac{1}{1 + K \cdot n} + \varepsilon_{FQ} \left(1 - \sum_{n=0}^{\infty} P(n) \cdot \frac{1}{1 + K \cdot n} \right) \\ &= (\varepsilon_F - \varepsilon_{FQ}) \cdot \frac{\exp(-\langle q \rangle)}{K} \cdot (-q)^{-1/K} \cdot \gamma(1/K, -q) + \varepsilon_{FQ} \end{aligned} \quad (10)$$

whereas the elementary result in homogeneous solution—recast as to maximize the parallel to eqn (10)—is

$$\varepsilon([Q])_{\text{hom}} = (\varepsilon_F - \varepsilon_{FQ}) \cdot \frac{1}{1 + K'[Q]} + \varepsilon_{FQ} \quad (11)$$

The decomposition into partial fractions shown in eqn (7a) allows obtaining the solution for combined static and dynamic quenching in micelles within the same framework,

$$\begin{aligned} \left(\frac{I_0}{I} \right)_{\text{comb,mic}} &= \left(\sum_{n=0}^{\infty} \frac{\langle q \rangle^n \cdot \exp(-\langle q \rangle)}{n!(1 + k \cdot n)(1 + K \cdot n)} \right)^{-1} \\ &= \frac{(k - K) \cdot \exp(+\langle q \rangle)}{(-\langle q \rangle)^{-1/k} \gamma(1/k, -\langle q \rangle) - (-\langle q \rangle)^{-1/K} \gamma(1/K, -\langle q \rangle)} \end{aligned} \quad (12)$$

In particular, this obviates any necessity of integrating the time dependence given by eqn (1). As an alternative form, eqn (12) can be recast as a generalized hypergeometric function,³⁴

$$\left(\frac{I_0}{I} \right)_{\text{comb,mic}} = \frac{\exp(+\langle q \rangle)}{{}_2F_2(1/k, 1/K; 1 + 1/k, 1 + 1/K; \langle q \rangle)} \quad (13)$$

which permits a direct calculation also in the rather special case $k = K$, for which eqn (7c) and (12) apparently yield the indeterminate expression 0/0.

Gehlen *et al.* have arrived at a different result,¹⁶ which we will prove to be erroneous. They stopped at the stage of the series representation, as reproduced in the first line of eqn (14); but because this involves the series already treated in eqn (9), the transformation to a closed-form solution is straightforward.

$$\begin{aligned} \left(\frac{I_0}{I} \right)_{\text{comb,err}} &= (1 + K \cdot \langle q \rangle) \times \left(\sum_{n=0}^{\infty} \frac{\langle q \rangle^n \cdot \exp(-\langle q \rangle)}{n!(1 + k \cdot n)} \right)^{-1} \\ &= (1 + K \cdot \langle q \rangle) \times \frac{k \cdot \exp(+\langle q \rangle)}{(-\langle q \rangle)^{-1/k} \gamma(1/k, -\langle q \rangle)} \end{aligned} \quad (14)$$

A comparison of eqn (12) and (14) immediately reveals the difference: the treatment of eqn (14) assumes separability of static and dynamic quenching in the same way as for the homogeneous case (eqn (8)); in other words, neglects that the static quenching modifies the initial condition for the dynamic quenching.

3.3 Analysis of the models

On physical grounds, the Stern-Volmer observable for the “immobile probe/immobile quencher” scenario in micelles

must be confined to an interval

$$1 \leq \left(\frac{I_0}{I}\right)_{\text{mic}} \leq \exp(+\langle q \rangle) \quad (15)$$

The lower boundary equally holds for the homogeneous case because by definition the unquenched intensity I_0 is the maximum the fluorophores can emit; it is therefore also reached as $[Q]$ or $\langle q \rangle$ approaches zero. However, the upper limit is specific for micelles with their Poisson distribution of guest molecules: even if the quenching is so efficient that the luminescence is already wiped out by a single quencher in the micelle, there still remains a quencher-free fraction of the micelles $\exp(-\langle q \rangle)$, which enters the denominator of the Stern–Volmer ratio.

All models respect the lower boundary, as is trivial to see in the homogeneous case (eqn (8)), and follows for eqn (9), (12) and (14) from the limit

$$\lim_{x \rightarrow 0} (-x)^{-a} \gamma(a, -x) = 1/a \quad (16)$$

which is obtained by applying L'Hospital's rule to the expression. With respect to the upper boundary, however, the models behave differently.

The function for the homogeneous Stern–Volmer case (eqn (8)) will always transgress $\exp(\langle q \rangle)$ for small $\langle q \rangle$ when the sum $K + k$ is larger than unity, as an expansion of the exponential to first order shows. This is paralleled by the evident inability of this function to reproduce the Stern–Volmer curve satisfactorily over the range of quencher concentrations used for the main plot of Fig. 2; and the systematic deviations are only obliterated by the random error on the data when that concentration range is restricted, as in the lower inset.

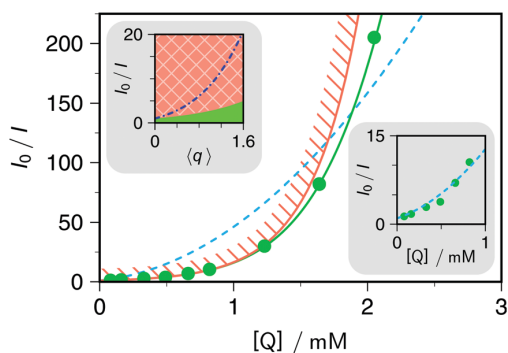


Fig. 2 Comparison of functions describing intracellular Stern–Volmer experiments for the “immobile probe/immobile quencher” case. Main plot, experimental data for quenching 10 μM pyrene in 50 mM aqueous SDS by variable concentrations $[Q]$ of MV^{2+} , and best fits of eqn (12) (solid green curve) vs. 10 (broken cyan curve). The solid red line with hatched borders is $\exp(\langle q \rangle)$ calculated (eqn (4)) with the cmc of 8.2 mM^{35} and $N_{\text{agg}} = 117$ as the lower limit consistent with the data. Right inset, a successful fit of eqn (8) is only possible for small $[Q]$. Left inset, allowed (green) and forbidden (red, cross-hatched) areas for I_0/I separated by the curve $\exp(\langle q \rangle)$. The dark blue dashed-dotted curve is the model by Gehlen *et al.* (eqn (14)) with their best-fit parameters ($K = 2.38$, $k = 17.2$).¹⁶ For further explanation, see text.

Factoring out the constant exponential from eqn (9) and (12) immediately shows the remaining sums be larger than unity for nonzero $\langle q \rangle$; and, as these sums appear in the denominator, both our models observe also the upper boundary of eqn (15). However, the model by Gehlen *et al.*¹⁶ does not, as the left inset of Fig. 2 unambiguously demonstrates. This inset uses the fit parameters and independent variable $\langle q \rangle$ of the original publication; and, as can be verified by inspection of Fig. 2 of that work, clearly represents the data reported there. This is uncontroversial proof of two things. First, that model suffers from an internal contradiction because for the—*not* in any way excessively large or small—values of k and K in the figure it yields values of I_0/I that are much higher than $\exp(\langle q \rangle)$ and thus physically impossible. Second, the data on which the fit was based seemingly exhibit the same problem; and that problem does not originate from errors in I_0/I , as our repetition of the measurements established, but from systematic deviations of the “independent” variable $\langle q \rangle$, which in reality depends on the choice of a value for N_{agg} . When the data are recalculated differently, namely, when $\langle q \rangle$ is calculated with a larger value of N_{agg} , the horizontal scale for the data points is dilated such as to move I_0/I below the limit of $\exp(\langle q \rangle)$. We stress that the two deficiencies exist separately: the model of eqn (14) has an internal inconsistency that renders it worthless; and the data have been compromised by preconditioning them with an inappropriate value of N_{agg} . The fact that the wrong model yields a very good fit to the wrong data is thus highly problematic, and emphasizes the necessity of excluding such sources of errors by consistency checks and control experiments.

In the main plot of Fig. 2, we have therefore chosen the quencher weight-in concentration as an assumption-free independent variable. By using the untransformed data as benchmark, we estimated the minimum value of N_{agg} for which $\exp(\langle q \rangle)$ is able to accommodate them as 117. This value is much higher than commonly assumed, and we will present further experimental corroboration in Section 3.4 as well as an explanation in Section 3.5. However, before addressing this problem together with that of fit reliability, we shall briefly discuss a few other properties of the models derived in the preceding section.

When the function for purely dynamic intracellular quenching that we presented in eqn (9) is differentiated with respect to $\langle q \rangle$ and the observable is back-substituted, one obtains

$$\frac{d}{d\langle q \rangle} \left(\frac{I_0}{I} \right)_{\text{dyn.mic}} = \frac{1}{k \cdot \langle q \rangle} \left(\frac{I_0}{I} \right)_{\text{dyn.mic}} \left\{ 1 + k \cdot \langle q \rangle - \left(\frac{I_0}{I} \right)_{\text{dyn.mic}} \right\} \quad (17)$$

On physical grounds, a downward slope of a Stern–Volmer plot for dynamic quenching—tantamount to higher emission when the quencher concentration is increased—appears inconceivable. By this reasoning, the term enclosed by the curly braces in eqn (17) should always be positive. A rigorous mathematical proof (*i.e.*, based only on the functional form of eqn (9) instead of invoking physical arguments) of this statement is unavailable but extensive numerical simulations indeed gave only positive values

of that term. As a corollary of a nondecreasing Stern–Volmer function, one thus arrives at a much more stringent upper limit for large $\langle q \rangle$ than by eqn (15), namely,

$$1 \leq \left(\frac{I_0}{I} \right)_{\text{dyn,mic}} \leq \min[\exp(+\langle q \rangle), 1 + k\langle q \rangle] \quad (18)$$

The same result, but with K substituted for k , holds for static intramolecular quenching.

As is textbook knowledge, a Stern–Volmer plot in homogeneous solution is linear for purely dynamic ($K = 0$) or purely static ($k = 0$) quenching but curved upwards for combined quenching (eqn (8)). On this basis, a curvature of a Stern–Volmer plot in micellar medium is often taken to indicate combined quenching.^{12–15,36} However, this is a misconception that again arises from the use of a wrong model. Although the expression obtained by a second differentiation of eqn (17) with respect to $\langle q \rangle$ is unwieldy, the following simple conclusion can be drawn from numerical simulations over a wide range of parameter combinations: for reasonable quencher concentrations ($\langle q \rangle \lesssim 5$) there always is an upward curvature; and even in the case of excessively large $\langle q \rangle$, an inflexion point only exists if k surpasses unity.

An inequality similar to eqn (18) can be derived when the Stern–Volmer observable for combined intramolecular quenching is expressed by I_0/I for pure static and pure dynamic quenching. Eliminating the terms $(-x)^{-\alpha} \gamma(a, -x)$ in the denominator of eqn (12) by using eqn (9) and its analogue with k replaced by K , one has

$$\begin{aligned} \left(\frac{I_0}{I} \right)_{\text{comb,mic}} &= \frac{(k-K)(I_0/I)_{\text{dyn,mic}}(I_0/I)_{\text{stat,mic}}}{k(I_0/I)_{\text{dyn,mic}} - K(I_0/I)_{\text{stat,mic}}} \\ &= \left[\frac{k}{k-K} \left(\frac{I_0}{I} \right)_{\text{dyn,mic}}^{-1} - \frac{K}{k-K} \left(\frac{I_0}{I} \right)_{\text{stat,mic}}^{-1} \right]^{-1} \end{aligned} \quad (19)$$

Differentiation of eqn (12) with respect to $\langle q \rangle$ and back-substitution of the Stern–Volmer observables with the aid of eqn (19) yields, after some rearrangement,

$$\frac{d}{d\langle q \rangle} \left(\frac{I_0}{I} \right)_{\text{comb,mic}} = \frac{1}{k \cdot \langle q \rangle} \left(\frac{I_0}{I} \right)_{\text{comb,mic}} \left\{ 1 + k \cdot \langle q \rangle - \frac{(I_0/I)_{\text{comb,mic}}}{(I_0/I)_{\text{stat,mic}}} \right\} \quad (20)$$

and by the same physical arguments as before (*i.e.*, nondecreasing behaviour of a Stern–Volmer observable when the quencher concentration is increased) the term in curly braces on the r.h.s. of eqn (20) must be positive, which can be recast to give

$$1 \leq \left(\frac{I_0}{I} \right)_{\text{comb,mic}} \leq \min[\exp(+\langle q \rangle), (1 + K\langle q \rangle) \times (1 + k\langle q \rangle)] \quad (21)$$

Eqn (18) and (21) thus sum up intramolecular quenching as follows: for small quencher concentrations, the Stern–Volmer observable has the reciprocal probability of finding a quencher-free micelle as an upper boundary; but at high quencher concentrations, the

result in homogeneous solution provides an upper limit that is reached asymptotically.

Finally, we prove that the earlier model in the literature (eqn (14))¹⁶ does not respect the upper boundary of I_0/I for small $\langle q \rangle$. An expansion to first order yields

$$\left(\frac{I_0}{I} \right)_{\text{comb,err}} = 1 + \left(1 + K - \frac{1}{1+k} \right) \langle q \rangle + \mathcal{O}(\langle q \rangle^2) \quad (22a)$$

$$\exp(+\langle q \rangle) = 1 + \langle q \rangle + \mathcal{O}(\langle q \rangle^2) \quad (22b)$$

A comparison of the first-order coefficients in eqn (22a) and (22b) shows that I_0/I given by eqn (14) surpasses $\exp(+\langle q \rangle)$ whenever K is larger than $1/(1+k)$: in other words, for any such combination of parameters, the Stern–Volmer observable would lie in a physically impossible range.

3.4 Fit uniqueness

With nonlinear multiparameter fits, sometimes many parameter sets represent the data almost equally well even in an ideal (fluctuation-free) situation. Direct consequences in the presence of experimental uncertainties are impaired fit convergence and parameter confidence.

In stationary measurements of combined static and dynamic quenching, these problems are immediately suggested by the invariance of the Stern–Volmer functions under an exchange of the two constants k and K , in both the homogeneous case (eqn (8)) and the micellar one (eqn (12)). Not only is it intrinsically impossible without additional information to determine which parameter belongs to which process, but it is also to be expected that an increase of one parameter can be compensated by a decrease of the other. Fig. 3 demonstrates the uniqueness issues that arise when stationary Stern–Volmer experiments as in Fig. 2 provide the only observables. To avoid artifacts caused by measurement errors, we performed the analysis with synthetic data based on the parameters ($N_{\text{agg,ref}} = 122$, $K_{\text{ref}} = 0.95$, $k_{\text{ref}} = 18$) determined by the more robust experiments described and discussed in the second half of this section.

The main plot of Fig. 3 delivers the first strong warning against uncritically fitting eqn (12) to such data: values of N_{agg} between 117, *i.e.*, the previously mentioned lower limit dictated by the term $\exp(+\langle q \rangle)$, and 127 give only minute deviations from the Stern–Volmer reference curve provided that K and k are adjusted suitably; but the associated changes of these two kinetic parameters span more than an order of magnitude. This strong dependence of K and k on N_{agg} constitutes the first high-risk issue: on one hand, it forbids a brute-force approach by a three-parameter fit, which would not only be unreliable but frequently does not converge; on the other hand, it renders equally problematic choosing some literature value as fixed N_{agg} , because N_{agg} is so susceptible to the sample composition (see, Section 3.5) and the best-fit kinetic parameters K and k in turn respond so sensitively to variations of N_{agg} .

The insets of Fig. 3 address the correlation between the parameters K and k when the influence of N_{agg} is eliminated by calculating on the basis of $\langle q \rangle$. As is evident from the left inset,

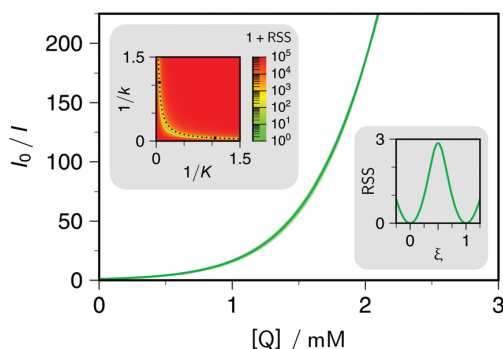


Fig. 3 Parameter correlations in a fit of eqn (12) to synthetic data with $N_{\text{agg,ref}} = 122$, $K_{\text{ref}} = 0.95$, $k_{\text{ref}} = 18.0$ (compare, Fig. 4 and 5). Main plot, influence of N_{agg} . The solid dark green curve is the reference obtained with the above parameter set, but the underlaid lighter green curves give very similar representations of the Stern–Volmer experiment with widely different kinetic parameters when N_{agg} is changed by $\pm 4\%$ ($N_{\text{agg}} = 117$, $K = 0.067$, $k = 103$; or $N_{\text{agg}} = 127$, $K = 4.01$, $k = 4.00$). Insets, residual sum of squares RSS for 12 equidistant synthetic data points between $\langle q \rangle = 0.5$ and $\langle q \rangle = 6$. Left inset, colour-coded error surface as function of $1/K$ and $1/k$. The dotted line is the hyperbola given by $1/k = (1/K_{\text{ref}}) \times (1/k_{\text{ref}}) \times (1/K)^{-1}$, and the two bigger dots represent the two equivalent exact solutions $1/K = 1/k_{\text{ref}}$ and $1/K = 1/k_{\text{ref}}$. Right inset, RSS along the valley bottom of the left inset, with the exact solutions corresponding to $\xi = 0$ and $\xi = 1$. For further explanation, see text.

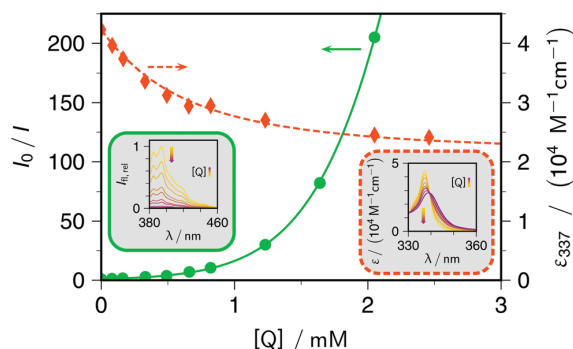


Fig. 4 Combining quencher-dependent absorption and luminescence in a global fit for robust parameter estimation. Conditions, $10 \mu\text{M}$ pyrene in 50 mM aqueous SDS at variable concentrations MV^{2+} as the quencher Q. Main plot, Stern–Volmer data (green circles, luminescence excited at 355 nm and observed at the 394 nm maximum) and effective extinction coefficient (red diamonds) at 337 nm , *i.e.*, the spectral maximum in the absence of Q; fit functions given by eqn (12) (green solid curve) and 12 (dashed red curve) with shared best-fit parameters ($N_{\text{agg}} = 122$, $K = 0.95$, $k = 18$, $\epsilon_{\text{FQ},337} = 21500 \text{ M}^{-1} \text{ cm}^{-1}$) and independently determined fixed parameter $\epsilon_{\text{F},337} = 42450 \text{ M}^{-1} \text{ cm}^{-1}$. The insets displays the actual spectra (left, green solid border, emission; right, red dashed border, absorption) with colours from gold to magenta signifying increasing concentration of Q. For further explanation, see text.

the error surface features a deep valley along a path that is very nearly hyperbolic, *i.e.*, characterized by a constant value of the product $(1/K) \times (1/k)$. What is worse, the bottom of that valley is extremely flat, as the right inset illustrates: with the underlying 12 equally spaced synthetic data points, the threshold separating the minima for the above parameter set and the one with K_{ref} and k_{ref} interchanged is less than what would result from an experimental error in Fig. 2 of 1% for the highest data point only. As the second high-risk issue, a fit by using eqn (12) alone is thus mathematically ill-conditioned even when N_{agg} is known precisely.

The dilemma can be resolved in two ways. The first remedy combines the measurements of the stationary luminescence with those of the stationary absorption. The absorption (eqn (10)) does not depend on k at all, hence a simultaneous fit to both experiments eliminates the correlation between K and k . Fig. 4 illustrates the success of this global approach, which is always applicable if the absorption of the ground-state complex differs sufficiently from that of the fluorophore itself. Issues with the very different magnitudes of I_0/I and ϵ are safely avoided by pre-fit normalization to their respective averages. Eqn (10) introduces ϵ_{FQ} as an additional fit parameter; however, the experiment with the highest quencher concentration already provides an excellent initial value for ϵ_{FQ} . The global fit, which is free from convergence problems, yields a unique parameter set: it neither tolerates interchanging K and k nor accommodates different pairs of these kinetic parameters with the same product $K \times k$.

The second solution utilizes time-resolved luminescence measurements. Their fit function is given by eqn (1), which we have previously derived and verified with a quasi infinitely long-lived probe.¹⁷ As the main plot and left inset of Fig. 5

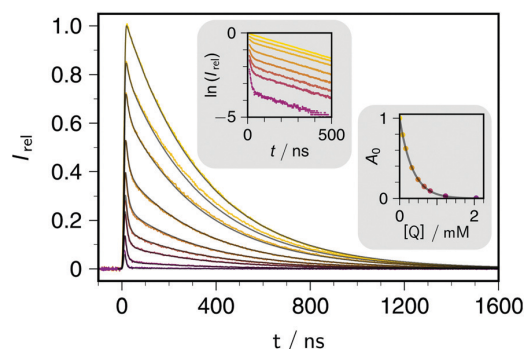


Fig. 5 Time-resolved luminescence of $10 \mu\text{M}$ pyrene in 50 mM aqueous SDS and variable concentrations of MV^{2+} as the quencher Q between zero and about 2 mM , (same colour code, from gold to magenta, throughout); excitation with 5 ns laser pulses at 355 nm , detection at 394 nm ; all luminescence curves normalized to the maximum in unquenched solution. Main plot, recorded decays with overlaid global fit curves (eqn (1)); after convolution with the instrument response function; best-fit parameters, $N_{\text{agg}} = 122$, $K = 0.95$, $\tau_0 = 338 \text{ ns}$, $k_{\text{q}} = 6.6 \times 10^7 \text{ s}^{-1}$ corresponding to $k = 22$. Left inset, log–lin plot of the decays over approximately 1.5 unquenched lifetimes τ_0 . The first 10 ns have been blanked because they are distorted by the instrumental rise time, and the curve with the highest quencher concentration has been omitted for better vertical resolution. Right inset, amplitude A_0 , of a monoexponential fit excluding the first 100 ns of each decay, as function of the quencher concentration. The solid curve is $\exp(-N_{\text{agg}}[Q]/([\text{SDS}] - \text{cmc}))$ with a fixed cmc of 8.2 mM^{35} and best-fit parameter N_{agg} of 122. For further explanation, see text.

epitomize, this approach achieves separation through the different time domains of the processes. Static quenching is

instantaneous, hence K controls the initial amplitude of the fluorescence; dynamic intramolecular quenching occurs on a time scale of some 50 ns with our systems even at our lowest nonzero quencher concentration, hence the influence of k is confined to this region; and after some 100 ns excited fluorophores are only present in the quencher-free micelles, hence the decay curves after that point of time obey perfect first-order kinetics determined by a global τ_0 for the exponential part and—through the probability $\exp(-q)$ of a micelle being unoccupied— N_{agg} for the preexponential factor A_0 . Given that both K and N_{agg} thus hinge on the signal amplitude as function of the quencher concentration, single photon counting with its inherent dependence of the vertical axis on the experiment duration and the kinetic parameters would introduce undesirable complications. To avoid these, we instead measured the luminescence decays with our laser flash photolysis setup.

The analysis of A_0 is especially valuable because it allows accessing the crucial quantity N_{agg} in a way that is not only direct but above all certain to be free from any interference by K and k . As is evident from the right inset of Fig. 5, A_0 exhibits the exponential dependence on the quencher concentration specified by eqn (4) and (5). The extracted value of N_{agg} , 122, corroborates the result obtained by the four-parameter fit to the two stationary observables of Fig. 4. Together with our above discussion of Fig. 2, which identified 115 as the minimum N_{agg} compatible with eqn (12), the experiments of Fig. 4 and 5 thus provide ample support of the unexpectedly large value of N_{agg} , which the next Section will address.

We emphasize that this determination of N_{agg} does not require fits of a complicated special function but is based simply on the directly verifiable facts (see, left inset of Fig. 5) that all intramolecular quenching processes are completed on a timescale much shorter than τ_0 , and that at later times the logarithmized decay curves are parallel straight lines. Their slopes in that regime correspond to a global value of 338 ± 9 ns for τ_0 , in close agreement with other reports on pyrene in SDS micelles;^{16,28} and obtaining A_0 involves back extrapolation over an interval shorter than 30% of τ_0 , hence is not critical. A global fit of eqn (1) to the early part of the curves finally gave exactly the same association constant K as the stationary experiments of Fig. 4, and a rate constant k larger by 20%, which we ascribe to some smoothing of the curves by the finite laser pulse width and instrumental rise time. The two methods thus yield essentially identical results for our test system.

As has emerged, both the stationary absorption in combination with the stationary luminescence (Fig. 4) and the time dependence of the luminescence alone (Fig. 5) avoid the strong correlations between the best-fit parameters K , k , and N_{agg} that were the bane of Stern–Volmer experiments on their own (Fig. 3). In addition, the time-resolved approach provides the most direct access to the aggregation number N_{agg} , and leaves partially no uncertainty of this key quantity.

3.5 Quencher influence on association constant and aggregation number

Table 1 collects the results of time-resolved experiments as in Fig. 5 for the viologens investigated in this work.

Table 1 Kinetic parameters for dynamic and static fluorescence quenching of pyrene by different viologens in SDS micelles, and micellar aggregation numbers; all obtained by experiments as in Fig. 5

Viologen ^a	$k_{\text{q}}/(10^7 \text{ s}^{-1})$	K	N_{agg}
MV ²⁺	6.6	0.95	122
EV ²⁺	6.2	0.74	112
BV ²⁺	6.3	0.45	104
BuV ²⁺	5.9	0.43	100
HV ²⁺	6.7	0.15	88

^a For the abbreviations and structural formulas, see Fig. 1.

The rate constants k_{q} are seen to be essentially identical, randomly deviating from their average of $6.3 \times 10^7 \text{ s}^{-1}$ by not more than $\pm 5\%$. The natural explanation by diffusion control is made plausible by the strong exergonicity of about 1.7 eV (energy of the pyrene S_1 state, 3.3 eV; $E^\circ(\text{F}^{\bullet+}/\text{F})$, 1.4 V; $E^\circ(\text{RV}^{2+}/\text{RV}^{\bullet+})$, -0.2 V for the viologens with aliphatic substituents and -0.1 V in the case of BV²⁺);³⁷ and the magnitude of k_{q} is consistent with results for other diffusion-controlled quenching reactions of pyrene in SDS micelles.³⁸

In striking contrast, the quencher structure obviously exerts a significant influence not only on the association constant K but also on the measured aggregation number N_{agg} , with both quantities even exhibiting a good linear correlation (Fig. 6). Considering that all error sources, be they related to the mathematical models or to fit uniqueness, have been eliminated by the analyses of Sections 3.2 to 3.4, the following two observations are highly surprising: on one hand, that the obtained values of N_{agg} surpass the aggregation number expected under our conditions (about 80 for a 50 mM SDS solution at 20 °C, according to a recent NIST study carried out by small-angle neutron scattering)³⁹ by up to 50%; on the other hand, that they depend on the viologen substituents at all, given that all our quenchers bear the same charges and are employed at such small

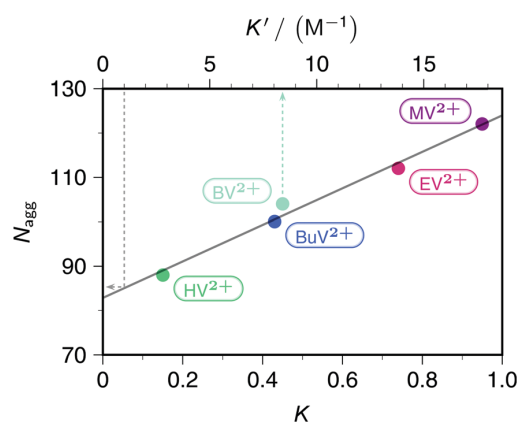


Fig. 6 Observed aggregation number N_{agg} as function of the complexation constant K for the viologens of this study; data from Table 1. Regression line given by $82.8 + 41.1K$. Upper horizontal axis, equilibrium constant K' , with the proportionality factor obtained by using BV²⁺ as reference. Dashed gray arrow, determination of the true aggregation number N_{agg}' from the regression value at $K' = 1 \text{ M}^{-1}$. For further explanation, see text.

concentrations as to cause negligible ionic-strength effects on the aggregation number.

A consistent explanation is provided by the modification of the micellar occupations that the formation of a ground-state complex necessarily entails. Whenever the pertaining equilibrium constant K' (expressed in concentration units, as opposed to K) is larger than 1 M^{-1} , thermodynamics requires a preference of the quencher Q for micelles containing the fluorophore F . Although the same argument applies to F , the very low fluorophore-micelle concentration ratio in our experiments still makes it improbable to find a micelle hosting more than one molecule of F , such that the micelles with a single F remain the only source of luminescence; but within that subensemble, there is an apparent enrichment of Q relative to the expected value based on the quencher-micelle weight-in concentration ratio.

Because thermodynamic equilibrium is established before each measurement, that enrichment simply equals the contribution of FQ , hence the total concentration of Q within the observed micelles containing a single F is given by

$$[Q]_F = [Q] + [FQ] = [Q](1 + K'[F]) \quad (23)$$

and through eqn (4) and the proportionality between K' and K , this translates into an analogous relationship between the apparent and true aggregation numbers N_{agg} and N_{agg}' ,

$$N_{\text{agg}} = N_{\text{agg}}'(1 + \alpha K) \quad (24)$$

For BV^{2+} /pyrene, the complexation constant K' is 8.4 M^{-1} in methanol,⁴⁰ and the effective polarity experienced between the palisade and Stern layers of an SDS micelle is very similar to that of the alcohol.²⁶ Therefore, we took BV^{2+} as the reference compound to establish the proportionality factor between the scales of K and K' . As displayed in Fig. 6, a projection of the point $K' = 1$ back onto the regression line yields a value of 85 for N_{agg}' , in good agreement with the literature.³⁹ The apparent anomalies concerning the size and variability of the observed N_{agg} are thus resolved both qualitatively and quantitatively.

Because our alkyl-substituted viologens possess identical redox potentials,³⁷ the systematic trend in their equilibrium constants of forming a ground-state complex with pyrene must have steric reasons. Steric interactions are known to exert a strong influence on association equilibria featuring π - π stacking, which is typical for aromatic donor-acceptor complexes.⁴¹ The entropy control of these reactions is underlined most impressively by the observation that for hexaalkylbenzene-chloranil complexes with $K' \gtrsim 1 \text{ M}^{-1}$ the face-to-face distance of the aromatic rings is practically constant and equal to the van der Waals contact distance.⁴¹ The substituent-dependent entropic penalty in the formation of pyrene-viologen complexes can only originate from the loss of rotational degrees of freedom when the sidechains can no longer explore their full configuration space in the stacked arrangement, as is illustrated by the inset of Fig. 7.

Its ionic nature confines the viologen to the Stern layer, where it is retained through Coulombic attractions. In contrast, pyrene is known to be located in the palisade layer of an SDS micelle.⁴² Up to and including the two carbon atoms anchoring

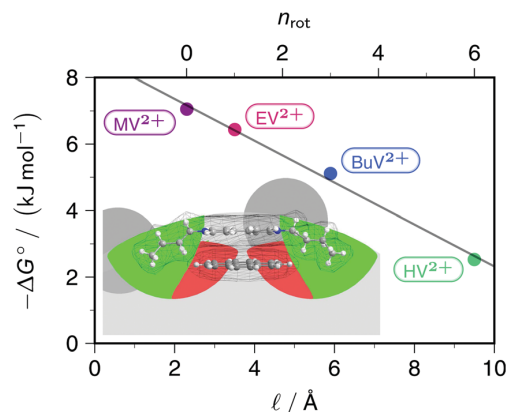


Fig. 7 Entropy-controlled complex formation of aliphatically substituted viologens RV^{2+} with pyrene in the ground state. Main plot, dependence of the free energy ΔG° of the association equilibrium on the length ℓ or the number of rotors n_{rot} of the viologen sidechains (lower or upper horizontal scale, connected through $\ell/\text{\AA} = 1.2 \times n_{\text{rot}} + 2.3$). Abbreviations and colour code of the viologens as in Fig. 1. Regression line given by $(-8.6 + 0.63/\text{\AA}) \text{ kJ mol}^{-1}$. Inset, isometric stick-and-ball representation of the complex with BuV^{2+} in an SDS micelle (headgroups and interior, dark and light gray); stacking distance, 3.7 \AA . The grids represent the total charge density surfaces obtained from extended Hückel calculations, *i.e.*, the van der Waals surfaces. The green areas (volumes) are accessible to the sidechains, the red ones are exclusion zones. For further explanation, see text.

each sidechain, the viologen skeleton is rigid; and the distance between these atoms is practically identical to the equatorial diameter of pyrene. In a stacked arrangement of the aromatic systems with touching van der Waals surfaces, a bending back of the sidechains is thus progressively inhibited the longer they are or, by the same token, the greater the number of added rotors is. The green and red areas of the inset, which has been drawn to scale, depict the accessible and forbidden spaces in the case of BuV^{2+} . Compared to homogeneous solution, these side chains are also barred from moving into the region facing away from the pyrene. However, the associated entropy effects cancel because they are the same for the viologen not contained in a complex.

The main plot of Fig. 7 demonstrates the good linear correlation between the number of rotors in the side chain and the free energy of complex formation as calculated from K' in Fig. 6. Such linear relationships are well documented for other homologous series featuring bimolecular interactions, and have been interpreted by a constant entropic cost per restricted rotor, which depends on the packing details and reaches 5 – 6 kJ mol^{-1} at room temperature for a completely frozen rotor.⁴³ Considering the two identical sidechains of the viologens, the entropic penalty per rotor in our case amounts to less than a tenth of that value, which is in keeping with unrestricted motion outside a size-dependent forbidden region.

4 Conclusions

The detailed mathematical analyses of this work have not only proved existing models of combined static and dynamic

intracellular quenching to be erroneous but also identified a number of important guidelines for the meaningful application of the correct model derived herein.

1. The luminescence in stationary Stern–Volmer experiments should never be used as the only observable because correlations among the key parameters (the quenching rate constant k , the equilibrium constant of ground-state complexation K , and the apparent aggregation number N_{agg}) are so pronounced as to render best-fit results highly unreliable.

Although the present work has only explored this for micellar systems, we expect that the interdependence of k and K constitutes a similar issue in homogeneous solution.

2. The described problem can be solved either by observing stationary emission in parallel with stationary absorption or by time-resolved emission measurements. Each approach reliably eliminates the parameter correlations. The former can be performed with the simplest instrumentation but requires that the absorption spectrum changes upon complex formation; the latter necessitates more advanced equipment but allows separating the quenching processes almost by visual inspection of the decay traces, and provides a direct access to N_{agg} .

3. The formation of ground-state complexes modifies the distribution of the guest molecules. In consequence, the observed N_{agg} equals the product of the true aggregation number of the surfactant with a linear function of the equilibrium constant.

This leads to apparent paradoxes, namely, values of N_{agg} that seem much too high and depend on the nature of the quencher. To the best of our knowledge, this work is the first report of such phenomena and their explanation.

The elimination of mathematical and conceptual errors as well as of issues pertaining to uniqueness of the fit parameters has paved the way for reliably quantifying steric influences in our test systems. Clear evidence that these reactions are entropy controlled follows from a linear relationship between the free energy of complexation and the number of rotors in the side-chains. As we envisage, the results of this work provide a starting point for investigating intracellular complexation in much more detail than hitherto.

Conflicts of interest

There are no conflicts to declare.

References

- V. P. Torchilin, *Pharm. Res.*, 2007, **24**, 1–16.
- D. V. Tulumello and Ch. M. Deber, *Biochemistry*, 2009, **48**, 12096–12103.
- D. M. Vriezema, M. C. Aragonès, J. A. A. W. Elemans, J. J. L. M. Cornelissen, A. E. Rowan and R. J. M. Nolte, *Chem. Rev.*, 2005, **105**, 1445–1489.
- M. H. Gehlen and F. C. De Schryver, *Chem. Rev.*, 1993, **93**, 199–221.
- G. B. Behera, B. K. Mishra, P. K. Behera and M. Panda, *Adv. Colloid Interface Sci.*, 1999, **82**, 1–42.
- I. Capek, *Adv. Colloid Interface Sci.*, 2002, **97**, 91–149.
- F. H. Quina and E. A. Lissi, *Acc. Chem. Res.*, 2004, **37**, 703–710.
- B. D. Wagner, *Molecules*, 2009, **14**, 210–237.
- P. P. Infelta, M. Grätzel and J. K. Thomas, *J. Phys. Chem.*, 1974, **78**, 190–195.
- M. Tachiya, *Chem. Phys. Lett.*, 1975, **33**, 289–292.
- N. Boens and M. van der Auweraer, *ChemPhysChem*, 2005, **6**, 2352–2358.
- H.-J. Timpe, G. Israel, H. G. O. Becker, I. R. Gould and N. J. Turro, *Chem. Phys. Lett.*, 1983, **99**, 275–280.
- C. N. Lunardi, J. B. S. Bonilha and A. C. Tedesco, *J. Lumin.*, 2002, **99**, 61–71.
- C. Tablet, I. Matei and M. Hillebrand, *J. Mol. Liq.*, 2011, **160**, 57–62.
- A. R. Soemo and J. E. Pemberton, *J. Fluoresc.*, 2014, **24**, 295–299.
- M. H. Gehlen and F. C. De Schryver, *J. Phys. Chem.*, 1993, **97**, 11242–11248.
- T. Kohlmann, R. Naumann, C. Kerzig and M. Goetz, *Phys. Chem. Chem. Phys.*, 2017, **19**, 8735–8741.
- D. Wang, J. Wang, D. Moses, G. C. Bazan and A. J. Heeger, *Langmuir*, 2001, **17**, 1262–1266.
- C.-Q. Jiang, M.-X. Gao and J.-X. He, *Anal. Chim. Acta*, 2002, **452**, 185–189.
- K. Campbell, A. Zappas, U. Bunz, Y. S. Thio and D. G. Bucknall, *J. Photochem. Photobiol., A*, 2012, **249**, 41–46.
- Y.-J. Hu, Y. Liu, L.-X. Zhang, R.-M. Zhao and S.-S. Qu, *J. Mol. Struct.*, 2005, **750**, 174–178.
- S. Doose, H. Neuweiler and M. Sauer, *ChemPhysChem*, 2009, **10**, 1389–1398.
- C. B. Murphy, Y. Zhang, T. Troxler, V. Ferry, J. J. Martin and W. E. Jones, *J. Phys. Chem. B*, 2004, **108**, 1537–1543.
- M. K. Johansson and R. M. Cook, *Chem. – Eur. J.*, 2003, **9**, 3466–3471.
- T. Hirano, J. Akiyama, S. Mori and H. Kagechika, *Org. Biomol. Chem.*, 2010, **8**, 5568–5575.
- T. Kohlmann, R. Naumann, C. Kerzig and M. Goetz, *Photochem. Photobiol. Sci.*, 2017, **16**, 185–192.
- J. Sangster, *J. Phys. Chem. Ref. Data*, 1989, **18**, 1111–1227.
- M. A. J. Rodgers and M. F. Da Silva E Wheeler, *Chem. Phys. Lett.*, 1978, **53**, 165–169.
- M. Almgren, F. Grieser and J. K. Thomas, *J. Am. Chem. Soc.*, 1979, **101**, 279–291.
- S. G. Bertolotti, J. J. Cosa, H. E. Gsponer, M. Hamity and C. M. Previtali, *Can. J. Chem.*, 1986, **64**, 845–848.
- J. R. Lakowicz, *Principles of Fluorescence Spectroscopy*, Springer, New York, 3rd edn, 2006.
- F. M. Martens and J. W. Verhoeven, *J. Phys. Chem.*, 1981, **85**, 1773–1777.
- D. Fornasiero and F. Grieser, *J. Chem. Soc., Faraday Trans.*, 1990, **86**, 2955–2960.
- NIST Handbook of Mathematical Functions*, ed. F. W. J. Olver, Cambridge University Press, New York, 2010.

[View Article Online](#)

PCCP

Paper

- 35 A. Malliaris, J. Le Moigne, J. Sturm and R. Zana, *J. Phys. Chem.*, 1985, **89**, 2709–2713.
- 36 M. Kumbhakar, S. Nath, T. Mukherjee and H. Pal, *J. Chem. Phys.*, 2005, **122**, 084512.
- 37 M. Montalti, A. Credi, L. Prodi and M. T. Gandolfi, *Handbook of Photochemistry*, Taylor and Francis, Boca Raton, 3rd edn, 2006.
- 38 R. Ranganathan, C. Vautier-Giongo and B. L. Bales, *J. Phys. Chem. B*, 2003, **107**, 10312–10318.
- 39 B. Hammouda, *J. Res. Natl. Inst. Stand. Technol.*, 2013, **118**, 151–167.
- 40 M. S. Matos and M. H. Gehlen, *Spectrochim. Acta, Part A*, 1998, **54**, 1857–1867.
- 41 R. Rathore, S. V. Lindeman and J. K. Kochi, *J. Am. Chem. Soc.*, 1997, **119**, 9393–9404.
- 42 N. J. Turro and P. L. Kuo, *Langmuir*, 1985, **1**, 170–172.
- 43 M. S. Searle and D. H. Williams, *J. Am. Chem. Soc.*, 1992, **114**, 10690–10697.

7.2 Publikation B

Photochemical & Photobiological Sciences



PAPER

View Article Online

View Journal | View Issue



Cite this: *Photochem. Photobiol. Sci.*, 2020, **19**, 71

Pyrene–viologen complexes in SDS micelles: quenching parameters and use as probes of aggregation numbers

Tim Kohlmann and Martin Goez *

Through a formal-kinetic treatment, we rigorously derive the micellar occupations in the presence of fluorophore–quencher ground-state complexes and the resulting expressions for the time-dependent and stationary observables in the case of combined static and dynamic quenching. We present a protocol for data analysis that effectively isolates the processes, thereby ensuring rapid fit convergence and unique parameter sets. By this approach, we interpret time-resolved fluorescence measurements on pyrene quenched by a homologous series of viologens in SDS micelles. The dynamic intramicellar quenching is diffusion limited; and the formation of the ground-state complexes is entropy driven, with a constant increment per methylene group in the viologen sidechains. The micellar aggregation numbers are obtained with a precision comparable to neutron scattering, including their temperature dependence.

Received 9th November 2019,
Accepted 10th December 2019

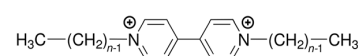
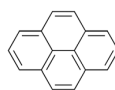
DOI: 10.1039/c9pp00439d

rsc.li/pps

1. Introduction

Quenching processes in micelles are fascinating phenomena,^{1–5} not least because such microreactors are the simplest model membranes.^{6–9} In the first place, the confined space increases the efficiency, most noticeably that of the static quenching, through orientational effects and easily attainable high local concentrations;^{10–12} and what can be learned about the ground-state complexes from the static quenching is often much more diverse^{13–17} than the insight provided by the dynamic quenching, which is frequently diffusion controlled and thus independent of the fluorophore–quencher combination. Second, the solubilizates are useful probes of the microenvironment, for instance through their response to the local polarity;¹⁸ or, as a benefit of the otherwise less revealing diffusion-limited quenching, to the microviscosity.¹⁹ Third, the distribution of the guest molecules can yield valuable information on a key property of the micelles, namely, their aggregation number N_{agg} .^{20–28}

Over and above our interest in the quenching parameters and their structure–activity relationships, the sometimes conspicuous differences between N_{agg} obtained with different fluorophore–quencher pairs for the same micelles and otherwise identical conditions prompted us to look into the source of these discrepancies. We surmised that a ground-state complexation would bias the Poisson distributions of fluorophore



Scheme 1 Structural formulas of the fluorophore pyrene (left) and the quenchers alkyviologens (right), where n is the number of carbon atoms in the aliphatic sidechains.

and quencher such as to lead to apparent deviations of N_{agg} . We present a rigorous theoretical treatment that takes into account that effect, and we complement this by a temperature-dependent study on quenching the same fluorophore (pyrene) by a homologous series of quenchers (viologens). For the structural formulas of these compounds, see Scheme 1.

On the basis of a data-analysis procedure that minimizes parameter interdependence, two-fold verification of the theory is provided by comparing, first, the quenchers among themselves, which yield the same N_{agg} at given temperature despite significantly different ground-state complexation; and second, our experimental results with those obtained by a completely independent, non-photochemical method (neutron scattering),²⁹ where our approach will be seen to reproduce the reported N_{agg} throughout the temperature range investigated.

2. Experimental

1,1'-Dipropyl-4,4'-bipyridinium dibromide and 1,1'-dibutyl-4,4'-bipyridinium dibromide were synthesized by refluxing 4,4'

Martin-Luther-Universität Halle-Wittenberg, Institut für Chemie, Kurt-Mothes-Str. 2, D-06120 Halle, Saale, Germany. E-mail: martin.goez@chemie.uni-halle.de

Paper

Photochemical & Photobiological Sciences

bipyridine with three times the molar amount of the respective alkyl bromide in acetonitrile for 72 h. Workup included cooling, filtering, washing the precipitate twice with smaller amounts of acetonitrile, and drying. The procedures were not optimized for maximum yields. All other viologens, pyrene, and SDS were used as received.

To ensure reliable absolute concentrations of the quenchers, the water content of all viologens was measured thermogravimetrically and taken into account when preparing the solutions. Ultrapure Millipore Milli-Q water (specific resistance, 18.2 MΩ cm⁻¹) was used as the solvent, and oxygen was excluded by purging the solutions with argon 5.0 prior to sealing the cuvettes.

At the excitation wavelength (341 nm) the viologens are transparent. By employing a sufficiently low pyrene concentration (10 μM), we kept the solutions optically thin, such that filter effects were absent. The SDS weight-in concentration was 50 mM throughout.

Stationary and time-resolved emission was measured with a PerkinElmer LS 50B spectrometer and with an Edinburgh Instruments FS5 time-correlated single-photon counting spectrometer (excitation source, EPLED-340; 341 nm, 0.8 ns FWHM). Both spectrometers were equipped with thermostated cell holders. Pulse pileup in the time-resolved experiments was safely avoided by setting the interpulse delay to 5 μs, which is significantly longer than ten times the unquenched lifetime of excited pyrene.

3. Results and discussion

3.1. Theory

Herein, we adapt and extend Moroi's treatment³⁰ to derive the micellar occupations through formal kinetics in section 3.1.1. On their basis, we then obtain the functions describing the time dependence and Stern–Volmer relationship of the luminescence (section 3.1.2). We abbreviate the fluorophore as F, the quencher as Q, and the complex between the two as FQ.

3.1.1. Micellar occupations. We first partition the micelles into classes according to the number of guest molecules F, Q, and FQ they contain, for which we use the integer variables i , j , and n . Any class $\mathcal{M}_{i,j,n}$ is thus uniquely specified by its triple index, and the calligraphic symbol \mathcal{M} shall indicate this kind of partitioning, as opposed to the one in the final parts of this section.

According to the principle of detailed balancing, at overall chemical equilibrium each sub-equilibrium is also established separately. There are five sub-equilibria: three for the solubilization processes (*i.e.*, of F, Q, and FQ), and two for the formation of ground-state complexes FQ (*i.e.*, in the aqueous bulk and in the micelles).

The solubilizations of F, Q, and FQ are each described by an entry from the aqueous phase into the micelles with an occupation-independent rate constant, *e.g.*, $k_{F,in}$,

and an exit with an occupation-proportional rate constant, *e.g.*, $i \times k_{F,ex}$; and we abbreviate the solubilization-specific ratios $k_{X,in}/k_{X,ex}$ as K_X . With the concentration $[X]$ of the solubilization in the aqueous phase, the solubilization equilibria are thus

$$[\mathcal{M}_{i,j,n}] = [\mathcal{M}_{i-1,j,n}] \frac{K_F[F]}{i} = [\mathcal{M}_{0,j,n}] \frac{(K_F[F])^i}{i!} \quad (1a)$$

$$[\mathcal{M}_{i,j,n}] = [\mathcal{M}_{i,j,n-1}] \frac{K_Q[Q]}{j} = [\mathcal{M}_{i,0,n}] \frac{(K_Q[Q])^j}{j!} \quad (1b)$$

$$[\mathcal{M}_{i,j,n}] = [\mathcal{M}_{i,j,n-1}] \frac{K_{FQ}[FQ]}{n} = [\mathcal{M}_{i,j,0}] \frac{(K_{FQ}[FQ])^n}{n!} \quad (1c)$$

where the rightmost expressions are obtained by repeated application of the preceding recursions.

The association equilibrium of F and Q to give ground-state complexes FQ is specified in the usual way for the homogeneous phase, whereas that inside the micelles is formulated for the micellar carriers

$$[FQ] = K_{aq}[F][Q] \quad (2a)$$

$$[\mathcal{M}_{i-1,j-1,n}] = [\mathcal{M}_{i,j,n-1}] \frac{j}{n} K_{mic} \quad (2b)$$

The coupling of n with i and j in eqn (2b) is removed when the recursion of eqn (1c) is inserted. After rearrangement and elimination of $[FQ]$ by using eqn (2a), this yields

$$[\mathcal{M}_{i,j,n}] = [\mathcal{M}_{i-1,j-1,n}] \frac{K_{FQ}K_{aq}[F][Q]}{K_{mic}ij} \quad (3)$$

However, the same transformation of $[\mathcal{M}_{i-1,j-1,n}]$ into $[\mathcal{M}_{i,j,n}]$ is also effected by successively applying eqn (1a) and (1b); and a comparison of coefficients thus reveals that K_{FQ} is fully defined by the other equilibrium constants,

$$K_{FQ} = \frac{K_{mic}}{K_{aq}} K_F K_Q \quad (4)$$

Combining eqn (1a)–(1c), in the case of 1(c) after back-substituting eqn (3) and inserting eqn (2a), shows that the formation of ground-state complexes FQ inside and/or outside the micelles results in a coupled Poisson distribution,

$$[\mathcal{M}_{i,j,n}] = [\mathcal{M}_{0,0,0}] \frac{(K_F[F])^i}{i!} \frac{(K_Q[Q])^j}{j!} \frac{(K_F[F]K_Q[Q]K_{mic})^n}{n!} \quad (5)$$

where, by summing over all variables and normalization,

$$[\mathcal{M}_{0,0,0}] = [M]_{tot} \exp\{-(K_F[F] + K_Q[Q] + K_F[F]K_Q[Q]K_{mic})\} \quad (6)$$

with the total concentration of micelles $[M]_{tot}$ which is calculated in the usual way from the surfactant weight-in concen-

tration $[\text{Surf}]_{\text{tot}}$, the critical micelle concentration cmc, and the aggregation number N_{agg} ,

$$[\text{M}]_{\text{tot}} = \frac{[\text{Surf}]_{\text{tot}} - \text{cmc}}{N_{\text{agg}}} \quad (7)$$

Eqn (5) and (6) were already derived for microemulsions under more restrictive conditions (neither formation of FQ in the bulk phase nor transfer of FQ between phases, *i.e.*, omitting eqn (2a) and (1c));³¹ but they are generally valid, as we have shown here.

A reduction to a two-variable representation—based on total intramicellar content of F and Q, regardless of free or complexed as FQ—relies on the 1 : 1 stoichiometry of the complexation and the fact that none of the numbers i, j , and n can become negative. Let the non-calligraphic symbol $M_{r,s}$ denote the micelles with total content r of F and s of Q: obviously, r equals $i + n$ and s equals $j + n$. The connection between representations is

$$\begin{aligned} [M_{r,s}] &= \sum_{n=0}^{\min(i,j)} [\mathcal{M}_{i-n,j-n,n}] \\ &= [\mathcal{M}_{0,0,0}] (K_F[\text{F}])^r (K_Q[\text{Q}])^s \sum_{n=0}^{\min(r,s)} \frac{1}{(r-n)!} \frac{1}{(s-n)!} \frac{K_{\text{mic}}^n}{n!} \\ &= [M_{0,0}] \frac{(K_F[\text{F}])^r}{r!} \frac{(K_Q[\text{Q}])^s}{s!} \sum_{n=0}^r \binom{r}{n} \binom{s}{n} n! K_{\text{mic}}^n \end{aligned} \quad (8)$$

where we have obtained the second line by inserting eqn (5). In the third line, we utilize that the concentrations of empty micelles must be equal in both representations, *i.e.*, $[M_{0,0}] = [\mathcal{M}_{0,0,0}]$; and the binomial coefficients ensure that the minimum condition of the summation limit is respected. This sum in that last line of eqn (8) is a polynomial in K_{mic} , which can be regarded as a function of r (or of s , when the upper limit of the final sum is changed accordingly). Its value is unity for $r = 0$ or $s = 0$, as well as for any value of these variables when $K_{\text{mic}} = 0$.

At given fluorophore content r , the average occupation $\langle q \rangle_r$ of micelles with Q illustrates the enrichment by the formation of the complexes,

$$\begin{aligned} \langle q \rangle_r &= \frac{\sum_{s=0}^{\infty} s [M_{r,s}]}{\sum_{s=0}^{\infty} [M_{r,s}]} \\ &= K_Q[\text{Q}] \left(1 + r \times \frac{K_{\text{mic}}}{1 + K_Q[\text{Q}]K_{\text{mic}}} \right). \end{aligned} \quad (9)$$

The final expression is directly verified for the first values of r , and in general follows from the recursion relationships of binomial coefficients. As it must, eqn (9) turns into the well-known result for noninteracting solubilizes when $K_{\text{mic}} = 0$ or for $r = 0$, and the analogous equation for the occupation with F is straightforward.

$$\langle f \rangle_0 = K_Q[\text{Q}] \quad (10a)$$

$$\langle f \rangle_0 = K_F[\text{F}] \quad (10b)$$

As usual for strongly hydrophobic species, $\langle f \rangle_0$ and $\langle q \rangle_0$ can be identified with the weight-in concentrations divided by $[M]_{\text{tot}}$ (eqn (7)). We stress that the concentrations in the bulk phase are only dependent on the total composition of the system; therefore, $\langle f \rangle_0$ and $\langle q \rangle_0$ remain valid replacements of $K_F[\text{F}]$ and $K_Q[\text{Q}]$ for any sub-ensemble with $r \neq 0$ as well.

With the preceding results, the concentration of micelles with given number of fluorophore molecules, $[M_r]$, can be expressed as

$$\begin{aligned} [M_r] &= \sum_{s=0}^{\infty} [M_{r,s}] \\ &= [M_{0,0}] \frac{\langle f \rangle_0^r}{r!} \sum_{s=0}^{\infty} \frac{\langle q \rangle_0^s}{s!} \sum_{n=0}^r \binom{r}{n} \binom{s}{n} n! K_{\text{mic}}^n \\ &= \exp(-\langle f \rangle_0 (1 + \langle q \rangle_0 K_{\text{mic}})) \frac{(\langle f \rangle_0 (1 + \langle q \rangle_0 K_{\text{mic}}))^r}{r!} [M]_{\text{tot}} \end{aligned} \quad (11)$$

which not only proves the Poisson distribution of F despite the interaction with Q, but also shows rigorously that the effect is an the apparent increase of the weight-in concentration of F by a constant factor, *i.e.*, a scaling of the Poisson parameter.

This scaled Poisson distribution thus allows estimates in the same way as when the fluorophore is the sole solubilize: by choosing $\langle f \rangle_0$ sufficiently small one can render negligible the concentration of micelles hosting more than one such molecule. The ratio of their summed concentrations to the concentration of singly occupied micelles,

$$\frac{\sum_{r=2}^{\infty} [M_r]}{[M_1]} = \frac{\exp(+\langle f \rangle_0 (1 + \langle q \rangle_0 K_{\text{mic}})) - 1}{\langle f \rangle_0 (1 + \langle q \rangle_0 K_{\text{mic}})} - 1 \quad (12)$$

is lower than 0.036 in the worst case under the conditions of this work, which are $\langle f \rangle_0 \leq 0.02$, $\langle q \rangle_0 \leq 1.5$, $K_{\text{mic}} \leq 1.7$.

On the above premises that the highly hydrophobic F resides practically exclusively in the micelles and that more than one F per micelle is very unlikely, the fluorophore weight-in concentration $[F]_{\text{tot}}$ must equal the sum of all the $[M_{1,s}]$. Hence, the quencher occupations within that sub-ensemble are given by

$$\frac{[M_{1,s}]}{[F]_{\text{tot}}} = \frac{[M_{1,s}]}{[M_1]} = \frac{\exp(-\langle q \rangle_0) \langle q \rangle_0^s}{1 + \langle q \rangle_0 K_{\text{mic}} s!} (1 + s K_{\text{mic}}) \quad (13)$$

where we have used eqn (8) together with eqn (6) for the numerator, and eqn (11) for the denominator. The cancellation of terms containing $\langle f \rangle_0$ in the result also rationalizes our experimental observation that a variation of the fluorophore weight-in concentration has no effect on the extracted luminescence parameters despite its influence on the formation of FQ.

Up to and including eqn (12), the results of this section are of complete generality; and eqn (12) provides the means to establish whether the simplifying condition of eqn (13) is met (or, by which modifications it can be reached). The next

Paper

Photochemical & Photobiological Sciences

section will thus derive the formulas for the observables on the basis of eqn (13).

3.1.2. Time-resolved and stationary observables. The treatment of this section further presupposes that neither fluorophore nor quencher enter or leave a micelle during the radiative life, which holds true for pyrene/viologen systems as used in this work, because the former compound is localized near-exclusively within the micelles owing to its hydrophobicity, and the latter is so strongly bound to the micellar surface by the attractive coulombic interactions as to render negligible its concentration in the aqueous phase.²⁸

Only those micelles that contain uncomplexed F fluoresce; and their fraction is obtained by dividing the distribution by $(1 + K_{\text{mic}}s)$, which cancels the identical term in the numerator of eqn (13). The luminescence from these FQ-free micellar sub-ensembles hosting s quencher molecules decays according to $\exp[-(1/\tau_0 + k_q s)t]$, where τ_0 is the unquenched lifetime and k_q is the (apparent first-order) rate constant for a micelle containing a single available Q; and the integrated decay from them is $\tau_0(1 + k_q \tau_0 s)$. Assembling the expressions and carrying out the summations yields eqn (14) for the decay trace $I_{\text{rel}}(t)$,

$$\begin{aligned} I_{\text{rel}}(t) &= \sum_{s=0}^{\infty} \frac{[M_{1,s}]}{[F]_{\text{tot}}} \frac{1}{1 + K_{\text{mic}}s} \exp[-(1/\tau_0 + k_q s)t] \\ &= \exp(-t/\tau_0) \times \frac{\exp(-\langle q \rangle_0)}{1 + \langle q \rangle_0 K_{\text{mic}}} \\ &\quad \times \exp(\langle q \rangle_0 \exp(-k_q t)) \end{aligned} \quad (14)$$

and eqn (15) for the Stern–Volmer observable I_0/I ,

$$\begin{aligned} \frac{I_0}{I} &= \tau_0 \left(\sum_{s=0}^{\infty} \frac{[M_{1,s}]}{[F]_{\text{tot}}} \frac{1}{1 + K_{\text{mic}}s} \frac{\tau_0}{1 + k_q \tau_0 s} \right)^{-1} \\ &= \frac{1 + \langle q \rangle_0 K_{\text{mic}}}{\exp(-\langle q \rangle_0)} \\ &\quad \times \frac{k_q \tau_0}{(-\langle q \rangle_0)^{-1/(k_q \tau_0)} \cdot \gamma(1/(k_q \tau_0), -\langle q \rangle_0)}. \end{aligned} \quad (15)$$

The lower incomplete Gamma function in eqn (15),

$$\gamma(a, z) = \int_0^z \zeta^{a-1} \exp(-\zeta) d\zeta \quad (16)$$

takes on complex values for negative z and positive a , but these become real values again upon multiplication with z^{-a} , as in eqn (15). The libraries of all major programming languages contain efficient implementations of $\gamma(a, z)$.³²

Eqn (14) and (15) (represented as a Poisson weighted series) were already obtained in the literature by Gehlen and De Schryver by using a stochastic approach.²⁵ Our above treatment based on the formal kinetic model leads to the same final result but involves concepts more familiar to chemists. In two previous publications,^{28,33} we similarly attempted to take the complexation into account by suitably weighting $\langle q \rangle_0$ for a Poisson distribution of noninteracting guest molecules. However, through eqn (7) this suggests a dependence of the apparent micellar aggregation number on K_{mic} , which is a non-

physical artifact; hence, the method of the present work is to be preferred.

3.2. Parameter extraction

The photochemically relevant parameters obtainable by fitting eqn (14) and (15) to the corresponding data are the unquenched lifetime τ_0 of the excited fluorophore; the equilibrium constant K_{mic} pertaining to the formation of ground-state complexes inside the micelles, which causes the static quenching; and the rate constant k_q for the dynamic intramicellar quenching. Because τ_0 of pyrene is long (on the order of 350 ns), conditions can easily be chosen such that no deconvolution or iterative reconvolution is necessary to correct for the finite response time of the spectrometer. Our description of micellar compartmentalization in terms of numbers rather than concentrations of host molecules per micelle causes K_{mic} to be dimensionless and k_q to be an apparent first-order rate constant.

The additional variable in the time-resolved experiments and the single variable in the stationary experiments is the average number $\langle q \rangle_0$ of quencher molecules per (otherwise empty) micelle. Its calculation from the weight-in concentrations and the surfactant properties cmc and N_{agg} by using eqn (7) is standard. Whereas cmc is easily and reliably obtainable by photochemical methods,¹⁸ precise determinations of N_{agg} typically require small-angle neutron scattering.²⁹ However, when N_{agg} is unknown, the procedure of this section allows extracting it from the measurements through the proportionality between the quencher weight-in concentration and $\langle q \rangle_0$ without the fit problems we identified in an earlier publication.²⁸

Fig. 1a displays the outcome of time-resolved and, as the inset, stationary Stern–Volmer experiments with ethylviologen as the quencher of excited pyrene. The termination criteria of time-correlated photon-counting spectrometers, such as number of counts in the maximum channel or in total, or overall acquisition time, do not allow comparisons of curve heights between samples. As a remedy, we recorded the luminescences over times long enough for complete decay in all cases, summed the counts in all channels after the rise, and used the stationary Stern–Volmer data for appropriate scaling. This correction has already been applied in Fig. 1a.

Direct fits to the pertaining data exhibit sluggish convergence for eqn (14); and they are ill conditioned as well as unreliable with respect to parameter uniqueness for eqn (15). The situation can be improved by simultaneous fits to the data of both experiment types, but more is gained by separating the time-resolved data into different time domains, thereby effectively isolating the parameter influences. Taking the logarithm of each decay (Fig. 1b) reveals the clear trisection even to the naked eye: the static quenching is instantaneous and causes the curves to start from different initial heights; the dynamic quenching adds a fast component to the decay, which has come to a close after some 100 ns, as indicated by the shaded area of the figure; and afterwards the excited fluorophores in micelles devoid of quencher molecules exhibit their natural

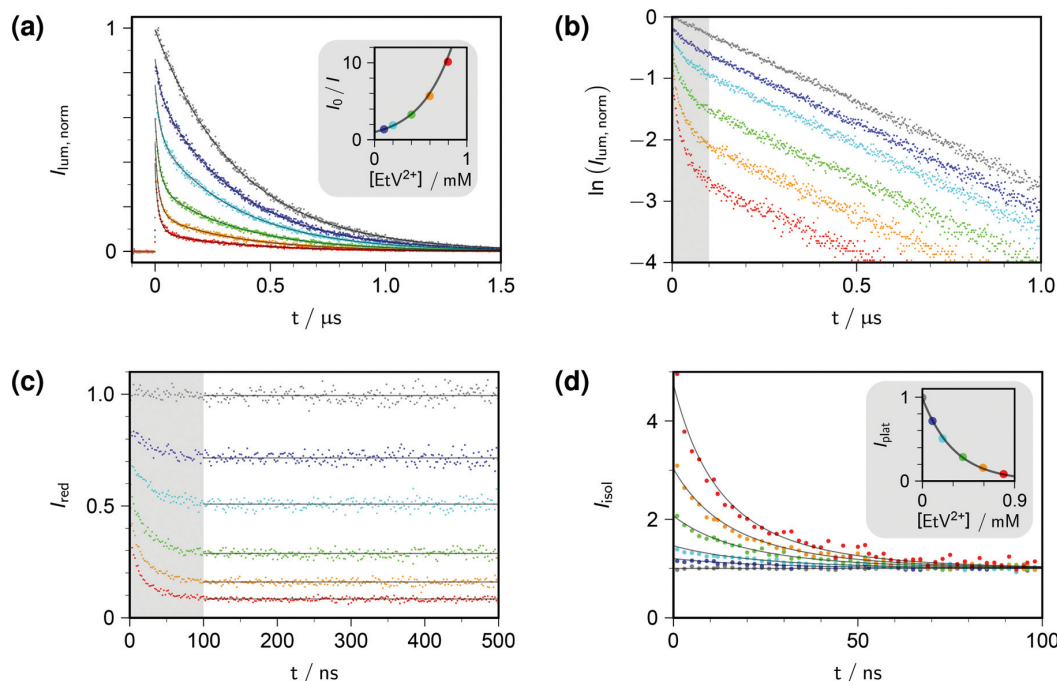


Fig. 1 Procedure for determining the quenching parameters. Experimental conditions, 10 μM pyrene and variable concentrations of ethylviologen EtV^{2+} (colour coded; gray, 0 mM; violet, 0.099 mM; cyan, 0.198 mM; green, 0.396 mM; orange, 0.594 mM; red, 0.792 mM) in 50 mM aqueous SDS at 283 K; excitation, 341 nm; detection, 395 nm. Graph (a), time-resolved fluorescence decays (main plot) normalized by using the stationary Stern–Volmer measurement shown as the inset; overlaid fit functions calculated by eqn (14) and (15) with the parameters isolated from plots (b)–(d). Graph (b), log–lin plot of the time-resolved data with the time regime of intracellular quenching overlaid with gray; extractable parameter, τ_0 . Graph (c), decays after removing the natural decay by multiplication with $\exp(+t/\tau_0)$; plateau values only depend on $\langle q \rangle_0$, with K_{mic} as concentration-independent parameter. Graph (d), separation of second factor (inset) and third factor (main plot) of eqn (14); overlaid curves, global fit with common fit parameter $\langle q \rangle_0/[\text{EtV}^{2+}]$ yielding N_{agg} , as well as local fit parameters K_{mic} (inset) and k_q (main plot). Extracted values: τ_0 , 360 ns; N_{agg} , 77 (based on $\text{cmc} = 8.6$ mM, from eqn (17)); K_{mic} , 0.92; k_q , 3.7×10^7 s $^{-1}$. Further explanation, see text.

decay, which manifests itself by parallel curves in the log–lin plot of Fig. 1b, corresponding to the subexpression $\exp(-t/\tau_0)$ of eqn (14).

Evidently, τ_0 occurs only in this leading term describing the long-time behaviour. Not only can τ_0 thus be extracted from the later portions of the decays, but a multiplication with $\exp(+t/\tau_0)$ removes its contribution entirely, as if the probe had an infinite lifetime. This multiplication is tantamount to back extrapolation over a time shorter than one third of τ_0 in our case, hence introduces a negligible uncertainty only. Fig. 1c illustrates that this transformation causes each curve to reach a constant floor after 100 ns; and, because the limiting long-time value of the third factor in eqn (14) is unity, that constant floor is given by the central fraction. We point out that a multiplication of the Stern–Volmer observable I_0/I with that term would reduce eqn (15) to the trailing fraction, thereby removing the issues with parameter uniqueness, although we shall not use this feature herein.

Fig. 1d contains the result of this separation procedure: the main plot and the inset display the isolated time dependence of the dynamic quenching process and the isolated concen-

tration dependence of the fraction of empty micelles, corresponding to the third and the second factor of eqn (14). For SDS in the temperature interval of this work, the temperature dependence of the cmc is given by³⁴

$$\text{cmc}(T) = 8.2 \text{ mM} \exp \left[-37.05 \left(1 - \frac{T}{298.15 \text{ K}} + \ln \frac{T}{298.15 \text{ K}} \right) \right]. \quad (17)$$

A simultaneous fit of the pertaining elements of eqn (14), in conjunction with eqn (7) and (17), to the main plot and inset of Fig. 1d not only converges rapidly but also yields a unique set of the parameters K_{mic} and k_q characterizing the quenching processes, as well as N_{agg} characterizing the micellar aggregates. Obviously, determining N_{agg} on the basis of the simple expression $\exp(-\langle q \rangle_0)$ instead of the second factor of eqn (14) would introduce a cross correlation with K_{mic} such that the apparent N_{agg} becomes a rising linear function of K_{mic} ; and at larger K_{mic} , this error would also reveal itself by systematic deviations in plots of the plateau value against the quencher concentration as in the inset of Fig. 1d.

The extremely good representation of all curves of Fig. 1d by our global fit speaks for itself; and success of our approach is borne out by the fact that the parameter set so obtained perfectly represents also the stationary Stern–Volmer experiments (see, the overlaid fit curves in the inset of Fig. 1a, which are not fits but were calculated with eqn (15) on the basis of the parameters extracted from the time-resolved experiments).

3.3. Parameter analysis

The fluorescence decays thus yield not only the dynamic and static quenching constants k_q and K_{mic} but also the micellar aggregation number N_{agg} , all as functions of the temperature. It is advantageous to begin with the discussion of N_{agg} , because this quantity determines the intramicellar volume, which is in turn necessary for obtaining the correct activation parameters from k_q and the correct thermodynamic parameters of the ground-state complexes from K_{mic} .

Fig. 2a juxtaposes the results of this work and those of an experimentally much more specialized neutron-scattering study²⁹ on the aggregation behaviour of SDS. At given surfactant weight-in concentration, N_{agg} can be represented by a decreasing linear function of temperature. Both slope and intercept depend only weakly on the SDS concentration such that an interpolation is expected to afford a reliable estimate for our conditions (50 mM). For the interpolation formula, which exactly reproduces the linear best fits to the literature data, see the figure caption.

The substituents on the quencher should not influence the observed N_{agg} ; and when the theory and procedure of sections 3.1–3.2 are used for extracting the parameters, this is indeed

found to hold true. Error bars on N_{agg} in this work were obtained from the randomly distributed differences between the results with our five quenchers, and their magnitudes are seen to be of comparable with those reported for the scattering experiments. Furthermore, the best-fit straight line to the data herein is exactly parallel to that of the interpolated literature data. The only discrepancy, a vertical displacement by 2 units, may well be due to an isotope effect, because the scattering experiments have to be carried out in deuterated water. Our fluorescence method thus compares well with the neutron-scattering approach. Especially appealing from a practical perspective is the fact that it does not need such sophisticated instrumentation: a commercially available time-resolved luminescence spectrometer suffices, which most photochemically orientated groups will possess or have access to.

In striking contrast to the good agreement between N_{agg} obtained by these two independent methods, the apparent N_{agg} extracted from luminescence experiments on the basis of the expected fraction $\exp(-q)_0$ of quencher-free micelles cover a wide range; and for otherwise comparable conditions, reported values with pyrene as the fluorophore are strongly quencher dependent (30, cetylpyridinium chloride;²⁷ 73, *m*-dicyanobenzene;²³ 122, methylviologen²⁸). This is not surprising because the underlying expression is incorrect when there are ground-state complexes between fluorophore and quencher: as shown in section 3.1, it has to be replaced by the second factor of eqn (14).

To transform k_q and K_{mic} to the usual units, a multiplication with the inner volume per one mole of the micelles, $V_{mic}N_A$, is necessary. Fig. 2b addresses that issue by recalculat-

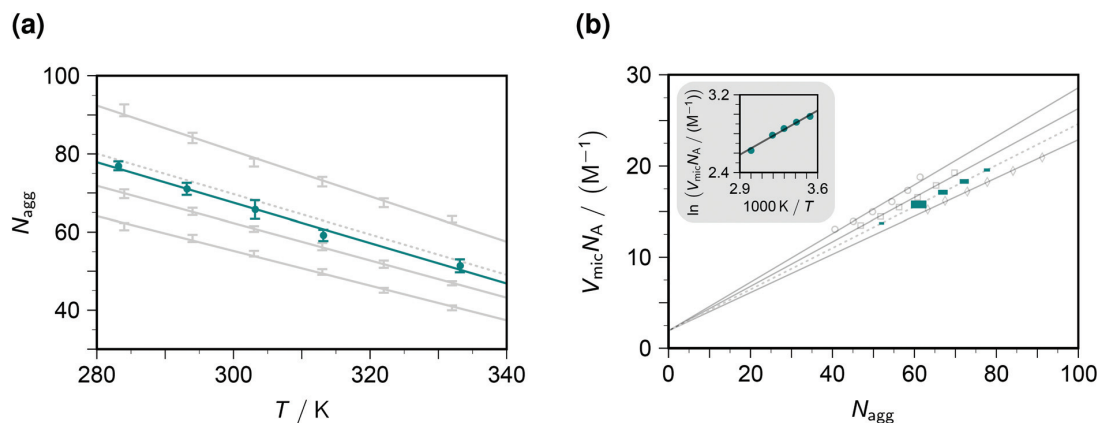


Fig. 2 Influence of the temperature T and the SDS weight-in concentration on the micellar aggregation. Graph (a), aggregation number N_{agg} ; graph (b), accessible molar volume of the micellar microreactors as dependent quantity, with a van 't Hoff type plot as the inset. Gray solid lines and data points, results from the literature²⁹ for 17.4 mM, 34.7 mM, and 69.4 mM SDS (from bottom to top in graph (a), data represented by error bars; and with opposite order in graph (b), data represented by open circles, squares, and diamonds). Gray dotted lines, interpolation results for 50 mM SDS, based on the best-fit relationships $N_{agg} = 177 + 0.523c + 0.00871c^2 - (0.425 + 0.000785c + 0.0000212c^2)T$ and $V_{mic}N_A = 1.92 + (0.293 - 0.00164c + 6.25 \times 10^{-6} c^2)N_{agg}$, where the weight-in concentration c is in mM. Teal, results of this work; graph (a), solid circles with error bars estimated from the distribution of N_{agg} with the five quenchers; graph (b), solid squares of sizes representing the expected error propagation from graph (a). The slope of the regression line in the inset of graph (b) corresponds to a false contribution of 5.4 kJ mol⁻¹ to the activation energy from k_q and to the enthalpy of formation of the ground-state complexes from K_{mic} . For further explanation, see the text.

ing the data of the above-mentioned neutron-scattering study²⁹ accordingly. Not unexpectedly, $V_{\text{mic}}N_{\text{A}}$ is a rising linear function of N_{agg} . Its slope weakly decreases when the weight-in concentration of the anionic surfactant increases, and the fit quality improves significantly when a concentration-independent intercept is included in the fits. We attribute the former effect to the influence of the ionic strength and the latter to a packing nonideality. An interpolation formula as specified in the figure caption again reproduces the literature data extremely well and should thus provide a very good approximation of $V_{\text{mic}}N_{\text{A}}$ for the SDS weight-in concentration herein. In Fig. 2b, the uncertainty of the independent variable N_{agg} propagates to an uncertainty of the dependent variable $V_{\text{mic}}N_{\text{A}}$, which we have indicated by the horizontal and vertical size of each data point on the interpolated line.

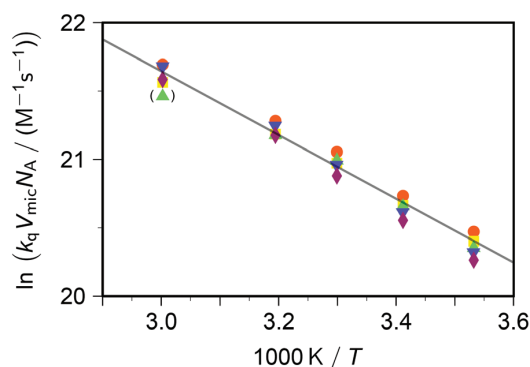


Fig. 3 Arrhenius plot for the dynamic intracellular quenching of excited pyrene by viologens, concentrations as in Fig. 1. Methyl-viologen, red circles; ethylviologen, yellow squares; propylviologen, green triangles; butylviologen, blue inverted triangles; heptylviologen, purple diamonds. The slope of the solid regression line corresponds to an activation energy E_{a} of 19.4 kJ mol⁻¹. The outlier in parentheses was not included in the fit. For further explanation, see the text.

Unfortunately, our observables do not yield any information on $V_{\text{mic}}N_{\text{A}}$; and, therefore, a surfactant less thoroughly investigated than SDS would require an estimation as described in the literature,²⁵ which is usually available for room temperature only. As the inset of Fig. 2b demonstrates, the temperature dependence of $V_{\text{mic}}N_{\text{A}}$ would falsely suggest the activation energy of the dynamic quenching to be too high by about 5 kJ mol⁻¹ if k_{q} were used instead of $k_{\text{q}}V_{\text{mic}}N_{\text{A}}$; and in the same way a too positive enthalpy of formation of the ground-state complexes would be found without transforming K_{mic} accordingly.

Taking into account this correction, Fig. 3 addresses the temperature dependence of $k_{\text{q}}V_{\text{mic}}N_{\text{A}}$ for all five quenchers in an Arrhenius plot. Owing to the exergonic quenching ($\Delta G_{\text{q}}^{\circ} \approx -1.7$ eV for all our viologens),²⁸ diffusion control is expected. This prediction is confirmed by the facts that at each temperature, the five viologens exhibit very similar rate constants; and that the viologen substituent exerts only a very small modifying effect. Although the general trend of a lower rate constant for longer sidechains is clearly perceived, the differences are too small for meaningful evaluation in view of the measurement uncertainties.

The extracted activation energy E_{a} should thus be that of intracellular diffusion, *i.e.*, of the microviscosity. The Arrhenius plot of Fig. 3, whose parameters we obtained by fitting the underlying nonlinear function to the untransformed data to ensure correct statistical weights, is seen to exhibit good linearity. It yields an activation energy of 19 kJ mol⁻¹, which is one-half of that determined by the self-quenching of 1,3-dipyrenylpropane P3P in SDS micelles (38 kJ mol⁻¹).¹⁹ However, with P3P both the fluorophore and the quencher reside exclusively in the micellar interior, whereas with our systems only the fluorophore occupies that region. Our cationic quenchers are confined to the Stern layer and undergo surface diffusion there. Hence, we ascribe the discrepancy of E_{a} to the changed localizations, and in particular to the reduced diffusional dimensionality this entails.

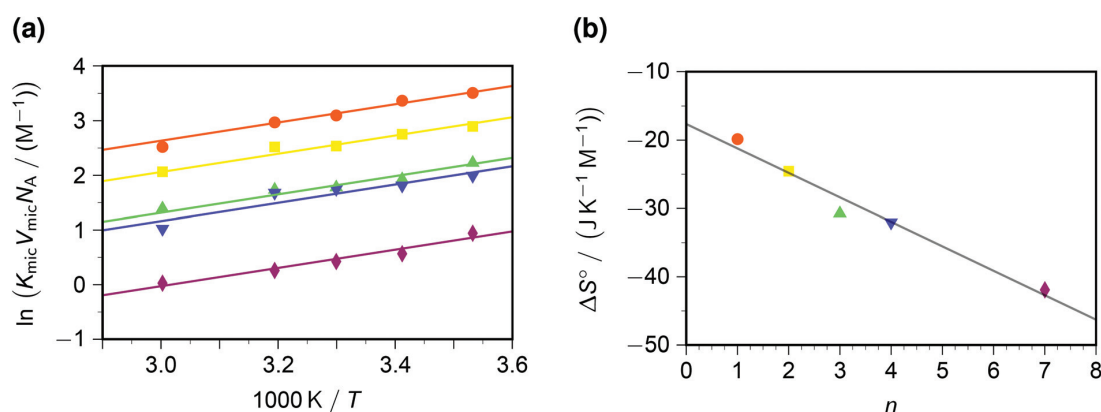


Fig. 4 Static intracellular quenching of excited pyrene by viologens; conditions, colour code and symbols as in Fig. 3. Graph (a), van 't Hoff plot; fits with global standard enthalpy of complex formation (best-fit value, -13.9 kJ mol⁻¹) and quencher-specific standard entropy ΔS° . Graph (b), ΔS° as function of the number n of carbon atoms in the viologen sidechains (compare, Scheme 1). The regression line for ΔS° is $-(17.7 + 3.58n)$ J K⁻¹ mol⁻¹. For further explanation, see the text.

Paper

Photochemical & Photobiological Sciences

In contrast to the dynamic quenching, the static quenching exhibits a pronounced structure-related influence, as Fig. 4a shows. For the same reason as with the Arrhenius analysis of k_q , the van 't Hoff fit of Fig. 4a was performed prior to linearizing the data. The behaviour with all quenchers can be well represented by the same standard enthalpy ΔH° of complex formation, but a substrate-specific standard entropy ΔS° . The rationale behind the quencher-independent enthalpic driving force is again the identical redox potential of the five viologens; and the entropy control can be interpreted by a loss of rotational degrees of freedom of the sidechains in the—in all likelihood, π - π stacked³⁵—ground-state complex.

In a previous study at constant temperature,²⁸ we have already reported a computed model of the complexes and of the associated restriction of the volume accessible to rotation of the sidechains. There, we tried to gauge the volume-based equilibrium constants by comparing the complex of pyrene with that in methanol;³⁶ but herein, knowledge of $V_{\text{mic}}N_A$ allows a renormalization without assumptions. As emerges from Fig. 4b, an entropic penalty of slightly less than $4 \text{ J K}^{-1} \text{ mol}^{-1}$ per CH_2 unit in the sidechains has to be paid, which is about one-fifth the entropic cost of a completely frozen internal rotor.³⁷

4. Conclusions

The rigorously derived theory and the parameter separation procedure of this work have paved the way for a reliable analysis of combined static and dynamic intramolecular quenching. On their basis, our time-resolved and temperature-dependent experiments on excited pyrene quenched by viologens have provided the thermodynamic parameters of the ground-state complexes, as well as the activation energy of the microviscosity and the temperature dependence of the aggregation number N_{agg} of the surfactant SDS.

With respect to N_{agg} , the fluorescence method utilized herein can undoubtedly be employed routinely, as the only equipment it relies on is part of the standard instrumentation of every major photochemical laboratory. If, and only if, the correct theoretical relationships of this report are used for analysis, the extracted aggregation numbers and their uncertainties are essentially the same as those obtained by neutron scattering, which is a much less widely available specialist technique.

As its limitation, the photochemical approach cannot yield the internal molar volume of the micelles $V_{\text{mic}}N_A$, or at best only indirectly, when additional assumptions are included. Our present study was able to input the values of $V_{\text{mic}}N_A$ and their temperature dependence from the literature,²⁹ but in the absence of this information, the apparent activation energy of the dynamic quenching and apparent standard enthalpy of formation of ground-state complexes would deviate from their true values by the same surfactant-specific amount. For the same reason similarly shifted would be the preexponential

factor of the Arrhenius relationship and the absolute values of the standard entropy of complex formation. However, the correct entropy differences are always accessible, which is of interest because the complex formation appears to be entropy-driven.

Conflicts of interest

There are no conflicts of interest to declare.

References

- 1 M. H. Gehlen and F. C. De Schryver, *Chem. Rev.*, 1993, **93**, 199–221.
- 2 G. B. Behera, B. K. Mishra, P. K. Behera and M. Panda, *Adv. Colloid Interface Sci.*, 1999, **82**, 1–42.
- 3 I. Capek, *Adv. Colloid Interface Sci.*, 2002, **97**, 91–149.
- 4 F. H. Quina and E. A. Lissi, *Acc. Chem. Res.*, 2004, **37**, 703–710.
- 5 B. D. Wagner, *Molecules*, 2009, **14**, 210–237.
- 6 R. H. Bisby and A. W. Parker, *Arch. Biochem. Biophys.*, 1995, **317**, 170–178.
- 7 G. Gramlich, J. Zhang and W. M. Nau, *J. Am. Chem. Soc.*, 2002, **124**, 11252–11253.
- 8 G. Gramlich, J. Zhang and W. M. Nau, *J. Am. Chem. Soc.*, 2004, **126**, 5482–5492.
- 9 S. Nagaoka, T. Kakiuchi, K. Ohara and K. Mukai, *Chem. Phys. Lipids*, 2007, **146**, 26–32.
- 10 V. K. Balakrishnan, X. Han, G. W. VanLoon, J. M. Dust, J. Toullec and E. Buncel, *Langmuir*, 2004, **20**, 6586–6593.
- 11 T. Dwars, E. Paetzold and G. Oehme, *Angew. Chem., Int. Ed.*, 2005, **44**, 7174–7199.
- 12 I. Rico-Lattes, E. Perez, S. Franceschi-Messant and A. Lattes, *C. R. Chim.*, 2011, **14**, 700–715.
- 13 D. Wang, J. Wang, D. Moses, G. C. Bazan and A. J. Heeger, *Langmuir*, 2001, **17**, 1262–1266.
- 14 C.-Q. Jiang, M.-X. Gao and J.-X. He, *Anal. Chim. Acta*, 2002, **452**, 185–189.
- 15 K. Campbell, A. Zappas, U. Bunz, Y. S. Thio and D. G. Bucknall, *J. Photochem. Photobiol., A*, 2012, **249**, 41–46.
- 16 Y.-J. Hu, Y. Liu, L.-X. Zhang, R.-M. Zhao and S.-S. Qu, *J. Mol. Struct.*, 2005, **750**, 174–178.
- 17 S. Doose, H. Neuweiler and M. Sauer, *ChemPhysChem*, 2009, **10**, 1389–1398.
- 18 J. R. Lakowicz, *Principles of Fluorescence Spectroscopy*, Springer, New York, 3rd edn, 2006.
- 19 R. Zana, *J. Phys. Chem. B*, 1999, **103**, 9117–9125.
- 20 N. J. Turro and A. Yekta, *J. Am. Chem. Soc.*, 1978, **100**, 5951–5952.
- 21 P. Lianos and R. Zana, *J. Phys. Chem.*, 1980, **84**, 3339–3341.
- 22 J. Löfroth and M. Almgren, *J. Chem. Phys.*, 1982, **76**, 2734–2743.

Photochemical & Photobiological Sciences

Paper

- 23 Y. Croonen, E. Geladé, M. V. D. Zegel, M. V. D. Auweraer, H. Vandendriessche, F. C. D. Schryver and M. Almgren, *J. Phys. Chem.*, 1983, **87**, 1426–1431.
- 24 S. Bhattacharya, H. T. Das and S. P. Moulik, *J. Photochem. Photobiol., A*, 1993, **71**, 257–262.
- 25 M. H. Gehlen and F. C. De Schryver, *J. Phys. Chem.*, 1993, **97**, 11242–11248.
- 26 P. J. Tummino and A. Gafni, *Biophys. J.*, 1993, **64**, 1580–1587.
- 27 M. Pisárčik, F. Devínský and M. Pupák, *Open Chem.*, 2015, **13**, 922–931.
- 28 T. Kohlmann and M. Goetz, *Phys. Chem. Chem. Phys.*, 2019, **21**, 10075–10085.
- 29 B. Hammouda, *J. Res. Natl. Inst. Stand. Technol.*, 2013, **118**, 151–167.
- 30 Y. Moroi, *J. Phys. Chem.*, 1980, **84**, 2186–2190.
- 31 P. P. Infelta, R. Graglia, C. Minero and E. Pelizzetti, *Colloids Surf.*, 1970, **28**, 289–299.
- 32 *NIST Handbook of Mathematical Functions*, ed. F. W. J. Olver, Cambridge University Press, New York, 2010.
- 33 T. Kohlmann, R. Naumann, C. Kerzig and M. Goetz, *Phys. Chem. Chem. Phys.*, 2017, **19**, 8735–8741.
- 34 N. Muller, *Langmuir*, 1993, **9**, 96–100.
- 35 R. Rathore, S. V. Lindeman and J. K. Kochi, *J. Am. Chem. Soc.*, 1997, **119**, 9393–9404.
- 36 M. S. Matos and M. H. Gehlen, *Spectrochim. Acta, Part A*, 1998, **54**, 1857–1867.
- 37 M. S. Searle and D. H. Williams, *J. Am. Chem. Soc.*, 1992, **114**, 10690–10697.

7.3 Publikation C



PCCP

PAPER

[View Article Online](#)[View Journal](#) | [View Issue](#)

Cite this: *Phys. Chem. Chem. Phys.*,
2021, **23**, 9709

Do equilibrium and rate constants of intramicellar reactions depend on micelle size?†

Tim Kohlmann and Martin Goez *

We have studied the combined static and dynamic quenching of pyrene by methyl viologen in sodium alkyl sulfate micelles varying in volume by a factor of more than 4. Size controls were the temperature T (283 K–333 K) and the alkyl chain length n (9–14) as well as, with $n = 12$ only, added NaCl (up to 9 times the surfactant weight-in concentration). At high [NaCl], up to 40% of the viologen resides in the aqueous bulk and quenches dynamically across the micelle–water interface with a rate limited by its diffusion-controlled attachment to the micelle. The micellar aggregation numbers depend linearly both on n and on the difference between T and the Krafft temperature; we have derived interpolation formulas for them as well as for the associated molar volumes of the micelles; the aggregation numbers at the critical micelle concentration are also linear functions of T , and the exponent relating them to the aggregation numbers at other concentrations is temperature independent. At given T , the volume-based quenching rate constants for different n or [NaCl] are very similar, and the same holds true for the equilibrium constants of the static quenching. Arrhenius plots identify the microviscosity inside the micelles as octanol-like; van't Hoff plots give virtually the same reaction enthalpies and entropies as in homogeneous methanolic solution; and the underlying kinetic and thermodynamic parameters are not modified by the micelle size.

Received 27th January 2021,
Accepted 5th April 2021

DOI: 10.1039/d1cp00400j

rsc.li/pccp

1 Introduction

The question asked in the title is of obvious importance for the systematic design and optimization of any synthesis involving micelles as microreactors, an approach continuously gaining in popularity,¹ especially in the field of green chemistry.^{2,3} The micellar confinement boosts the local concentrations of guest molecules through their nonuniform distribution among the micelles, which is well understood,⁴ but does the microheterogeneity of the micelle itself influence thermodynamics and kinetics over and above this concentration effect?

Optical spectroscopy, in particular time-resolved luminescence quenching, is well suited for addressing such issues because it can separate processes by virtue of a well-developed theoretical framework^{4,5} and is sensitive to the surroundings of the reporter molecules.⁶ Dynamic quenching is usually highly exergonic, hence diffusion controlled, and has already been shown to follow the Einstein–Smoluchowski relationship inside micelles surprisingly well.⁷ The situation is much less clear-cut with respect to static quenching through ground-state complexes, where widely

different equilibrium constants between micelles and homogeneous solution with the same polarity as that of the micelle interior were reported.^{8–12} Furthermore, long after the first treatment of combined static and dynamic intramicellar quenching appeared,⁵ a disturbing number of such studies still arrive at their conclusions through Stern–Volmer analyses that are only valid for homogeneous solution,^{13–18} but fits based on an inappropriate model, even if they superficially accommodate the experimental data within some restricted range of variables, will not yield parameters that reflect physical reality.

Herein, we present a systematic investigation of intramicellar quenching exhibiting both a static and a dynamic component in anionic micelles of surfactants with the same basic structure (sodium alkyl sulfates) but volumes varying by a factor of more than 4, and we compare the results with those in homogeneous methanolic solution. The characterization of an additional dynamic quenching pathway through the micelle–water interface and the determination of the micellar aggregation numbers as functions of temperature and surfactant size are not only by-products of our experiments, but also prerequisites for extracting meaningful thermodynamic and kinetic parameters of the intramicellar target reaction. To keep this article concise, we make extensive use of the ESI,† referring to its sections as ESI-*x*. Our main measurement method is time-correlated single-photon counting.

Martin-Luther-Universität Halle-Wittenberg, Institut für Chemie, Kurt-Mothes-Str. 2, D-06120 Halle (Saale), Germany. E-mail: martin.goez@chemie.uni-halle.de

† Electronic supplementary information (ESI) available: Experimental details; data analysis; auxiliary experiments and calculations. See DOI: 10.1039/d1cp00400j

2 Results and discussion

In sodium alkyl sulfate micelles S_nS of chain length n , methyl viologen (hereafter abbreviated as MV^{2+} when its specific properties are concerned, and as Q in a more general context) quenches the fluorophore pyrene (Py) both statically and dynamically; the static quenching involves ground-state complexes; and under normal circumstances neither reactant migrates between micelles during the lifetime of the excited Py.^{5,19} This scenario causes the luminescence decay $f(t)/f_0$ to obey eqn (1),^{4,5}

$$\frac{f(t)}{f_0} = \frac{1}{1 + K_m \langle q \rangle} \times \exp[-\langle q \rangle (1 - \exp[-k_m t])] \times \exp[-t/\tau] \quad (1)$$

where f_0 is the initial luminescence in an identical experiment without quencher. Static quenching (equilibrium constant K_m) is seen to prepend an overall scaling factor to the product of a dynamic quenching term (rate constant k_m) with the decay of the fluorophores in quencher-free micelles (lifetime τ). Hence, all three processes are separable, with the procedure explained in ESI-2 (ESI[†]) minimizing cross-correlations between fit parameters. As an experimental prerequisite, all decays have to be recorded with the same vertical scaling, which for single-photon counting is only feasible indirectly, through parallel measurements of the stationary luminescence (see ESI-1, ESI[†]).

Because eqn (1) is based on mean micellar occupations $\langle Q \rangle$ by the quencher, K_m is dimensionless and the unit of k_m is s^{-1} . Both parameters can be converted into the usual units of quenching in homogeneous solution by multiplying them with the molar volume V_m of the micelles; and eqn (2),

$$\langle q \rangle = N_{\text{agg}} \times \frac{[Q_m]}{[\text{Surf}_m]} \quad (2)$$

relates $\langle Q \rangle$ to the concentration ratio of the micellized quencher Q_m and the surfactant in the aggregated state Surf_m , with the aggregation number N_{agg} of the micelles as constant of proportionality. Although $[Q_m]$ is often identical to the weight-in

concentration $[Q_i]$, deviations occur and will be addressed below. In contrast, $[\text{Surf}_m]$ is always smaller than the weight-in concentration $[\text{Surf}_i]$: it is frequently approximated by subtracting the critical micelle concentration cmc from $[\text{Surf}_i]$, but a more accurate value is obtained through solving eqn (S13) (ESI[†]) numerically.²⁰ We chose $[\text{Surf}_i]$ such as to keep $[\text{Surf}_m]$ within the interval 40–50 mM throughout, which makes comparisons more reliable, in particular through ensuring that our low-level additions (<1 mM) of Q leave undisturbed both $[\text{Surf}_m]$ and the constant of proportionality linking $[Q_m]$ and $[Q_i]$. For the pertaining parameters and further design considerations, see ESI-3.3 (ESI[†]).

As Fig. 1a demonstrates, eqn (1) affords a convincing fit of all the time-resolved curves simultaneously when $[Q_i]$ is varied at given temperature T . Our set of fit parameters comprised not only the kinetic constants K_m , k_m , and τ , but also N_{agg} . This micellar descriptor was made adjustable because it (i) depends too strongly on the experimental conditions as to allow literature data to be used reliably, (ii) can be determined independently only by more demanding methods such as neutron scattering,²¹ but (iii) enters eqn (1) in a way that does not compromise parameter uniqueness. Concentration variations as in Fig. 1a provided our main data sources herein, and in their fits we always treated K_m , k_m , and N_{agg} as global parameters (for τ , see below). A more detailed mathematical analysis can be found in ESI-2 (ESI[†]).

A successful fit of the time-resolved data implies the self-same for their integrals, hence for the Stern–Volmer data, which are displayed as the inset of Fig. 1a and perfectly reproduced by the pertaining eqn (S2b) with the identical parameter set. However, the converse does not hold true, because $f(t)$ of eqn (1) is not uniquely characterized by its integral; thus, the Stern–Volmer data taken on their own would accommodate a multitude of parameter sets almost equally well, making them unsuitable for reliable parameter extraction. The same applies to static absorption measurements, which do not allow a separation of K_m and N_{agg} .¹⁹

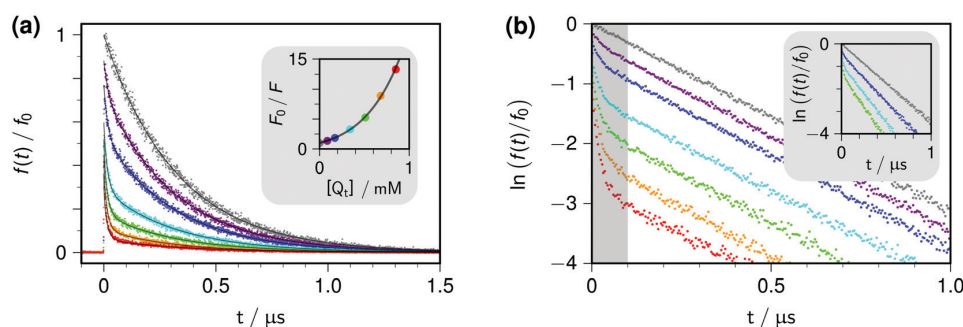


Fig. 1 Quenching of pyrene (weight-in concentration, 10 μM) by methyl viologen Q (colour code/weight-in concentration $[Q_i]$ in mM: gray, 0; violet, 0.085; dark blue, 0.17; cyan, 0.34; green, 0.51; orange, 0.68; red, 0.85) in micelles of 50 mM sodium tridecyl sulfate S13S at 30 $^\circ\text{C}$; excitation, 341 nm; detection, 395 nm. Graph (a): time-resolved fluorescence decays (main plot) and Stern–Volmer plot (inset); global fits (see ESI-2, ESI[†]) superimposed as solid curves on the data of the main plot; best-fit parameters, $\tau_0 = 352$ ns, $N_{\text{agg}} = 102$, $K_m = 0.86$, $k_m = 4.9 \times 10^7$ s^{-1} ; theoretical curve in the inset calculated with these parameters. Graph (b): main plot, log-lin plot of the time-resolved data of graph (a), temporal regime of the intramicellar quenching overlaid with gray, sets of four data points averaged for better visibility of the parallelism at long times; inset, same plot for 50 mM S12S micelles at 40 $^\circ\text{C}$ and with 250 mM NaCl added, nonparallel decays caused by quenching across the micelle–water interface. For further explanation, see the text.

The biphasic kinetics of eqn (1) are revealed most clearly by log-lin plots (Fig. 1b). Within 100 ns or earlier, the intracellular quenching has run its course such that no excited fluorophores survive except in quencher-free micelles; afterwards, these remaining fluorophores in their isolation decay only through first-order processes (including, if it were present, quenching by the micellar matrix), which all combine to give a single lifetime τ . Hence, the “late” regime of the log-lin plots features straight lines whose intercepts reflect the percentage of quencher-free micelles and thus decrease with increasing quencher concentration (eqn (S7), ESI[†]).

When these lines are also strictly parallel to one another, as in the main plot of Fig. 1b, the underlying concentration independence of τ establishes that the quencher is only operative during the intracellular “early” regime, hence must be completely solubilized and apparently immobile. This scenario holds true for all our surfactants, and alters only when extra Na^+ has been added in sufficiently high concentration, for which we used sodium chloride at concentration $[\text{NaCl}]$: as the inset epitomizes, the straight lines then become progressively steeper with rising quencher concentration, indicating a “late” participation of dynamic quenching through the micelle–water interface. That process, which follows the same pseudo first-order rate law as does quenching in homogeneous medium, in turn implies that some fraction of $[\text{Q}_t]$ must reside in the aqueous bulk.

We have investigated this salt-induced partitioning of our quencher MV^{2+} by independent experiments focusing on S12S, which offers the largest data base with respect to common-ion influences on its micellar properties. Excess Na^+ ions partially displace MV^{2+} from the micellar surfaces,²² whereupon its first absorption band shifts slightly to the blue.²³ Through spectral decomposition (ESI-3.1, ESI[†]), we determined the concentrations $[\text{Q}_{\text{aq}}]$ in the aqueous phase relative to the weight-in concentrations $[\text{Q}_t]$. The results have been compiled in the upper inset of

Fig. 2a. They show that almost 40% of MV^{2+} have moved into the aqueous bulk at the highest salt concentration $[\text{NaCl}]$ and temperature of our experiments.

At given T and $[\text{NaCl}]$, the partition coefficient between the micelles and the aqueous bulk is a constant, and quenching through the micellar interface thus contributes to $1/\tau$ an increment k' that is strictly proportional to $[\text{Q}_t]$ (see eqn (S5), ESI[†]). That dependence is verified by the lower inset of Fig. 2a, which further demonstrates that the diverging straight lines for k' with different $[\text{NaCl}]$ all collapse into a single line when the concentrations of free quencher $[\text{Q}_{\text{aq}}]$ from the upper inset are used as the independent variable instead of $[\text{Q}_t]$. The slope of this line is the second-order rate constant k_{ext} ; and the Arrhenius diagram of k_{ext} in the main plot of Fig. 2a finally yields an activation energy E_A of 15 kJ mol⁻¹ and a value at room temperature of $2.2 \times 10^{10} \text{ M}^{-1} \text{ s}^{-1}$. Because water exhibits an Arrhenius energy of its viscosity of 15.8 kJ mol⁻¹,²⁴ and the room-temperature quenching rate constant k_{h} for the Py/ MV^{2+} couple in homogeneous aqueous medium is $5.3 \times 10^9 \text{ M}^{-1} \text{ s}^{-1}$,²⁵ our results on k_{ext} clearly indicate diffusion control accelerated by the Coulombic attraction between MV^{2+} and the anionic micelles. A comparison with quenching experiments in methanol (Fig. 2b) further corroborates this: at room temperature, k_{h} is three times as large ($1.6 \times 10^{10} \text{ M}^{-1} \text{ s}^{-1}$) in the less viscous MeOH but still 30% smaller than k_{ext} , whereas E_A associated with k_{h} is 9 kJ mol⁻¹, which again closely parallels the Arrhenius energy of the viscosity (10.1 kJ mol⁻¹).²⁴ By this reasoning, k_{ext} is identified as the rate constant of MV^{2+} attachment to an S12S micelle.

The results of Fig. 2a have two other applications. First, they provide the actual concentrations $[\text{Q}_m]$ of micelle-bound quencher, which are prerequisites for analyzing the intracellular processes in all experiments with added NaCl. Second, they allow estimating the rate constant of the exit of MV^{2+} from the micelles (ESI-3.2, ESI[†]) to give, for instance, a value of less than $3 \times 10^6 \text{ s}^{-1}$

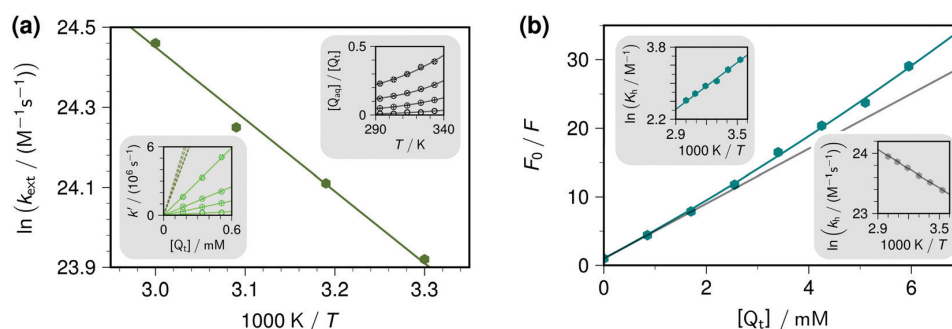


Fig. 2 Quenching of pyrene (10 μM) by methyl viologen Q through the phase boundary of aqueous S12S micelles (a) and in homogeneous methanolic solution (b). Graph (a): 50 mM S12S weight-in concentration, with NaCl added (concentration in mM/symbol type; 50/open circle; 150/circled plus sign; 250/circled multiplication cross; 450/circled asterisk). The upper inset displays the spectrophotometrically determined fraction of Q residing in the aqueous phase (compare ESI-3.1, ESI[†]), fit functions without physical significance. The dependence of the pseudo first-order rate constant k' of this quenching on $[\text{Q}_t]$ with $[\text{NaCl}]$ as parameter (from experiments as in the inset of Fig. 1b) is given in the lower inset, with the dashed lines being the recalculations for $[\text{Q}_{\text{aq}}] = [\text{Q}_t]$ to give the bimolecular rate constant k_{ext} . The main graph shows an Arrhenius plot of k_{ext} , yielding an activation energy of 15 kJ mol⁻¹. Graph (b): main plot, Stern–Volmer plot in MeOH (teal data points and fit curve), with the gray line being the dynamic quenching component k_{h} determined by time-resolved measurements; lower inset, Arrhenius plot for k_{h} , activation energy 9 kJ mol⁻¹; upper inset, van’t Hoff plot for the static quenching component K_{h} , giving $\Delta H^\circ = -14 \text{ kJ mol}^{-1}$ and $\Delta S^\circ = -21 \text{ J K}^{-1} \text{ mol}^{-1}$. For further explanation, see the text.

for the conditions pertaining to the inset of Fig. 1b. Such a slow exit is noncompetitive on the timescale of the intramicellar quenching, which is seen to be at least 10 times faster on account of the higher T and larger N_{agg} . This justifies continuing the description of the intramicellar processes at high $[\text{NaCl}]$ by eqn (1).

With $[Q_m]$ thus unambiguously determined and $[\text{Surf}_m]$ reliably computable with eqn (S13) (ESI[†]), whose only parameter is the well-understood degree of counterion dissociation α of the S_nS micelles,^{26,27} global fits of the fluorescence decays as in Fig. 1a yield the micellar aggregation numbers $N_{\text{agg}}(n, T, c_{\text{add}})$ as functions of the alkyl chain length n , the temperature T and—herein studied for S12S only—the NaCl concentration c_{add} . There have only been sporadic reports on the temperature dependence of N_{agg} ,^{4,21,28} and none of them has featured odd n or excess Na^+ . Fig. 3 reveals N_{agg} to be a linear function of T regardless of whether n (Fig. 3a) or c_{add} (inset of Fig. 3b) is the secondary variable, with standard deviations between the data and the fit functions (see Table S3, ESI[†]) not exceeding one unit.

Comparisons with existing data in the literature are complicated by a dependence of N_{agg} on the total concentration $[\text{Na}_{\text{aq}}^+]$ of the common counterion in the aqueous phase, hence on both $[\text{Surf}_i]$ and c_{add} : when $[\text{Na}_{\text{aq}}^+]$ is not kept constant, values of N_{agg} are thus expected to differ even at the same temperature. What is well documented, but only for specific values of T ,^{26,29} is the power law displayed as formula and investigated through a combined variation of $[\text{Na}_{\text{aq}}^+]$ and T in Fig. 3b. Its three input parameters, the critical micelle concentration without added salt cmc_0 , the aggregation number $N_{\text{agg},0}$ at cmc_0 , and the exponent γ are all surfactant-specific. The same holds true for the “hidden” parameter α , which is included in $[\text{Na}_{\text{aq}}^+]$ through eqn (S13) (ESI[†]) and is furthermore known to be temperature independent.²⁷

Given that cmc_0 changes only weakly throughout the temperature range investigated herein (compare ESI-3.3, ESI[†]), our observations of linear relationships between N_{agg} and T suggest the same linear forms for $N_{\text{agg},0}(T)$ combined with no appreciable influence of T on γ . This is corroborated by the successful fit of Fig. 3b (main plot), which well represents the data for all $[\text{Na}_{\text{aq}}^+]$ and T simultaneously with one global γ and local $N_{\text{agg},0}(T)$ that again depend linearly on T (see, the inset of the Figure). Our best-fit value of γ (0.17) is about 30% lower in comparison to earlier reports,^{20,26} but a fit with the higher value could not reproduce the experimental data of Fig. 3b.

As a natural conclusion from the described results on S12S, γ should be essentially temperature independent also for the other S_nS . On this premise, we recalculated the data of the main plot of Fig. 3a with eqn (S17) (ESI[†]) and the values of γ collected in Table S2 (ESI[†]) to give $N_{\text{agg},0}(T)$ displayed in the inset with n as parameter. A linear dependence on n was found when the set of $N_{\text{agg},0}$ for S9S–S12S at 20 °C was combined with that for S13S–S14S at 40 °C.²⁶ However, when we assembled $N_{\text{agg},0}$ for the complete set S9S–S14S at identical temperatures, linearity with n was poor. In conjunction with the linear temperature dependences, this suggested a dependence not on T alone but on the difference between T and the surfactant-specific Krafft temperature T_K . Plotting $N_{\text{agg},0}$ in this way (see the inset of Fig. 3a) indeed gave a good correlation such that the boxed expression at the top of the Figure provides a model function for $N_{\text{agg},0}$ that is linear in both chain length n and temperature difference $(T - T_K)$, and represents all our experimental results with a standard deviation of less than 3 units.

The central importance of N_{agg} for the intramicellar kinetics and equilibria stems from its direct connection with the molar volume V_m of the micelle, which only involves the partial molar volume Φ_m as the constant of proportionality. In ESI-3.5 (ESI[†]),

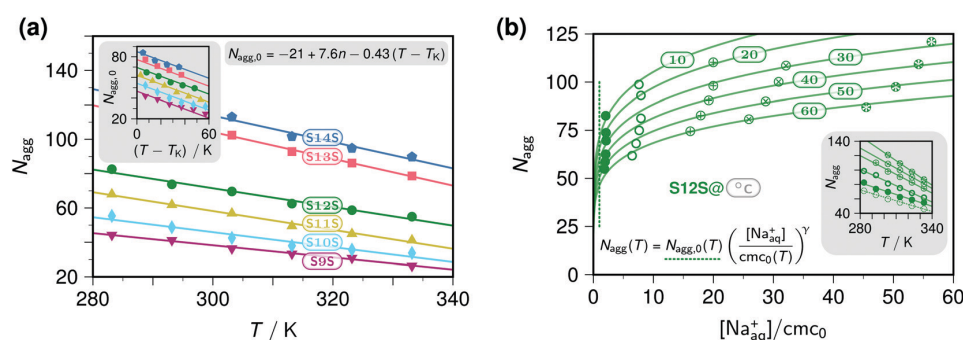


Fig. 3 Micellar aggregation numbers N_{agg} as determined by fluorescence quenching. For the global experimental conditions and the surfactant weight-in concentrations, see Fig. 1 and Table S2 (ESI[†]). “Missing” data points are due to insolubilities. Graph (a): different sodium alkyl sulfates S_nS (see also curve labels in the main plot)/colour code/symbol type (solid throughout); S9S/purple/inverted triangle, S10S/cyan/diamond, S11S/yellow/triangle, S12S/green/circle, S13S/red/square, S14S/blue/pentagon; main plot, N_{agg} as functions of T , with linear fits (Table S3, ESI[†]) as solid lines; inset, $N_{\text{agg},0}$ (calculated from the data with eqn (S17), ESI[†]) as functions of the difference between T and the Krafft temperature T_K , solid lines given by the global fit function in the gray box. Graph (b): S12S (green) with added NaCl; $[\text{NaCl}]$ in mM/symbol type; 0/solid circle, 50/open circle, 150/circled plus, 250/circled multiplication cross, 450/open asterisk; main plot, N_{agg} as functions of the total sodium-ion concentration Na_{aq}^+ in the aqueous phase at different T (given as curve labels in °C), curves displaying the functions specified in the formula at the bottom of the graph with independently calculated $\text{cmc}_0(T)$ (ESI-3.3, ESI[†]), best-fit global $\gamma = 0.17$ and local values of $N_{\text{agg},0}$ given by the intersections with the dashed vertical line; inset, N_{agg} (symbol meanings as in the main plot) and $N_{\text{agg},0}$ (dotted circles) as functions of T with linear fits as solid and dashed lines. For further explanation, see the text.

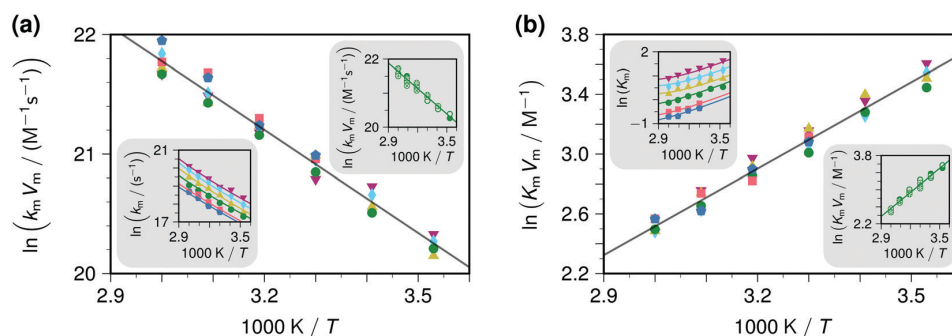


Fig. 4 Dynamic (a) and static (b) intramicellar quenching of pyrene by MV^{2+} in sodium alkyl sulfate micelles S_nS of chain length n and in $S_{12}S$ with NaCl added (right insets of both figures), symbol types and colour codes as defined in Fig. 3. Graph (a): Arrhenius plots for the quenching rate constants based on particle numbers and concentrations k_m (left inset) and $k_m V_m$ (main plot and right inset); fit lines corresponding to activation energies of 24 kJ mol^{-1} and 21 kJ mol^{-1} ; Graph (b): van't Hoff plots for the analogous equilibrium constants K_m (left inset) and $K_m V_m$ (main plot and right inset); fit lines corresponding to $\Delta H^\circ = -16 \text{ kJ mol}^{-1}$ and $\Delta S^\circ = -27 \text{ J K}^{-1} \text{ mol}^{-1}$, and to $\Delta H^\circ = -16 \text{ kJ mol}^{-1}$ and $\Delta S^\circ = -26 \text{ J K}^{-1} \text{ mol}^{-1}$, respectively. For both (a) and (b), the curves in the left inset are not standalone fits, but are given by the fit of the main plot divided by V_m calculated with the pertaining interpolation formula of Table S4 (ESI[†]). For further explanation, see the text.

we have derived an interpolation formula for Φ_m based on literature data and combined it with our best-fit linear representations of $N_{\text{agg}}(T, n, c_{\text{add}})$ to obtain closed-form approximations to V_m for all the experiments of this work (see Table S4, ESI[†]). At constant temperature, these volumes V_m exhibit a dispersion by a factor of more than 4; and so do our best-fit rate constants k_m and equilibrium constants K_m , as can be seen in the left insets of Fig. 4a and b.

However, the trend of the reaction-related constants with n is inverse to that of V_m , hence reflects the volume available to the single quencher molecule per micelle that is implicit in the definitions of k_m and K_m . A multiplication with the pertaining V_m serves to remove this volume effect and transforms the constants k_m and K_m , which are based on particle numbers, to concentration-based constants k and K . When the experimental data at each temperature in the two insets are treated in this way, their differences over n practically vanish, with the spread reduced by a factor of almost 20 in the dynamic case (from $\pm 220\%$ for k_m to $\pm 12\%$ for k) and of more than 30 in the static case (from $\pm 220\%$ for K_m to $\pm 7\%$ for K). In the same way, each slice through the data for different c_{add} at given T essentially collapses into a single point upon multiplication with V_m , as the results in the right insets of Fig. 4a and b bear out.

The Arrhenius diagrams of k in Fig. 4a yield activation energies of 24 kJ mol^{-1} and 21 kJ mol^{-1} (main plot and right inset) depending on whether the secondary variable is n or c_{add} . This discrepancy may well be due to slightly different microviscosities; but, paying heed to the principle of Occam's razor, we have refrained from analyzing k with a more detailed shell-core micellar model,⁷ in view of the absence of an obvious systematic trend in the data with n and of the noticeable fluctuations around the regression line (e.g., for S9S). The ratio \bar{k}/k_h of the room-temperature average of k , as based on simple nonstructured volumes, to k_h (from the right inset of Fig. 2b) indicates a microviscosity between 14 and 18 times the viscosity of methanol, i.e., comparable to that of 1-octanol,³⁰ whose

Arrhenius energy of the viscosity (25.0 kJ mol^{-1})²⁴ is also consistent with the activation energy of our diffusion-controlled intramicellar reactions.

Turning to the analogous van't Hoff diagrams in the main plot and right inset of Fig. 4b, a modulation of the underlying thermodynamic quantity K by the microviscosity is neither expected nor observed: not only do the reaction enthalpies and entropies for the same two scenarios match much more closely (ΔH° , -16 kJ mol^{-1} in both cases; ΔS° , $-27 \text{ J K}^{-1} \text{ mol}^{-1}$ and $-26 \text{ J K}^{-1} \text{ mol}^{-1}$) than the activation energies did, but they are also very similar to the values we measured in homogeneous methanolic solution (compare the upper inset of Fig. 2b, with ΔH° of -14 kJ mol^{-1} and ΔS° of $-21 \text{ J K}^{-1} \text{ mol}^{-1}$). Methanol is a solvent with a polarity nearly identical to the micropolarity of S_nS micelles,⁷ and with respect to K , there is practically no difference between all these reaction media.

3 Conclusions

Hence, as far as intramicellar chemical reactivity is concerned, a consistent picture has emerged. Local reactant concentrations are already approximated sufficiently well by the simplest approach that uses only the molar volume V_m of the micelle; and on this basis, the micellar size does not influence the thermodynamic and kinetic parameters significantly. This insensitivity of the equilibrium and rate constants unleashes the full potential of the concentration increase by the compartmentalization: a micellar occupation $\langle Q \rangle$ of unity, which is typically attained with 1 mM quencher weight-in concentration herein, corresponds to a local quencher concentration of V_m^{-1} , which provides a concentration boost by a factor between 30 (S14S) and 130 (S9S).

Pointedly formulated, an S_nS micelle thus behaves just like an alcohol nanodroplet with a volume that is precomputable and can be adjusted as desired through temperature, alkyl chain

length, and salt addition. From a thermodynamic perspective, this nanodroplet is composed of methanol; from a kinetic perspective, of 1-octanol. Facilitated by the predictive power of the findings herein, such as the interpolation formulas for the dependence of the aggregation number or the partial molar volume on chain length n and temperature, rational planning and improvement of syntheses that rely on intracellular equilibria should thus only require a small number of experiments and/or literature data.

Conflicts of interest

There are no conflicts of interest to declare.

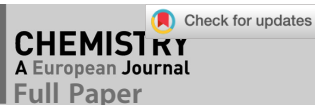
References

- 1 T. Dwars, E. Paetzold and G. Oehme, *Angew. Chem., Int. Ed.*, 2005, **44**, 7174–7199.
- 2 G. La Sorella, G. Strukul and A. Scarso, *Green Chem.*, 2015, **17**, 644–683.
- 3 B. H. Lipshutz, S. Ghorai and M. Cortes-Clerget, *Chem. – Eur. J.*, 2018, **24**, 6672–6695.
- 4 T. Kohlmann and M. Goez, *Photochem. Photobiol. Sci.*, 2020, **19**, 71–79.
- 5 M. H. Gehlen and F. C. De Schryver, *J. Phys. Chem.*, 1993, **97**, 11242–11248.
- 6 J. R. Lakowicz, *Principles of Fluorescence Spectroscopy*, 3rd edn, Springer, New York, 2006.
- 7 R. Ranganathan, C. Vautier-Giongo and B. L. Bales, *J. Phys. Chem. B*, 2003, **107**, 10312–10318.
- 8 F. M. Martens and J. W. Verhoeven, *J. Phys. Chem.*, 1981, **85**, 1773–1777.
- 9 M. Hamity and R. H. Lema, *Can. J. Chem.*, 1988, **66**, 1552–1557.
- 10 D. Fornasiero and F. Grieser, *J. Chem. Soc., Faraday Trans.*, 1990, **86**, 2955–2960.
- 11 S. M. Hubig, *J. Phys. Chem.*, 1992, **96**, 2903–2909.
- 12 S. C. Bhattacharya, H. T. Das and S. T. Moulik, *J. Photochem. Photobiol., A*, 1993, **71**, 257–262.
- 13 C. N. Lunardi, J. B. S. Bonilha and A. C. Tedesco, *J. Lumin.*, 2002, **99**, 61–71.
- 14 T. K. Mukherjee, P. P. Mishra and A. Datta, *Chem. Phys. Lett.*, 2005, **407**, 119–123.
- 15 C. Tablet, I. Matei and M. Hillebrand, *J. Mol. Liq.*, 2011, **160**, 57–62.
- 16 M. Panda and Kabir-ud-Din, *Arabian J. Chem.*, 2014, **7**, 261–266.
- 17 A. R. Soemo and J. E. Pemberton, *J. Fluoresc.*, 2014, **24**, 295–299.
- 18 S. Mukherjee, S. Gupta, K. Ganorkar, A. Kumar and S. K. Ghosh, *Spectrochim. Acta, Part A*, 2020, **228**, 117723.
- 19 T. Kohlmann and M. Goez, *Phys. Chem. Chem. Phys.*, 2019, **21**, 10075–10085.
- 20 F. H. Quina, P. M. Nassar, J. B. S. Bonilha and B. L. Bales, *J. Phys. Chem.*, 1995, **99**, 17028–17031.
- 21 B. Hammouda, *J. Res. Natl. Inst. Stand. Technol.*, 2013, **118**, 151–167.
- 22 T. Tominaga, H. Ohtaka-Saiki, Y. Nogami and H. Iwata, *J. Mol. Liq.*, 2006, **125**, 147–150.
- 23 H. J. D. McManus, Y. S. Kang and L. Kevan, *J. Phys. Chem.*, 1992, **96**, 2274–2277.
- 24 A. Messâdi, N. Dhouibi, H. Hamda, F. B. M. Belgacem, Y. H. Adbelkader, N. Ouerfelli and A. H. Hamzaoui, *J. Chem.*, 2015, 1–12.
- 25 Y. Kusumoto, S. Ihara, J. Kurawaki and I. Satake, *Chem. Lett.*, 1986, 1647–1650.
- 26 R. Ranganathan, L. Tran and B. L. Bales, *J. Phys. Chem. B*, 2000, **104**, 2260–2264.
- 27 N. V. Lebedeva, A. Shahine and B. L. Bales, *J. Phys. Chem. B*, 2005, **109**, 19806–19816.
- 28 S. Vass, *Struct. Chem.*, 1991, **2**, 357–395.
- 29 H. F. Huisman, *Proc. Kon. Ned. Akad. Wetensch.*, 1964, **B67**, 407–424.
- 30 I. M. Smallwood, *Handbook of Organic Solvent Properties*, Wiley, New York, 1996.

7.4 Publikation D



DOI: 10.1002/chem.201901618

Photochemistry | *Hot Paper* |

Laser-Induced Wurtz-Type Syntheses with a Metal-Free Photoredox Catalytic Source of Hydrated Electrons

Tim Kohlmann,^[a] Christoph Kerzig,^[a, b] and Martin Goez^{*[a]}

Abstract: Upon irradiation with ns laser pulses at 355 nm, 2-aminoanthracene in SDS micelles readily produces hydrated electrons. These “super-reductants” rapidly attack substrates such as chloro-organics and convert them into carbon-centred radicals through dissociative electron transfer. For a catalytic cycle, the aminoanthracene needs to be restored from its photoionization by-product, the radical cation, by a sacrificial donor. The ascorbate monoanion can only achieve this across the micelle–water interface, but the monoanion of ascorbyl palmitate results in a fully micelle-contained regenerative electron source. The shielding by the micelle in the latter case not only increases the life of the catalyst but also

strongly suppresses the interception of the carbon-centred radicals by the hydrogen-donating ascorbate moiety; and in conjunction with the high local concentrations effected by the pulsed laser, termination by radical dimerization thus dominates. We have obtained a complete and consistent picture through monitoring the individual steps and the assembled system by flash photolysis on fast and slow time-scales, from microseconds to minutes; and in preparative studies on a variety of substrates, we have achieved up to quantitative dimerization with a turnover on the order of 1 mmol per hour.

Introduction

It seems natural to associate sustainable photochemistry with solar photochemistry. However, the advantages of not having to succumb to the course of the sun and the vagaries of the weather are overpowering arguments in favour of artificial radiation sources. As a corollary, this approach equally well accommodates wavelengths outside the visible range.^[1] Pursuing this line further, herein we employ a pulsed (5 ns) near-UV (355 nm) laser for organic syntheses, maintaining chemical sustainability through a catalytic cycle that consumes only an approved food additive. An organic chemist’s instinctive recoil at working with a class 4 laser on account of anticipated cost and safety issues is understandable but groundless: the longevity of such lasers reduces their moderate initial price to a very minor concern,^[2] as is emphasized by the growing use even of significantly more expensive fs lasers in industrial and medicinal photopolymerization;^[3–5] and it is much easier to safeguard against laser radiation than against toxicity or explosion, risks that chemists routinely handle despite the impossibility of ren-

dering them non-existent as simply, instantaneously and permanently as by flicking a switch of the laser power supply.

The unique opportunity a pulsed laser provides is the very high light intensity during a flash; and in this work, we have put this to good use in two ways. First, we access a “super-reductant” (the hydrated electron e_{aq}^{*-} ; standard potential, -2.9 V)^[6] through photon pooling but without the necessity of storing the energy of the first photon in a long-lived intermediate, as a low-intensity source would mandate.^[7,8] The advantage of the two-photon approach lies in its longer operating wavelength, which is not absorbed so strongly and by so many substrates as is the UV-C (≈ 250 nm) used by the iodide and sulfite processes of e_{aq}^{*-} generation.^[9–11] Second, we prepare e_{aq}^{*-} in high local concentration such that its rapid interception by a chloro-organic to give a chloride ion and a carbon-centred radical favours dimerization of the latter over the usual decay pathways of hydrogen abstraction from a donor or addition to a coupling component.^[12,13] This photochemical analogue of the Wurtz and related reactions,^[14] which also encompasses carbonyl substrates, is metal-free; and the same holds true for our e_{aq}^{*-} source, which is based on 2-aminoanthracene AntNH₂ as the (commercially available) catalyst Cat.

Results and Discussion

Figure 1 a displays the two subtypes of the general mechanism of e_{aq}^{*-} production^[15,16] explored herein. To shield the catalyst against destruction by e_{aq}^{*-} or the substrate-derived radicals, we have enclosed it in an anionic micelle (of sodium dodecylsulfate: SDS). Two-photon ionization of Cat via an excited state 1 Cat ejects e_{aq}^{*-} into the aqueous bulk, whereas the accompany-

[a] T. Kohlmann, Dr. C. Kerzig, Prof. Dr. M. Goez
Martin-Luther-Universität Halle-Wittenberg, Institut für Chemie
Kurt-Mothes-Str. 2, 06120 Halle (Saale) (Germany)
E-mail: martin.goez@chemie.uni-halle.de

[b] Dr. C. Kerzig
Present address: Department of Chemistry, University of Basel
St. Johanns-Ring 19, 4056 Basel (Switzerland)

Supporting information and the ORCID identification number(s) for the author(s) of this article can be found under:
<https://doi.org/10.1002/chem.201901618>.

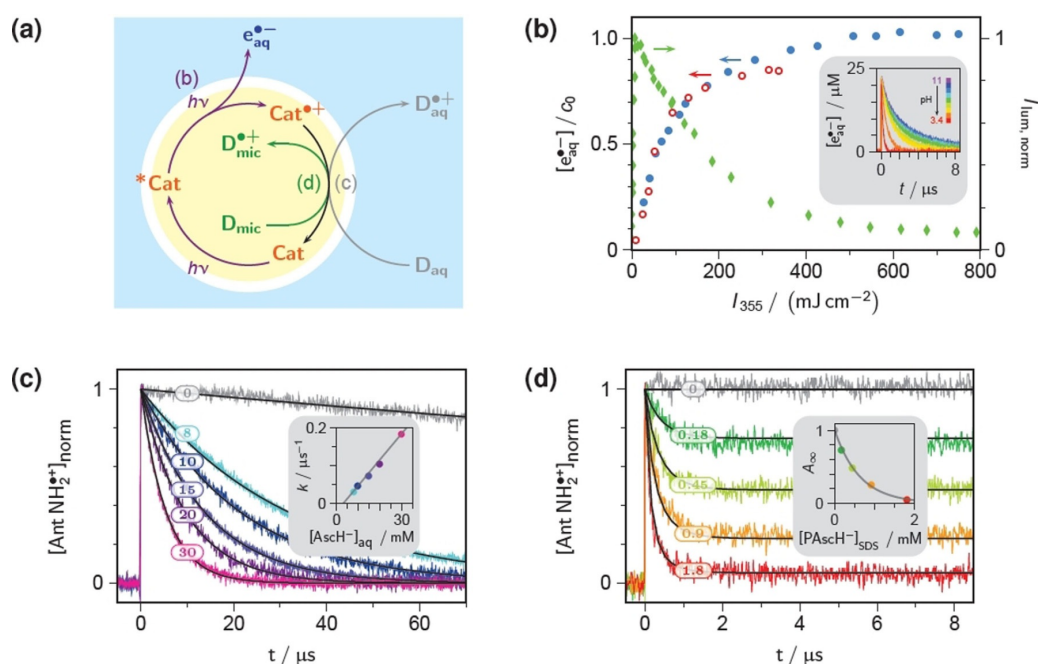


Figure 1. Mechanism of the e_{aq}^- source (a) and characterisation of its steps (b)–(d) by laser flash photolysis (355 nm; flash intensity, I_{355}). a) The catalyst Cat is AntNH₂; the donors D_{aq} and D_{mic} are AsCH[−] and PAsCH[−]; the anionic micelle is symbolized by the yellow circle with the white border; and the light blue area denotes the aqueous bulk. Conditions, unless varied or specified explicitly, are: catalyst concentration, c_0 , 35 μM ; 50 mM aqueous SDS at pH 8; I_{355} , 100 mJ cm^{-2} . b) Photoionization step. Main plot, intensity dependence of e_{aq}^- formation (filled blue circles, pH 8.5; open red circles, pH 4.0) and normalized luminescence (green diamonds). Inset, e_{aq}^- traces at different pH (3.4, 4.0, 4.5, 5.0, 5.5, 6.0, 6.4, 8.5, 11.0). c, d) Regeneration step with AsCH[−]_{aq} and with PAsCH[−]_{SDS}. Main plots, decay traces of the radical cation normalized to the maximum without donor D; unquenched decay rate constant k_0 , $2.2 \times 10^3 \text{ s}^{-1}$; donor concentrations in mM given at the traces. Insets: extracted key parameters; identical colour code as in the pertaining main plot. Solid curves in the main plot of (c) are best-fit monoexponential decays; and the obtained first-order rate constants are displayed in the inset as function of the donor concentration; slope of the regression line in the inset, $7 \times 10^6 \text{ M}^{-1} \text{ s}^{-1}$, with the apparent negative intercept being an artefact caused by the nonconstant ionic strength. Solid curves in the main plot of (d) are global best-fit curves with the model of SI-4.1; best-fit intramicellar rate constant k_{ip} , $2.2 \times 10^6 \text{ s}^{-1}$. The inset of (d) shows the exponential decrease of the residual amplitude A_{∞} with increasing donor concentration.

ing radical cation Cat⁺ remains micelle-bound; and an electron transfer from a sacrificial donor D to Cat⁺ finally restores the starting state. For that last step, we compare regenerations across the micelle–water interface and within the micelle by selecting for D the monoanions of ascorbate AsCH[−] and ascorbyl palmitate PAsCH[−], both of which are antioxidants approved by the EU and the FDA.

Any regenerative electron source operating according to Figure 1a has to meet the following three criteria; and the better these conditions are fulfilled the higher the activity and stability. First, the two-photon ionization of Cat is required to be as efficient as possible; second, Cat must be regenerated quantitatively by D; and third, parasitic side reactions such as interference of D with ¹Cat or scavenging of e_{aq}^- by D should be minimized. Our mechanistic and kinetic investigations of these key aspects on μs timescales are summarized by Figure 1b–d and the pertaining sections of the Supporting Information, which we will use extensively for conciseness and refer to by SI- \langle number \rangle . All experimental details can be found in SI-1.

Figure 1b focuses on the liberation of e_{aq}^- from the catalyst, with the laser intensity as the independent variable. By the procedure of SI-2.2, the concentration e_{aq}^- can be monitored

without interference from other species; and this includes its time evolution, as Figure 2a or the inset of Figure 1b illustrates.

The widespread notion that monophotonic or biphotonic ionizations can be easily diagnosed as such by linear or quadratic dependences on the light intensity is a fallacy: these relationships are merely limiting laws for low intensities, where the measurement uncertainty is largest; and their validity range can be extremely small.^[17] However, because the triplet state of the catalyst is not involved (SI-3.1), an unambiguous differentiation is possible by simultaneously tracking the amount of excited catalyst, through its fluorescence.^[18] With a monophotonic ionization, fluorescence and e_{aq}^- ejection are parallel reactions, hence must exhibit the same intensity dependence. With a biphotonic ionization, the excited catalyst is the intermediate of a consecutive photoreaction: with increasing light intensity, the fluorescence must thus initially rise and then fall again; and this characteristic pattern is clearly discernible in Figure 1b.

As the Figure also evidences, a single flash of 100 mJ cm^{-2} already suffices to ionize more than 50% of the catalyst molecules AntNH₂. This high overall conversion efficiency at the native (i.e., without beam narrowing) intensity employed for

all our later preparative illuminations represents an improvement by a factor of two over previously investigated similar precursors.^[15,18]

A further unique feature is the largely unchanged $e_{\text{aq}}^{\bullet-}$ yield when the electron-donating ability of the amino group is suspended by a protonation (the pK_a of the protonated catalyst in our medium is 6.1, as determined in SI-2.1.1). Two compensating effects provide the explanation. On one hand, AntNH_3^+ absorbs our laser light more strongly than does AntNH_2 (for the spectra, see also SI-2.1.1), hence the first photon is used more productively. On the other hand, the excited state $^*\text{AntNH}_3^+$ is a photoacid that possesses a pK_a of 0.2 and is deprotonated within the duration of the laser flash with an efficiency slightly larger than 0.8 (SI-2.3). The same excited state as with the unprotonated catalyst is thus reached, though not quantitatively, as is reflected in Figure 1b by the lowering of the maximum $e_{\text{aq}}^{\bullet-}$ concentration attainable. The absorption effect increases the steepness of the $e_{\text{aq}}^{\bullet-}$ rise in the intensity dependence but the changed photokinetic parameters delay its onset such that the curves for AntNH_2 and AntNH_3^+ cross in the synthetically relevant intensity range of 50–100 mJ cm^{-2} . The inset of Figure 1b verifies that under these circumstances the catalyst liberates the same amount of $e_{\text{aq}}^{\bullet-}$ regardless of its protonation state. Although our catalyst thus qualifies as a virtually pH-independent $e_{\text{aq}}^{\bullet-}$ precursor, other considerations will restrict the workable pH range: for instance, decreasing the pH below 4.5 progressively curbs the preparative usage of $e_{\text{aq}}^{\bullet-}$, which are scavenged rapidly by protons, as can be perceived from the $e_{\text{aq}}^{\bullet-}$ decays in the inset.

Figures 1c,d address the post-ionization regeneration of the catalyst from its radical cation afforded by the ejection of $e_{\text{aq}}^{\bullet-}$ from $^*\text{AntNH}_2$. Our procedure for the isolated observation of $e_{\text{aq}}^{\bullet-}$ (SI-2.2) simultaneously allows the undisturbed monitoring of the by-products and their subsequent species. This yielded the calibrated absorption spectra of $\text{AntNH}_2^{\bullet+}$ and of the corresponding deprotonated radical AntNH^{\bullet} , as well as the pertaining pK_a of 11.3 (SI-2.1.2). Because a pH higher than 10 impairs the stability of one of our sacrificial donors and/or causes inner filter effects (SI-2.1.2), we avoided these conditions, and AntNH^{\bullet} will thus play no mechanistic role in this work. Furthermore, neither the sacrificial donors employed herein nor their radicals interfere with our time-resolved quantitative measurements of the $\text{AntNH}_2^{\bullet+}$ concentrations (SI-2.1.2 and 2.1.3).

Both AntNH_2 and AntNH_3^+ reside with the aromatic system inside the SDS micelle and the amino or ammonium substituent between the SDS headgroups (SI-2.4), and the same localization is thus expected for $\text{AntNH}_2^{\bullet+}$. Corroboration is provided by a lifetime of this radical cation in excess of 450 μs when sacrificial donors are absent (top trace of Figure 1c), which indicates strong shielding by the micelle against influences from the aqueous phase, in particular against attacks by $e_{\text{aq}}^{\bullet-}$ or other radicals.

The corresponding effect on a regeneration through the micelle–water interface manifests itself in Figure 1c. With the ascorbate monoanion AsCH^- , we have chosen a sacrificial donor so hydrophilic that it does not associate with SDS micelles to a noticeable degree.^[19] As the Figure illustrates, AsCH^- concen-

trations on the order of 10 mM are needed to drive the catalyst regeneration to completion within some 100 μs (rate constant from the inset, $7 \times 10^6 \text{ M}^{-1} \text{ s}^{-1}$). Only the long intrinsic life of $\text{AntNH}_2^{\bullet+}$ thus makes a near-quantitative recovery of the catalyst possible.

The other extreme, an exclusively intramicellar regeneration, is epitomized by Figure 1d. The sacrificial donor in this case is the monoanion PAsCH^- of ascorbyl palmitate, a derivative made so hydrophobic by the modification of the side chain that it is solubilized virtually quantitatively,^[20] and exchanges between SDS micelles on a ms timescale only.^[16] As emerges from comparing Figure 1c and 1d, the intramicellar regeneration—at basically the same thermodynamic driving force, on account of the identical redox system—is faster by several orders of magnitude, but incomplete in the sense that $\text{AntNH}_2^{\bullet+}$ in micelles free from PAsCH^- remains. However, that fraction obeys Poisson statistics as shown in the inset of Figure 1d, and thus becomes negligibly small (<1 ppm) when PAsCH^- is employed in the same 10 mM concentration as was AsCH^- (for details of the kinetic analysis, see SI-4.1.).

The ester bond of PAsCH^- hydrolyses appreciably fast above pH 10; and in our medium, we measured a pK_a of 6.5 for PAsCH_2 (SI-2.1.2), which shares with AsCH_2 the incapacity to regenerate the catalyst from its radical cation. Together with the inherent limitation that in acidic medium $e_{\text{aq}}^{\bullet-}$ becomes too short-lived for practicable syntheses, this restricts the applicability of our $e_{\text{aq}}^{\bullet-}$ source to pH values between about 5 and 10, an important range despite its confined width, because it surrounds the physiological pH.

Neither of the two donors interferes with the photoionization step, but AsCH^- scavenges $e_{\text{aq}}^{\bullet-}$ ten times faster than does PAsCH^- (SI-3.2). While the repetitive decay traces of $e_{\text{aq}}^{\bullet-}$ in Figure 2a highlight this difference, they primarily demonstrate the successful operation of either system as a regenerative electron source. For these experiments, we let the laser run with our flow-through system disabled such that the non-exchanged solution was excited multiple times. At the intensity used, each flash ionized more than 50% of AntNH_2 (see also SI-2.2); and over the total series of 21 sub-experiments, the accumulated $e_{\text{aq}}^{\bullet-}$ concentration amounted to more than 10 times the catalyst concentration. The gradual reduction of the peak $e_{\text{aq}}^{\bullet-}$ concentration corresponds to a catalyst loss per flash of 1.5% with AsCH^- , and as little as 0.6% with PAsCH^- . These results obviously are very promising.

Figure 2b aims at bridging the gap between the sphere of the physical chemist, as exemplified by the measurements on short timescales in Figure 2a, and the domain of the synthesis-orientated organic chemist, as typified by the yields and product distributions at the reaction end point in Table 1. It draws on the reductive detoxification of chloroacetate ClAc , which is an environmentally relevant application of $e_{\text{aq}}^{\bullet-}$ and at the same time provides a specific assay for benchmarking and studying $e_{\text{aq}}^{\bullet-}$ generators.^[2,7,10,16,21] An attack of $e_{\text{aq}}^{\bullet-}$ triggers the quasi-instantaneous dissociation of ClAc into a chloride ion and a carboxymethyl radical.^[6] The main plot of Figure 2b utilizes this reaction to characterize our $e_{\text{aq}}^{\bullet-}$ source with PAsCH^- as the sacrificial donor through concentration profiles of key species.

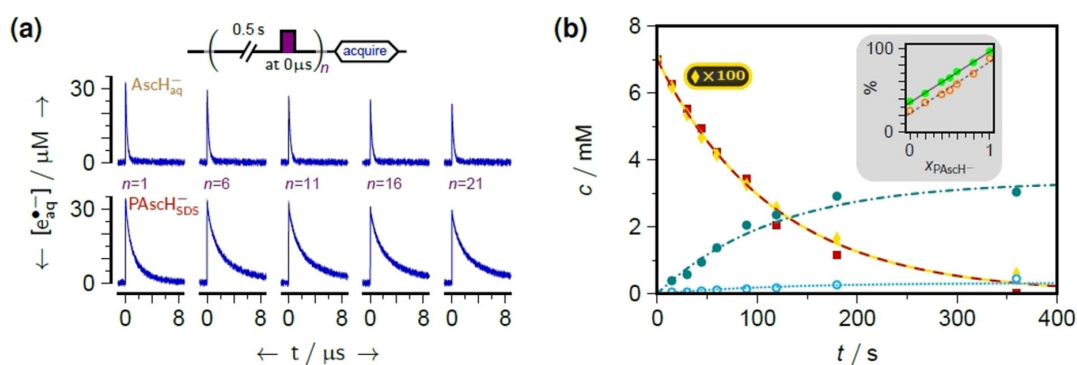


Figure 2. Performance of the assembled systems. Common conditions are 70 μM AntNH₂ in 50 mM aqueous SDS at pH 8; 10 mM donor; laser parameters, 355 nm and 100 mJ cm^{-2} . a) Demonstration of the regenerative operation by time-resolved experiments; pulse sequence displayed at the top; no exchange of illuminated solution between flashes. The progressive lengthening of the e_{aq}^* lifetime in the PAsch⁻ experiments is due to the gradual removal of traces of an e_{aq}^* -scavenging contaminant, possibly Asch⁻. b) Preparative photolysis with 7 mM chloroacetate CIAC as the substrate; sample volume, 3 mL; laser repetition rate, 10 Hz; rapidly stirred solution. The main plot displays the time dependence of the concentrations with PAsch⁻ as the donor: AntNH₂, multiplication factor 100, yellow diamonds and solid line; CIAC, red squares and long dashed line; hydrogen abstraction product acetate Ac, open cyan circles and dotted line; dimerization product succinate Su, filled teal circles and dashed-dotted line. Fit curves are based on a common exponential $\exp[-t/\tau]$ and a partitioning of the carboxymethyl radicals formed by attack of e_{aq}^* on CIAC between Ac and Su (factors f_h and f_d). Best-fit values are τ , 117 s; f_h , 0.047; f_d , 0.48. Inset: end-point values in Asch⁻/PAsch⁻ mixtures as functions of the molar fraction of PAsch⁻. Green filled circles and solid regression line, recovery of the carboxymethyl radicals as Ac or Su; open orange circles, dashed regression line, percentage of the radicals undergoing dimerization.

These comprise the catalyst AntNH₂, the substrate CIAC, and the two substrate-derived end products, namely, succinate Su afforded by the combination of two carboxymethyl radicals, and acetate Ac formed by hydrogen abstraction by one such radical. Our detection methods, luminescence (AntNH₂), electroanalysis with an ion-selective electrode (CIAC, through chloride), and NMR spectroscopy (CIAC, Asch⁻, Su and Ac) not only yield the concentrations but also allow checking the authenticity. The only species not trackable is PAsch⁻, because of an overlap with the surfactant signals and the proximity to the presaturation frequency in the NMR spectra.

With Asch⁻, the kinetics can only be modelled numerically because this sacrificial donor is also consumed by parasitic reactions with e_{aq}^* and the carboxymethyl radicals, which in turn influences the catalyst regeneration.^[7,16] In contrast, the much lower accessibility of PAsch⁻ to the species in the aqueous bulk virtually removes this coupling (SI-3.2 and 4.2.2). As detailed in SI-4.2.1, the direct consequences during at least two thirds of the extent of the reaction in Figure 2b are: i) the catalyst decays with near-perfect first-order kinetics; ii) after correction for the final value, which by a coincidence of parameters is practically zero under the conditions shown in the Figure, the current concentration of the substrate is proportional to that of the catalyst; iii) the carboxymethyl radicals undergo combination and hydrogen abstraction in an almost constant (i.e., time-independent) ratio, such that the rise of Su and Ac also follows first-order kinetics with the same rate constant as the catalyst disappearance. This simple model is seen to reproduce the time evolution under illumination of our (optically thin, and continuously mixed) system extremely well.

The inclusion of both the catalyst and the sacrificial donor in the micelle not only increases the productive utilization of e_{aq}^* , as was demonstrated by Figure 2a, but also brings two further synthetic benefits that are addressed by the inset of Figure 2b.

Both are due to the virtual absence of donor-derived species from the aqueous bulk, where the carboxymethyl radicals reside. On one hand, the number of potential side reactions drastically decreases: whereas two thirds of the carboxymethyl radicals are squandered in a multitude of combination products with the donor Asch⁻, their recovery as Su and Ac is quantitative with the donor PAsch⁻. On the other hand, the probability of radical dimerization significantly rises: whereas the competition with hydrogen abstraction from the archetypal antioxidant Asch⁻ only allows a quarter of the carboxymethyl radicals to combine, that fraction rises to almost 90% when the access to the hydrogen-donating moiety is restricted by the micellar confinement of PAsch⁻. Through their linear dependence on the molar fraction in mixed Asch⁻/PAsch⁻ systems, both effects are clearly identified as donor-related.

SI-4.2.2 derives mathematical expressions for the product ratio in such competing first and second-order reactions, both following a single flash and in the case of exhaustive illumination. On their basis, the rate constant of the hydrogen abstraction across the micelle-water interface is estimated to be slower by a factor of at least twenty compared to the homogeneous process in our systems. This parallels a factor of 70 observed in the repair of the relatively unreactive resveratrol radical by Asch⁻,^[19] and the factor of 10 in the case of the intrinsically more mobile and aggressive radical e_{aq}^* that is evident from Figure 2a. The calculations of SI-4.2.2 also reveal that the modification of the product ratio during the reaction (i.e., as the radical concentration progressively decreases) is only a small, secondary effect. This provides a posteriori justification for the simplified model of Figure 2b.

To test whether upscaling introduces new aspects, we repeated the experiment of Figure 2b in a larger cuvette. Its five times longer optical path length made better use of the laser light by absorbing all of it but influenced the product distribu-

Table 1. Transformations with the AntNH₂-based e_{aq}^{•-} sources of this work.^[a]

Substrate	Conversion ^[b] [%]		Dimerization product	Yield ^[c] [%]		H-abstraction product	Yield ^[c] [%]	
	AscH ⁻	PAscH ⁻		AscH ⁻	PAscH ⁻		AscH ⁻	PAscH ⁻
chloroacetate	87	100	succinate	25	89	acetate	11	9
chlorodifluoroacetate	65	96	tetrafluorosuccinate	80	91	difluoroacetate	8	1
2-chloropropionate	68	100	2,3-dimethylsuccinate ^[d]	7	46	propionate	29	42
2-chlorobutyrate	71	100	– ^[e]	– ^[e]	– ^[e]	butyrate	23	47
3-chloropropionate ^[f]	28	85	adipate	– ^[e]	58	propionate	9	– ^[e]
3-chloropivalate ^[f]	24	86	2,2,5,5-tetramethyladipate	– ^[e]	73	pivalate	38	16
2-chloroethanol	25	100	1,4-butanediol	– ^[e]	39	ethanol	57	20
benzylchloride ^[g]	16	61	1,2-diphenylethane	50	90	toluene	12	5
4-chlorobenzoate	100	100	– ^[e]	– ^[e]	– ^[e]	benzoate	94	95
acetone	72	100	pinacol	5	2	2-propanol	93	92
pinacolone	40	100	– ^[e]	– ^[e]	– ^[e]	pinacolyl alcohol	95	90
acetophenone	64	66	2,3-diphenyl-2,3-butanediol ^[d]	76	97	– ^[e]	– ^[e]	– ^[e]
benzaldehyde	84	81	1,2-diphenyl-1,2-ethanediol	67	98	benzyl alcohol	– ^[e]	1
cysteine ^[g]	67	83	– ^[e]	– ^[e]	– ^[e]	alanine	66	61

[a] Default conditions as in Figure 2b; end-point values after 20 min. [b] Consumption of substrate. [c] Relative to the amount of radicals. [d] *meso* + *RR*/SS. [e] Product undetectable. [f] Slow hydrolysis in water to the corresponding alcohol. [g] Reaction carried out at pH 6.

tion only marginally, again in accordance with the results of SI-4.2.2. We achieved a dimerization turnover of 70 mg h⁻¹ (0.75 mmol h⁻¹), based on the first half life. This compares very favourably with reaction durations and turnover rates reported for other photon-pooling systems capable of cleaving carbon–chlorine bonds.^[22–24]

Table 1 collects yields at illumination end points for a number of synthetic applications tested with our systems. Being sum parameters, these yields cannot provide as specific information as do the concentration profiles (Figure 2b), let alone the surgical laser-flash investigations of the individual processes (Figure 1b–d); but on the basis of those preceding results, the trends in the Table can be rationalized by two key factors each for the substrate conversion and for the product distribution.

The productive utilization of e_{aq}^{•-} is decided by the competition between its attack on the substrate and its decay by all other pathways, most importantly that with the sacrificial donor. For the examples in the Table, a fixed concentration ratio of 100:100:1 was chosen for these two ingredients and the catalyst because for the majority of substrates this allowed a near-quantitative conversion before the catalyst was exhausted. The order-of-magnitude difference between the lifetimes of e_{aq}^{•-} with our two donors (Figure 2a) makes the rate constant k_{att} of e_{aq}^{•-} attachment, which is known for all our substrates,^[6] a determinant. However, this primary influence is modulated by the propensity of the substrate-derived radicals to enter the micelle, where they can attack the catalyst and thus impair the conversion through a lower stability of the electron source. This manifests itself most clearly with PAscH⁻ and the last three substrates of the Table, for which k_{att} indicates diffusion control,^[6] yet the conversion falls noticeably short of the 100% observed for CIAC with its ten times lower value of k_{att} . The significance of the productive use of e_{aq}^{•-} reveals itself when the substrate-enhanced catalyst destruction is blanked out by taking the ratio of conversion with AscH⁻ and with PAscH⁻: that ratio (*r*) exhibits an approximate correlation with log k_{att} such that *r* is near unity for $k_{att} \gtrsim 10^{10} \text{ M}^{-1} \text{ s}^{-1}$ (i.e., diffusion

control) and decreases by about 0.3 per order of magnitude in k_{att} .

After the radicals have been formed by the attack of e_{aq}^{•-} on the substrate, their further fate is governed by the competition between dimerization and hydrogen abstraction. Phenyl radicals generally do not couple with each other,^[25] hence the absence of a dimerization product in the case of chlorobenzoate is consistent with expectation. On the other hand, the rate constants for the combination of two alkyl radicals respond only weakly to structure and substituents,^[26] which singles out the hydrogen abstraction as the controlling factor; and therefore both the reactivity of these radicals towards hydrogen donors and the availability as well as accessibility of such donors play a role. The ascorbate moiety is a classical donor, but in PAscH⁻ it is well shielded by the micelles. Consequently, PAscH⁻ favours dimerization through avoiding hydrogen abstraction; and for several of our substrates selecting this sacrificial donor is the only way to achieve dimerization. With AscH⁻, only radicals with little abstraction tendency can be dimerized with good yields, among them the highly stabilized aromatic ketyl radicals derived from acetophenone or benzaldehyde, the benzylic radical derived from benzyl chloride, and the fluorine-substituted radical derived from chlorodifluoroacetate. When the substrate itself or its reaction product is a good hydrogen donor, even PAscH⁻ no longer succeeds in effecting dimerization, as the cases of cysteine or the two aliphatic ketones highlight.

The unimpaired photoionizability of our catalyst by protonation (Figure 1b) finally allowed operation at pH 6, thereby extending the applicability to substrates that hydrolyse in the strongly basic medium of our previously reported laser-driven e_{aq}^{•-} sources.^[2,15] Examples are also contained in Table 1.

Conclusions

In summary, we have shown that SDS-micellized 2-aminoanthracene as catalyst and ascorbyl palmitate as sacrificial donor constitute a workable system for laser-induced dimerisations

with hydrated electrons. Our experiments on short and long timescales have identified the three factors responsible for the good efficiency. First, this catalyst has a high electron output, with one-half its concentration ionized by a single ns flash of an unfocussed 355 nm laser; second, the sacrificial donor restores the starting catalyst on a sub- μ s timescale and practically quantitatively, which provides the key to many ionization cycles; and third, the micelle adds the final touch by isolating the electron source from its aggressive product and the subsequent species. In conjunction, these three characteristics afford relatively high local radical concentrations when the hydrated electrons attack a substrate by dissociative electron transfer, which is a fast process on account of the extreme reducing power; but the system itself exhibits a low hydrogen-donating propensity, such that radical dimerization is the preferred outcome, and in several cases even nearly quantitative. Very gratifying is the turnover rate on the order of 1 mmol h^{-1} , which is another direct consequence of the high photon flux provided by the pulsed laser.

Conflict of interest

The authors declare no conflict of interest.

Keywords: hydrated electrons • laser chemistry • photocatalysis • radical reactions • sustainable chemistry

- [1] S. P. Pitre, C. D. McTiernan, J. C. Scaiano, *Acc. Chem. Res.* **2016**, *49*, 1320–1330.
- [2] M. Brautzsch, C. Kerzig, M. Goez, *Green Chem.* **2016**, *18*, 4761–4771.
- [3] X. Allonas, C. Croutxe-Barghorn, J.-P. Fouassier, J. Laveve, J.-P. Malval, F. Morlet-Savary in *Lasers in Chemistry* (Ed.: M. Lackner), Wiley-VCH, Weinheim, **2008**.
- [4] Y.-L. Zhang, Q.-D. Chen, H. Xia, H.-B. Sun, *Nano Today* **2010**, *5*, 435–448.
- [5] C. F. Koch, S. Johnson, D. Kumar, M. Jelinek, D. B. Chrisey, A. Doraiswamy, C. Jin, R. J. Narayan, I. N. Mihailescu, *Mater. Sci. Eng. C* **2007**, *27*, 484–494.
- [6] G. V. Buxton, C. L. Greenstock, W. P. Heiman, A. B. Ross, *J. Phys. Chem. Ref. Data* **1988**, *17*, 513–886.
- [7] R. Naumann, F. Lehmann, M. Goez, *Angew. Chem. Int. Ed.* **2018**, *57*, 1078–1081; *Angew. Chem.* **2018**, *130*, 1090–1093.
- [8] C. Kerzig, X. Guo, O. S. Wenger, *J. Am. Chem. Soc.* **2019**, *141*, 2122–2127.
- [9] H. Park, C. D. Vecitis, J. Cheng, W. Choi, B. T. Mader, M. R. Hoffmann, *J. Phys. Chem. A* **2009**, *113*, 690–696.
- [10] X. Li, J. Ma, G. Liu, J. Fang, S. Yue, Y. Guan, L. Chen, X. Liu, *Environ. Sci. Technol.* **2012**, *46*, 7342–7349.
- [11] Z. Song, H. Tang, N. Wang, L. Zhu, *J. Hazard. Mater.* **2013**, *262*, 332–338.
- [12] P. Neta, J. Grodkowski, A. B. Ross, *J. Phys. Chem. Ref. Data* **1996**, *25*, 709–1050.
- [13] G. J. Rowlands, *Tetrahedron* **2009**, *65*, 8603–8655.
- [14] M. B. Smith, J. March, *March's Advanced Organic Chemistry*, Wiley, Hoboken, 6th ed., **2007**.
- [15] C. Kerzig, M. Goez, *Phys. Chem. Chem. Phys.* **2015**, *17*, 13829–13836.
- [16] T. Kohlmann, R. Naumann, C. Kerzig, M. Goez, *Photochem. Photobiol. Sci.* **2017**, *16*, 1613–1622.
- [17] U. Lachish, A. Shafferman, G. Stein, *J. Chem. Phys.* **1976**, *64*, 4205–4211.
- [18] T. Kohlmann, R. Naumann, C. Kerzig, M. Goez, *Photochem. Photobiol. Sci.* **2017**, *16*, 185–192.
- [19] C. Kerzig, M. Hoffmann, M. Goez, *Chem. Eur. J.* **2018**, *24*, 3038–3044.
- [20] J. Narkiewicz-Michalek, M. Szymula, C. Bravo-Diaz in *Trends in Colloid and Interface Science XXIV*, Springer, Berlin, **2011**, pp. 183–187.
- [21] M. Rossberg, W. Lendle, G. Pfeleiderer, A. Tögel, E.-L. Dreher, E. Langer, H. Rassaerts, P. Kleinschmidt, H. Strack, R. Cook, U. Beck, K.-A. Lipper, T. R. Torkelson, E. Löser, K. K. Beutel, T. Mann in *Ullmann's Encyclopedia of Industrial Chemistry*, Wiley-VCH, Weinheim, **2000**.
- [22] A. U. Meyer, T. Slanina, A. Heckel, B. König, *Chem. Eur. J.* **2017**, *23*, 7900–7904.
- [23] R. Matsubara, T. Yabuta, U. M. Idros, M. Hayashi, F. Ema, Y. Kobori, K. Sakata, *J. Org. Chem.* **2018**, *83*, 9381–9390.
- [24] M. Neumeier, D. Sampedro, M. Májek, V. A. D. L. P. O'Shea, A. Jacobi von Wangelin, R. Pérez-Ruiz, *Chem. Eur. J.* **2018**, *24*, 105–108.
- [25] R. G. Kryger, J. P. Lorand, N. R. Stevens, N. R. Herron, *J. Am. Chem. Soc.* **1977**, *99*, 7589–7600.
- [26] P. Neta, M. Simic, E. Hayon, *J. Am. Chem. Soc.* **1969**, *73*, 4207–4213.

Manuscript received: April 8, 2019
Revised manuscript received: May 2, 2019
Accepted manuscript online: May 6, 2019
Version of record online: July 3, 2019

7.5 Publikation E

Chemistry—A European Journal

Full Paper
doi.org/10.1002/chem.202001956

■ Laser Chemistry

Laser Access to Quercetin Radicals and Their Repair by Co-antioxidants

Tim Kohlmann and Martin Goez*^[a]

Abstract: We have demonstrated the feasibility and ease of producing quercetin radicals by photoionization with a pulsed 355 nm laser. A conversion efficiency into radicals of 0.4 is routinely achieved throughout the pH range investigated (pH 2–9), and the radical generation is completed within a few ns. No precursor other than the parent compound is needed, and the ionization by-products do not interfere with the further fate of the radicals. With this generation method, we have characterized the quercetin radicals and studied the kinetics of their repairs by co-antioxidants such as ascorbate and 4-aminophenol. Bell-shaped pH de-

pendences of the observed rate constants reflect opposite trends in the availability of the reacting protonation forms of radical and co-antioxidant and even at their maxima mask the much higher true rate constants. Kinetic isotope effects identify the repairs as proton-coupled electron transfers. An examination of which co-antioxidants are capable of repairing the quercetin radicals and which are not confines the bond dissociation energies of quercetin and its monoanion experimentally to 75–77 kcal mol⁻¹ and 72–75 kcal mol⁻¹, a much narrower interval in the case of the former than previously estimated by theoretical calculations.

Introduction

Quercetin (for the structural formula see Scheme 2) is one of the most abundant representatives of the flavonoid antioxidants, a subgroup of the polyphenols, and boasts of an activity four times as high as that of α -tocopherol (vitamin E) or ascorbate (vitamin C).^[1] An impressive collection of other health benefits has been reported, including antihypertensive,^[2] cardioprotective,^[3] antithrombotic as well as anti-inflammatory,^[4] antitumor,^[5] and antiviral effects, the latter in particular against RNA viruses such as SARS-CoV,^[6] MERS-CoV,^[7] Ebola-CoV,^[8] Zika-CoV,^[9] and possibly SARS-CoV-2.^[10]

The oral bioavailability of quercetin is severely limited by its low solubility in water, hence carriers^[6] or glucosylation^[7–9] have been tested to overcome that limitation. An alternative strategy—although the link between the antioxidative and the other health-protecting properties of quercetin is not clearly proven yet—is provided by redox cycling with the aid of a hydrophilic co-antioxidant exhibiting higher plasma levels such as ascorbate, which repairs the oxidized quercetin radicals.

There is indeed evidence that the antioxidant activity of quercetin is substantially improved by,^[11] and that its antitumor and antiviral potency even relies crucially on,^[12,13] the presence of ascorbate. Yet, and despite nearly 80 000 publications on quercetin listed by SciFinder to date, very little is known about the repair of its radicals by ascorbate and related co-antioxidants. Practically all such investigations were carried out through incubation experiments on long timescales,^[14] which inherently can only yield indirect information on the fast processes and are prone to interpretational ambiguities because the quercetin oxidation products may themselves function as secondary antioxidants.^[15–17] To our knowledge, there have only been two kinetic studies on short timescales,^[18,19] and both used pulse radiolysis with its innate problems of delayed quercetin radical generation through scavenging, as well as a considerable number of transients and reactions interacting simultaneously.

Herein, we explore an alternative approach, which we have already successfully applied to the antioxidant resveratrol,^[20] namely, direct generation of the quercetin radicals by laser-induced photoionization. As we will show, this access to the radicals is not only completely selective over a wide pH range but also quasi-instantaneous compared to the subsequent reactions of the radicals, such that the repair kinetics can be observed in isolation, their complicated pH dependence can be unravelled, and the bond dissociation energy of quercetin can be bracketed experimentally with a significantly lower uncertainty compared to reported quantum-mechanical estimates.

Experimental Section

All chemicals were used as received in the purity specified by the manufacturer (Sigma–Aldrich; quercetin, > 96%; sodium ascorbate,

[a] T. Kohlmann, Prof. Dr. M. Goez
Martin-Luther-Universität Halle-Wittenberg
Institut für Chemie
Kurt-Mothes-Str. 2, 06120 Halle (Saale) (Germany)
E-mail: martin.goez@chemie.uni-halle.de

The ORCID identification number(s) for the author(s) of this article can be found under:
<https://doi.org/10.1002/chem.202001956>.

© 2020 The Authors. Published by Wiley-VCH GmbH. This is an open access article under the terms of Creative Commons Attribution NonCommercial License, which permits use, distribution and reproduction in any medium, provided the original work is properly cited and is not used for commercial purposes.

$\geq 99.0\%$; ascorbic acid, $\geq 99.7\%$; 4-aminophenol, $> 98\%$; Trolox, 97% ; hydroquinone, $> 98\%$; NaOH, 99% ; HCl, 99%). The solvent was ultrapure Millipore Milli-Q water (specific resistance, $18.2 \text{ M}\Omega \text{ cm}^{-1}$) or—for measuring the H/D kinetic isotope effects— D_2O (99.9% deuteration, DEUTERO).

The solutions were deoxygenated with argon, or with N_2O when the hydrated electron had to be blanked out as explained in the main text, for at least 30 minutes. Both gases were of purity 5.0 and obtained from AirLiquide. The quercetin weight-in concentration was $5 \mu\text{M}$ throughout, which kept the solutions optically thin and thus avoided filter effects caused by nonlinear absorption. The desired pH values were adjusted under pH meter control by the addition of NaOH or HCl. All measurements were carried out at room temperature.

Mechanistic and kinetic experiments studies were performed on a home-made laser flash photolysis setup described elsewhere.^[21] Its main characteristics pertinent to this investigation are excitation with a frequency-tripled (355 nm) pulsed Nd:YAG laser (Continuum Surelite-III; pulse width, ca. 5 ns); homogeneous illumination of the observed volume (window, $2 \times 4 \text{ mm}$; optical path length, 4 mm) in a suprasil flow cell; detection at right angles to the excitation beam and with a time resolution down to 1 ns.

The steady-state absorption and the fluorescence spectra were recorded on a Shimadzu UV-1800 spectrophotometer and an Edinburgh Instruments FS5 TCSPC spectrometer.

Results and Discussion

Access to the quercetin radicals

Figure 1 focuses on the photophysics of quercetin as far as is essential for this work. The antioxidant exists in five protonation states with typical separations between pK_a values by less than 2 units,^[22] which is comparable to the spread of the reported individual values (e.g., between 5.50 and 7.65 for the lowest pK_a).^[22,23] Herein, only the fully protonated and singly deprotonated forms H_2Q and HQ^- (for the structures see the summarizing Scheme 2) play a role because we observed sample deterioration above pH 9 on the timescale of 1–2 h, which restricted the pH range accessible to our experiments.

The complexity of the system is reflected by the pH-dependent absorption spectra of Figure 1a, which exhibit no well-defined isosbestic points; however, 376 nm provides a good approximation of such a point up to $\text{pH} \approx 8.5$, i.e., except for the highest pH in Figure 1. Excitation at 376 nm thus allowed recording the fluorescence spectra (Figure 1b) with no, or only a minor ($\approx 7\%$) correction. At the wavelength of our ionizing laser, 355 nm, the profile displayed as the inset of Figure 1a can be fitted with a titration curve with a pK_a of 7.5, although no plateau value is reached at the high-pH end of the region. The observed ground-state extinction coefficient ϵ_{GS} decreases by about one third when going from pH 4 to pH 9. This reduces the rate of excitation by our laser in proportion but does not cause sensitivity problems because ϵ_{GS} is still quite high in the basic medium.

The absorption-corrected fluorescence spectra of Figure 1b clearly show a weakly emitting species at lower pH and a much more strongly emitting species at higher pH, with emission maxima at 521 nm and 554 nm. A profile at the longer wavelength (see, inset of the Figure) is represented well by a titration curve with a pK_a of 7.3. On account of the distinct and complete curve shape, we regard this pK_a —which hardly differs from the above one—as reliable; and we interpret the data of Figure 1 by absorption of, and emission from, the same protonation state, the concentration of which is determined by the ground-state equilibrium between H_2Q and HQ^- , with pertaining pK_a of 7.3. Phenols are more acidic in the excited S_1 state compared to the ground state,^[24] hence, the obvious absence of proton transfer in the excited state points to a very short S_1 lifetime.

Laser flash photolysis at 355 nm affords transient spectra that can be decomposed into the spectral signatures displayed in Figure 2a. The occurrence of the hydrated electron e_{aq}^- is evidenced by its characteristic strong and broad absorption with maximum at about 720 nm, and by the fact that this spectral feature is absent when the solution has been saturated with the specific e_{aq}^- scavenger N_2O or when the pH lies below about 2. Both N_2O and H^+ are known to react diffusion-con-

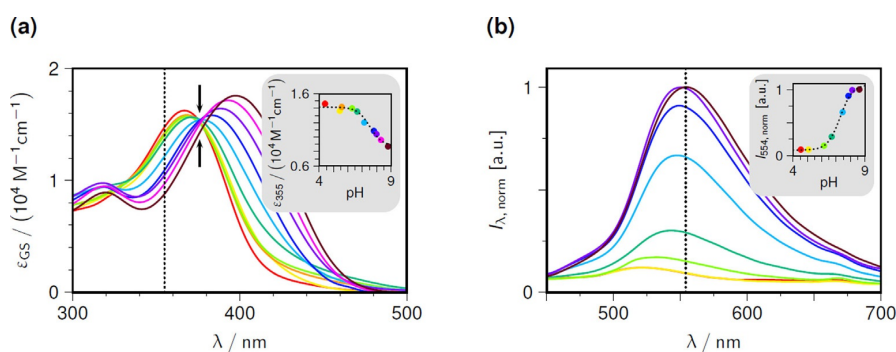


Figure 1. Photophysics of quercetin ($5.05 \mu\text{M}$) in homogeneous aqueous solution at different pH (between 4.4 and 8.8; identical colour coding between inset and main plot of each subfigure). Graph (a): main plot, ground-state absorption spectra, with the dotted line and the arrows indicating our photoionization wavelength (355 nm) and the approximate isosbestic point (376 nm); inset, pH dependence of the observed extinction coefficient at 355 nm, with the dotted best-fit titration curve corresponding to a pK_a of 7.5. Graph (b): main plot, fluorescence spectra upon excitation at 376 nm, after pH-dependent correction for ϵ_{376} and normalization to the maximum (554 nm) at the highest pH; inset, profile at 554 nm (as indicated by the dotted line in the main plot), with dotted best-fit titration curve yielding a pK_a of 7.3. For further explanation, see the text.

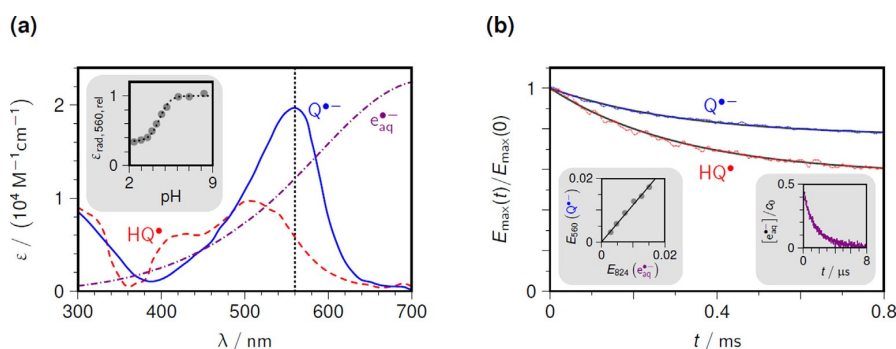


Figure 2. Characterization of the intermediates (radical anion $Q^{\bullet-}$, blue; neutral radical HQ^{\bullet} , red; hydrated electron $e_{aq}^{\bullet-}$ violet) following quercetin photoionization in homogeneous aqueous solution. Graph (a): main plot, calibrated absorption spectra corrected for absorption of the starting quercetin; inset, pH dependence of the apparent extinction coefficient of the quercetin radicals at 560 nm ($pK_a = 4.5$, from the dotted best-fit titration curve). Graph (b): main plot, slow decays of the relative absorptions at 560 nm of $Q^{\bullet-}$ (pH 8.2) and HQ^{\bullet} (pH 2.3) superimposed on monoexponential fits (gray curves) with global rate constant of $1/(320 \mu\text{s})$ and local end values of 0.76 and 0.57; right inset, fast $e_{aq}^{\bullet-}$ decay (pH 8.2) from a starting concentration c_0 of about $2.2 \mu\text{M}$; left inset, illustration of the spectral calibration of $Q^{\bullet-}$ at pH 8.2 by comparing the initial extinctions E of $Q^{\bullet-}$ at 560 nm and of $e_{aq}^{\bullet-}$ at 824 nm. For further explanation, see the text.

trolled with $e_{aq}^{\bullet-}$ to give the nonabsorbing radicals HO^{\bullet} and H^{\bullet} ,^[25] and under the described conditions the life of $e_{aq}^{\bullet-}$ is shortened so much (to a few ns, which is the duration of our laser pulses) as to render it undetectable. These observations thus identify the laser-induced process as a photoionization.

When $e_{aq}^{\bullet-}$ is blanked out by N_2O saturation, the transient spectra of the accompanying quercetin-derived radicals are obtained in pure form because any subsequent attack of HO^{\bullet} on residual HQ^{\bullet} or H_2Q affords the same radical as the photoionization does.^[27] By the two independent procedures described below, we calibrated the spectra and corrected them for depletion of the starting quercetin (Figure 2a). In accordance with a pulse-radiolytic study and a theoretical investigation, which concluded that the radical cation initially resulting from H_2Q is deprotonated quasi-instantaneously,^[19,28] the limiting spectra at the low and high ends of our pH range are assigned to the neutral radical HQ^{\bullet} and the radical anion $Q^{\bullet-}$ (see Scheme 2). Compared to the previously reported experimental results,^[19] we find a similar pK_a of HQ^{\bullet} (4.5, i.e., higher by 0.3 units) but much higher extinction coefficients at maximum ($19750 \text{ M}^{-1} \text{ cm}^{-1}$ and $9700 \text{ M}^{-1} \text{ cm}^{-1}$ for $Q^{\bullet-}$ and HQ^{\bullet} ; i.e., higher by factors of about 2 and 4). These observations strongly suggest the spectral calibration as the origin of the discrepancies because a calibration error will additionally distort the weaker and hypsochromic absorption of HQ^{\bullet} (maximum at 510 nm, i.e., in the outer wing of the longest-wavelength bands in Figure 1a) through depletion of the starting quercetin, whereas that effect is absent for the stronger and bathochromic absorption of $Q^{\bullet-}$ (maximum at 560 nm); and calibration errors cancel to first order in the pK_a determination at the maximum of the $Q^{\bullet-}$ band.

Figure 2b addresses the post-generation fate of the transients. Both HQ^{\bullet} and $Q^{\bullet-}$ are seen to be intrinsically long-lived intermediates that decay on the timescale of a few hundreds of μs to give other absorbing species. A successful global fit of a first-order kinetic model indicates that the rate constants of these transformations are independent of pH, and that the ex-

tinction coefficients of the products are similar to, but slightly smaller than, those of $Q^{\bullet-}$ and HQ^{\bullet} , respectively. The products are most likely different protonation states of the structure displayed at the lower right in Scheme 2,^[29] but further characterization was not warranted because these conversions fall outside the temporal window of the repair reactions by our co-antioxidants.

In contrast to the quercetin-derived radicals, the natural decay of $e_{aq}^{\bullet-}$ occurs within a few μs in basic medium (see, right inset of the Figure) and increasingly more rapidly when the pH is lowered. This has two implications. On one hand, an attack of $e_{aq}^{\bullet-}$ on H_2Q or HQ^{\bullet} plays no role in this work because the μM concentrations render these reactions noncompetitive; and the same holds true for HO^{\bullet} when N_2O saturation is employed, or for H^{\bullet} when $e_{aq}^{\bullet-}$ is generated in acidic medium. On the other hand, down to about pH 3 the life of $e_{aq}^{\bullet-}$ is long enough for precise determinations of the initial post-flash concentrations, which in turn provides the basis for our first calibration procedure: On the premise that the ejection of $e_{aq}^{\bullet-}$ is the only pathway to the quercetin radicals, stoichiometric equivalence demands a proportionality between the ratio of the extinctions and that of the extinction coefficients. The possibility of blanking out $e_{aq}^{\bullet-}$ makes this a trivial task. First, the superposition of the absorptions of $e_{aq}^{\bullet-}$ plus HQ^{\bullet} and/or $Q^{\bullet-}$ is recorded in argon-saturated solution; then, N_2O saturation is used to record only the absorptions of the quercetin radicals; and a difference of the two measurements yields the pure $e_{aq}^{\bullet-}$ absorption. The concentrations of the transients are varied most conveniently through the laser intensity. The left inset of Figure 2b illustrates the proportionality for the spectral maximum of $Q^{\bullet-}$ (560 nm) and a convenient wavelength for $e_{aq}^{\bullet-}$ (not the 720 nm maximum but 824 nm, entirely for technical reasons).^[30]

Obviously, the validity of this calibration approach hinges on the absence of homolytic photodissociation of the O–H bond as a major pathway to the quercetin radicals that bypasses photoionization. However, this assumption is very reasonable

because for phenols in water the quantum yields of such homolyses are known to be practically zero.^[31] This is corroborated by juxtaposing the photolyses at pH 5.8 and pH 8.2. These start out near quantitatively from H₂Q and from HQ⁻ (including their S₁ states as discussed above), and despite significantly different bond dissociation energies (according to the literature: 77.2 ± 5.9 kcal mol⁻¹ for H₂Q;^[28,32–35] and 73.0 ± 2.1 kcal mol⁻¹ for HQ⁻)^[28,32,35] yield practically the same calibrated extinction coefficient of Q⁻ (with HQ⁻ accounting for less than 5% in both experiments). It is also vindicated by our second calibration procedure (see next section).

Figure 3 finally deals with the efficiency of the photoionization access to the quercetin radicals. The intensity dependences of the e_{aq}⁻ concentrations (main plot) show that more than 40% of the starting quercetin can be converted into radicals by a single laser pulse, meaning that radical concentrations of 2 μM are routinely attainable in situ and within 5 ns. Surprisingly, the protonation state of the quercetin plays only an insignificant role: at given laser intensity, H₂Q (at pH 5) and HQ⁻ (above pH 8) afford e_{aq}⁻ concentrations that are so similar as to fall nearly within the margin of experimental error.

Phenol(ate) ionizations are known to be biphotonic.^[31] In apparent opposition, no dependence of the e_{aq}⁻ yield on the square of the laser intensity is discernible, but it is well understood that unfavourable combinations of parameters often prevent a clear manifestation of this limiting relationship.^[30,36] As the best-fit curve to a biphotonic ionization model in the main plot of Figure 3 shows, the validity of the quadratic approximation is restricted to an almost imperceptibly small range near the origin. More importantly, the fit converges on complete ionization at infinite intensity, in other words, suggests that homolytic dissociation of the phenolate O–H bond is absent under our conditions, which further supports our above calibration of the extinction coefficients of the quercetin radicals.

The unexpectedly negligible influence on the e_{aq}⁻ yield of the decrease of the ground-state extinction coefficient by 30% when going from HQ⁻ to H₂Q is revealed most clearly by the

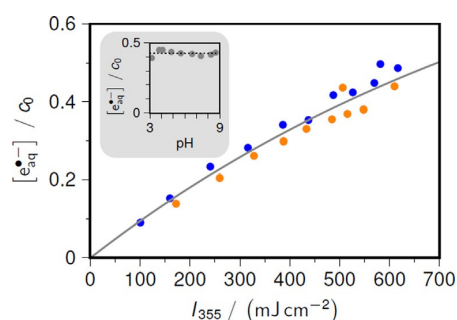


Figure 3. Photoionization process of quercetin in homogeneous aqueous solution. Main plot, dependence of the e_{aq}⁻ yields relative to the quercetin weight-in concentration c₀ (5 μM) on the laser intensity I₃₅₅. Blue data points, pH 8.1; orange data points, pH 5.0. The solid curve is the fit of a biphotonic model to all data; best-fit limiting e_{aq}⁻ yield at infinite intensity, 100%; other fit parameters without relevance. Inset, pH dependence of relative e_{aq}⁻ yield at I₃₅₅ = 507 mJ cm⁻². For further explanation, see the text.

absence of a pH dependence at constant laser intensity in the inset of the Figure. The reason must be an accidental cancellation by different extinction coefficients of, lifetimes of, and photodetachment efficiencies from, the excited states of H₂Q and HQ⁻. All these parameters are inaccessible to our experiments on ns timescales, but in the context of this work, their knowledge is also irrelevant. It is sufficient that photoionization of quercetin, regardless of whether it is present as H₂Q or HQ⁻, with a 355 nm laser provides a direct access to useable concentrations of quercetin radicals, as the experiments of this section have demonstrated and Scheme 2 at the end of this “Results and Discussion” section sums up.

Repair reactions by co-antioxidants

Whereas transformations of HQ⁻ and/or Q⁻ on their own are hardly noticeable during the first 20 μs after the generating laser flash, the addition of the archetypal co-antioxidant ascorbate changes the situation. Figure 4a epitomizes the effects, on which our second procedure for calibrating the extinction coefficients of the quercetin radicals is based.

The experimental pH of 6.5 ensures a single protonation state for the quercetin radicals and for the ascorbate, namely, Q⁻ and the monoanion HAsc⁻ (compare Scheme 1; HAsc⁻ is completely transparent above 320 nm). The same condition is fulfilled for the ascorbyl radical Asc⁻ (Scheme 1), which has an absorption maximum at 360 nm with an extinction coefficient of 4500 M⁻¹ cm⁻¹.^[26] Best suited for observation at this pH are thus 560 nm (maximum of the Q⁻ absorption) and 360 nm. The former wavelength responds to Q⁻ only whereas the latter captures Q⁻, depletion of quercetin, and Asc⁻.

We stress that all three contributions are already present directly after the laser flash, i.e., at 0 μs: because the experiment is performed in N₂O saturated solution, e_{aq}⁻ yields HO[•] within nanoseconds; in turn, HO[•] is scavenged even faster by the high concentration of HAsc⁻ (100 mM) to give Asc⁻; in sum, e_{aq}⁻ is thus quantitatively and quasi-instantaneously converted into Asc⁻. Experimental proof is provided by comparing the initial absorption at 360 nm, which deceptively lies near zero, with that in a control experiment without HAsc⁻ but under otherwise identical conditions. The negative and persistent transient absorption in the control experiment reveals the true contributions of Q⁻ and quercetin depletion. In the experiment with ascorbate, a transient spectrum after 15 μs is completely dominated by the band of Asc⁻, which identifies the main reaction as the repair of the quercetin radical, in accordance with expectation.

The absorption trace at 560 nm does not decay to zero but to a small residual value, about 4% of the initial absorption, on account of the competition of the repair with the natural conversion of Q⁻ into an unspecified absorbing product (compare, Figure 2b). However, at 360 nm that product and Q⁻ must have practically the same extinction coefficient, as is evident from the constant absorption trace in the control experiment. After the straightforward and very small corrections for the described side reaction, the final absorption at 360 nm in the experiment with ascorbate is proportional to twice the extinction

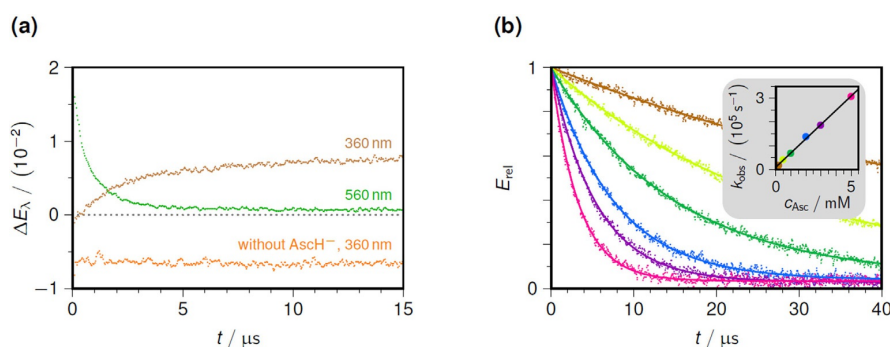
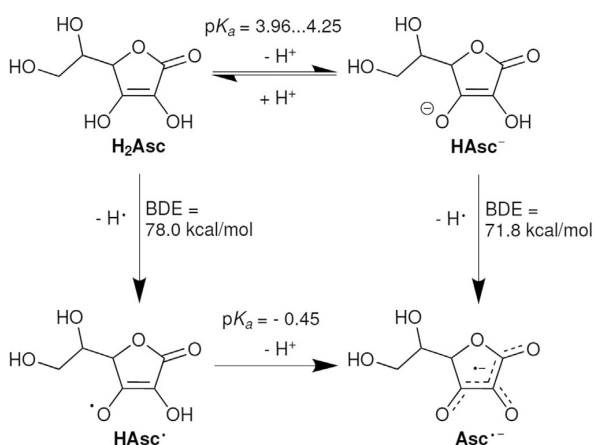


Figure 4. Repair of the quercetin radical (about $2.1 \mu\text{M}$) by ascorbate in homogeneous aqueous solution saturated with N_2O . Graph (a): extinction traces ΔE_λ used for calibrating ε_{max} of $\text{Q}^{\cdot-}$; pH 6.5; ascorbate weight-in concentration, 100 mM and 0 mM (control experiment). Green trace, 560 nm; detection of $\text{Q}^{\cdot-}$. Brown and orange traces, 360 nm; superposition of (starting) quercetin depletion, $\text{Q}^{\cdot-}$ decay, and $\text{Asc}^{\cdot-}$ formation (not in the control experiment without ascorbate). The dotted gray line ($\Delta E=0$) serves to guide the eye. Graph (b): dependence of the observed repair rate constant k_{obs} on the ascorbate weight-in concentration c_{Asc} (color-coded identically in the main plot and the inset) at pH 4.25. Main plot, decay curves of the quercetin radicals, measured through the extinctions E_{rel} (at 515 nm, each curve normalized to the initial post-flash value) with overlaid best fits of pseudo first-order decays to a residual floor; inset, Stern–Volmer plot giving an apparent bimolecular rate constant of $6.0 \times 10^7 \text{ M}^{-1} \text{ s}^{-1}$. For further explanation, see the text.



Scheme 1. Relations between the ascorbate-derived species relevant for this work, with $\text{p}K_{\text{a}}$ values^[37–39] and bond dissociation energies (BDEs)^[39] taken from the literature.

coefficient of $\text{Asc}^{\cdot-}$; and the constant of proportionality is the same as that between the initial absorption and the extinction coefficient of $\text{Q}^{\cdot-}$ in the 560 nm trace.

The extinction coefficients obtained by this second calibration procedure (standard, $\text{Asc}^{\cdot-}$) and by the above-described first one (standard, $\text{e}_{\text{aq}}^{\cdot-}$) differ by 2% only. This consistency not only lends support to the much higher value herein compared to the literature^[19] but also, and far more importantly, establishes that $\text{Q}^{\cdot-}$ is exclusively formed through photoionization and not to any significant degree through homolytic photocleavage of the O–H bond.

Even though the maximum of the $\text{Q}^{\cdot-}$ absorption band (560 nm) intuitively appears best suited for observation, two considerations were instrumental for our choice of a shorter monitoring wavelength for all further experiments of this Section, namely, 515 nm. First, the sensitivity of our detection system is noticeably higher at 515 nm; and second, the dy-

namic range of the detection signal is better equalized at 515 nm when the pH is varied (compare the spectra of HQ^{\cdot} and $\text{Q}^{\cdot-}$ in Figure 2a). By control experiments, we established that the decay curves at the two wavelengths are linear functions to one another.

On the basis of the first-order intrinsic decay (Figure 2b), the repair is expected to obey Stern–Volmer kinetics. Figure 4b illustrates that this surmise holds true, and that the pseudo first-order rate constant k_{obs} at constant pH is a linear function of the ascorbate weight-in concentration c_{Asc} . However, the apparent bimolecular rate constant obtained from the slope in the inset is not meaningful per se, on account of a pronounced and intriguing pH dependence, which Figure 5a investigates at constant c_{Asc} . The relationship is seen to be a bell-shaped curve with an asymmetric tail to the side of higher pH. For improved precision, we measured $k_{\text{obs}}(\text{pH})$ in that region with a higher c_{Asc} (100 mM) and recalculated it to c_{Asc} of the rest of the data (5 mM) as in Figure 4b.

In the pH range from 2 to 9, the quercetin radicals can exist as HQ^{\cdot} or $\text{Q}^{\cdot-}$ and ascorbate as the acid H_2Asc or the monoanion HAsc^- ; hence, four combinations of radical and co-antioxidant need to be taken into account. However, a significant involvement of the pair $\text{HQ}^{\cdot}/\text{H}_2\text{Asc}$ is immediately ruled out by the evident decrease of $k_{\text{obs}}(\text{pH})$ towards zero in acidic medium, where HQ^{\cdot} and H_2Asc are present practically exclusively.

By contrast, a reaction between $\text{Q}^{\cdot-}$ and HAsc^- clearly takes place, as is manifest from the constant nonzero rate constant in the higher pH range where $\text{Q}^{\cdot-}$ and HAsc^- are the only protonation forms. This process adds a contribution $k'(\text{pH})$ to k_{obs} [Eq. (1)]

$$k'(\text{pH}) = k_{\text{dep}} \times \frac{1}{1 + 10^{\text{p}K_{\text{a}1} - \text{pH}}} \times \frac{1}{1 + 10^{\text{p}K_{\text{a}2} - \text{pH}}} \quad (1)$$

where k_{dep} —the true, pH-independent rate constant of the reaction between $\text{Q}^{\cdot-}$ and HAsc^- —constitutes the upper limit of

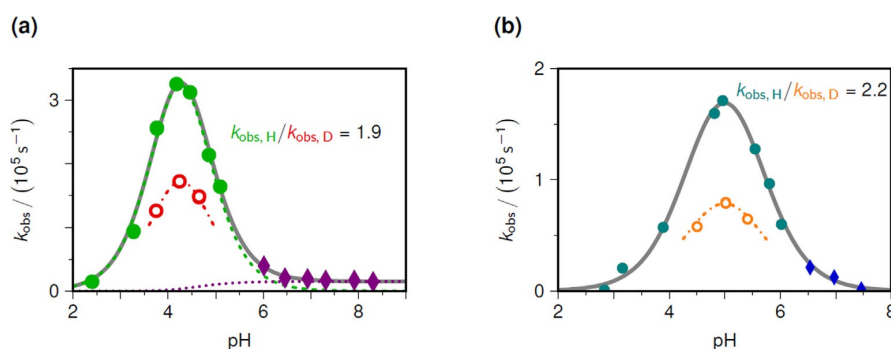


Figure 5. Influence of pH and isotope substitution on the repair of the quercetin radicals (initial concentration, about $2\mu\text{M}$) by the co-antioxidants ascorbate (graph (a)) and 4-aminophenol (graph (b)) in homogeneous aqueous solution, observation at 515 nm. Shown are the observed pH-dependent pseudo first-order rate constants k_{obs} at constant co-antioxidant weight-in concentration (circles, 5 mM; diamonds, 100 mM (a) and 50 mM (b), both recalculated to 5 mM). The solid gray curves are the best fits: (a), composed of Equations (1) and (4), with the individual contributions displayed as dashed green and dotted magenta curves; (b) Equation (4) only. Fixed parameter, $\text{p}K_{\text{a}1}$, 4.50. Best-fit parameters in (a) and (b): $\text{p}K_{\text{a}2}$, 4.02 and 5.51; k' , $1.5 \times 10^4 \text{ s}^{-1}$ and not applicable in the case of (b); k , $8.05 \times 10^5 \text{ s}^{-1}$ and $3.02 \times 10^6 \text{ s}^{-1}$. Open circles and dashed-dotted curves, experiments in D_2O under otherwise identical conditions, with limited pD variation and fit for bracketing the maximum and ensuring equal vertical scaling factor [Eq. (5)]. For further explanation, see the text.

$k'(\text{pH})$, which is approached at high pH. Equation 1 is seen to remain invariant when $\text{p}K_{\text{a}1}$ and $\text{p}K_{\text{a}2}$ are interchanged; its plot is virtually indistinguishable from a titration curve characterized by the higher of the two $\text{p}K_{\text{a}}$ values as long as $|\text{p}K_{\text{a}1} - \text{p}K_{\text{a}2}|$ is larger than about 1.5; and when that absolute difference becomes smaller, the mid-point slightly shifts to higher pH, with a maximum deviation of 0.4 pH units being reached for identical $\text{p}K_{\text{a}}$ values.

The two “mixed” reactions, between one protonated and one deprotonated species, are indistinguishable by their pH dependence: in terms of the average \bar{M} and the half-difference $\bar{\Delta}$ of the two $\text{p}K_{\text{a}}$ values [Eq. (2), Eq. (3)]

$$\bar{M} = \frac{\text{p}K_{\text{a}1} + \text{p}K_{\text{a}2}}{2} \quad (2)$$

$$\bar{\Delta} = \frac{\text{p}K_{\text{a}1} - \text{p}K_{\text{a}2}}{2} \quad (3)$$

their rate constant $k(\text{pH})$ can be formulated to give [Eq. (4)]

$$k(\text{pH}) = k_{\text{mix}} \times \frac{1}{1 + 10^{\text{pH} - \text{p}K_{\text{a}1}}} \times \frac{1}{1 + 10^{\text{p}K_{\text{a}2} - \text{pH}}} = k_{\text{mix}} \times \frac{10^{\bar{\Delta}}}{10^{\bar{\Delta}} + 10^{-\bar{\Delta}} + 10^{\bar{M} - \text{pH}} + 10^{\text{pH} - \bar{M}}} \quad (4)$$

The invariance of the denominator of the final expression with respect to an interchange of $\text{p}K_{\text{a}1}$ and $\text{p}K_{\text{a}2}$ is obvious. Equation (4) has been set up for species 1 reacting in its protonated form and species 2 in its deprotonated form, but an interchange of the two species, tantamount to an interchange of the two $\text{p}K_{\text{a}}$ values, thus merely leads to a scaling of the numerator that cannot be separated from a different value of k_{mix} .

To determine whether k_{mix} is the pH-independent rate constant of the reaction between HQ^{\cdot} and HAsc^- or that between $\text{Q}^{\cdot-}$ and H_2Asc (or a superposition of the two) and thereby to extract its correct numerical value, arguments outside mathematics have to be invoked. Fortunately, this is straightforward

in our system because HAsc^- is a far better antioxidant than is H_2Asc (compare the bond dissociation energies BDE in Scheme 1). Hence, we assign the mixed process exclusively to the repair of HQ^{\cdot} by HAsc^- . Even without knowledge of the BDE, this is entirely consistent with it being much faster than the high-pH repair of $\text{Q}^{\cdot-}$ by HAsc^- , meaning that HQ^{\cdot} is more reactive than is $\text{Q}^{\cdot-}$ and implying that a reaction between $\text{Q}^{\cdot-}$ and H_2Asc would be slower than the already unobservable one between HQ^{\cdot} and H_2Asc .

Equations (1) and (4) share the same $\text{p}K_{\text{a}}$ values, one of which (the $\text{p}K_{\text{a}}$ of HQ^{\cdot}) was determined herein under exactly the same experimental conditions. Because of considerable spread in the reported $\text{p}K_{\text{a}}$ of H_2Asc (between 3.96^[37] and 4.25^[38]), we treated that parameter as adjustable, in addition to k_{dep} and k_{mix} . The resulting three-parameter best fit of the sum of Equations (1) and (4) to $k_{\text{obs}}(\text{pH})$ is displayed in Figure 5a. As emerges from the separated contributions that have also been plotted, the fit is extremely well-conditioned because k_{dep} can practically be read off from the data in the region of high pH.

The fit converged near the lower of the two $\text{p}K_{\text{a}}$ values of H_2Asc cited above; and dividing k_{mix} and k_{dep} by c_{Asc} finally yielded the true second-order rate constants, $1.6 \times 10^8 \text{ M}^{-1} \text{ s}^{-1}$ and $3.0 \times 10^6 \text{ M}^{-1} \text{ s}^{-1}$ for the reactions of HAsc^- with HQ^{\cdot} and with $\text{Q}^{\cdot-}$.

Only two kinetic investigations on fast timescales were carried out on quercetin/ascorbate systems so far, and both were performed at a single pH only, 8.5^[18] or 10.8.^[19] The latter work lists a rate constant of $2.4 \times 10^5 \text{ M}^{-1} \text{ s}^{-1}$ but, according to the authors' conclusions, the quercetin radicals are doubly deprotonated at pH 10.8 (second $\text{p}K_{\text{a}}$, 9.4); hence, that rate constant applies to a reaction different from ours. From a highly complex kinetic modelling, the former study extracts a rate constant of $5.0 \times 10^6 \text{ M}^{-1} \text{ s}^{-1}$ for what must be the reaction between $\text{Q}^{\cdot-}$ and HAsc^- . Our result is 40% lower but we believe

it to be more reliable because we obtained it by direct kinetic measurements of the isolated process.

For the reaction between HQ[•] and HAsc^{•-}, no rate constant seems to have been reported to date. We stress that, in view of the bell-shaped pH dependence (Figure 5a) and its underlying formula, measurements at a single pH would have suggested values that are grossly too low: even if, through lucky coincidence, these experiments had been carried out at the maximum of the bell-shaped curve [Eq. (5)],

$$k(\text{pH} = \bar{M}) = k_{\text{mix}} \times \frac{10^{\bar{d}}}{2 + 10^{\bar{d}} + 10^{-\bar{d}}} \quad (5)$$

the pK_a-dependent fraction in Equation (5) would have necessitated a correction by a factor of 2.5 with our parameters (pK_{a1}–pK_{a2}=0.48) to obtain k_{mix} ; this would have risen to a factor of 4 if both pK_a values happened to be equal; and, from Equation (4), to much more if some pH in the outer wings of the curve had accidentally been chosen.

The regeneration of the quercetin from HQ[•] could be a concerted process (proton-coupled electron transfer PCET) or a sequential one (rate-determining electron transfer followed by proton transfer, SETPT; or rate-determining proton loss followed by electron transfer, SPLET). The pertinent pK_a values, 11.74 of HAsc^{•-} and –0.45 of HAsc[•],^[38,39] already disfavor SETPT and SPLET, and the H/D kinetic isotope effects (KIEs), which have also been included in Figure 5a, provide direct experimental evidence. SETPT could only lead to a small secondary KIE, and SPLET to a similarly small thermodynamic isotope effect on the deprotonation equilibrium of HAsc^{•-},^[40] whereas PCET is expected to exhibit a primary KIE.

Because all hydroxylic protons of quercetin and ascorbate are exchangeable and the reagent concentrations are very small, complete deuteration at the relevant positions is achieved before the start of the photoionization in D₂O. Determining KIEs for a reaction with complex pH dependence faces the problem that pK_a values in H₂O and D₂O might be slightly different; and the same applies to pH and pD readings. Potential pitfalls are thus comparing data at the maximum of the curve (Figure 5a) in one solvent with off-maximum data in the other solvent; and, independent from the former, overlooking different trailing fractions in Equation (5) caused by a discrepancy of $\bar{\Delta}$ in the two solvents. To avoid these sources of errors, we carried out a limited pD variation to localize the maximum in D₂O and to ensure that the width of the bell-shaped dependence, which is only related to $\bar{\Delta}$ but not to \bar{M} , does not change. Figure 5a displays the outcome, which gave the same $\bar{\Delta}$ in D₂O and apparently also the same \bar{M} as in H₂O. Although the latter might well be due to an equal influence of the deuterated solvent on the potential of the glass electrode, Equation (4) is insensitive to such a shift of the horizontal scale as a whole. Direct comparison of the maxima yields a KIE of 1.9, whose magnitude can only be reconciled with a primary KIE and thus the PCET mechanism.^[40]

Only an estimate can be given for the KIE in basic medium because the reaction in D₂O becomes so slow that the correction for the decay without quencher (compare, Figure 2b) en-

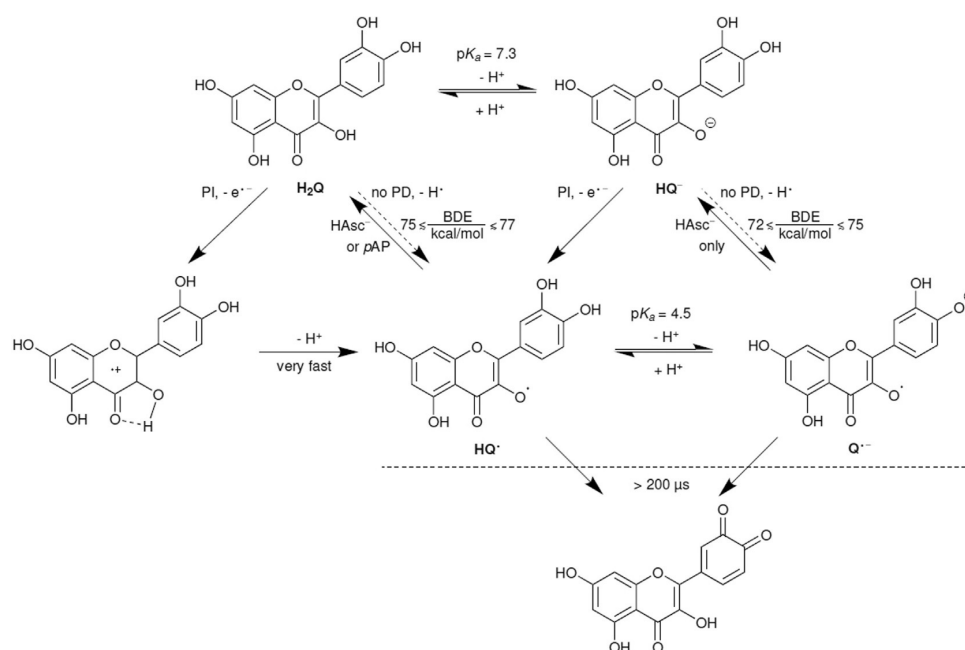
tails a rather large error. Single-point measurements at pH 8.0 gave a KIE between 3 and 5, which suggests a PCET mechanism for the repair of Q^{•-} by HAsc^{•-} as well.

Theoretical investigations report bond dissociation energies (BDEs) in aqueous solution between 71.3 kcal mol⁻¹ and 83.1 kcal mol⁻¹ for H₂Q,^[32,35] and between 70.9 kcal mol⁻¹ and 75.0 kcal mol⁻¹ for HQ^{•-}.^[32,35] Precise experimental values are unavailable, but our results of Figure 5a allow bracketing these key quantities, in particular that of H₂Q with a much lower uncertainty. A PCET is thermodynamically feasible when the BDE of the co-antioxidant is smaller than the BDE of the regenerated quercetin, each in its respective protonation state. The combination of no discernible repair of the quercetin radicals by H₂Asc (BDE, 78.0 kcal mol⁻¹)^[39] and successful repairs by HAsc^{•-} (BDE, 71.8 kcal mol⁻¹)^[39] thus puts a first upper and lower limit on the BDEs of H₂Q and HQ^{•-}; in full accordance with this, we found reduced glutathione (BDE, 87.2 kcal mol⁻¹)^[39] to be inoperative as a repairing agent; the upper boundary is substantiated and even slightly tightened by our observations that neither hydroquinone (BDE, 79.7 kcal mol⁻¹)^[39] nor a water-soluble analogue of α -tocopherol (Trolox; BDE, 76.7 kcal mol⁻¹)^[39] are capable of repairing the quercetin radicals in the pH range of Figure 5a, where no deprotonations of the co-antioxidant hydroxylic groups need to be taken into account; and our following experiments (Figure 5b), which demonstrate that *p*-aminophenol *p*AP (BDE, 75.0 kcal mol⁻¹)^[39] can repair HQ[•] but not Q^{•-}, both raise the lower limit for H₂Q and decrease the upper limit for HQ^{•-} still further.

The deprotonation of the phenolic OH-group of *p*AP falls outside the pH range investigated, but the amino group already becomes protonated in slightly acidic medium (pK_a, 5.48),^[41] whereby this phenol loses its good antioxidant properties. In line with expectation, no repair is thus observed at low pH, where only HQ[•] and N-protonated *p*AP exist. When the pH is raised, the increase of available co-antioxidant through deprotonation at N is countered by the transformation of HQ[•] into the less readily repaired Q^{•-}, such that again a bell-shaped pH dependence of k_{obs} results. On its high-pH side, however, no constant floor is detectable; hence, no repair of Q^{•-} by *p*AP occurs.

As the main difference to the ascorbate case of Figure 5a, $\bar{\Delta}$ [Eq. (3)] is negative for HQ[•]/*p*AP. From the above discussion it emerges that this does not influence the shape of the pH dependence in any way. However, it strongly decreases the scale factor given by Equation (5) such that the curve at its maximum amounts to less than 6% of k_{mix} only, whereas that factor was seven times higher for HQ[•]/HAsc^{•-}. The resulting lower k_{obs} thus totally masks that the true rate constant for the repair of HQ[•] by *p*AP, $6.0 \times 10^8 \text{ m}^{-1} \text{ s}^{-1}$, is about four times larger than that with the co-antioxidant HAsc^{•-}. We stress that this difference is not due to a change of mechanism: the KIE of 2.2 in Figure 5b, which was obtained by the same procedure as before, confirms that the reaction remains a PCET when *p*AP replaces HAsc^{•-}.

Despite the lower thermodynamic driving force, *p*AP repairs HQ[•] faster than does HAsc^{•-}. We have already observed the same phenomenon for the repairs of the resveratrol radical by



Scheme 2. Quercetin-derived species^[35] with their abbreviations; connecting pathways pertinent to this work, pK_a values, and bond dissociation energies BDE, as determined herein.

these two co-antioxidants.^[20] Most likely, steric constraints on the highly ordered PCET transition state provide the underlying reason.

The findings of this work regarding the pathways to the quercetin radicals HQ[•] and Q^{•-}, the feasibility or infeasibility of their repairs by co-antioxidants, and the derived intervals for the BDEs of H₂Q and HQ⁻ have been collected in Scheme 2.

Conclusions

As has emerged, flash photolysis with an inexpensive near-UV pulsed solid-state laser (355 nm) provides an extremely convenient access to quercetin radicals through photoionization. In fact, not a single additive is needed per se, although as a variant one can blank out the only by-product e_{aq}⁻ by saturating the solution with N₂O. Neither e_{aq}⁻ nor its blanking product HO[•] interfere with residual quercetin or its radicals for kinetic reasons; the timescale of the radical generation is set by the duration of the laser flash, a few ns, which is tantamount to instantaneous generation when typical secondary reactions with co-antioxidants on μs timescales are studied; and within a wide pH range (between 2–3 and 9), the attainable post-flash radical concentration is up to one-half the substrate concentration while being easily controlled by the laser power.

Besides allowing a characterization of the neutral and anion radicals HQ[•] and Q^{•-}, including a recalibration of their absorption spectra with very different results compared to the literature, the photoionization approach paved the way to a detailed study of the interactions of HQ[•] and Q^{•-} with the ascorbate monoanion HAsc⁻ and other co-antioxidants, such as 4-

aminophenol. Most conspicuous were the bell-shaped pH dependences of the repair kinetics of HQ[•], in consequence of which the maxima of the observed rate constants as functions of the pH represent only a fraction of the true rate constants for the repair of HQ[•] by the co-antioxidant, such that single-point measurements even at the exact maxima could be grossly misleading. Given that we were able to identify the repair mechanisms as proton-coupled electron transfers, a comparison of different co-antioxidants with known bond dissociation energies allowed us to specify the bond dissociation energies of quercetin and its monoanion with much smaller uncertainties than previously estimated by quantum-mechanical calculations.

On the basis of the Stern–Volmer behavior of the repairs with ascorbate, the 50 times lower reactivity of the quercetin radical anion compared to the neutral radical, and a pK_a value of the latter below 5, it is evident that no complete repair is achievable with reasonable ascorbate concentrations at physiological pH in homogeneous solution. However, that pessimistic picture should no longer be valid in organized systems; and we envisage that our laser flash photolysis approach, which generates the radicals at the exact locations of their precursors, will prove useful in such situations, as we have already shown in the case of the antioxidant resveratrol and its repairs through micelle–water interfaces.^[42]

Acknowledgements

Open access funding enabled and organized by DEAL.

Conflict of interest

The authors declare no conflict of interest.

Keywords: antioxidants · kinetics · laser chemistry · photoionization

- [1] C. A. Rice-Evans, N. J. Miller, P. G. Bolwell, P. M. Bramley, J. B. Pridham, *Free Radic. Res.* **1995**, *22*, 375–383.
- [2] A. J. Larson, J. D. Symons, T. Jalili, *Adv. Nutr. Res.* **2012**, *3*, 39–46.
- [3] S. Egert, A. Bosity-Westphal, J. Seiberl, C. Kuerbitz, U. Settler, S. Plachta-Danielzik, A. E. Wagner, J. Frank, J. Schrezenmeier, G. Rimbach, S. Wolf-gram, M. J. Müller, *Br. J. Nutr.* **2009**, *102*, 1065–1074.
- [4] S. C. Bischoff, *Curr. Opin. Clin. Nutr. Metab. Care* **2008**, *11*, 733–740.
- [5] Y. J. Moon, X. Wang, M. E. Morris, *Toxicol. in Vitro* **2006**, *20*, 187–210.
- [6] T. T. H. Nguyen, S.-H. Yu, J. Kim, E. An, K. Hwang, J.-S. Park, D. Kim, *Funct. Food Health Dis.* **2015**, *5*, 437–449.
- [7] S. Jo, H. Kim, S. Kim, D. H. Shin, M. S. Kim, *Chem. Biol. Drug Des.* **2019**, *94*, 2023–2030.
- [8] X. Qiu, A. Kroeker, S. He, R. Kozak, J. Audet, M. Mbikay, M. Chrétien, *Antimicrob. Agents Chemother.* **2016**, *60*, 5182–5188.
- [9] G. Wong, S. He, V. Siragam, Y. Bi, M. Mbikay, M. Chrétien, X. Qiu, *Viol. Sin.* **2017**, *32*, 545–547.
- [10] C. Sargiacomo, F. Sotgia, M. P. Lisanti, *Aging* **2020**, *12*, 6511–6517.
- [11] L. Choueiri, V. S. Chedea, A. Calokerinos, P. Kefalas, *Food Chem.* **2012**, *133*, 1039–1044.
- [12] R. Vrijnsen, L. Everaert, A. Boeyé, *J. Gen. Virol.* **1988**, *69*, 1749–1751.
- [13] C. Kandaswami, E. Perkins, D. S. Soloniuk, G. Drzewiecki, E. Middleton, *Anti-Cancer Drugs* **1993**, *4*, 91–96.
- [14] G. Galati, O. Sabzevari, J. X. Wilson, P. J. O'Brien, *Toxicology* **2002**, *177*, 91–1043.
- [15] E. Atala, J. Fuentes, M. J. Wehrhahn, H. Speisky, *Food Chem.* **2017**, *234*, 479–485.
- [16] J. Fuentes, E. Atala, E. Pastene, C. Carrasco-Pozo, H. Speisky, *J. Agric. Food Chem.* **2017**, *65*, 11002–11010.
- [17] A. Vásquez-Espina, O. Yañez, E. Osorio, C. Areche, O. García-Beltrán, L. M. Ruiz, B. K. Cassels, W. Tiznado, *Front. Chem.* **2019**, *7*, 818.
- [18] W. Bors, C. Michel, S. Schikora, *Free Radic. Biol. Med.* **1995**, *19*, 45–52.
- [19] S. V. Jovanovic, S. Steenken, Y. Hara, M. G. Simic, *J. Chem. Soc. Perkin Trans 2* **1996**, 2497–2504.
- [20] C. Kerzig, S. Henkel, M. Goez, *Phys. Chem. Chem. Phys.* **2015**, *17*, 13915–13920.
- [21] M. Goez, C. Kerzig, R. Naumann, *Angew. Chem. Int. Ed.* **2014**, *53*, 9914–9916; *Angew. Chem.* **2014**, *126*, 10072–10074.
- [22] T. Momić, J. Z. Savić, U. Černigoj, P. Trebse, V. Vasić, *Collect. Czechoslov. Chem. Commun.* **2007**, *72*, 1447–1460.
- [23] K. Lemańska, H. van der Woude, H. Szymusiak, M. G. Boersma, A. Gliszczynska-Świgło, I. M. Rietjens, B. Tyrakowska, *Free Radic. Res.* **2004**, *38*, 639–647.
- [24] J. R. Lakowicz, *Principles of Fluorescence Spectroscopy*, 3rd ed., Springer, New York, **2006**.
- [25] G. V. Buxton, C. L. Greenstock, W. P. Heiman, A. B. Ross, *J. Phys. Chem. Ref. Data* **1988**, *17*, 513–886.
- [26] M. Brautzsch, C. Kerzig, M. Goez, *Green Chem.* **2016**, *18*, 4761–4771.
- [27] F. Di Meo, V. Lemaur, J. Cornil, R. Lazzaroni, J.-L. Duroux, Y. Olivier, P. Trouillas, *J. Phys. Chem. A* **2013**, *117*, 2082–2092.
- [28] K. Lemańska, H. Szymusiak, B. Tyrakowska, R. Zieliński, A. E. Soffers, I. M. Rietjens, *Free Radic. Biol. Med.* **2001**, *31*, 869–881.
- [29] A. Zhou, O. A. Sadik, *J. Agric. Food Chem.* **2008**, *56*, 12081–12091.
- [30] C. Kerzig, M. Goez, *Phys. Chem. Chem. Phys.* **2015**, *17*, 13829–13836.
- [31] J.-C. Mialocq, J. Sutton, P. Goujon, *J. Chem. Phys.* **1980**, *72*, 6338–6345.
- [32] D. Amić, V. Stepanić, B. Lučić, Z. Marković, J. M. Dimitrić Marković, *J. Mol. Model.* **2013**, *19*, 2593–2603.
- [33] L. Lu, M. Qiang, F. Li, H. Zhang, S. Zhang, *Dyes Pigm.* **2014**, *103*, 175–182.
- [34] Y.-Z. Zheng, G. Deng, Q. Liang, D.-F. Chen, R. Guo, R.-C. Lai, *Sci. Rep.* **2017**, *7*, 7543–7553.
- [35] R. Amorati, A. Baschieri, A. Cowden, L. Valgimigli, *Biomimetics* **2017**, *2*, 9–21.
- [36] U. Lachish, A. Shafferman, G. Stein, *J. Chem. Phys.* **1976**, *64*, 4205–4211.
- [37] M. Kimura, M. Yamamoto, S. Yamabe, *J. Chem. Soc. Dalton Trans.* **1982**, 423–427.
- [38] M. B. Davies, J. Austin, D. A. Partridge, *Vitamin C: Its Chemistry and Biochemistry*, 1st ed., The Royal Society of Chemistry, Cambridge, **1991**.
- [39] J. J. Warren, T. A. Tronic, J. M. Mayer, *Chem. Rev.* **2010**, *110*, 6961–7001.
- [40] I. J. Rhile, T. F. Markle, H. Nagao, A. G. DiPasquale, O. P. Lam, M. A. Lockwood, K. Rotter, J. M. Mayer, *J. Am. Chem. Soc.* **2006**, *128*, 6075–6088.
- [41] *CRC Handbook of Chemistry and Physics*, 97th ed. (Ed.: W. M. Haynes), CRC press, Boca Raton, **2016**.
- [42] C. Kerzig, M. Hoffmann, M. Goez, *Chem. Eur. J.* **2018**, *24*, 3038–3044.

Manuscript received: April 21, 2020

Accepted manuscript online: August 9, 2020

Version of record online: November 20, 2020

7.6 Manuskript F

The radicals of quercetin-derived antioxidants in Triton X-100 micelles†

Tim Kohlmann and Martin Goez*

Abstract: We have employed photoionization with a pulsed laser (5 ns, 355 nm) as a direct access to the radicals of quercetin, five of its monoethers and three of its diethers in nonionic micelles. On a submicrosecond timescale, the first detectable intermediates are neutral radicals NR_x, which can then be deprotonated to give radical anions RAN_{xy}, where *x* and *y* denote the phenoxy positions bearing spin and/or charge. Alkylation at oxygen *x* blocks the formation of NR_x and RAN_{xy} but barely changes the spectra of all other structurally possible radical isomers. Through systematic comparison, this allowed unambiguous radical identification and spectral assignment by experiment in all cases: NR₃ is preferred over NR_{4'}, all other NR_x are negligible; NR₃ and NR_{4'} are deprotonated at oxygens 4' and 3', respectively, unless barred by substitution, else at oxygen 7. As a caveat, B3LYP calculations on the radicals with a 6-311++g(2d,2p) basis set and a PCM solvation model gave only partially correct energy orderings and spectra, the former most likely due to an inability fully to describe the intramolecular hydrogen bonds and the latter possibly due to spin contamination. The favored deprotonation of NR₃ is associated with a typical pK_a of 4.8 and first-order kinetics, that of NR_{4'} with a pK_a of 3.9 and complex kinetics suggesting NR_{3'} as a fleeting intermediate. Both reverse reactions are diffusion controlled.

1 Introduction

The antioxidant quercetin (for the structural formula, see Figure 2a below) currently elicits 4000–5000 annual publications in scientific journals indexed by SciFinder®. They credit this molecule with a remarkable list of health-related assets, among them antiinflammatory^[1] and antiallergic^[2] properties, the prevention of cardiovascular^[3] and neurodegenerative^[4] diseases, as well as antibacterial^[5] and antiviral^[6] action. Despite this immense interest in applications, fundamental issues related to the antioxidative function of quercetin and its derivatives have not yet been cleared up sufficiently. Herein, we identify the structures and assign the UV/vis spectra of their neutral radicals and radical anions through laser-induced photoionization at weakly acidic and at neutral pH as a direct access.

The limited water-solubility of our substrates necessitated working in micellar solutions, which also is a known strategy for increasing the oral bioavailability of quercetin.^[7] As surfactant, we selected the widely used nonionic Triton X-100 on account of three benefits. Its low cmc minimizes the concentration of unnecessary free molecules;^[8] its good membrane

*Tim Kohlmann, Prof. Dr. Martin Goez,
Martin-Luther-Universität Halle-Wittenberg, Institut für Chemie, Kurt-Mothes-Str. 2, D-06120 Halle (Saale),
Germany.
E-mail: martin.goez@chemie.uni-halle.de

†Supporting Information available: Experimental details, ground-state properties, radical properties and reactions, quantum-mechanical calculations. See DOI: ...

permeabilization makes it well suited for target applications;^[9] and nonionic surfactants are better tolerable physiologically than are ionic ones.^[10]

The five hydroxy groups of quercetin theoretically allow five oxygen-centered neutral radicals and ten radical anions; monosubstitution at oxygen reduces these numbers to four and six, disubstitution to three. Quantum-mechanical calculations abound,^[11–16] but many of the radicals lie too close in energy for reliable predictions. Instead, we have resorted to an experimental approach based on blocking oxygens through alkylation. As evidenced by the absorption spectra, this hardly perturbs the conjugated system and thus allows unambiguous distinctions between radical structures. Comparisons with DFT results pinpoint where the calculations exhibit weaknesses: mainly, with respect to the intramolecular hydrogen bonds.

Accessing an intermediate by a different route compared to the "normal" reaction (i.e., the biological antioxidative process) is a standard approach in mechanistic chemistry. Herein, photons serve this purpose. In contrast to electrochemical^[17] or incubation techniques,^[18,19] our laser photolysis method generates the radicals within nanoseconds, hence we can conveniently study their subsequent reactions on microsecond timescales. Through focusing on "early" species and events, the present work thus complements the other approaches; our kinetic examples are the proton transfers connecting the neutral radicals and radical anions of our substrates.

2 Results and discussions

To keep this paper concise, we have relegated all experimental and calculational details to the Supporting Information[†], whose sections we shall refer to as ESI–x.

We have already successfully employed the photoionization access to resveratrol radicals in different media^[20–22] as well as to quercetin radicals in homogeneous aqueous solution,^[23] and ESI-3.1 demonstrates its applicability also to quercetin derivatives in the micellar system of this work. To summarize, a single flash of our laser (355 nm, 5 ns) converts up to 40% of a quercetin-based antioxidant into radical cations, which are deprotonated quasi-instantaneously to give neutral phenoxyl radicals;^[23–25] the ejected electron $e_{\text{aq}}^{\bullet-}$ (whose radical nature we explicitly signify in its abbreviation to maintain stoichiometric correctness) can be sensitively monitored through its strong absorption in the red; yet, undisturbed observation of the substrate radicals is equally possible because the $e_{\text{aq}}^{\bullet-}$ signal can be suppressed completely by presaturating the solution with N_2O , which converts $e_{\text{aq}}^{\bullet-}$ into nonabsorbing hydroxyl radicals within the duration of the flash; neither the strongly reducing $e_{\text{aq}}^{\bullet-}$ nor the strongly oxidizing hydroxyl radicals interfere with the substrate in any discernible way at our low weight-in concentrations (10 μM); all our substrates are solubilized (see ESI-2.1), hence their radicals are generated directly inside the micelles; the Poisson distribution of guest molecules among micelles^[26] ensures that neither interradsical reactions nor reactions

between radicals and surplus substrate can take place under our conditions (50 mM weight-in concentration of the surfactant Triton X-100, corresponding to micellar occupations of less than 0.03); and our experimental setup safely avoids photodegradation because each laser flash hits fresh solution (ESI-1).

2.1 Radical identifications and spectral assignments

Figure 1 juxtaposes the transient absorption spectra following laser flash photolysis of quercetin, its five monoethers, and three of its diethers in acidic (pH 3; no changes observed at lower pH) and near-neutral (typically, pH 6.5) medium. These two pH values were chosen — with hindsight — such that the higher of them lies more than one unit below the first pK_a of all our substrates (ESI-2.2) and that they bracket the first pK_a of the deprotonable radicals with distances of at least one unit to either side. Hence the photoreactions involve only the fully protonated substrates and ultimately afford only radicals in a single, thermodynamically stable protonation state.

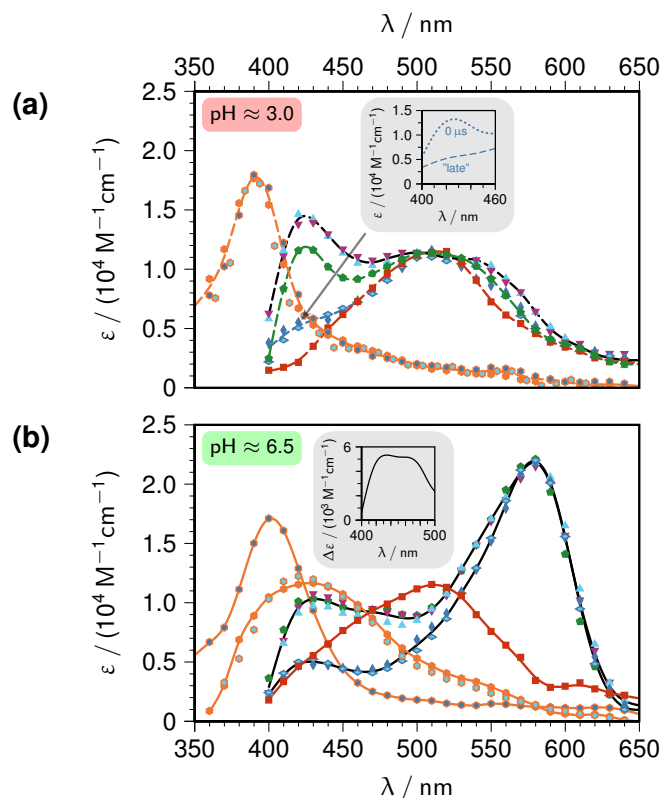


Figure 1: Radical spectra of quercetin and derivatives, following ns laser photoionization at 355 nm in acidic (a) and neutral (b) medium; extinction coefficients ϵ corrected for ground-state depletion with, and calibrated against, the separately determined electron concentration, then vertically rescaled by a factor s near unity for clarity. Common conditions, 10 μM of substrate in 50 mM aqueous Triton X-100 micellar solution, N_2O saturation. Substrate / s (pH 3) / s (pH 6.5) / color code / symbol type: quercetin Q / 1.035 / 1.067 / green / pentagon; rutin $\text{Q}\bar{3}_g$ or (indistinguishable) 3-O-methylquercetin $\text{Q}\bar{3}$ / 1.059 / 1 / orange / hexagon; narcissin $\text{Q}\bar{3}_g\bar{3}'$ / 0.943 / 1 / orange-blue bicolored / hexagon; rhamnetin-3-galactoside $\text{Q}\bar{3}_g\bar{7}$ / 1.14, and red-shifted by 4 nm for clarity / 1.07 / orange-cyan bicolored / hexagon; azaleatin $\text{Q}\bar{5}$ / 1.116 / 0.976 / purple / inverted triangle; rhamnetin $\text{Q}\bar{7}$ / 0.927 / 0.959 / cyan / triangle; isorhamnetin $\text{Q}\bar{3}'$ / 0.995 / 0.884 / blue / diamond; rhamnazin $\text{Q}\bar{3}'\bar{7}$ / 0.995 / 0.884 / cyan-blue bicolored / rotated diamond; tamarixetin $\text{Q}\bar{4}'$ / 0.978 / 1 / red / square. Main plots, constant final spectra (from the averaged traces between 15 and 25 μs post-flash); inset of graph (a), initial (dotted) and final (dashed) band of $\text{Q}\bar{3}'$ in the blue; inset of graph (b), difference spectrum between the scaled groups $\{\text{Q}, \text{Q}\bar{5}, \text{Q}\bar{7}\}$ and $\{\text{Q}\bar{3}', \text{Q}\bar{3}'\bar{7}\}$ at pH 6.5. For further explanation, see the text.

The "late" spectra in the main plots were acquired some 20 μs post-flash, when an apparently final state has been reached such that all further spectral changes are about 50 times slower (ESI-3.2). In contrast to Figure 1, "early" spectra recorded immediately after the laser flash are identical at both pH values; and they are also for their most part identical with the "late" spectra at pH 3, except for intensity changes of the band displayed in the inset of Figure 1a for isorhamnetin as the most conspicuous example. In conjunction, these observations make the "late" species at pH 3 precursors to those at pH 6.5 and establish that the "late" spectra at pH 3 and pH 6.5 stem from the protonated and deprotonated forms of the same radicals.

Basing the corrections for substrate depletion on $[\text{e}_{\text{aq}}^{\bullet-}]$ left no negative absorbances, which indicates negligible homolytic photocleavage of O—H compared with photoionization followed by radical-cation deprotonation. This absence is in line with expectation because our micelles contain large numbers of hydrogen-bond donating and accepting sites, which suppress such phenol homolyses.^[27,28]

To allow numerical comparisons, we had to resort to calibrating the radical spectra against $\text{e}_{\text{aq}}^{\bullet-}$, although one substrate can produce more than one radical isomer. Relative extinction coefficients are obviously unaffected by this approach; and the absolute errors induced by this radical partitioning are much less severe than one might expect, because each spectrum is largely dominated by one peak when the integrals over the bands are properly taken into account (see the discussion of Figure 2e below).

The radical spectra thus calibrated reveal that our compounds segregate into groups (of 3 + 6 in Figure 1a, and of (1 + 2) + (1 + 5) in Figure 1b) characterized by near-identical positions and very similar extinction coefficients of the lowest-energy peaks. To emphasize this in Figure 1, we have made the heights of those peaks within each group coincide through a further vertical rescaling by $\pm 7\%$ r.m.s., which does not introduce a significant additional error in view of the discussed calibration uncertainties, but greatly helps clarify the situation.

The pH-independent "early" spectra and the "late" spectra in acidic medium (Figure 1a) comprise two distinctive features, namely, a sharp band (full width at half maximum, FWHM, about 50 nm) in the violet or the near ultraviolet and a much broader band (FWHM \approx 150 nm) in the green. When both are present initially, their relative heights depend on the substrate and the sharp band rapidly decreases towards a lower final value — in the inset even vanishes completely — whereas the broad band practically retains its intensity; when only one of them occurs, there is no significant change over time. Even when the sharp band visually dominates the combination, Gaussian curve fitting shows that its integral amounts to less than 20 % of that of the broad band.

On the grounds of their substrate-specific contributions and different kinetic behavior, the two spectral features must arise from different radical species. Neither band is found for all nine substrates. This eliminates as possible candidates the radical cations RC, which

are unique for each substrate, and leaves only the (neutral) phenoxyl radicals NR, of which several isomers exist.

Given that NR x can only be formed at positions x that have not been blocked by O-alkylation, the radicals can be identified through the dependence of the spectral pattern on the substitution pattern, which we specify by overlining the numbers of the blocked positions (for the numbering of the quercetin skeleton, see Figure 2a) and adding the subscript "g" to indicate glycosylation instead methylation. This analysis is greatly facilitated by the fact that this etherification barely modulates the peak wavelengths, the only general exception being a near-constant blue shift upon 3-substitution, which is already evident in the absorption spectra of the substrates themselves (Supplementary Figure 11). Rhamnazin-3-galactoside Q $\overline{3}_g\overline{7}$ represents the single case requiring a minute spectral shift (by not more than 4 nm, and in Figure 1a only) to improve visual clarity, on account of its sharp peak.

When the blocking at a particular position x does not change a spectral feature, that feature obviously cannot originate from NR x . Thus, the identical two-band "late" spectra of rhamnetin Q $\overline{7}$ and azaleatin Q $\overline{5}$ rule out NR5 and NR7 beyond any doubt; and, although the — again identical — "late" spectra of isorhamnetin Q $\overline{3'}$ and rhamnazin Q $\overline{3'7}$ lack the sharp band, its unmistakable presence in their "early" spectra (inset of Figure 1a) similarly excludes NR3' while further corroborating the absence of NR7. Comparing the spectra of 3-O-methylquercetin Q $\overline{3}$ — or, also spectrally indistinguishable, its glycosylated analogue rutin Q $\overline{3}_g$ and the disubstituted derivatives of the latter, narcissin Q $\overline{3}_g\overline{3'}$ as well as rhamnetin-3-galactoside Q $\overline{3}_g\overline{7}$ — and tamarixetin Q $\overline{4'}$, each of which exhibits only one of the two features, makes the assignment unambiguous: the sharp band must belong to NR4' and the other to NR3.

Proceeding to the experiments in neutral solution, Figure 1b analyzes the correlations between the substitution patterns and the spectra for the radical anions RAN xy on the basis of the same exclusion argument. As is evident, the monoethers azaleatin Q $\overline{5}$ and rhamnetin Q $\overline{7}$ afford identical spectra as does their parent quercetin Q; hence neither spin nor charge can be centered on oxygens 5 and 7 of all three of these radical anions. The former is in line with expectation because it would destroy the strongly stabilizing hydrogen bond between O⁵H and the carbonyl oxygen,^[29] and the latter is further substantiated by the likewise identical spectra of isorhamnetin Q $\overline{3'}$ and its disubstituted derivative rhamnazin Q $\overline{3'7}$. In addition, the groups {Q, Q $\overline{5}$, Q $\overline{7}$ } and {Q $\overline{3'}$, Q $\overline{3'7}$ } share the same dominant peak at about 580 nm, which thus cannot have anything to do with position 3' and must be assigned to RAN34'. The absence of a peak in this spectral region when oxygens 3 or 4' are blocked, as with 3-O-methylquercetin Q $\overline{3}$ or rutin Q $\overline{3}_g$, narcissin Q $\overline{3}_g\overline{3'}$, rhamnetin-3-galactoside Q $\overline{3}_g\overline{7}$, and tamarixetin Q $\overline{4'}$ allows a corroborating cross-check.

As regards the pronounced shoulder with maximum at about 430 nm, the two groups {Q, Q $\overline{5}$, Q $\overline{7}$ } and {Q $\overline{3'}$, Q $\overline{3'7}$ } split. We have displayed their difference spectrum between 400 and 500 nm in the inset as the black curve. For interpretation, its aspect above 450 nm

depends too strongly on the relative scaling factors but at the short-wavelength edge can be considered reliable. Because this minor signature only arises when position 3' is unblocked, it must stem from RAN33' or RAN3'4'; and our experiments on the 3-substituted compounds (below) strongly suggest the latter of the two.

The same four derivatives that stood out in Figure 1a through affording only one of the two neutral radicals NR3 and NR4' on account of their substitution pattern ($Q\overline{3}_g/Q\overline{3}$, $Q\overline{3}_g\overline{3}'$, and $Q\overline{3}_g\overline{7}$ vs. $Q\overline{4}'$) again exhibit striking differences from the other substrates in Figure 1b. Superficially, the transient spectra of $Q\overline{3}_g\overline{3}'$ and $Q\overline{4}'$ appear to be identical to those in acidic solution, suggesting that pH 6.5 does not suffice for deprotonating NR4'($Q\overline{3}_g\overline{3}'$) and NR3($Q\overline{4}'$). However, this is rendered unlikely by control experiments at pH 9–10 (i.e., above the first pK_a of these substrates; see ESI-2.2), which give no difference to pH 6.5; and a close comparison of the spectra at pH 6.5 with those at pH 3.0 reveals a red shift by some 10 nm with $Q\overline{3}_g\overline{3}'$ and slight changes of the band shapes and widths with both compounds.

On the strength of the similarities, we assign these transient spectra of $Q\overline{3}_g\overline{3}'$ and $Q\overline{4}'$ to radical anions without a conjugation between the deprotonation site and the site bearing the unpaired spin and with the latter site furthermore identical to that in the precursor radical NRx: that is, to RAN4'7($Q\overline{3}_g\overline{3}'$) and RAN37($Q\overline{4}'$). Without an energetically costly involvement of the 5-position, the substitution pattern of $Q\overline{3}_g\overline{3}'$ obviously allows no other radical anion besides RAN4'7; and, leaving corroboration by quantum-mechanical calculations for later, Lewis formulas of RAN33' and RAN3'7, which are the other structurally possible radical anions of $Q\overline{4}'$, point to spectra significantly different from that of NR3 owing to the symmetrical distribution of spin and charge between O^3 and $O^{3'}$ in RAN33' and to the changed localization of the spin in RAN3'7.

The last piece of the puzzle is the radical-anion spectrum of the 3-O-monosubstituted quercetin ($Q\overline{3}_g/Q\overline{3}$), whose broad band with maximum at around 430 nm resembles none of the dominant peaks of the other monosubstituted quercetins. On the basis of the substitution pattern and the disregard of the 5-position, the only possibilities comprise RAN4'7, RAN3'7, and RAN3'4'. A clear experimental decision is possible with the aid of rhamnetin-3-galactoside $Q\overline{3}_g\overline{7}$. Only RAN3'4' is accessible to this disubstituted substrate on account of its blocked 7-position; and the fact that its spectrum in Figure 1b is identical to that of $Q\overline{3}_g/Q\overline{3}$ thus establishes that RAN3'4' is solely responsible for the radical-anion spectrum of the monosubstituted compound $Q\overline{3}_g/Q\overline{3}$, with negligible participation of RAN4'7. When this spectrum is slightly red-shifted to undo the hypsochromic effect of the 3-substitution (Supplementary Figure 11), it is so similar to the secondary peak observed with the parent Q and its A-ring substituted derivatives $Q\overline{5}$ and $Q\overline{7}$ as to make it highly likely that RAN3'4' is also the origin of that shoulder.

2.2 Comparisons between experiments and calculations

DFT calculations with Gaussian 16^[30] on the NR x , which we undertook to understand the reasons underlying the findings of Figure 1a, are summed up by Figure 2. For further details, see also ESI-4 and its subsections. These calculations on radicals and radical anions possessing hydrogen bonds as important structural features required a basis set with diffuse and polarization functions. As a compromise between computational cost and accuracy, we selected the B3LYP hybrid functional with a 6-311++g(2d,2p) triple-zeta basis set; control calculations showed this to give better agreement with experiment than did smaller double-zeta ones without diffuse functions such as 6-31G**, as anticipated.^[31] The polarity inside TX-100 micelles has been reported to be similar to that of either ethanol or methanol, depending on the probe used;^[32,33] and because our substrates are not very hydrophobic, we expect them to reside nearer the micelle–water interface, hence chose the more polar methanol for an implicit solvation model (PCM). Absorption spectra were obtained with TDDFT at the stationary geometries and the same level of theory.

The computed relative free energies of the NR x , with all structures both fully converged as evidenced by frequency calculations (optimum scale factor for our method and basis set, 0.9877)^[34] and possessing all intramolecular hydrogen bonds (Figure 2c) allowed by the respective substitution pattern, are visualized in Figure 2b. They are consistent with our experimental results to some extent, yet by no means completely.

What they clearly agree with is the absence of NR5 and NR7 in Figure 1a, as they predict an 8 kcal mol⁻¹ average gap between the groups {NR3, NR3', NR4'} (lower) and {NR5, NR7} (higher), whose width is modulated by which group members are structurally possible but never falls below 4.4 kcal mol⁻¹. Responsible for this partitioning into groups is the cross conjugation by the carbonyl function, which effectively isolates the longer conjugated system extending from ring B up to and including the carbonyl double bond of ring C from the shorter — and much less reactive — one comprising ring A and the same carbonyl substituent.^[16] The projection of NR5 as the radical invariably highest in energy also conforms to expectation because NR5 has lost the strongest of the intramolecular hydrogen bonds, namely, that between O⁵H and the carbonyl oxygen.^[29]

However, the calculations do not satisfactorily reproduce the experimental preference for NR3 over NR4' when both are possible: they predict NR3 to be noticeably less stable in the three cases (Q, Q $\bar{5}$, and Q $\bar{7}$; by 2.5, 4.1, and 2.3 kcal/mol) where Figure 1a shows the opposite on the basis of the integrals over the bands; and with Q and Q $\bar{5}$, they even put NR3' below NR3 although the spectra provide no indication of NR3' formation. Control calculations with water as the solvent — suggested by the deep infiltration of water into TX-100 micelles^[33] — alleviated the problem but did not remove it.

This crucial shortcoming surprised us in view of the fact that recent calculations on quercetin in water^[13] arrived at a realistic energy order (NR3 < NR4' < NR3') despite an

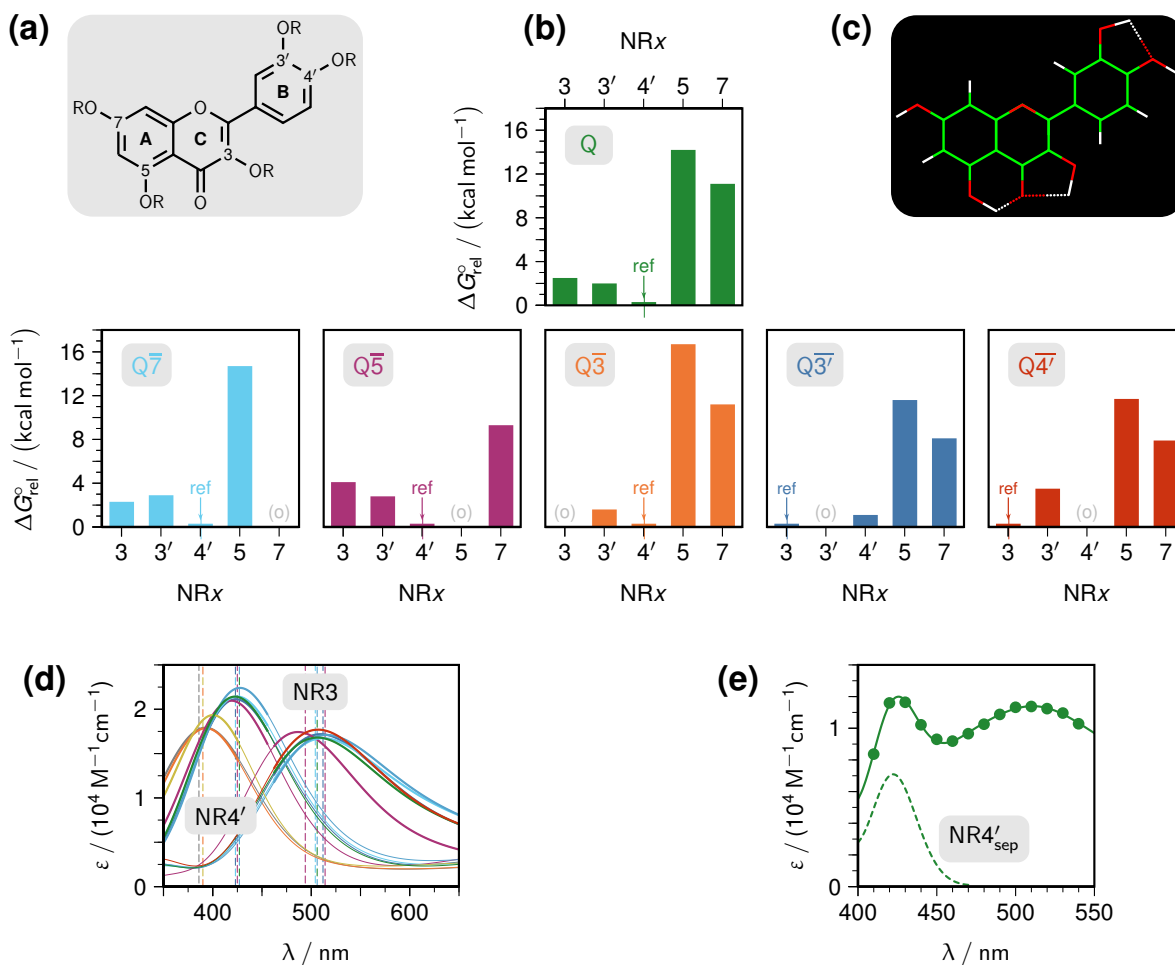


Figure 2: Quantum-mechanical calculations on the neutral radicals NR_x of Quercetin Q (formula, graph (a) with all R = H) and its monomethyl ethers *n*-O-methylquercetin Q \bar{n} (also, in graph (d), three dimethyl ethers Q $\bar{m}\bar{n}$). Substrate color code as in Figure 1 except for rhamnazin Q3'7' (medium blue), 3,3'-di-O-methylquercetin Q33' (yellow), and 3,7-di-O-methylquercetin Q37 (gray). Graph (b): computed (UB3LYP/6-311++G(2d,2p); frequency scale factor, 0.9877; PCM, solvent methanol) free energies $\Delta G_{\text{rel}}^{\circ}$ of the NR_x. Each lowest-energy radical is denoted with "ref", and "(o)" marks the respective radical excluded by the substitution; energy tickmarks and labels not repeated within row of subplots. Graph (c): structure with emphasized intramolecular hydrogen bonds (dashed). Graph (d): comparison of experimental peak positions (dashed vertical lines) and spectra calculated with TDDFT (solid curves) for NR3 and NR4'; calculational model as in graph (b) with constant parameter $\sigma = 0.4$ eV (Gaussian 16 default). Graph (e): separation of the radical contributions for quercetin; circles, experimental data; solid curve, best fit of the TDDFT spectra; dashed curve, isolated contribution of NR4'. The best fit parameters for NR3 / NR4' are σ , 3710 cm⁻¹ (0.46 eV) / 1129 cm⁻¹ (0.14 eV); peak shift from computed maximum, -242 cm⁻¹ (-0.03 eV) / 726 cm⁻¹ (+0.09 eV); weight in the superposition, 0.71 / 0.15. For further explanation, see the text.

older program version (Gaussian 03), a smaller basis set (6-311+g(d,p)), and methodological deficiencies (use of the vacuum structures for calculating the PCM energies) imposed by the discontinuities of the reaction field in the older PCM algorithm. ESI-4.1 describes our attempts to reproduce the published results. In a nutshell, this is only approximately possible even in compatibility mode of Gaussian 16; the reason for the discrepancies between the program versions is the solvent model, which from Gaussian 09 onwards was greatly improved with respect to speed and convergence by constructing a cavity surface with a smooth, differentiable contour; hence, the accompanying reparametrization apparently removed an accidental error compensation that was operating in the earlier version of the program.

On the reasonable assumption that the improved reaction-field shape is valid, the following separations of factors help pinpoint the origin of the problem with our calculations of Figure 2b. A breakdown of numerical values is given in ESI-4.2.

The intrinsic stability difference of NR3' and NR4', without the effects of the catechol hydrogen bonds, can be equated with the energy differences between those two radicals in Q and in Q $\bar{7}$; alternatively, with the difference of the energy differences between NR7 (as a reference point) and NR3' for Q $\bar{4}$ ' or NR4' for Q $\bar{3}$ '. In the former set, the catechol hydrogen bonds are intact; in the latter, absent; and in both sets, the conjugated systems in ring C are absolutely identical, including the two hydrogen bonds surrounding the carbonyl group. The result that NR3' intrinsically lies 2.5 ± 0.4 kcal/mol above NR4' reflects the confinement of the unpaired electron to the B-ring in the case of NR3' as opposed to a stabilizing further delocalization into the C-ring in the case of NR4'.

The contribution of the catechol hydrogen bond can be estimated analogously, again taking NR7 as reference radical that is neither hydrogen-bonded nor electronically coupled to the B-ring. We consider the energy differences between NR7 and NR4' for the pairs Q/Q $\bar{3}$ ' and Q $\bar{3}$ /Q $\bar{33}$ ' as well as those between NR7 and NR3' for the pair Q/Q $\bar{4}$ '. In each of these pairs, only the first compound contains a catechol hydrogen bond while the second cannot. Apart from that, the pairs are directly comparable. Hence, the difference of their differences yields the energy gain by the catechol hydrogen bond, which is calculated to be 4.4 ± 0.3 kcal/mol.

Similarly, the strength of the hydrogen bond between O⁵H and the carbonyl group is obtained as 3.5 ± 0.3 kcal/mol from the energy differences between NR5 and NR7 for those compounds with the other hydrogen bond from O³H to the carbonyl oxygen intact (Q, Q $\bar{4}$ ', and Q $\bar{3}$ '). Intrinsic electronic differences between these radicals are expected to be insignificant because relative to the carbonyl substituent and the oxygen contained in ring C positions 5 and 7 both are ortho/para and meta, respectively.

Less clear-cut is the situation with NR3. This radical will have an intrinsic energy unlike that of the others and cannot be formed without destroying the hydrogen bond between O³H and carbonyl; and the removal of that hydrogen bond by O³-alkylation will raise the energy of all other radicals by basically the same amount, with any unequal impacts on NR4' or NR5 being second-order corrections only. The energetic differences between NR7 and NR3 in the comparable cases of Q, Q $\bar{4}$ ', and Q $\bar{3}$ ', all of which feature both the O⁵H \cdots O=C and the catechol hydrogen bond, are 8.2 ± 0.3 kcal/mol. This value is composed of the intrinsic stability difference between NR3 and the A-radicals minus by the energy contained in the O³H \cdots O=C hydrogen bond.

From these separations, an obvious deficiency of the DFT calculations with respect to the hydrogen bonds emerges. As is well documented, O⁵H \cdots O=C is significantly stronger than are the other two hydrogen bonds for geometric reasons;^[29] but our computations give the opposite, in other words, overestimate the weaker catechol hydrogen bond. This

agrees with the observation that B3LYP even with triple-zeta basis sets similar to ours describes hydrogen bonds only moderately well, with r.m.s. errors of several kcal/mol.^[31] Although our comparison of different NR_x may effect a partial cancellation, this necessarily remains imperfect because the number of hydrogen bonds depends on where the radical center is located as well as on the alkylation pattern. The remaining error can explain the difference between theory and experiment: on the premise that the calculations similarly overestimate the weaker hydrogen bond between O³H and carbonyl, which is lost in the formation of NR₃, they will necessarily give too high an energy for NR₃ throughout and thus put this radical above NR₄'. This hypothesis is supported by the cases of isorhamnetin Q $\bar{3}$ ' and rhamnazin Q $\bar{3}$ ' $\bar{7}$ '. They are the only substrates for which NR₄' exists without a catechol hydrogen bond; and for them, consequently, the calculations no longer predict NR₄' to be more stable than NR₃. Evidently, a considerable amount of NR₄' is still produced initially through the deprotonation of the energy-rich radical cation but then vanishes as thermodynamic equilibration sets in (inset of Figure 1a).

In contrast to the energies of the neutral radicals, their transitions obtained with TDDFT through the same calculational model reproduce the experimental peak positions very well (Figure 2d). Substituent effects are almost absent except for a small blue shift for NR₃ of azaleatin Q $\bar{5}$ and a much more pronounced one for NR₄' of the 3-O-substituted derivatives (Q $\bar{3}$ and Q $\bar{3}$ ' $\bar{3}$ '), which parallels the same observation as the only alkylation-induced trend in the spectra of the substrates themselves (Supplementary Figure 11).

For convenience, the calculated spectra of the neutral radicals and radical cations of all derivatives investigated herein have been compiled in ESI-4.3. The position of their lowest-energy maxima invariably follows the order, from red to blue, NR₃ — NR₄' — NR₃' \approx NR₇ — NR₅. The radical cation band in the visible range is almost indistinguishable from that of NR₄' except for the 3-O-substituted derivatives where it does not exhibit the above-mentioned blue shift of NR₄' but instead constitutes the longest-wavelength peak of Q $\bar{3}$, Q $\bar{3}$ ' $\bar{3}$ ', and Q $\bar{3}$ ' $\bar{7}$ ' as far as radical species at low pH are concerned.

Because the calculations of Figure 2d aimed at the positions of the maxima, they were carried out with fixed width of the Gaussian peaks. Experimentally, however, the peak of NR₄' has a much smaller FWHM. Figure 2e presents a spectral decomposition for quercetin with two adjustable width-parameters $\tilde{\sigma}$ (Supplementary Equation S13), in which the two peak positions were also allowed to vary slightly. As is evident, a near-perfect representation of the experimental spectrum is obtained with the radicals NR₃ and NR₄' contributing 0.71 and 0.15 to it.

This result has two implications. On one hand, the sum of these factors is smaller than unity. This would allow a retrospective recalibration of the maximum extinction coefficients, which must both be larger by a factor of 1.16 than based on our gross calibration against $e_{\text{aq}}^{\bullet-}$. On the other hand, the ratio 4.7 of the statistical weights of NR₃ to NR₄' corresponds to a difference in ΔG° of slightly more than 0.9 kcal/mol, which suggests that the effect of

the inappropriate description of the hydrogen bonds by our calculational model amounts to as much as 3.4 kcal/mol.

Figure 3, complemented by ESI-4.2 and ESI-4.4, collates our DFT results on the radical anions RAN xy obtained at the same level of theory. In accordance with the literature,^[13] we found all radical anions involving the 5-position to be too energy-rich for realistically playing a role; hence, we have omitted them from the following discussion.

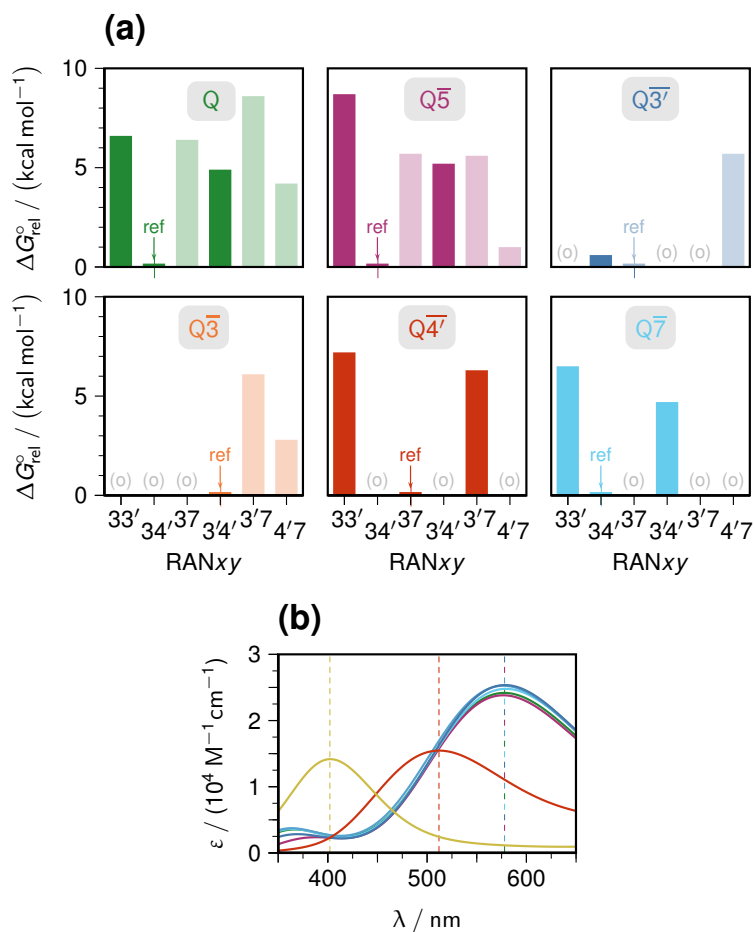


Figure 3: Quantum-mechanical calculations on the radical anions RAN xy of Quercetin Q (for the formula and numbering of the skeleton, see Figure 2a) and its monomethyl ethers *n*-O-methylquercetin Q \bar{n} (also, in graph (b), two dimethyl ethers Q \bar{mn}). Substrate color code as in Figure 1 except for rhamnazin Q $\bar{3}'7'$ (medium blue) and 3,3'-di-O-methylquercetin Q $\bar{3}'3'$ (yellow). Graph (a): computed (UB3LYP/6-311++G(2d,2p); frequency scale factor, 0.9877; PCM, solvent methanol) free energies $\Delta G_{\text{rel}}^{\circ}$ of the RAN xy . Each lowest-energy radical anion is denoted with "ref". RAN xy excluded by the substitution and by the comparison experiments of Figure 1b are indicated by "(o)" and by faded bars. Energy or radical tickmarks and labels are not repeated within rows or columns of subplots. Graph (b): comparison of experimental peak positions (dashed vertical lines) and spectra calculated with TDDFT (solid curves) for RAN $4'7$ (Q $\bar{3}'$), RAN 37 (Q $\bar{4}'$), and RAN $34'$ (Q, Q $\bar{5}$, Q $\bar{7}$, Q $\bar{3}'$, and Q $\bar{5}$), calculational model as in graph (a) with constant parameter $\sigma = 0.4 \text{ eV}$ (Gaussian 16 default) and r.m.s. peak shifts of 1355 cm^{-1} (0.17 eV). For further explanation, see the text.

Especially with a view to unique assignments and/or decompositions of the experimental spectra, three issues reduce the reliability and applicability of these computations on the RAN xy as opposed to those on the NR x . First, the greater number of radical anions leads to more densely spaced absorption bands in our observation range. Second, the charge on these species gives rise to much larger solvation effects, with the added complication that the polarity of their microheterogeneous surroundings is known only approximately. Third,

the generally observed red shift upon deprotonation of NR_x to give RAN_{xy} moves into the visible and near-uv spectral range more transitions that do not involve the SOMO and, therefore, experience spin contamination to a much larger degree.^[35] As the sole means for interpreting the experimental spectrum of an unknown radical anion, these calculations are thus problematic; but much safer conclusions can be drawn by combining them with our described analysis of the links between the spectral pattern and the substitution pattern.

In addition to the structural exclusions of certain RAN_{xy}, the connections between the groups {Q, Q $\bar{5}$, Q $\bar{7}$ }, {Q $\bar{3}$ ' , Q $\bar{3}$ ' $\bar{7}$ '}, and {Q $\bar{3}$, Q $\bar{3}$ ' $\bar{7}$ '} established above have been put to good use in the energy comparisons of Figure 3a, where faded colors in the bar charts identify NR_{xy} that are not observed experimentally despite favourable energies predicted for them in some cases (RAN4'7 of azaleatin Q $\bar{5}$ and RAN37 of isorhamnetin Q $\bar{3}$ '). We again ascribe these discrepancies to deficiencies in the calculations of the intramolecular hydrogen bonds.

To isolate the energy gain by the catechol hydrogen bond to a phenolate acceptor in RAN_{xy}, we compare $\Delta G^\circ(\text{RAN34}')$ for the pair Q/Q $\bar{3}$ ' or $\Delta G^\circ(\text{RAN33}')$ for the pair Q/Q $\bar{4}$ ' , taking the respective $\Delta G^\circ(\text{RAN37})$ as energetic reference (for the numerical values, see ESI-4.2.5). With Q, there is no change in hydrogen bonding, so $\Delta G^\circ(\text{RAN37}) - \Delta G^\circ(\text{RAN3z}')$ captures the intrinsic energy of RAN3z' and the stabilization by the catechol hydrogen bond; with the second member of each pair, only the intrinsic effect remains whereas the catechol hydrogen bond is absent; hence, the difference elicits the energy gain by that hydrogen bond, 7.0 kcal/mol in both cases. It does not come as a surprise that —O⁻ is a much better hydrogen bond acceptor than is —OH, but the hydrogen-bond related calculational errors already manifest for the NR_x are thus expected to be even larger for the NR_{xy}.

Blaming this factor for the above-mentioned obvious discrepancies of RAN4'7(Q $\bar{5}$) and RAN37(Q $\bar{3}$ '), the following three regularities emerge from Figure 3a. Whenever RAN34' is structurally possible, as for the substrates in the top row as well as (not shown) rhamnazin Q $\bar{3}$ ' $\bar{7}$ ' , it is the most favourable radical anion. Under the analogous premises, RAN33' is less stable than is RAN34' , by 7.0 ± 0.6 kcal/mol (ESI-4.2.6), while RAN3'4' with its energy of 4.9 ± 0.2 kcal/mol above RAN34' occupies an intermediate position (ESI-4.2.7). Likewise, but with a much larger variability, RAN3'7 is seen always to lie higher than RAN4'7.

The calculations thus fully agree with the experiment-based assignment of the dominant peak as RAN34' for Q, Q $\bar{5}$, and Q $\bar{7}$; as RAN37 for Q $\bar{4}$ ' ; and as RAN3'4' for Q $\bar{3}$ /Q $\bar{3}$ ' \bar{g} ' . They are only in partial accordance with the experimental results on Q $\bar{3}$ ' , as they correctly project the formation of RAN34' but counterfactually predict a participation of, and even a preference for, RAN37; and they notably deviate with respect to the spectral shoulder of Q and Q $\bar{7}$, in both cases prognosticating unrealistically high energies that would bar the formation of any minor radical anions, at variance with observation.

Figure 3b displays the computed spectra of the key radical anions for our set of quercetin-derived antioxidants except Q $\bar{3}$ and Q $\bar{3}$ ' $\bar{7}$ ' (see below), using substrate-specific horizontal

offsets to match them to the experimental peak maxima; and a complete compilation without such shifts is given in ESI-4.4, again omitting structures with participation of position 5. The interpretational value of these theoretical spectra of the RAN_{xy}, when taken on their own, is much more limited than it was in the case of the NR_x. Responsible is the following unfavourable combination of factors.

One the one hand, the bands of the RAN_{xy} are closely spaced, as the example of the parent quercetin demonstrates: the computed peak maxima of its six radical anions are positioned nearly equidistantly, with only about 20 nm between each adjacent pair of them. On the other hand, solvent effects are imperfectly reproduced by the calculations: this is manifest from the fact that the spectra of RAN34' have to be shifted by twice this wavelength difference on average; and on top of this global constant, further individual modifications by ± 15 nm are necessary to correct for predicted but experimentally nonexistent differences within the group {Q, Q $\bar{5}$, Q $\bar{7}$, Q $\bar{3}'\bar{7}$, Q $\bar{3}'$ }.

Also unsatisfactorily reproduced by the calculations are secondary features of the bands. This is highlighted by the case of isorhamnetin Q $\bar{3}'$, whose spectrum in Figure 1b has been shown above to stem exclusively from RAN34'. The experimental intensity ratio of the shoulder at 430 nm and the dominant peak at 580 nm is 1:4.4, but the computed spectrum of Figure 3b reflects the shape no better than qualitatively, predicting the shoulder to lie 60 nm lower (at 370 nm) when the same energy shift is applied as for the dominant peak and to be half as high (intensity ratio 1:9.0).

We tentatively suggest spin contamination as an underlying reason because the TDDFT calculations on NR3, which agree well with the experiments, yield $\langle S^2 \rangle > 1$ only for transitions below 400 nm, whereas for the less-well represented RAN34' that switch occurs 50 nm higher. Especially strong is the contamination in the case of RAN3'4', for which the crossover point lies at about 500 nm; and this is accompanied by a striking mismatch between the experimental and calculated spectra of this radical anion. The identical transient spectra of 3-O-methylquercetin/rutin (Q $\bar{3}/\bar{Q}\bar{3}_g$) and rhamnetin-3-galactoside (Q $\bar{3}_g\bar{7}$) have filtered out RAN3'4' as their sole source, leaving no interpretational latitude because the substitution pattern of Q $\bar{3}_g\bar{7}$ excludes any participation of the 7-position; but the observed single band with maximum at 428 nm cannot even remotely be reconciled with the double band computed for Q $\bar{3}$ or Q $\bar{3}'\bar{7}$ (Supplementary Figure 16), whose two maxima (352 nm and 529 nm) bracket the experimental position nearly symmetrically and with a distance of more than 0.5 eV. Because of the obvious unreliability of the calculations on RAN3'4', we have excluded these two derivatives from Figure 3b.

2.3 Proton transfer kinetics

The existence of both neutral radicals and radical anions naturally raises the question of their interconversions. To monitor these proton transfers for substrates capable of forming

RAN34', the absorbance A_{580} of the dominant peak at 580 nm provides the most convenient observable: the high extinction coefficient of RAN34', both absolute and relative to that of NR3, ensures a good sensitivity, and an absence of appreciable absorptions by other NR x or RAN xy in this spectral region affords an uncompromised reliability. To keep the radical concentrations constant, we carefully controlled the laser intensity during each series of experiments; and to base the analysis on an intrinsic property, we additionally recorded the absorbances at the isosbestic point (515 nm) of NR3 and RAN34' under the same conditions and took the ratios of A_{580} and the — ideally, constant; but in the case of some minute time dependence, "late" — values of A_{515} . Figure 4a for quercetin Q furnishes a typical example of the outcome with pH as the secondary variable, and the fairly similar plots for the other substrates in that category (azaleatin Q $\bar{5}$, rhamnetin Q $\bar{7}$, isorhamnetin Q $\bar{3}$, and rhamnazin Q $\bar{3}$ ' $\bar{7}$) have been relegated to ESI-3.3.

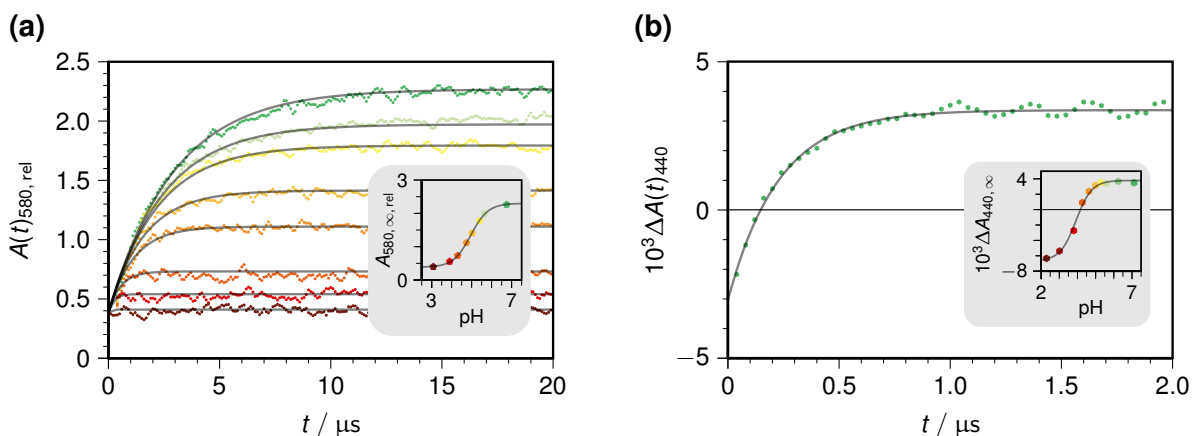


Figure 4: Deprotonation of the neutral radicals NR3 of quercetin Q (a) and NR4' of rutin Q $\bar{3}_g$ (b). Shown are the time-resolved (main plots) and final (insets) absorbances; in (a) at 580 nm and relative to the final absorbances at the isosbestic point at 515 nm, in (b) as the differences between 440 nm and 400 nm. Experimental conditions, 10 μ M of substrate in 50 mM Triton X-100 aqueous micellar solution; pH values color-coded identically in each main plot and corresponding inset. Fit functions given by Equations 1–2; global fit in (a), local fit in (b); best-fit values of pK_a and k_{dep} , 4.95 and $3.3 \times 10^5 \text{ s}^{-1}$ in (a), 3.92 and $4.5 \times 10^6 \text{ s}^{-1}$ in (b). For further explanation, see the text.

These time-resolved measurements yield important thermodynamic, kinetic, and mechanistic information.

With respect to thermodynamics, the "late" values $A_{580, \infty, \text{rel}}$ follow the titration curve of Equation 1 (with λ and λ' being 580 and 515 nm in this case),

$$A_{\lambda, \infty, \text{rel}} = \frac{A_{\lambda, \infty}}{A_{\lambda', \infty}} = \frac{\alpha}{1 + 10^{\text{pH} - \text{p}K_a}} + \frac{\beta}{1 + 10^{\text{p}K_a - \text{pH}}} \quad (1)$$

whose limiting values in acidic and basic solution, α and β , each are composed of three extinction coefficients. The pertaining plot is shown as the inset of Figure 4a and gives a best-fit pK_a of 4.95. An inclusion of the above-mentioned four other substrates (ESI-3.3) leads to 4.78 ± 0.15 r.m.s. as the average pK_a of NR3. This marginal spread highlights the negligible perturbations of the quercetin electronic system when —OH is replaced by —OR and thus again vindicates our strategy of systematic radical analysis through blocking

oxygen positions by O-alkylation.

As regards kinetics, the time-dependent observable $A(t)_{580, \text{rel}}$ — analogously defined as $A(t)_{580}/A_{515, \infty}$ in the example — is found to exhibit strictly monoexponential behavior as described by Equation 2,

$$A(t)_{\lambda, \text{rel}} = A_{\lambda, \infty, \text{rel}} + \frac{\alpha - \beta}{1 + 10^{\text{p}K_{\text{a}} - \text{pH}}} \times \exp \left[-k_{\text{dep}} \left(1 + 10^{\text{p}K_{\text{a}} - \text{pH}} \right) t \right] \quad (2)$$

with the parameter set $\{\alpha, \beta, \text{p}K_{\text{a}}\}$ and the dependent limit $A_{\lambda, \infty, \text{rel}}$ of Equation 1 complemented by the first-order rate constant k_{dep} for deprotonation of NR3. A global best-fit parameter k_{dep} of $3.3 \times 10^5 \text{ s}^{-1}$ and the above $\text{p}K_{\text{a}}$ fix the second-order rate constant k_{p} for the reverse reaction, the protonation of RAN34', at $2.9 \times 10^{10} \text{ M}^{-1} \text{ s}^{-1}$. This high value clearly points to a diffusion-controlled reaction between oppositely charged species, the proton and the radical anion, which is not unreasonable given the deep penetration of water into TX-100 micelles.^[33] As corroborative evidence, the results for the other four substrates are quite similar, yielding an average k_{p} of $(3.0 \pm 0.6) \times 10^{10} \text{ M}^{-1} \text{ s}^{-1}$ r.m.s (ESI-3.3).

Mechanistically, the successful global fit of the time and pH dependences with Equation 2 establishes that the measurements of Figure 4a isolate a single protonation equilibrium. However, this contradicts two experimental facts documented above, namely, that in addition to NR3 and RAN34' the neutral radical NR4' also participates (see the peak at 420 nm in Figure 1a) and at least one other radical anion, most likely RAN3'4', is formed in neutral solution (inset of Figure 1b). In a closed system of three species, such as $\{\text{NR3}, \text{NR4}', \text{RAN34}'\}$, one of the three equilibria depends on the other two, hence the formal kinetic result must be biexponential; the involvement of a fourth species would increase the number of independent equilibria, and thus exponential terms in the integrated rate law, to three; but the curves of Figure 4a and/or ESI-3.3 do not deviate from single exponentials to any perceptible degree.

This discrepancy can be resolved if the rate constants associated with each equilibrium differ sufficiently. Taking NR3 and NR4' as examples, their interconversions are decoupled from their deprotonations when they are either much slower or much faster. The former means independent fates of the two neutral radicals, the latter a fast preequilibrium between NR3 and NR4'; and only in the former situation can the observed rate constant be assigned to a single chemical process, whereas in the latter it is a weighted average.

Attempts to distinguish between these alternatives by monitoring, in parallel, the time evolution of the NR4' peak at 420 nm gave inconclusive results. The decays were complex, did not exhibit discernible relationships to the formation kinetics of RAN34', and involved slower components that we ascribe to unidentified parasitic processes. Isorhamnetin $\text{Q}\bar{3}'$ provides a case in point. At pH3, its signal of RAN34' reaches its final value quite fast (Supplementary Figure 14d; rate constant under these circumstances, $2.2 \times 10^7 \text{ s}^{-1}$, as inferred from the global fit) but that of NR4' (inset of Figure 1a) vanishes with biexponential kinetics, whose well-resolvable fast component of $2.7 \times 10^6 \text{ s}^{-1}$ is eight times slower already

and superimposed on a component still slower by another order of magnitude.

Some support of independent decays of NR3 and NR4' can be derived from Lewis structures. According to them, deprotonation of NR3 at O^{4'} allows an unhindered delocalization of the negative charge to the carbonyl oxygen at the other end of the pertaining half of the cross-conjugated system, but a deprotonation of NR4' at O³ is not facilitated in the same way; no obvious direct pathway from NR4' to RAN34' can be formulated on their basis; and the same also applies to the transformation of NR4' to RAN3'4'. However, in the latter case an intramolecular hydrogen swap between O^{3'} to O^{4'} in the neutral radical, an idea already mentioned in the literature,^[16] could help circumvent the obstacle: the energy differences between NR4' and NR3' are not prohibitive (Figure 2b) and deprotonation of NR3' at O^{4'} is assisted by the same charge delocalization onto the carbonyl group as with NR3.

Both rutin Q $\overline{3}_g$ and rhamnetin-3-galactoside Q $\overline{3}_g\overline{7}$ have position 3 blocked and positions 3' as well as 4' unblocked, hence structurally should not only allow a reaction NR4' \rightarrow RAN3'4' through a hydrogen swap but also isolate it by ruling out a process NR3 \rightarrow RAN3'4'. Further to simplify the kinetics, we took differences of the traces at 440 nm (RAN3'4' dominant) and 400 nm (NR4' dominant), which should considerably decrease any spectral contributions of NR3' (see Supplementary Figure 15) but does not distort Equations 1–2 or their more convoluted variants, because they are all involve linear combinations of the same exponential terms.

Upon this transformation, the global kinetics remain complex, as they must for a three-component cyclic equilibrium, but parameters can still be extracted in the following two limiting situations. First, the "late" values yield titration curves with pK_a values of 3.92 and 3.81 for the two substrates, as illustrated for Q $\overline{3}_g$ by the inset of Figure 4b. Second, in neutral medium the reverse reaction (protonation of RAN3'4') becomes negligibly slow owing to the minute proton concentration; and, as an intramolecular hydrogen swap is expected to be faster than an intermolecular deprotonation, a consecutive reaction such as NR4' \rightarrow NR3' \rightarrow NR3'4' should reduce to an apparent first-order process. The limited availability of Q $\overline{3}_g\overline{7}$ did not allow enough accumulations for a reliable determination but the result for Q $\overline{3}_g$ has been displayed as the main plot of Figure 4b. The ten times higher value of k_{dep} ($4.5 \times 10^6 \text{ s}^{-1}$) for Q $\overline{3}_g$ compared to Q is the logical consequence of a pK_a lower by one unit when one assumes protonation with the same (diffusion-controlled) rate constant k_p in both cases.

3 Conclusions

This work has established the systematic suppression of radical isomers by O-alkylation at various positions of the quercetin skeleton as a highly valuable tool for the identification and spectral assignment of the neutral radicals and radical anions. In essence, it is a

comparison method whose feasibility rests on the very small influences of such substitutions on the relative energies and absorption spectra of the radical isomers in these systems; and it should be broadly applicable to the field of other flavonols and related polyphenol antioxidants.

Our generation of the radicals through photoionization does not involve diffusion and/or species other than the substrates. Hence, it is more direct than pulse radiolysis, let alone electrochemical or incubation methods. In particular, its application to micellized substrates (herein, Triton X-100) does not present any problems, and the kinetics of subsequent reactions of the transients on submicrosecond timescales are straightforward to investigate.

The following generalities have emerged from this access to the radicals of quercetin and its ethers. For the initially formed neutral radicals, the chroman ring — that is, O³ as the radical site — is preferred over the catechol moiety, which only exhibits the radical centered at O^{4'}. Subsequent deprotonation of the former radical occurs at O^{4'}; of the latter at O^{3'}; and only when these positions are blocked at O⁷. The pK_a values of the neutral radicals centered at O³ all lie very near to 4.8, and the kinetics cannot be distinguished from first order; when the radical site is O^{4'} and the 3'-position is not blocked by alkylation, the pK_a is lower by one unit, and the transformation exhibits complex kinetics, pointing to an intermediate hydrogen swap between positions 3' and 4'. In all cases, the reverse reactions are diffusion controlled.

Quantum-mechanical calculations were not fully consistent with our experimental results even at a computational level (DFT with a triple zeta basis set) that only recently became practicable for everyday work on our large number of species (9 substrates, with a total of 86 radicals to be considered). Our systematic analysis suggested inaccurate descriptions of the intramolecular hydrogen bonds, which are characteristic for quercetin systems, as the main reason; spin contamination may be responsible for gross discrepancies with respect to the experimental spectrum of the catechol radical anion with spin and charge residing on O^{3'/O4'}; and, almost ironically, the older Gaussian 03 fares better than the current Gaussian 16 in reproducing the experimentally found energetic ordering of the neutral radicals. We traced this back to the PCM solvent model, which apparently featured an accidental error compensation in the older version that disappeared in the reparametrized, and greatly improved, newer implementation. All these findings show that despite the huge advancements in computational speed, which allow increasingly sophisticated calculational methods to be used routinely, theory still is a long way from making experiments superfluous.

Conflicts of interest

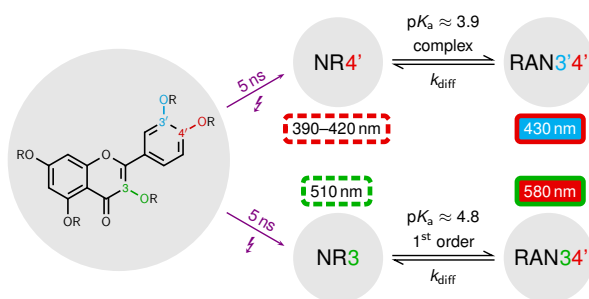
There are no conflicts of interest to declare.

References

- [1] S. Chirumbolo, *Inflamm. Allergy Drug Targets*, 2010, **9**, 263–285.
- [2] J. Mlcek, S. Skrovankova, T. Jurikova and J. Sochor, *Molecules*, 2016, **21**, 623–637.
- [3] F. Perez-Vizcaino and J. Duarte, *Mol. Asp. Med.*, 2010, **31**, 478–494.
- [4] N. A. Kelsey, H. M. Wilkins and D. A. Linseman, *Molecules*, 2010, **15**, 7792–7814.
- [5] T. T. Cushnie and A. J. Lamb, *Int. J. Antimicrob. Agents*, 2005, **26**, 343–356.
- [6] A. Maalik, F. A. Khan, A. Mumtaz, A. Mehmood, S. Azhar, M. Atif, S. Karim, Y. Altaf and I. Tariq, *Trop. J. Pharm. Res.*, 2014, **13**, 1561–1566.
- [7] L. Dian, E. Yu, X. Chen, X. Wen, Z. Zhang, L. Qin, Q. Wang, G. Li and C. Wu, *Nanoscale Res. Lett.*, 2014, **9**, 684–694.
- [8] S. K. Hait and S. P. Moulik, *J. Surfactants Deterg.*, 2001, **4**, 303–309.
- [9] A. L. van de Ven, K. Adler-Storthz and R. Richards-Kortum, *J. Biomed. Opt.*, 2009, **14**, 021013/1–021013/13.
- [10] S. Schreier, S. V. Malheiros and E. de Paula, *Biochem. Biophys. Acta*, 2000, 210–234.
- [11] M. Leopoldini, T. Marino, N. Russo and M. Toscano, *Theor. Chem. Acc.*, 2004, **111**, 210–216.
- [12] S. Fiorucci, J. Golebiowski, D. Cabrol-Bass and S. Antonczak, *J. Agric. Food Chem.*, 2007, **55**, 903–911.
- [13] R. Amorati, A. Baschieri, A. Cowden and L. Valgimigli, *Biomimetics*, 2017, **2**, 9–21.
- [14] Y.-Z. Zheng, G. Deng, Q. Liang, D.-F. Chen, R. Guo and R.-C. Lai, *Sci. Rep.*, 2017, **7**, 7543–7553.
- [15] Z. Li, M. Moalin, M. Zhang, L. Vervoort, E. Hursel, A. Mommers and G. R. M. M. Haenen, *Int. J. Mol. Sci.*, 2020, **21**, 6015–6030.
- [16] M. Spiegel, T. Andruniów and Z. Sroka, *Antioxidants*, 2020, **9**, 461–482.
- [17] A. M. O. Brett and M.-E. Ghica, *Electroanalysis*, 2003, **15**, 1745–1750.
- [18] G. Galati, O. Sabzevari, J. X. Wilson and P. J. O'Brien, *Toxicology*, 2002, **177**, 91–1043.
- [19] J. Treml and K. Šmejkal, *Compr. Rev. Food Sci. Food Saf.*, 2016, **15**, 720–738.
- [20] C. Kerzig, S. Henkel and M. Goez, *Phys. Chem. Chem. Phys.*, 2015, **17**, 13915–13920.
- [21] C. Kerzig and M. Goez, *Phys. Chem. Chem. Phys.*, 2016, **18**, 20802–20811.
- [22] C. Kerzig, M. Hoffmann and M. Goez, *Chem. Eur. J.*, 2018, **24**, 3038–3044.
- [23] T. Kohlmann and M. Goez, *Chem. Eur. J.*, 2020, **26**, 17428–17436.
- [24] S. V. Jovanovic, S. Steenken, Y. Hara and M. G. Simic, *J. Chem. Soc., Perkin Trans. 2*, 1996, 2497–2504.
- [25] K. Lemańska, H. Szymusiak, B. Tyrakowska, R. Zieliński, A. E. Soffers and I. M.

- Rietjens, *Free Radic. Biol. Med.*, 2001, **31**, 869–881.
- [26] Y. Moroi, *J. Phys. Chem.*, 1980, **84**, 2186–2190.
- [27] J.-C. Mialocq, J. Sutton and P. Goujon, *J. Chem. Phys.*, 1980, **72**, 6338–6345.
- [28] C. Grieco, A. T. Hanes, L. Blancafort and B. Kohler, *J. Phys. Chem. A*, 2019, **123**, 5356–5366.
- [29] R. Amorati and L. Valgimigli, *Org. Biomol. Chem.*, 2012, **10**, 4147–4158.
- [30] M. J. Frisch, G. W. Trucks, H. B. Schlegel, G. E. Scuseria, M. A. Robb, J. R. Cheeseman, G. Scalmani, V. Barone, G. A. Petersson, H. Nakatsuji, X. Li, M. Caricato, A. V. Marenich, J. Bloino, B. G. Janesko, R. Gomperts, B. Mennucci, H. P. Hratchian, J. V. Ortiz, A. F. Izmaylov, J. L. Sonnenberg, D. Williams-Young, F. Ding, F. Lipparini, F. Egidi, J. Goings, B. Peng, A. Petrone, T. Henderson, D. Ranasinghe, V. G. Zakrzewski, J. Gao, N. Rega, G. Zheng, W. Liang, M. Hada, M. Ehara, K. Toyota, R. Fukuda, J. Hasegawa, M. Ishida, T. Nakajima, Y. Honda, O. Kitao, H. Nakai, T. Vreven, K. Throssell, J. A. Montgomery, Jr., J. E. Peralta, F. Ogliaro, M. J. Bearpark, J. J. Heyd, E. N. Brothers, K. N. Kudin, V. N. Staroverov, T. A. Keith, R. Kobayashi, J. Normand, K. Raghavachari, A. P. Rendell, J. C. Burant, S. S. Iyengar, J. Tomasi, M. Cossi, J. M. Millam, M. Klene, C. Adamo, R. Cammi, J. W. Ochterski, R. L. Martin, K. Morokuma, O. Farkas, J. B. Foresman and D. J. Fox, *Gaussian 16 Revision C.01*, 2016, Gaussian Inc. Wallingford CT.
- [31] A. D. Boese, *ChemPhysChem*, 2015, **16**, 978–985.
- [32] B. K. Paul, N. Ghosh and S. Mukherjee, *RSC Adv.*, 2015, **5**, 9381–9388.
- [33] C. C. Ruiz and J. Aguiar, *Langmuir*, 2000, 7946–7953.
- [34] M. P. Andersson and P. Uvdal, *J. Phys. Chem. A*, 2005, **109**, 2937–2941.
- [35] A. Ipatov, F. Cordova, L. J. Doriol and M. E. Casida, *J. Mol. Struct.-Theochem*, 2009, **914**, 60–73.

Table of contents entry



Experiment is better than theory at identifying which neutral radicals NR_x of the popular antioxidant quercetin and its derivatives are formed in a nonionic micelle and how they are deprotonated to give radical anions RAN_{xy} .

1 Experimental Details

All chemicals (quercetin, > 96 %, Sigma-Aldrich; 3-O-methylquercetin, \geq 97 %, Sigma-Aldrich; rutin, 95.7 %, Sigma-Aldrich; narcissin, 99 %, Phytolab; azaleatin, 97 %, abcr; rhamnetin, 99.5 %, Sigma-Aldrich; rhamnazin, \geq 99 %, Sigma-Aldrich; isorhamnetin, \geq 95 %, Sigma-Aldrich; tamarixetin, 99 %, abcr; rhamnetin-3-galactoside, ChemFaces, > 98 %; Triton X-100, Sigma-Aldrich, BioXtra) were used as received.

Solutions were always freshly prepared with ultrapure Millipore Milli-Q water (specific resistance, $18.2 \text{ M}\Omega \text{ cm}^{-1}$). Prior to use, they were deoxygenated for at least 30 minutes with Ar 5.0 or — when $e_{\text{aq}}^{\bullet-}$ had to be scavenged — with N_2O 5.0, both from AirLiquide. For the steady-state absorption measurements, sealed cuvettes were employed; and for the flow-through laser flash photolysis experiments, a stream of the respective inert gas was continuously maintained above the solution in the stock vessel.

Unless otherwise stated, the substrate concentration was always $10 \mu\text{M}$ and the surfactant concentration 50 mM . The desired pH values were adjusted under pH meter control by the addition of HCl or NaOH, with volume changes rendered negligible by adding the concentrated acid or base with microliter syringes.

Steady-state absorption measurements were carried out with a Shimadzu UV-1800 spectrophotometer. For the laser flash studies we used a home-made setup described in detail elsewhere.^[1] Its following features are of particular importance for the present work. Photolysis is performed with a frequency-tripled (355 nm) pulsed Nd:YAG laser (Continuum Surelite-III; pulse width, 5 ns). The laser beam is collimated such that it homogeneously fills a $46 \mu\text{L}$ volume (height, 2.9 mm; width and depth, 4 mm each) of a suprasil cell with intensities of up to 500 mJ cm^{-2} . Up to 40 % of the substrates can thus be photoionized with a single flash; and, on account of the optically thin solutions, calibrated absorption spectra and kinetics of the transients can be reliably recorded with a time resolution down to 1 ns. A syringe-driven flow-through system ensures that each acquisition takes place on fresh solution.

Specific experimental procedures are explained in the pertaining sections, and details of the quantum-mechanical calculations are given in ESI-4.

2 Ground-State Properties

2.1 Micellar Complexation

Moroi's formal-kinetic treatment of solubilization,^[2] which properly takes into account the Poisson distribution of the micellar occupants, shows that the equilibrium between the guest molecules in the aqueous bulk and in the micelles, Q_{aq} and Q_{mic} , is simply describable by Supplementary Equation S1, i.e., as if the surfactant Surf_m in its aggregated state were an

ordinary chemical reactant,



except that its concentration does not change in the process.

The weight-in concentration $[Q_t]$ obviously equals the sum of $[Q_{\text{aq}}]$ and $[Q_{\text{mic}}]$, and the concentration of Surf_m is connected with its weight-in concentration $[\text{Surf}_t]$ through Supplementary Equation S2,

$$[\text{Surf}_m] = \frac{[\text{Surf}_t] - \text{cmc}}{N_{\text{agg}}} \quad (\text{S2})$$

with the surfactant-specific critical micelle concentration cmc and aggregation number N_{agg} .

Rearranging the mass-action law for the chemical equilibrium of Supplementary Equation S1 and inserting the described relationships one arrives at Supplementary Equations S3a and S3b for the relative concentrations of Q in the different surroundings,

$$\frac{[Q_{\text{aq}}]}{[Q_t]} = \frac{1}{1 + (K/N_{\text{agg}}) ([\text{Surf}_t] - \text{cmc})} = \frac{1}{1 + K' ([\text{Surf}_t] - \text{cmc})} \quad (\text{S3a})$$

$$\frac{[Q_{\text{mic}}]}{[Q_t]} = \frac{(K/N_{\text{agg}}) ([\text{Surf}_t] - \text{cmc})}{1 + (K/N_{\text{agg}}) ([\text{Surf}_t] - \text{cmc})} = \frac{K' ([\text{Surf}_t] - \text{cmc})}{1 + K' ([\text{Surf}_t] - \text{cmc})} \quad (\text{S3b})$$

As is evident from these equations, no separation of K and N_{agg} is possible, and both combine into a single constant K' .

With the extinction coefficients ε_{aq} and ε_{mic} for Q in the respective (pseudo)phase, the observed extinction coefficient ε follows from Supplementary Equation S4,

$$\varepsilon = \frac{\varepsilon_{\text{aq}} + \varepsilon_{\text{mic}} K' ([\text{Surf}_t] - \text{cmc})}{1 + K' ([\text{Surf}_t] - \text{cmc})} \quad (\text{S4})$$

The quantity ε_{aq} can be precisely measured in the absence of the surfactant; cmc can be determined by independent experiments; and ε_{mic} will usually be accessible in the limit of high $[\text{Surf}_t]$. This leaves K' as the only freely adjustable parameter.

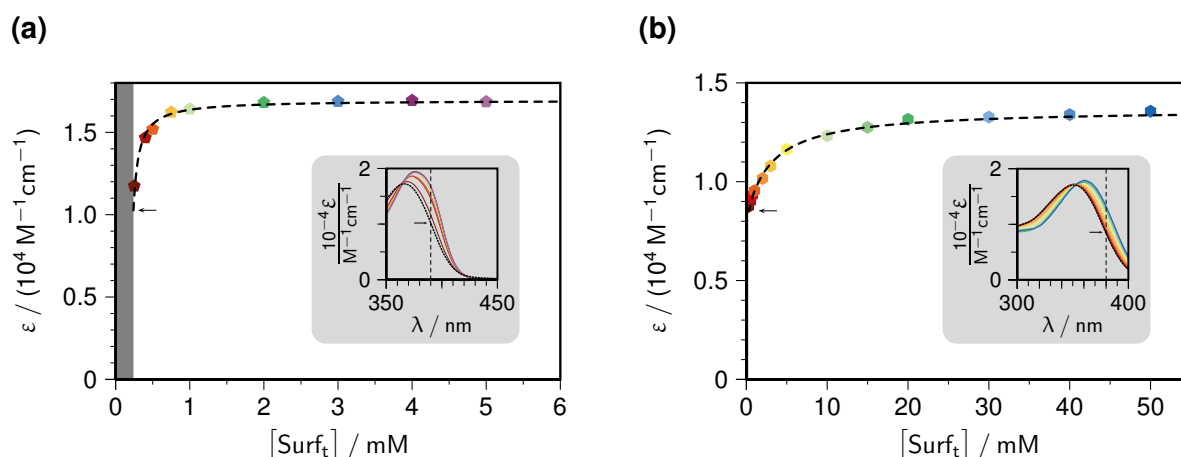
We stress that the only approximation involved in the derivation of Supplementary Equation S4 concerns Supplementary Equation S2: for charged surfactants such as SDS, the relationship between $[\text{Surf}_m]$ and $[\text{Surf}_t]$ depends in a more complex way on the concentration of the common counterion.^[3]

Transforming Supplementary Equation S4 to give a Benesi–Hildebrand-type equation would be straightforward,

$$\frac{1}{\varepsilon - \varepsilon_{\text{aq}}} = \frac{1}{\varepsilon_{\text{mic}} - \varepsilon_{\text{aq}}} + \frac{1}{K' (\varepsilon_{\text{mic}} - \varepsilon_{\text{aq}})} \times \frac{1}{[\text{Surf}_t] - \text{cmc}} \quad (\text{S5})$$

but the nonlinear fit of Supplementary Equation S4 possesses the advantage over the linear fit of Supplementary Equation S5 that it does not distort the statistical weights of the individual data points.

Supplementary Figures 1a and 1b display the results of complexation experiments by Triton TX-100 for the parent compound quercetin and its more hydrophilic derivative rutin. A pH of 4.5 ensured that each substrate was present practically exclusively in its protonated form. The micellar medium causes a bathochromic shift of the longest-wavelength absorption band by about 10 nm compared to aqueous medium (quercetin, 367 nm \rightarrow 376 nm; rutin, 351 nm \rightarrow 361 nm), which is accompanied by a small rise of the maximum height (quercetin, 13%; rutin, 7%). To improve the sensitivity by increasing the changes, we took slices through the spectra at about half-height of the respective band, to the right of its maximum (quercetin, 390 nm; rutin, 380 nm). The cmc of TX-100 is 0.24 mM.^[4] As expected, the complexation constant K' is found to be much larger for quercetin than for rutin ($1.8 \times 10^4 \text{ M}^{-1}$ vs $3.1 \times 10^2 \text{ M}^{-1}$). Inserting these results into Supplementary Equation S3a reveals that less than 6 % of rutin reside in the aqueous phase at the surfactant concentration used in all other experiments of this work (50 mM); that fraction decreases to 0.1 % for quercetin, and must be utterly negligible in the case of the even more hydrophobic methyl ethers.



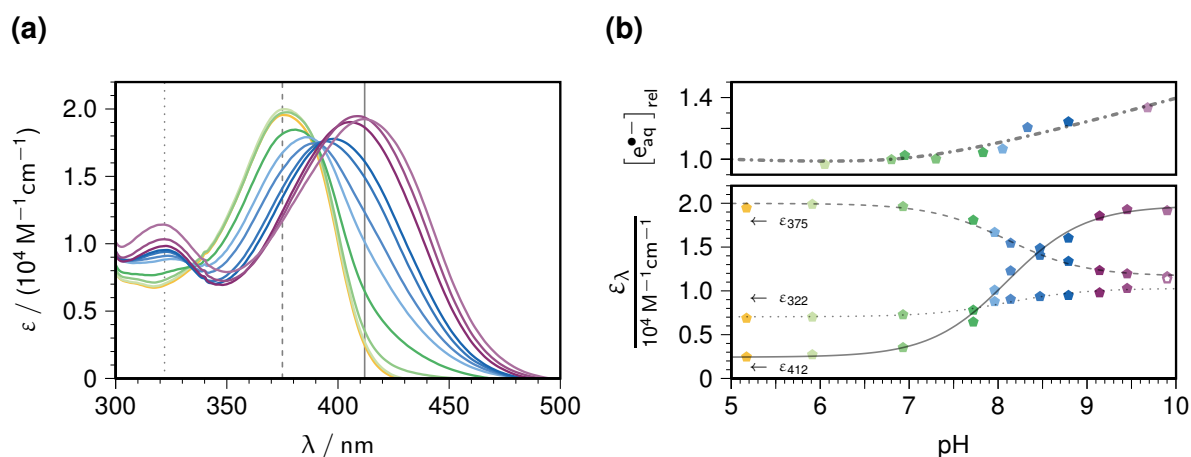
Supplementary Figure 1: Complexation of 10 μM quercetin (a) or rutin (b) by Triton TX-100 micelles at pH 4.5. Insets, spectra at different surfactant weight-in concentrations $[\text{Surf}_t]$; main plots, extinction coefficients ϵ as functions of $[\text{Surf}_t]$ at the wavelength indicated by the vertical dashed line in the corresponding inset. Identical color code for $[\text{Surf}_t]$ between each main plot and its inset; spectra in water displayed as dotted curves; pertaining ϵ at the observation wavelength indicated by horizontal arrows; cmc of TX-100 (0.24 mM) shown as an exclusion zone by a rectangle filled with gray in the main plot of graph (a), and invisible in the case of (b). Dashed curves in the main plots, fits of Supplementary Equation S4; best-fit values of K' , $1.8 \times 10^4 \text{ M}^{-1}$ (a) and $3.1 \times 10^2 \text{ M}^{-1}$ (b). For further explanation, see the text.

2.2 Ground-State pKa

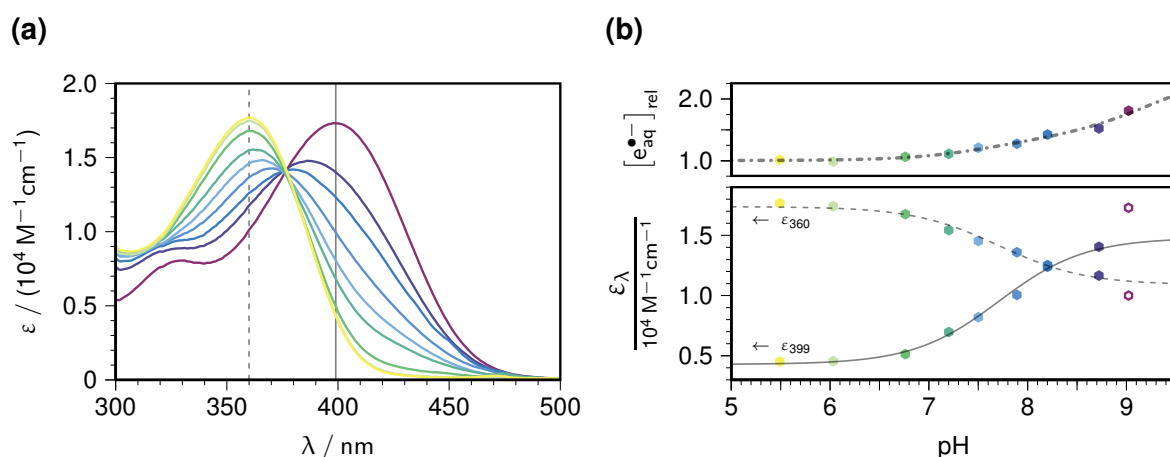
Supplementary Figures 2–10 display pH-dependent absorption spectra, which were recorded to determine the first $\text{p}K_a$ of our substrates. Well-defined isosbestic points are only found for rutin $\text{Q}\bar{3}_g$ and azaleatin $\text{Q}\bar{5}$; their lack for the other compounds indicates closely-lying $\text{p}K_a$ values of their other deprotonation sites, such that their first $\text{p}K_a$ is an apparent quantity.

However, knowledge of that apparent pK_a provides a pH window within which the generation of the radicals starts out from the fully protonated substrates ($pH \leq 6.5$ in most cases; $pH \leq 6.2$ with rutin and 3-O-methylquercetin, $Q\bar{3}_g$ and $Q\bar{3}$).

For better comparison with the titration curves, the relative photoionization yields have been included in Supplementary Figures 2b, 3b, 4b, and 5b. These will be discussed in ESI-3.1.

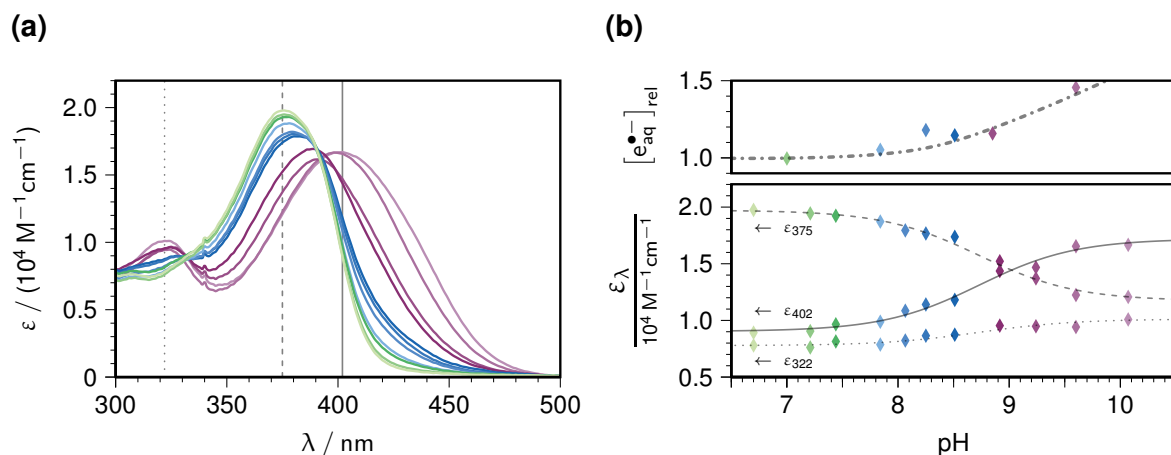


Supplementary Figure 2: Deprotonation and photoionization of quercetin Q. Graph (a), pH dependent absorption spectra. Graph (b), lower part: determination of the first pK_a by taking slices through the spectra at 412 nm (solid), 375 nm (dashed), and 322 nm (dotted); global best-fit pK_a , 8.10, highest pH (open data points) excluded. Graph (b), upper part: pH-dependent relative photoionization yields; fit function without physical significance. Concentrations, 10 μ M of substrate in 50 mM aqueous Triton TX-100 micellar solution; identical color code for the pH between the graphs. For further explanation, see the text.

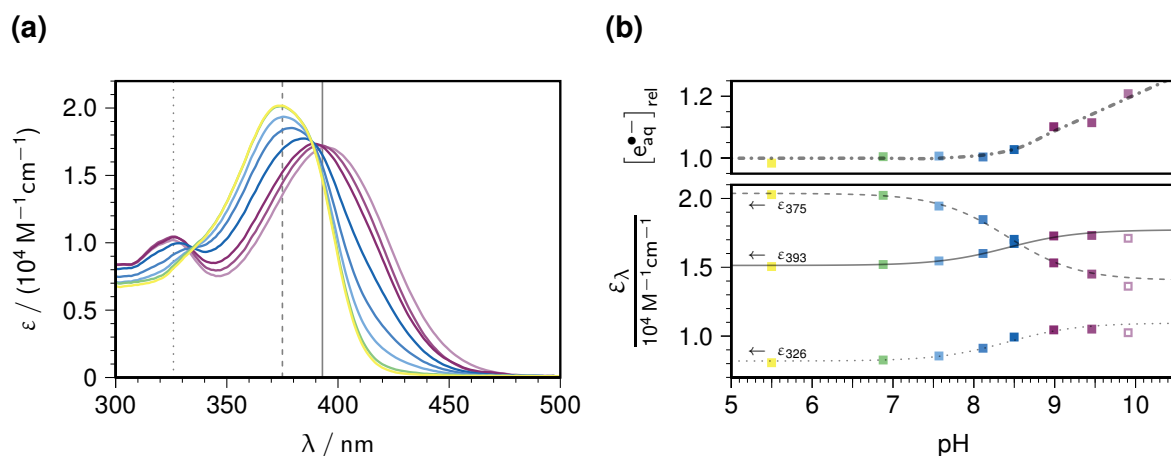


Supplementary Figure 3: Deprotonation and photoionization of rutin $Q\bar{3}_g^-$. Graph (a), pH dependent absorption spectra. Graph (b), lower part: determination of the first pK_a by taking slices through the spectra at 399 nm (solid) and 360 nm (dashed); global best-fit pK_a , 7.71, highest pH (open data points) excluded. Graph (b), upper part: pH-dependent relative photoionization yields; fit function without physical significance. Concentrations, 10 μ M of substrate in 50 mM aqueous Triton TX-100 micellar solution; identical color code for the pH between the graphs. For further explanation, see the text.

At pH 3 and 6.5, the ground-state spectra of 3-O-methylquercetin $\text{Q}\bar{3}$ are identical. Given that its transient spectra are also identical to those of rutin $\text{Q}\bar{3}_g$ at both pH values and in view of the relatively high price of $\text{Q}\bar{3}$, we did not determine its $\text{p}K_a$. It should be very similar to that of $\text{Q}\bar{3}_g$ on account of the identical substitution pattern.

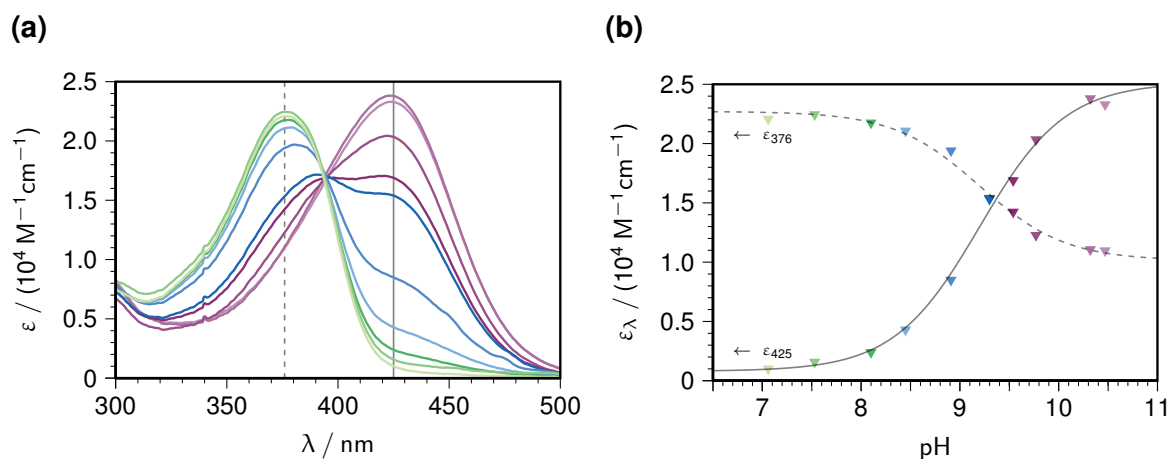


Supplementary Figure 4: Deprotonation and photoionization of isorhamnetin $\text{Q}\bar{3}$. Graph (a), pH dependent absorption spectra. Graph (b), lower part: determination of the first $\text{p}K_a$ by taking slices through the spectra at 402 nm (solid), 375 nm (dashed), and 322 nm (dotted); global best-fit $\text{p}K_a$, 8.73. Graph (b), upper part: pH-dependent relative photoionization yields; fit function without physical significance. Concentrations, 10 μM of substrate in 50 mM aqueous Triton TX-100 micellar solution; identical color code for the pH between the graphs. For further explanation, see the text.

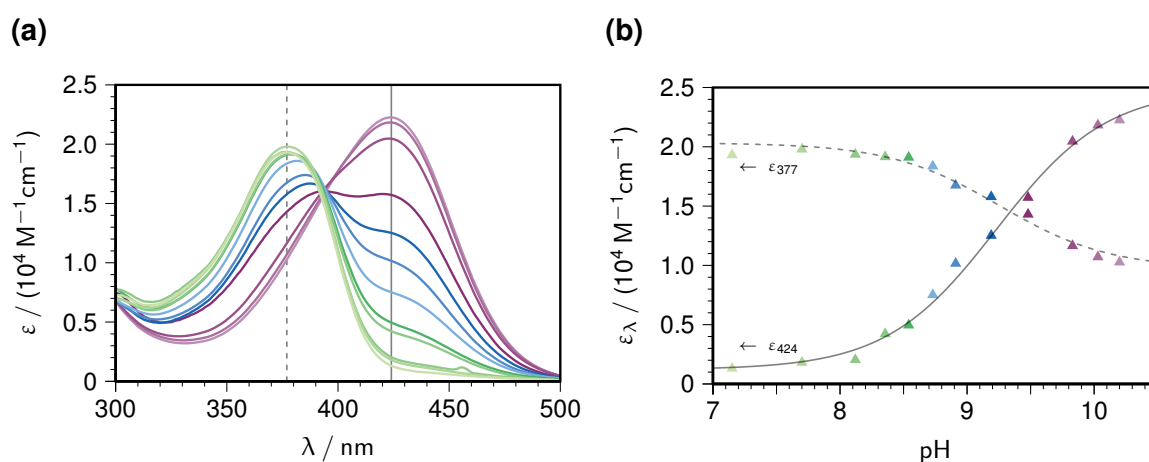


Supplementary Figure 5: Deprotonation and photoionization of tamarixetin $\text{Q}\bar{4}$. Graph (a), pH dependent absorption spectra. Graph (b), lower part: determination of the first $\text{p}K_a$ by taking slices through the spectra at 393 nm (solid), 375 nm (dashed), and 326 nm (dotted); global best-fit $\text{p}K_a$, 8.42, highest pH (open data points) excluded. Graph (b), upper part: pH-dependent relative photoionization yields; fit function without physical significance. Concentrations, 10 μM of substrate in 50 mM aqueous Triton TX-100 micellar solution; identical color code for the pH between the graphs. For further explanation, see the text.

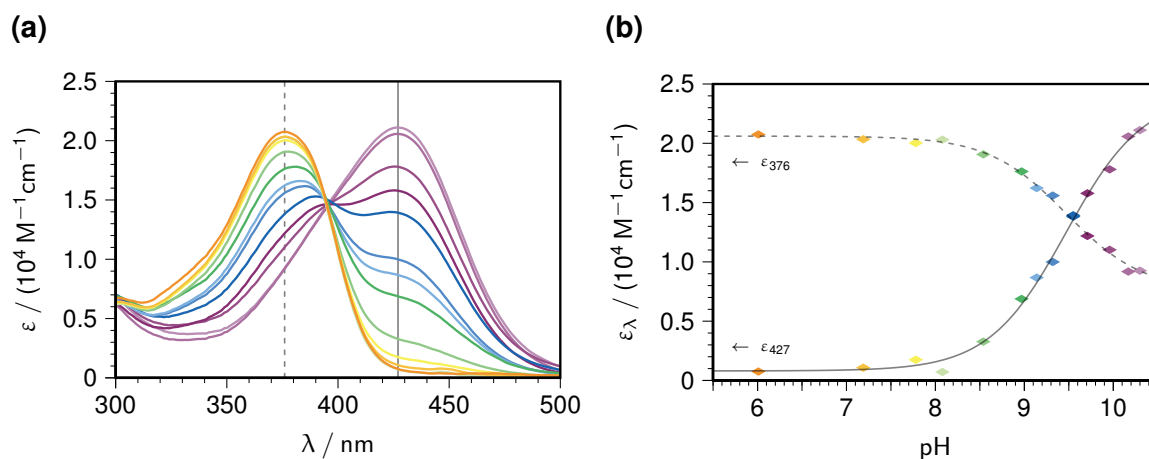
Because of availability and price, no pH-dependent photoionization yields were measured for azaleatin $\text{Q}\bar{5}$, rhamnetin $\text{Q}\bar{7}$, rhamnazin $\text{Q}\bar{3}'\bar{7}$, narcissin $\text{Q}\bar{3}_g\bar{3}'$, and rhamnetin-3-galactoside $\text{Q}\bar{3}_g\bar{7}$. The $\text{p}K_a$ values of these substrates are among the highest of all the derivatives, at least 8.6, and a participation of their monodeprotonated forms in the photoionizations is extremely unlikely at a pH two units below the $\text{p}K_a$.



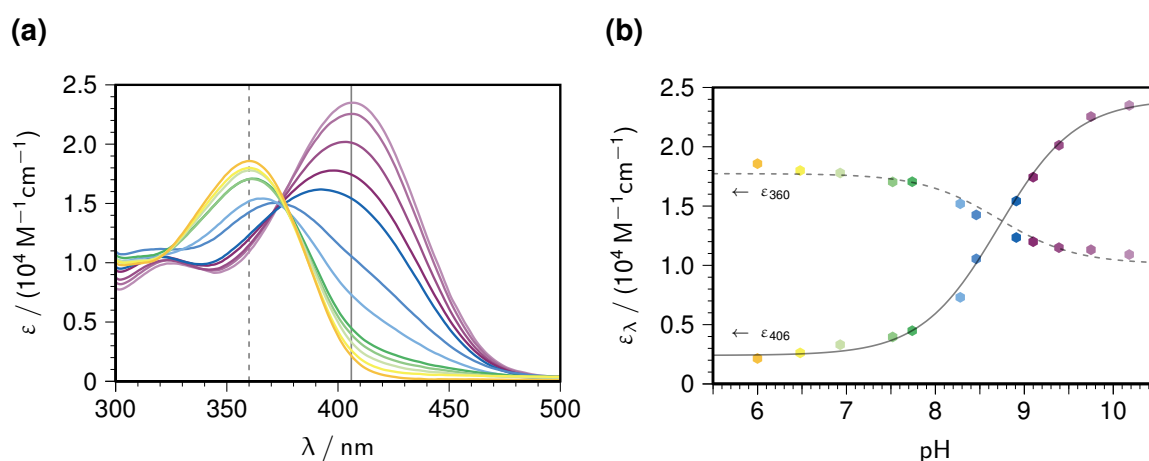
Supplementary Figure 6: Deprotonation of azaleatin $\text{Q}\bar{5}$. Graph (a), pH dependent absorption spectra. Graph (b), determination of the first $\text{p}K_a$ by taking slices through the spectra at 425 nm (solid) and 376 nm (dashed); global best-fit $\text{p}K_a$, 9.20. Concentrations, 10 μM of substrate in 50 mM aqueous Triton TX-100 micellar solution; identical color code for the pH between the graphs. For further explanation, see the text.



Supplementary Figure 7: Deprotonation of rhamnetin $\text{Q}\bar{7}$. Graph (a), pH dependent absorption spectra. Graph (b), determination of the first $\text{p}K_a$ by taking slices through the spectra at 424 nm (solid) and 377 nm (dashed); global best-fit $\text{p}K_a$, 9.23. Concentrations, 10 μM of substrate in 50 mM aqueous Triton TX-100 micellar solution; identical color code for the pH between the graphs. For further explanation, see the text.

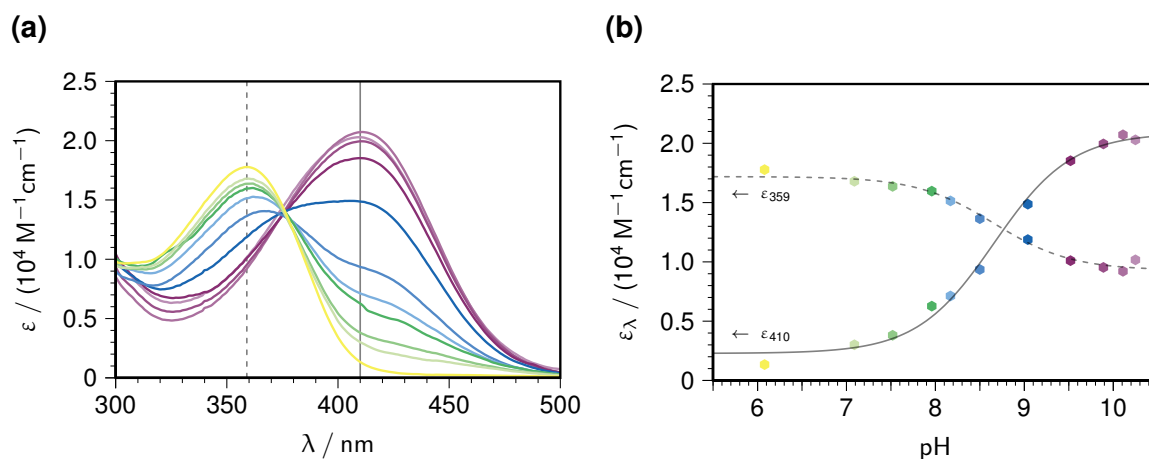


Supplementary Figure 8: Deprotonation of rhamnazin $\overline{Q377}$. Graph (a), pH dependent absorption spectra. Graph (b), determination of the first pK_a by taking slices through the spectra at 427 nm (solid) and 376 nm (dashed); global best-fit pK_a , 9.47. Concentrations, 11.5 μM of substrate in 50 mM aqueous Triton TX-100 micellar solution; identical color code for the pH between the graphs. For further explanation, see the text.



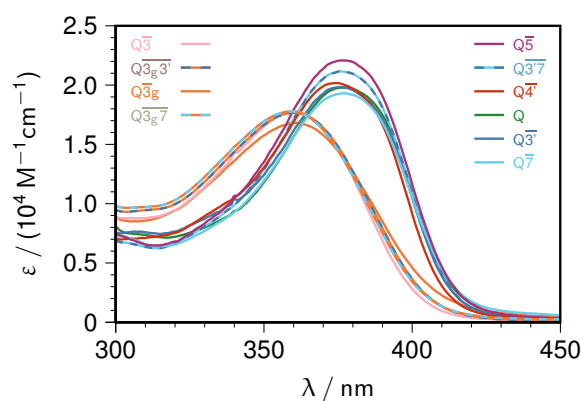
Supplementary Figure 9: Deprotonation of narcissin $\overline{Q3g3}$. Graph (a), pH dependent absorption spectra. Graph (b), determination of the first pK_a by taking slices through the spectra at 406 nm (solid) and 360 nm (dashed); global best-fit pK_a , 8.71. Concentrations, 10 μM of substrate in 50 mM aqueous Triton TX-100 micellar solution; identical color code for the pH between the graphs. For further explanation, see the text.

Points at pH values well above the pK_a have been excluded from the preceding fits when the next deprotonation step clearly takes over (Supplementary Figures 2, 3, and 5).



Supplementary Figure 10: Deprotonation of rhamnetin-3-galactoside $\overline{Q3_g7}$. Graph (a), pH dependent absorption spectra. Graph (b), determination of the first pK_a by taking slices through the spectra at 410 nm (solid) and 359 nm (dashed); global best-fit pK_a , 8.66. Concentrations, 10 μM of substrate in 50 mM aqueous Triton TX-100 micellar solution; identical color code for the pH between the graphs. For further explanation, see the text.

Supplementary Figure 11 collects the ground-state absorption spectra of all the investigated compounds in their protonated forms. Included have been the pair of analogues rutin $\overline{Q3_g}$ and 3-O-methylquercetin $\overline{Q3}$, as well as the disubstituted derivatives rhamnazin $\overline{Q3'7}$, narcissin $\overline{Q3_g3'}$, and rhamnetin-3-galactoside $\overline{Q3_g7}$. As is evident, alkyl substitution (etherification) at the oxygens in positions 3', 4', 5, and 7 has only a negligible influence on the spectra, whereas in position 3 it effects a hypsochromic shift by some 20 nm.



Supplementary Figure 11: Absorption spectra of all quercetin derivatives in their protonated forms (spectra invariant in an interval of at least $2 \leq \text{pH} \leq 6.5$; upper limit for the 3-monosubstituted compounds, 6.2). Common conditions, 10 μM of substrate in 50 mM aqueous Triton TX-100 micellar solution. Compound / abbreviation: 3-O-methylquercetin / $\overline{Q3}$; narcissin $\overline{Q3_g3'}$; rutin / $\overline{Q3_g}$; rhamnetin-3-galactoside / $\overline{Q3_g7}$; azaleatin / $\overline{Q5}$; rhamnazin / $\overline{Q3'7}$; tamarixetin / $\overline{Q4'}$; quercetin / \overline{Q} ; isorhamnetin / $\overline{Q3'}$; rhamnetin / $\overline{Q7}$. For further explanation, see the text.

3 Radical Properties and Reactions

3.1 Photoionization Access

Supplementary Figure 12 sums up the relevant aspects of our method to generate the radicals M^\bullet from our substrates MH. It uses an intense laser flash (355 nm, 5 ns, a few 100 mJ cm^{-2}) to achieve the conversion

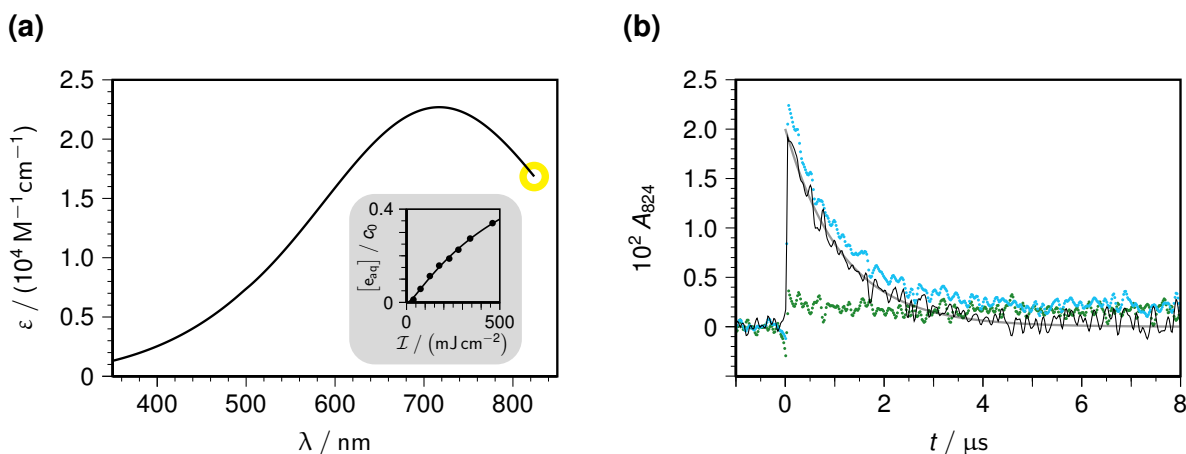


through photoionization. When the highly mobile and hydrophilic electron is ejected from MH inside a micelle, it will immediately relocalize to the surrounding aqueous bulk, which explains its formulation as hydrated electron $e_{\text{aq}}^{\bullet-}$ in Supplementary Equation S6.

For quercetin itself, it is known that the radical cation $\text{MH}^{\bullet+}$ is deprotonated quasi-instantaneously to give the desired neutral radical,^[5]



and we expect the O-alkylated derivatives of quercetin to behave in the same way. The sequence of Supplementary Equations S6 and S7 thus yields equal amounts of M^\bullet and $e_{\text{aq}}^{\bullet-}$, which can be used for calibrating the spectra of the neutral radical (or, when another deprotonation ensues, of the radical anion).

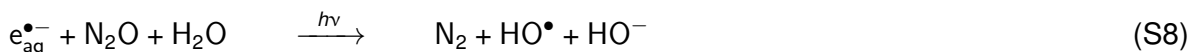


Supplementary Figure 12: Generation, characterization, and detection of the hydrated electron $e_{\text{aq}}^{\bullet-}$ through 355 nm laser photoionization of $10 \mu\text{M}$ (c_0) quercetin in 50 mM aqueous Triton TX-100 micellar solution. Graph (a): main plot, calibrated spectrum of $e_{\text{aq}}^{\bullet-}$ with the yellow circle indicating the chosen observation wavelength 824 nm; inset, relative $e_{\text{aq}}^{\bullet-}$ yield as function of the laser intensity \mathcal{I} overlaid with fit curve of biphotonic model, fit parameters without significance. Graph (b): dots, experimental absorption traces A_{824} at $\mathcal{I} = 461 \text{ mJ cm}^{-2}$ in solution saturated with argon (cyan) and N_2O (green); thin line, difference of the two measurements, corresponding to the pure $e_{\text{aq}}^{\bullet-}$ absorption at 824 nm; thick curve, fit to a first-order decay. Experimental pH, 6.5. For further explanation, see the text.

This calibration is facilitated by the strong absorption of $e_{\text{aq}}^{\bullet-}$. The spectrum of $e_{\text{aq}}^{\bullet-}$ was measured independently by laser flash photolysis of water at 266 nm,^[6] and calibrated by equating the maximum with the recently reported value of $22700 \text{ M}^{-1} \text{ cm}^{-1}$;^[7] it is displayed in the main plot of Supplementary Figure 12a. We did not monitor $e_{\text{aq}}^{\bullet-}$ at the maximum but

at 824 nm, where our detection system exhibits a better sensitivity on account of a spike in the emission spectrum of our light source.

The absorptions of $e_{\text{aq}}^{\bullet-}$ and all other transients were separated by a simple procedure, which Supplementary Figure 12b illustrates. Its essence is a difference experiment that draws on Supplementary Equation S8,



N_2O is a specific scavenger of $e_{\text{aq}}^{\bullet-}$, and the reaction products are completely transparent in the visible and near-uv range. Carrying out the same photoionization experiment (i.e., with identical flash parameters) on the same solution twice, first under argon and then after saturation with N_2O , yields the absorption trace of all species except $e_{\text{aq}}^{\bullet-}$ (in the second run) and the pure $e_{\text{aq}}^{\bullet-}$ trace (as the point-by-point difference of both traces). Because the scavenging is diffusion controlled, the saturation concentration of N_2O in water suffices to complete the blanking out of $e_{\text{aq}}^{\bullet-}$ well within the duration of our laser pulse.^[8]

We have already reported examples of the success of this procedure in micellar systems where it proved possible completely to eliminate "pathological" transient background effects near an insolubility limit.^[8,9] It might be thought that a different secondary chemistry should result from the replacement of $e_{\text{aq}}^{\bullet-}$, which is a strongly reducing radical, by the strongly oxidizing HO^\bullet . However, our substrates are confined to the micelles; and $e_{\text{aq}}^{\bullet-}$, hence also HO^\bullet , are separated from them by the micelle–water interface. Consistent with this, we could not detect any such secondary chemistry in control experiments, for example, by comparing the kinetics in the difference spectrum with the kinetics under argon and the $e_{\text{aq}}^{\bullet-}$ absorption separated through the spectrum of Supplementary Figure 12a.

The dependence of the $e_{\text{aq}}^{\bullet-}$ yield on the laser intensity is explored in the inset of Supplementary Figure 12a. The apparent negative intercept indicates a biphotonic process.^[6] No quantum yield can be extracted owing to the lack of a calibrated absorption spectrum of the S_1 excited state, but it is evident that up to 40 % of the substrate can be ionized by a single laser flash. The method is thus well suited as a radical generator in our systems.

As follows from Supplementary Equation S6, the substrate radicals should be formed in a concentration equal to $[e_{\text{aq}}^{\bullet-}]$, which allows a straightforward calibration of their extinction coefficients. If, however, the photoionization were accompanied by a direct photocleavage (i.e., homolysis) of phenolic O—H bonds as formulated in Supplementary Equation S9



this approach would give wrong results. Unfortunately, H^\bullet is as transparent in our spectral observation range as is HO^\bullet ; and control experiments by scavenging either H^\bullet or the antioxidant-derived radicals proved infeasible in our micellar system, as opposed to homogeneous aqueous solution where we were able to establish the absence of the process of Supplementary Equation S9 for quercetin itself.^[10] Based on the known fact that protic solvents strongly suppress phenolic homolyses,^[11,12] we regard it as improbable that they

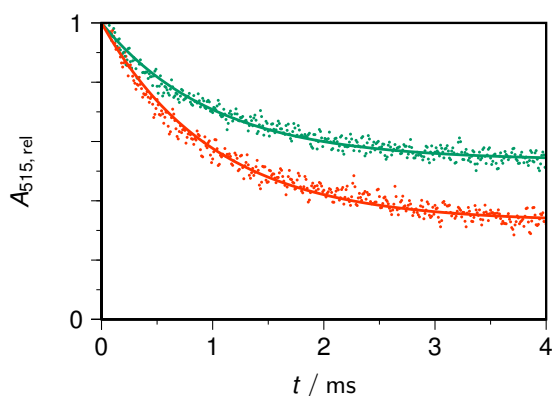
contribute to a significant degree in our systems on account of the TX-100 structure and the penetration of water into its micelles; but if that surmise were wrong, it would not falsify any of our results on the structures and kinetics of the radicals investigated herein.

In the example of Supplementary Figure 12b, the lifetime of $e_{\text{aq}}^{\bullet-}$ is slightly longer than 1 μs . With decreasing pH, the disappearance becomes faster because $e_{\text{aq}}^{\bullet-}$ is scavenged in a diffusion-controlled reaction with protons to give H^\bullet . By the same experiments as described above for HO^\bullet , we established that H^\bullet does not cause any observable secondary chemistry in our systems. Down to approximately pH 3, the $e_{\text{aq}}^{\bullet-}$ decay is slow enough for the quantitative determination of its initial concentration with sufficient precision for calibrating the concentration of the antioxidant radicals.

In the pH range from 3 to 6.5, the $e_{\text{aq}}^{\bullet-}$ concentration remains constant at given laser energy, which facilitates comparisons. Evidently, the intermediate S_1 state absorbing the second (i.e., the ionizing) photon does not undergo a proton transfer that significantly changes its absorption spectrum at 355 nm. When the pH of the solution rises, the $e_{\text{aq}}^{\bullet-}$ yield invariably increases as the first pK_a is passed (compare, Supplementary Figures 2b–5b). It is to be expected that the photoionization of an anion is easier than that of a neutral molecule, but neither absolute nor relative quantum yields can be extracted from these experiments because the S_1 spectra are unavailable.

3.2 Radical Stabilities

The neutral radicals and radical anions slowly decay, as manifest from decreases of their absorbances towards about one-third (acidic solution) to one-half (neutral to basic solution) of the initial values (compare Supplementary Figure 13). The rate constant does not depend on pH and is $1.00 \times 10^3 \text{ s}^{-1}$ for quercetin. Considering that we recorded the transient spectra and investigated the deprotonations of the neutral radicals on a 50 times shorter timescale, the instability evidenced by Supplementary Figure 13 is negligible.



Supplementary Figure 13: Stabilities of the dominant neutral radicals (red, pH 3.0) and radical anions (green, pH 8.5) of quercetin in 50 mM TX-100 micelles. The normalized initial absorbances at 515 nm correspond to actual absorbances of about 10^{-2} , and the solid curves are global monoexponential fits with a lifetime of 1.00 ms. For further explanation, see the text.

3.3 Deprotonation Kinetics of NR3

Figure 14 displays combined pH and time dependences for NR3 deprotonation of the other substrates besides quercetin Q whose positions 3 and 4' are not blocked by substitution, namely, azaleatin Q $\bar{5}$ (14a), rhamnetin Q $\bar{7}$ (14b), rhamnazin Q $\bar{3'7}$ (14c), and isorhamnetin Q $\bar{3}$ (14d).

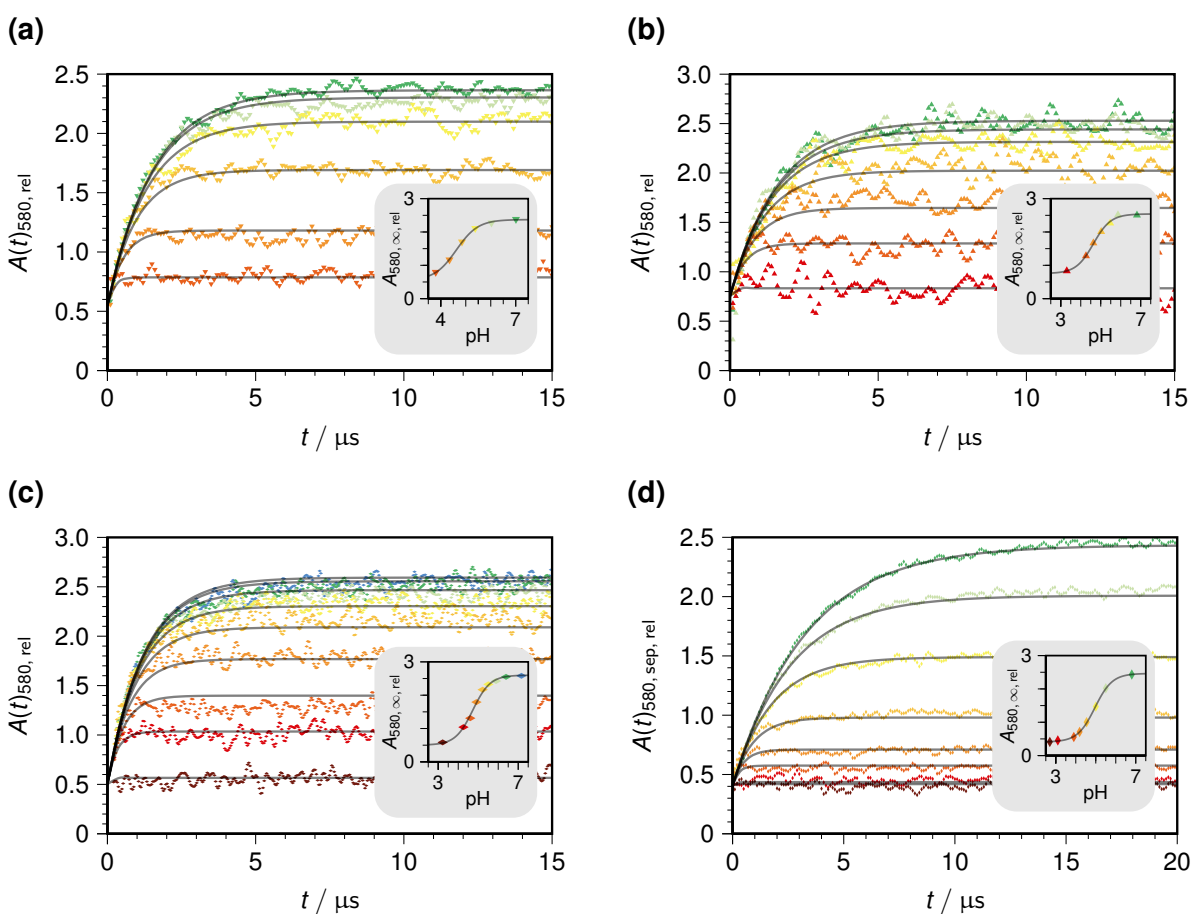
For convenience, the fit functions given in the main article are repeated here as Equation S10 for the titration curves,

$$A_{\lambda, \infty, \text{rel}} = \frac{A_{\lambda, \infty}}{A_{\lambda', \infty}} = \frac{\alpha}{1 + 10^{\text{pH} - \text{p}K_a}} + \frac{\beta}{1 + 10^{\text{p}K_a - \text{pH}}} \quad (\text{S10})$$

and as Equation S11 for the kinetics.

$$A(t)_{\lambda, \text{rel}} = A_{\lambda, \infty, \text{rel}} + \frac{\alpha - \beta}{1 + 10^{\text{p}K_a - \text{pH}}} \times \exp[-k_{\text{dep}} (1 + 10^{\text{p}K_a - \text{pH}}) t] \quad (\text{S11})$$

For Figure 14, λ and λ' are 580 and 515 nm.



Supplementary Figure 14: Deprotonation of the neutral radicals NR3 to give the radical anions RAN34'. Graph (a), azaleatin Q $\bar{5}$; graph (b), rhamnetin Q $\bar{7}$; graph (c), rhamnazin Q $\bar{3'7}$; graph (d), isorhamnetin Q $\bar{3}$. Insets, titration curves of the end values $A_{580, \infty, \text{rel}}$ at 580 nm relative to those at 515 nm; main plots, traces $A(t)_{580, \text{rel}}$ relative to the same reference, each with the same color code as in the pertaining inset. Best fit $\text{p}K_a$ (Equation S10) and rate constant k_{dep} (Equation S11): (a), 4.62 and $6.4 \times 10^5 \text{ s}^{-1}$; (b), 4.63 and $6.2 \times 10^5 \text{ s}^{-1}$; (c), 4.73 and $8.1 \times 10^5 \text{ s}^{-1}$; (d), 4.95 and $3.0 \times 10^5 \text{ s}^{-1}$. For further explanation, see the text.

4 Quantum-Mechanical Calculations

We used the Gaussian 16 program^[13] for all our DFT calculations. Unless noted otherwise, the level of theory was (U)B3LYP/6-311++g(2d,2p) and all computations were performed in the solvent MeOH with the IEFPCM model. After geometry optimization, frequencies were calculated; if the analytical gradients used in the latter step indicated that a stationary point was narrowly missed, the cycle was repeated. Lastly, TDDFT (15 states) computations on the stationary points yielded the transition wavelengths λ_i and oscillator strengths ρ_i .

It is convenient to convert wavelengths λ to wavenumbers $\tilde{\lambda}$ with Supplementary Equation S12,

$$\tilde{\lambda} [\text{in cm}^{-1}] = \frac{10^7}{\lambda [\text{in nm}]} \quad (\text{S12})$$

The formula (Supplementary Equation S13) to obtain the spectra $\varepsilon(\tilde{\lambda})$ from the list of $(\tilde{\lambda}_i, \rho_i)$ contains a width parameter $\tilde{\sigma}$ and a shift parameter \tilde{s} , both in units of cm^{-1} . For a given radical, we kept $\tilde{\sigma}$ and \tilde{s} constant.

$$\varepsilon(\tilde{\lambda}) [\text{in M}^{-1}\text{cm}^{-1}] = \frac{1.3063 \times 10^8}{\tilde{\sigma}} \sum_i \rho_i \exp \left[- \left(\frac{\tilde{\lambda} - \tilde{s} - \tilde{\lambda}_i}{\tilde{\sigma}} \right)^2 \right] \quad (\text{S13})$$

All spectra of Supplementary Figure 15–16 were calculated with $\tilde{\sigma}$ equal to 3226 cm^{-1} (0.4 eV, i.e., the default value of Gaussian 16).

4.1 Energy Comparisons between Gaussian 03 and Gaussian 16

Gaussian 03 calculations on the neutral radicals NRx of quercetin in water gave a stability order $\text{NR3} < \text{NR4}' < \text{NR3}' < \text{NR7} < \text{NR5}$, with Gibbs free energies relative to NR3 being 1.2, 3.0, 11.0 and 11.2 kcal/mol.^[5] However, when we repeated these calculations with Gaussian 16 using exactly the same geometry (which was fully specified in the original publication), quantum-mechanical model and basis set (B3LYP/6-311+g(d,p)), thermochemical scaling factor (0.9806) and solvent model (PCM), we obtained a stability order with NR3 and NR4' interchanged and deviations between our Gaussian 16 and the reported Gaussian 03 Gibbs free energies that were substantial for NR3 (+2.9 kcal/mol) and NR5 (+4.4 kcal/mol). This Section summarizes our attempts to find the reason.

Supplementary Table 1 first compares the electronic energies $EE(\text{vacuum})$ to ensure the absence of misprints in the published^[5] geometries. The very small discrepancies of $0.01 \pm 0.02 \text{ kcal/mol}$ rule out this source of errors.

Next, Supplementary Table 2 juxtaposes the results on the thermal corrections C_T to the Gibbs free energies. There are differences, which we ascribe to two factors. First, the Gaussian 03 calculations apparently used the correction for the frequencies in vacuum

Supplementary Table 1: Comparison between electronic energies EE in vacuum calculated for quercetin radicals with Gaussian 16 and reported for Gaussian 03^[5]

Radical	Gaussian 03 ^[a]	Gaussian 16	Comparison Δ ^[b] in kcal/mol
	$EE(\text{vacuum})$ in Ha	$EE(\text{vacuum})$ in Ha	
NR3	-1103.872719	-1103.872738	-0.01
NR3'	^[c]	-1103.882151	n/a
NR4'	-1103.8861223	-1103.886143	-0.01
NR5	-1103.8505164	-1103.850473	0.03
NR7	-1103.8638607	-1103.863829	0.02

^[a] Values from the Supporting Information of Ref 5 ^[b] Difference between the values computed with Gaussian 16 and reported for Gaussian 03^[5] ^[c] Value not specified

also for the solution. Second, the calculations were not really done at a stationary point because the geometry optimization was apparently performed at a slightly lower level than the frequency analysis and PCM calculation, 6-31+g(d,p) instead of 6-311+g(d,p). Despite these problems, differences C_T cannot account for the stability inversion of NR3 and NR4' although they favour the latter over the former by about 0.3 kcal/mol.

Supplementary Table 2: Comparison between thermal corrections to Gibbs Free Energy C_T calculated for quercetin radicals with Gaussian 16 and reported for Gaussian 03^[5]

Radical	Gaussian 03 ^[a]	Gaussian 16		Comparisons	
	$C_T(\text{vacuum})$ in Ha	$C_T(\text{vacuum})$ in Ha	$C_T(\text{water})$ in Ha	Δ_1 ^[b] in kcal/mol	Δ_1 ^[c] in kcal/mol
NR3	0.165424	0.165572	0.163998	0.09	-0.89
NR3'	0.166151	0.167132	0.166004	0.62	-0.09
NR4'	0.167690	0.167060	0.165835	-0.40	-1.16
NR5	0.164050	0.164430	0.163426	0.24	-0.39
NR7	0.165045	0.165293	0.163102	0.16	-1.22

^[a] Values from the Supporting Information of Ref 5 ^[b] Difference between the values in vacuum computed with Gaussian 16 and reported for Gaussian 03^[5] ^[c] Difference between the values computed with Gaussian 16 in water and reported for Gaussian 03 in vacuum only^[5]

This leaves the electronic energy $EE(\text{water})$ as the explanation for the discrepancy in the stability order. Because of the absence (see Supplementary Table 1 above) of a version effect on $EE(\text{vacuum})$, this pinpoints changes in the implementation and/or parametrization

of the PCM model that were introduced in Gaussian 09 (and retained, possibly modified again, in Gaussian 16) as the underlying reason. Supplementary Table 3 provides numerical corroboration. It is evident that the differential rise in $EE(\text{water})$ by 2.9 kcal/mol between NR3 and NR4' is more than twice as large than the stability difference calculated by Gaussian 03, leading to the observed inversion.

Supplementary Table 3: Comparison between electronic energies EE in water calculated for quercetin radicals with Gaussian 16 and and reported for Gaussian 03^[5]

Radical	Gaussian 03 ^[a] $EE(\text{water})$ ^[b] in Ha	Gaussian 16 $EE(\text{water})$ in Ha	Comparison Δ ^[c] in kcal/mol
NR3	-1103.902902	-1103.896811	3.82
NR3'	-1103.898842	-1103.897472	0.86
NR4'	-1103.903187	-1103.901760	0.90
NR5	-1103.883714	-1103.876146	4.75
NR7	-1103.884922	-1103.882595	1.46

^[a] Values from the Supporting Information of Ref 5 ^[b] Specified as "total free energy in solution: with all non-electrostatic terms" in Ref 5 ^[c] Difference between the values computed with Gaussian 16 and reported for Gaussian 03^[5]

We further checked whether the old Gaussian 03 results can be obtained by using Gaussian 16 in compatibility mode (keyword "G03defaults"; this also necessitates numerical second derivatives instead of analytical ones, keyword "Freq=Numer"). Supplementary Table 4 collects the results for the procedure of Ref 5. As is evident, the values for $EE(\text{water})$ displays a nearly constant offset of -10.80 ± 0.09 kcal/mol relative to the old ones, which indicates some change of the SCRF parameters even in compatibility mode. However, a constant offset plays no role when energy differences between radicals are considered; and on the basis of $EE(\text{water})$ alone, it would thus clearly be possible to reproduce the old energy order. That this does not work at the fixed geometry is solely due to C_T , which exhibits differences large enough to change the energetic ordering such that NR4' becomes lowest again.

Because according to the Gaussian manual "... it is meaningless to compute frequencies at any geometry other than a stationary point for the method used ... For example, computing 6-311G(d) frequencies at a 6-31G(d) optimized geometry produces meaningless results",^[13] we lastly reoptimized the geometries specified in Ref 5 with Gaussian 16 in Gaussian 03 compatibility mode and carried out the remainder of these calculations in the same mode. We restricted these comparisons to the three most important radicals NR3, NR3', and NR4'. As can be seen in Supplementary Table 5, this approach led to a near-constant decrease of $EE(\text{water})$ by as much as 1.2 kcal/mol but — in accordance

Supplementary Table 4: Comparisons between thermal corrections to Gibbs Free Energy C_T and electronic energy EE in water calculated for quercetin radicals with Gaussian 16 in compatibility mode (G03defaults) at the fixed geometry specified in Ref 5 and reported for Gaussian 03^[5]

Radical	Gaussian 16 compatibility mode		Comparisons		
	C_T (water) in Ha	EE (water) in Ha	$\Delta_1^{[a]}$ in kcal/mol	$\Delta_1^{[b]}$ in kcal/mol	$\Delta_1^{[c]}$ in kcal/mol
NR3	0.163898	-1103.920160	-0.96	-10.83	1.33
NR3'	0.163591	-1103.915994	-1.61	-10.76	3.76
NR4'	0.161946	-1103.920335	-3.60	-10.76	(0)
NR5	0.159952	-1103.901069	-2.57	-10.89	10.84
NR7	0.162124	-1103.902076	-1.83	-10.76	11.57

^[a] Differences between the second column of this Table and the second column of Supplementary Table 2 (values from the Supporting Information of Ref 5) ^[b] Differences between the third column of this Table and the second column of Supplementary Table 3 (values from the Supporting Information of Ref 5) ^[c] Sums of the values in the second and third columns of this Table relative to their minimum value

with expectation based on the above passage from the manual — to changes in C_T that amounted to more than just a constant offset, such that the reported stability order was obtained, albeit with differences in ΔG of typically ± 0.6 kcal/mol.

Supplementary Table 5: Comparisons between thermal corrections to Gibbs Free Energy C_T and electronic energy EE in water calculated for quercetin radicals with Gaussian 16 in compatibility mode (G03defaults) after reoptimizing the geometry specified in Ref 5 and reported for Gaussian 03^[5]

Radical	Gaussian 16 compatibility mode		Comparisons		
	C_T (water) in Ha	EE (water) in Ha	$\Delta_1^{[a]}$ in kcal/mol	$\Delta_1^{[b]}$ in kcal/mol	$\Delta_1^{[c]}$ in kcal/mol
NR3	0.162332	-1103.921940	-1.94	-11.95	(0)
NR3'	0.163983	-1103.918036	-1.36	-12.04	3.49
NR4'	0.163519	-1103.922316	-2.62	-12.00	0.51

^[a] Differences between the second column of this Table and the second column of Supplementary Table 2 (values from the Supporting Information of Ref 5) ^[b] Differences between the third column of this Table and the second column of Supplementary Table 3 (values from the Supporting Information of Ref 5) ^[c] Sums of the values in the second and third columns of this Table relative to their minimum value

Because the SCRF convergence rate of Gaussian 16 appears to be so much faster than that of Gaussian 03 was, the questions of whether a change of basis set is necessary or whether C_T needs to be calculated in vacuum instead of in the medium are no longer important for molecules of this size. The changes of EE (water) in Supplementary Table 4 are clear indications of a reparametrization of the SCRF model; but it is not believable that a newer program version would produce worse results with respect to one of its key output

elements (the electronic energy) than the more than ten years older antepenultimate version. On these grounds, we surmise that the "better" results of the older version are not caused by that version being better but by accidental error compensations in it.

4.2 Separating the Energy Contributions

In detail, the numbers for the separation discussion in the main article are the following. The Gibbs free energies are specified relative to the reference points in Figure 2b of the main article. Comparisons are only made between near-identical conjugated systems, and all errors are r.m.s. errors.

4.2.1 Intrinsic electronic difference between NR3' and NR4'

- Quercetin Q
 ΔG° (NR3'), 2.0 kcal/mol; ΔG° (NR4'), 0.0 kcal/mol
 Difference, 2.0 kcal/mol; all hydrogen bonds intact
 - Rhamnetin Q $\bar{7}$
 ΔG° (NR3'), 2.9 kcal/mol; ΔG° (NR4'), 0.0 kcal/mol
 Difference, 2.9 kcal/mol; all hydrogen bonds intact
 - Tamarixetin Q $\bar{4'}$ and Isorhamnetin Q $\bar{3'}$
 - Q $\bar{4'}$: ΔG° (NR7), 7.9 kcal/mol; ΔG° (NR3'), 3.5 kcal/mol
 Difference, 4.4 kcal/mol; catechol hydrogen bond missing, all others intact
 - Q $\bar{3'}$: ΔG° (NR7), 8.1 kcal/mol; ΔG° (NR4'), 1.1 kcal/mol
 Difference, 7.0 kcal/mol; catechol hydrogen bond missing, all others intact
- For this pair, NR3' is thus less stable than NR4' by 2.6 kcal/mol.

Averaging the three cases gives a stability difference of 2.5 ± 0.4 kcal/mol.

4.2.2 Catechol hydrogen bond in NRx

- Quercetin Q and isorhamnetin Q $\bar{3'}$
 - Q: ΔG° (NR7), 11.1 kcal/mol; ΔG° (NR4'), 0.0 kcal/mol
 Difference, 11.1 kcal/mol; all hydrogen bonds intact
 - Q $\bar{3'}$: ΔG° (NR7), 8.1 kcal/mol; ΔG° (NR4'), 1.1 kcal/mol
 Difference, 7.0 kcal/mol; catechol hydrogen bond missing, all others intact
- For this pair, NR4' without the catechol bond is thus less stable by 4.1 kcal/mol.
- 3-O-methylquercetin Q $\bar{3}$ and 3,3'-di-O-methylquercetin Q $\bar{33'}$
 - Q $\bar{3}$: ΔG° (NR7), 11.2 kcal/mol; ΔG° (NR4'), 0.0 kcal/mol
 Difference, 11.2 kcal/mol; all hydrogen bonds except O³H ··· O=C intact
 - Q $\bar{33'}$: ΔG° (NR7), 6.7 kcal/mol; ΔG° (NR4'), 0.0 kcal/mol

Difference, 6.7 kcal/mol; catechol hydrogen bond and $O^3H \cdots O=C$ missing, $O^5H \cdots O=C$ intact

For this pair, NR4' without the catechol bond is thus less stable by 4.5 kcal/mol.

- Quercetin Q and tamarixetin $Q\bar{4}'$

- Q: ΔG° (NR7), 11.1 kcal/mol; ΔG° (NR3'), 2.0 kcal/mol

- Difference, 9.1 kcal/mol; all hydrogen bonds intact

- $Q\bar{4}'$: ΔG° (NR7), 7.9 kcal/mol; ΔG° (NR3'), 3.5 kcal/mol

- Difference, 4.4 kcal/mol; catechol hydrogen bond missing, all others intact

For this pair, NR3' without the catechol bond is thus less stable by 4.7 kcal/mol.

Averaging the three cases gives a stability difference of 4.4 ± 0.3 kcal/mol.

4.2.3 Hydrogen bond between O^5H and carbonyl in NRx

- Quercetin Q

- ΔG° (NR5), 14.2 kcal/mol; ΔG° (NR7), 11.1 kcal/mol

- Difference, 3.1 kcal/mol; no change of hydrogen bonds other than for $O^5H \cdots O=C$

- Isorhamnetin $Q\bar{3}'$

- ΔG° (NR5), 11.6 kcal/mol; ΔG° (NR7), 8.1 kcal/mol

- Difference, 3.5 kcal/mol; no change of hydrogen bonds other than for $O^5H \cdots O=C$

- Tamarixetin $Q\bar{4}'$

- ΔG° (NR5), 11.7 kcal/mol; ΔG° (NR7), 7.9 kcal/mol

- Difference, 3.8 kcal/mol; no change of hydrogen bonds other than for $O^5H \cdots O=C$

Averaging the three cases gives a stability difference of 3.5 ± 0.3 kcal/mol.

4.2.4 NR3 (compounded energy)

- Quercetin Q

- ΔG° (NR7), 11.1 kcal/mol; ΔG° (NR3), 2.5 kcal/mol

- Difference, 8.6 kcal/mol; no change of hydrogen bonds other than for $O^3H \cdots O=C$

- Isorhamnetin $Q\bar{3}'$

- ΔG° (NR7), 8.1 kcal/mol; ΔG° (NR3), 0.0 kcal/mol

- Difference, 8.1 kcal/mol; no change of hydrogen bonds other than for $O^3H \cdots O=C$

- Tamarixetin $Q\bar{4}'$

- ΔG° (NR7), 7.9 kcal/mol; ΔG° (NR3), 0.0 kcal/mol

- Difference, 7.9 kcal/mol; no change of hydrogen bonds other than for $O^3H \cdots O=C$

Averaging the three cases gives a stability difference of 8.2 ± 0.3 kcal/mol. The gain by the electronically more stable radical NR3 is partly offset by the unavoidable loss of the

hydrogen bond between O³H and the carbonyl oxygen.

4.2.5 Catechol hydrogen bond in RAN_{xy}

- Quercetin Q and isorhamnetin Q^{3̄}
 - Q: ΔG° (RAN37), 6.4 kcal/mol; ΔG° (RAN34'), 0.0 kcal/mol
Difference, 6.4 kcal/mol; all hydrogen bonds intact
 - Q^{3̄}: ΔG° (RAN37), 0.0 kcal/mol; ΔG° (RAN34'), 0.6 kcal/mol
Difference, –0.6 kcal/mol; catechol hydrogen bond lost, all others intact

For this pair, the loss of the catechol bond costs 7.0 kcal/mol.

- Quercetin Q and tamarixetin Q^{4̄}
 - Q: ΔG° (RAN37), 6.4 kcal/mol; ΔG° (RAN33'), 6.6 kcal/mol
Difference, –0.2 kcal/mol; all hydrogen bonds intact
 - Q^{4̄}: ΔG° (RAN37), 0.0 kcal/mol; ΔG° (RAN33'), 7.2 kcal/mol
Difference, –7.2 kcal/mol; catechol hydrogen bond lost, all others intact

For this pair, the loss of the catechol bond costs 7.0 kcal/mol.

The two cases gives exactly the same energy contribution of 7.0 kcal/mol.

4.2.6 Intrinsic electronic difference between RAN33' and RAN34'

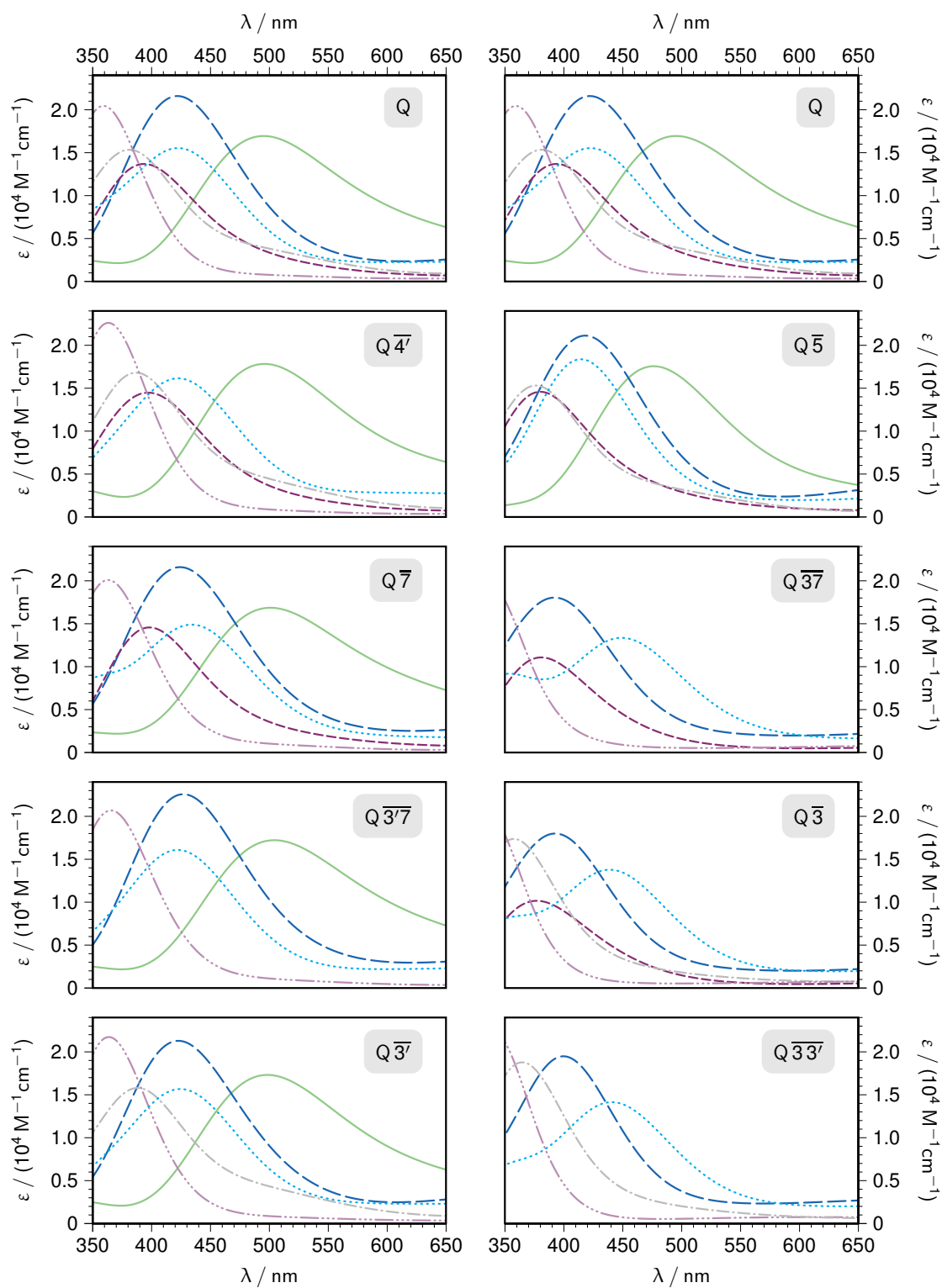
- With catechol hydrogen bond remaining intact
For quercetin Q and rhamnetin Q^{7̄}, RAN33' is higher in energy than RAN34' by 6.6 and 6.5 kcal/mol.
- With catechol hydrogen bond lost
From the data in Section 4.2.5, RAN33' of tamarixetin Q^{4̄} lies 7.2 kcal/mol above RAN37, and RAN34' of isorhamnetin Q^{3̄} lies 0.6 kcal/mol below RAN37. The difference is 7.8 kcal/mol.

Averaging the three cases gives 7.0 ± 0.6 kcal/mol. We have excluded azaleatin Q^{5̄} from this analysis because of the missing hydrogen bond to the end atom of the conjugated system, as opposed to the other three compounds.

4.2.7 Intrinsic electronic difference between RAN3'4' and RAN34'

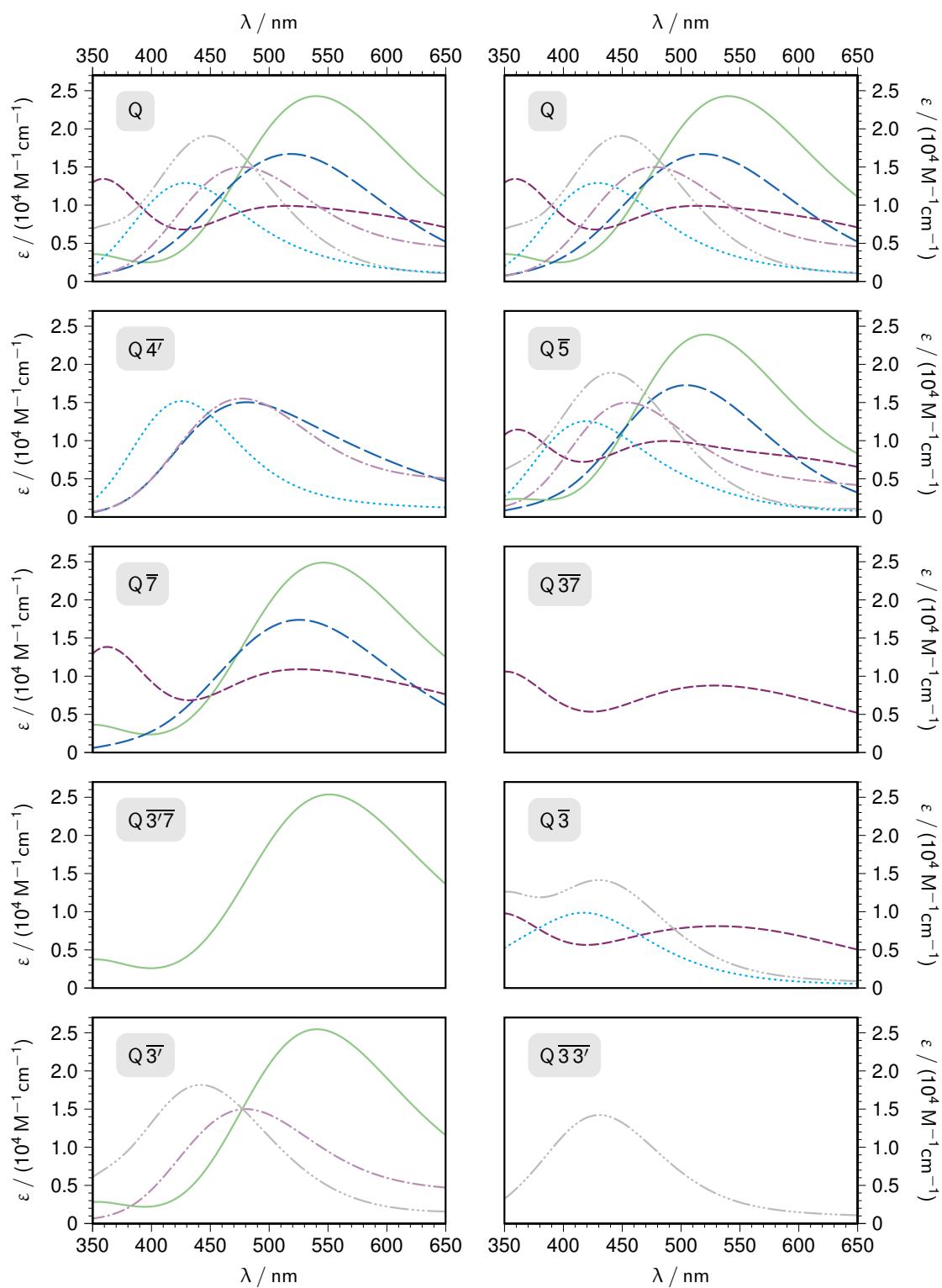
For quercetin Q, azaleatin Q^{5̄}, and Rhamnetin Q^{7̄}, where RAN34' as the lowest-energy radical anion always constitutes the reference point, the difference is 4.9, 5.2, and 4.7 kcal/mol. The average is thus 4.9 ± 0.2 kcal/mol.

4.3 Calculated Spectra of the Radical Cations and Neutral Radicals



Supplementary Figure 15: Calculated absorption spectra (TDDFT, B3LYP/6-311++G(2d,2p), IEFPCM, solvent MeOH) of the neutral radicals NR_x and radical cations RC of quercetin and O-alkylated derivatives thereof. Substrate abbreviation as in Supplementary Figure 11. Line type and color code: NR₃, solid, green; NR_{4'}, long dashed, blue; NR_{3'}, short dashed, violet; NR₇, dot-dash, gray; NR₅, dot-dot-dot-dash, pale violet; RC, dotted, cyan. For further explanation, see the text.

4.4 Calculated Spectra of the Radical Anions



Supplementary Figure 16: Calculated absorption spectra (TDDFT, B3LYP/6-311++G(2d,2p), IEFPCM, solvent MeOH) of the radical anions RAN_{xy} of quercetin and O-alkylated derivatives thereof. Substrate abbreviation as in Supplementary Figure 11. Line type and color code: RAN34', solid, green; RAN33', long dashed, blue; RAN3'4', short dashed, violet; RAN37, dot-dash, pale violet; RAN4'7, dot-dot-dot-dash, gray; RAN3'7, dotted, cyan. For further explanation, see the text.

Supplementary References

- [1] M. Goez, C. Kerzig and R. Naumann, *Angew. Chem. Int. Ed.*, 2014, **53**, 9914–9916.
- [2] T. Morisue, Y. Moroi and O. Shibata, *J. Phys. Chem.*, 1994, **98**, 12995–13000.
- [3] F. H. Quina, P. M. Nassar, J. B. S. Bonilha and B. L. Bales, *J. Phys. Chem.*, 1995, **99**, 17028–17031.
- [4] S. K. Hait and S. P. Moulik, *J. Surfactants Deterg.*, 2001, **4**, 303–309.
- [5] R. Amorati, A. Baschieri, A. Cowden and L. Valgimigli, *Biomimetics*, 2017, **2**, 9–21.
- [6] C. Kerzig and M. Goez, *Phys. Chem. Chem. Phys.*, 2015, **17**, 13829–13836.
- [7] P. M. Hare, E. A. Price and D. M. Bartels, *J. Phys. Chem. A*, 2008, **112**, 6800–6802.
- [8] T. Kohlmann, R. Naumann, C. Kerzig and M. Goez, *Photochem. Photobiol. Sci.*, 2017, **16**, 185–192.
- [9] M. Goez, D. von Ramin-Marro, M. Schiewek and M. H. O. Musa, *Z. Phys. Chem. (Muenchen, Ger.)*, 2014, **228**, 193–207.
- [10] T. Kohlmann and M. Goez, *Chem. Eur. J.*, 2020, **26**, 17428–17436.
- [11] J.-C. Mialocq, J. Sutton and P. Goujon, *J. Chem. Phys.*, 1980, **72**, 6338–6345.
- [12] C. Grieco, A. T. Hanes, L. Blancafort and B. Kohler, *J. Phys. Chem. A*, 2019, **123**, 5356–5366.
- [13] M. J. Frisch, G. W. Trucks, H. B. Schlegel, G. E. Scuseria, M. A. Robb, J. R. Cheeseman, G. Scalmani, V. Barone, G. A. Petersson, H. Nakatsuji, X. Li, M. Caricato, A. V. Marenich, J. Bloino, B. G. Janesko, R. Gomperts, B. Mennucci, H. P. Hratchian, J. V. Ortiz, A. F. Izmaylov, J. L. Sonnenberg, D. Williams-Young, F. Ding, F. Lipparini, F. Egidi, J. Goings, B. Peng, A. Petrone, T. Henderson, D. Ranasinghe, V. G. Zakrzewski, J. Gao, N. Rega, G. Zheng, W. Liang, M. Hada, M. Ehara, K. Toyota, R. Fukuda, J. Hasegawa, M. Ishida, T. Nakajima, Y. Honda, O. Kitao, H. Nakai, T. Vreven, K. Throssell, J. A. Montgomery, Jr., J. E. Peralta, F. Ogliaro, M. J. Bearpark, J. J. Heyd, E. N. Brothers, K. N. Kudin, V. N. Staroverov, T. A. Keith, R. Kobayashi, J. Normand, K. Raghavachari, A. P. Rendell, J. C. Burant, S. S. Iyengar, J. Tomasi, M. Cossi, J. M. Millam, M. Klene, C. Adamo, R. Cammi, J. W. Ochterski, R. L. Martin, K. Morokuma, O. Farkas, J. B. Foresman and D. J. Fox, *Gaussian 16 Revision C.01*, 2016, Gaussian Inc. Wallingford CT.

Danksagung

An dieser Stelle möchte ich einen Dank an alle die richten, die mich während meiner Promotionszeit begleitet haben.

Ein besonderer Dank gilt meinem Doktorvater Prof. Dr. Martin Goetz für den Freiraum bei der Wahl der ausgesprochen interessanten Teilprojekte und bei der Bearbeitung dieser, außerdem auch für fortwährende ausgezeichnete Betreuung. Ich danke ihm für die stetige Bereitschaft zu konstruktiven Diskussionen, für die zahlreichen nützlichen Hinweise und die gute Zusammenarbeit bei der Veröffentlichung der Ergebnisse. Das alles hat maßgeblich zum Gelingen dieser Arbeit beigetragen.

Bedanken möchte ich mich auch bei meinen Mitstudenten und Kollegen für die schöne gemeinsame Zeit, sowohl bei der Arbeit als auch bei außeruniversitären Aktivitäten.

Mein außerordentlicher Dank gilt meiner Familie und meinen Freunden für die immerwährende Unterstützung während der gesamten Promotionszeit und dafür, dass sie stets einen Ausgleich zu anstrengenden Arbeitsstunden geschaffen haben. Bedanken möchte ich mich auch besonders bei Jenny für ihre stete Geduld für lange Arbeitszeiten, ihre motivierenden Worte und den beständigen Rückhalt, den sie mir gibt.

Lebenslauf

Persönliche Angaben

Name	Tim Kohlmann
Geburtsdatum	28.01.1994
Geburtsort	Dessau
Staatangehörigkeit	Deutsch

Bildungsweg

seit 2/2018	Doktorand und wissenschaftlicher Mitarbeiter an der Martin-Luther-Universität Halle- Wittenberg in der Arbeitsgruppe von Prof. Dr. Martin Goetz
10/2015 - 2/2018	Masterstudium Chemie an der MLU Halle-Wittenberg Abschluss: Master of Science (Note: 1,2) Thema der Masterarbeit: 2-Aminoanthracen in SDS-Mizellen - Fluoreszenzkinetik und Photoionisierung in einem kompartimentierten System
10/2012 - 10/2015	Bachelorstudium Chemie an der MLU Halle-Wittenberg Abschluss: Bachelor of Science (Note: 1,0) Thema der Bachelorarbeit: Untersuchungen zur Photoionisierung von 3-Aminoperylen
06/2012	Allgemeine Hochschulreife (Note: 1,1), Gymnasium Carolinum Bernburg;

Sonstiges

10/2013 - 2/2018	Stipendiat der Studienstiftung des deutschen Volkes
10/2017 - 12/2017	Praktikum an der Vanderbilt University, Nashville bei Prof. Dr. Jens Meiler und Prof. Dr. Lauren Buchanan
2/2013 - 4/2013	Praktikum an der Vanderbilt University, Nashville bei Prof. Dr. Jens Meiler

Publikationsliste

10. T. Kohlmann, M. Goetz, "Do equilibrium and rate constants of intramolecular reactions depend on micelle size?", *Phys. Chem. Chem. Phys.*, **2021**, 23, 9709-9714.
9. T. Kohlmann, M. Goetz, "Laser Access to Quercetin Radicals and Their Repair by Co-antioxidants", *Chem. Eur. J.*, **2020**, 26, 17428-17436.
8. T. Kohlmann, M. Goetz, "Pyrene–viologen complexes in SDS micelles: quenching parameters and use as probes of aggregation numbers", *Photochem. Photobiol. Sci.*, **2020**, 19, 71-79.
7. T. Kohlmann, M. Goetz, "Combined static and dynamic intramolecular fluorescence quenching: effects on stationary and time-resolved Stern–Volmer experiments", *Phys. Chem. Chem. Phys.*, **2019**, 21, 10075-10085.
6. J. M. Gießel, T. Kohlmann, T. Zeitz, R. Kluge, R. Csuk, "Synthesis of sinapine and its unprecedented ruthenium-catalyzed [2+2] photodimerization", *Mediterr. J. Chem.*, **2019**, 9, 258-265.
5. T. Kohlmann, C. Kerzig, M. Goetz, "Laser-Induced Wurtz-Type Syntheses with a Metal-Free Photoredox Catalytic Source of Hydrated Electrons", *Chem. Eur. J.*, **2019**, 25, 9991-9996.
4. T. Kohlmann, R. Naumann, C. Kerzig, M. Goetz, "3-Aminoperylene and ascorbate in aqueous SDS, one green laser flash ... and action! Sustainably detoxifying a recalcitrant chloro-organic", *Photochem. Photobiol. Sci.*, **2017**, 16, 1613-1622.
3. T. Kohlmann, R. Naumann, C. Kerzig, M. Goetz, "Combined static and dynamic quenching in micellar systems – closed-form integrated rate laws verified using a versatile probe", *Phys. Chem. Chem. Phys.*, **2017**, 19, 8735-8741.
2. T. Kohlmann, R. Naumann, C. Kerzig, M. Goetz, "Green-light ionization of 3-aminoperylene in SDS micelles—a promising access to hydrated electrons despite a myth debunked", *Photochem. Photobiol. Sci.*, **2017**, 16, 185-192.
1. S. Heinze, D. K. Putnam, A. W. Fischer, T. Kohlmann, B. E. Weiner, J. Meiler, "CASP10–BCL2: Fold efficiently samples topologies of large proteins", *Proteins*, **2015**, 83, 547-563.

Eidesstattliche Erklärung

Hiermit erkläre ich an Eides statt, dass ich die vorliegende Arbeit selbstständig und ohne fremde Hilfe verfasst, und keine weiteren als die angegebenen Hilfsmittel und Quellen verwendet habe und die den benutzten Werken wörtlich oder inhaltlich entnommenen Stellen als solche kenntlich gemacht habe.

Die vorliegende Dissertation wurde bisher an keiner anderen Universität oder Hochschule vorgelegt.